Computer Modelling Studies of Gold Nanoclusters, Nanotubes and Nanowires

by

Mokete Abram Mahladisa

RESEARCH DISSERTATION
Submitted in fulfilment of the requirements for the degree of
DOCTOR OF PHILOSOPHY
in
Physics
in the
Faculty of Sciences & Agriculture
(School of Physical & Mineral Sciences)
at the
UNIVERSITY OF LIMPOPO

SUPERVISOR: Professor P.E. Ngoepe
CO-SUPERVISOR: Doctor L. Ackermann

2011

Abstract

The importance of gold for scientific uses is of fundamental importance to research and technology developments. The bulk gold shows reluctance to participate in chemical reactions, the effect which has been corrected by the change in the size towards nanoclusters. It is therefore imperative that the structure of gold nanomaterials is understood for better applications in catalysis and other developments. Molecular dynamics and the density functional theory have proven to be good tools in computational material science and have thus been used to greater lengths.

Molecular dynamics simulations on different gold nanoclusters and nanotubes were successfully carried out at different thermodynamic conditions. The effect of size on the melting of materials was duly tested and our results to some extend agree with what has already been reported. Gold nanoclusters show melting below the bulk and the melting temperatures increase with cluster size. However, the Au_{55} cluster shows different results in that it melts above the bulk due to structural reconstruction. The structure of the clusters changes from spherical shapes to tetragonal or face centred cubic (fcc) structures. Gold nanotubes show no resistance to temperature and different configurations are obtained in different ensembles. Single wall nanotubes form spherical clusters in the NVT while the NPT conditions give patches of clusters at elevated temperatures. The multi wall nanotubes also form spherical clusters in the NVT but fcc structures are obtained in the NPT Berendsen ensemble towards melting.

Ab initio calculations in $DMOL^3$ code on different gold nanoclusters show the stability of the clusters to increase with size and the Au_3 and Au_8 clusters contain the most stable structures. The Au-Au bond length in the dimer was obtained to within reasonable agreement with experiments and other theoretical works. Doping of the clusters further improved their stability although different impurities give different observations.

The QMERA code calculations show that a gold atom on top of the surface causes slanting of the outer MD layers. The morphology of the quantum atoms also changes as compared to the neutral surface and the results are compared by the $DMOL^3$ code which confirms the QMERA results.

Contents

List of Figures

List Tables

Declaration

I declare that the thesis hereby submitted to the University of Limpopo, for the degree of Doctor of Philosophy in Physics has not been previously submitted by me for a degree at this or any other university; that it is my own work in design and execution, and that all material contained therein has been duly acknowledged.

Mahladisa M.A. (Mr)

Date

Acknowledgements

I would like to acknowledge my supervisor Professor Phuti E. Ngoepe for the chance he offered me in giving me this challenging project, for his guidance, patience and encouragement through good and tough times, and for his innovative thinking when we seemed to be short of good ideas. Let me appreciate the commitment shown by Doctor Lutz Ackermann, the valuable discussions and inputs he gave all the times, for his patience, and for their ability to make time for my consultations.

Let me extend my sincere gratitude to the sponsors of this project: Mintek for their financial support and for involving me in the AuTEK project where three other companies (Anglogold Ashanti, Gold Fields and Harmony Gold) are also involved. This is a new initiative in the world of nanotechnology. The company has involved people with sound scientific knowledge and has occasionally made invaluable additions to the project and therefore that kind of help was what I could not do without. The financial help from the National Research Foundation (NRF) of South Africa has been there for me for the three years and I am grateful for the award granted to me.

Let me in passing thank Professor Nicholas Quirke at Imperial College of London for his inputs and guidance on the project during his visit to South Africa. Doctor Fernando Bresme has been a person I could rely on when I wanted to be reminded of some things I have forgotten. Let me put my heartfelt appreciation to Professor Steve Parker at University of Bath in the United Kingdom for his help with metadise code when the going got tough in the building of gold nanotubes.

I cannot forget my colleagues at the Materials Modelling Centre for their contributions during discussions and special thanks to our systems administrators for making sure all the programs run well for the calculations to finish.

Lastly, let me say thank you to the most valued people in my life, my family at large because singling out a single person will be selfish of me. Thank all of you for your encouragement and patience towards my studies. Modimo a be le lena ka nako tsohle.

Dedication

This thesis is dedicated to me and my whole family.

CHAPTER 1: General Introduction

1.1. Introduction

Gold's attractive colour, bright lustre, and malleability and ductility (to the point of durability) have endeared it to man throughout history. In ancient times, gold was mined exclusively in southern Africa, but apparently to a limited extent within South Africa. The first recorded discovery of gold in South Africa during the modern era occurred on the farm Eersteling, near Polokwane, in the Limpopo Province, during 1871 [Puddephatt 1978]. The discovery of gold in conglomerates on the farm Langlaagte (now Johannesburg) on the Witwatersrand, in 1886, led to the exploitation of the largest gold deposits the world has known to date. South Africa is still the world's largest gold producer, and it was reported to contribute 35% (35 877 tons) of the world's gold production in 1998. The lowest production was reported in 2003 where gold production fell by 6.5% to 373.074 kg. However, gold still accounted for an estimated 37% of dollar export revenue within the country, making gold the largest mineral foreign earner in South Africa by contributing 27.2% in mineral revenues and being responsible for 56% of South Africa's mine labour force [http://contrystudies.us/south-africa/66.html, http://www.mbendi.com/gold.htm].

Gold is specially relevant for both fundamental and applied research and has been important material to mankind both in everyday life and in scientific endeavours. Gold is special in its chemical and physical properties in that in its bulk form it is the most inert and soft metal in relation to its cohesive energy [Soler 2001]. The importance of the metal gold ranges from commercial, medical to scientific use. Because of its beauty, permanence and rarity, gold is still the material of choice for the fabrication of religious artifacts, decorative articles, and jewellery. However, the unique chemical and physical properties offered by this precious metal are increasingly being sought for use in a growing number of industrial and medical applications. These include uses within the fields of nanotechnology, medicine, and electronics for products such as smart-cards, automotive electronics, sensors, medical implants, and drug delivery systems. Scientific applications include the use in catalysis at the nano level.

Gold, the life-blood of South African economy, could hold the key to a new treatment for people suffering from HIV/AIDS and malaria. South African scientists and researchers working within Project AuTEK (Gold Technology) Biomed, and seven local universities are working on a series of gold-based drugs that could be used to fight HIV, while another group has started research into the development of a series of malaria gold-based drugs. Project AuTEK is a joint initiative between Mintek and three of South Africa's biggest mining houses, Anglo Gold Ashanti, Gold Fields and Harmony Gold. Gold-based drugs have demonstrated the ability to inhibit HIV replication in vitro and once fully developed could be considered as a potential choice of therapy for individuals infected with HIV, as it will slow down the progression of HIV. The malaria research project, which is very much on the early stages, intends to prepare gold-based drugs and then screen them to investigate anti-malarial effects. The treatment of humans with gold-based drugs is called Chrysotherapy [The Star 2006].

On the other side, scientists from the University of East Anglia have developed a golden bullet to help in the fight against cancer. This is achieved by adding tiny amounts of gold to an existing cancer drug, and the method was found to boost the power of the drug by 50%. This allows more malignant cells to be killed while healthy tissue is left unharmed. This development will replace chemotherapy which kills off fast growing cells but cannot differentiate between healthy cells and tumours. The metal has also long been used for biological purposes with the treatment of arthritis and as an implant in dentistry [Pudephatt 1978].

The ancient Romans were familiar with the processes for colouring glass by adding gold. Initially colourless, the glass takes on a ruby-red colour when heated in a controlled fashion. The source of this colour is finely divided gold clusters. The light absorption depends on the concerted oscillation of the conducting electrons in all of the gold atoms in the cluster, called plasmon oscillation. Variation of the size, shape, or electrical properties of the particles' surroundings should influence the frequency of the oscillation, and thus the colour of the absorbed light. This could allow for the production of materials that are suitable for use in nanophotonic components, including tiny optoelectronic circuits or optical storage devices.

Gold is one of the most noble metals and is also counted among those with the best electrical properties. These combined features make gold a logical choice for electronic interconnection applications. Naturally the relatively high price of this metal restricts its use to those applications where its unique properties make its use essential. Much of the technology associated with gold plating of electronic contacts and semiconductor devices has been directed toward minimizing use of the amount of metal per component, while striving for maintenance of deposit performance [Blair 2002].

Gold is applied to the surfaces of electronic components in one of the four ways. The first application is through electroplating, the second is by thermal decomposition of a screen-printed paste (thick-film technology), the third by vacuum deposition or thermal decomposition of a metallo-organic compound (thin film-technology) and lastly, by mechanical rolling to form a strip stock from which components can be stamped or punched (initially materials). Electroplating accounts for the greatest consumption of gold among these techniques, since it is generally more versatile than the others and offers more precise control of the precious metal used. The plating solutions employed usually contains potassium cyanide, $KAu(CN)^2$, sometimes referred to as PGC.

Nanoscience and nanotechnology are key interdisciplinary research areas in South Africa, which has recently launched a National Nanotechnology Strategy for the funding and implementation of nanotechnology research and development with the potential to bridge the innovation chasm between basic research and applied technology

Small clusters show properties that differ from those of the bulk. The structural, electronic, optical, thermodynamic, spectroscopic, magnetic, and chemical properties of isolated clusters and their assemblies have revealed unique properties differing from those found in the bulk [Michaelin *et al*. 19999, Luedtke and Landman 1996, Bilalbegović (1998), Zhao *et al*. 2003, Goodman 2004]. Metal nanoclusters containing a few atoms show quantum size effects which give them unique properties and make them interesting candidates for the building blocks of nanostructured materials and nanoelectronic digital circuits [Michaelin *et al*. 1999]. Metallic clusters provide an interesting subject of study because they constitute intermediate systems between isolated atoms and molecules, on the one extreme, and bulk solids, on the other. They have a large ratio of surface to volume atoms, and they often exhibit an interesting phenomenology of their own [Rogan *et al*. 2003, Rodriguez-Lopez *et al*. 2003]. The magnetic behaviour of clusters has higher magnetic moments than the corresponding bulk value mainly due to the reduced atomic coordination. This increases the electron localization and a corresponding reduced valence band width [Rodriguez-Lopez *et al*. 2003].

The regular crystalline packing of atoms, which usually minimises energy in a bulk solid, is known not to last indefinitely as physical size is decreased [Gülseren *et al*. 1998]. Small clusters of some metals were observed to abandon single crystal structures in favour of an icosahedral shape below a critical point and the stability of the icosahedral was also confirmed. The driving force causing this morphological change at small size can generally be traced back to two very distinct sources; firstly, to electronic magic sizes stabilised by filling of shells as in atoms and nuclei, and secondly, to competition between optimal internal packing and minimal surface energy, the latter dominating for sufficiently small size.

Gold clusters have special applications in catalysis when supported on metal oxides such as TiO_2 to form Au/TiO_2 catalyst. Gold shows extraordinary high activity for low-temperature catalytic combustion partial oxidation of hydrocarbons, hydrogenation of unsaturated hydrocarbons, and reduction of nitrogen oxides [Valden *et al*. 1998]. Gold clusters promote the reaction between CO and O_2 to form CO_2 at temperatures as low as 40 K [Goodman 2004, Valden *et al*. 1998, Haruta and Date 2000]. The activity of gold depends on the size of the cluster; when the catalyst is too small or too big it becomes less effective. There is a certain size range for the clusters to be effective. Valden *et al.* have found that the Au/TiO_2 catalyst is effective when the diameter of the cluster is about 3.5 nm (35 Å). The catalytic activity might be attributed to the highly abundant metal/support interface, the presence of ionic gold or to coordinatively unsaturated atoms in small gold clusters. Furthermore, the high catalytic activity of small Au clusters is caused by orbital roughness not necessarily by geometrical (low coordination) roughness.

The most challenging cluster phenomena is perhaps to find the stable structures of these small materials as clusters are known to be unstable even at lower temperatures [Michaelin *et al*. 1999, Garzón *et al*. 1998]. Michaelin *et al*. have found that certain Au nanoclusters between ~19 and 75 atoms in size are disordered in their lowest-energy configuration. The study of different structures of clusters has revealed that small clusters appear to be amorphous instead of crystalline or quasicrystalline structures. Gold clusters appear in different forms, some have icosahedra (*Ih*) form, some appear in decahedral (*Dh*) form and some hexagonal [Michaelin *et al*. 1999, Bilalbegoić 1998]. Icosahedra have been found to be the preferred form for the clusters [Bilalbegoić 1998].

Another aspect that needs more focus from the researchers is the determination of the melting point of nanoclusters and the resistance of the clusters towards high temperatures. It is a general knowledge that small nanomaterials are less stable and have melting points that are lower than the respective bulk materials [Puffat and Borrel 1976, Nakamura *et al*. 2001, Doye and Wales 2001, Cleveland *et al*. 1998, Cleveland *et al*. 1999, Kusche *et al*. 1999, Cortie and van der Lingen 2002, Schmidt *et al*. 1998, Chen and Yan]. Buffat and Borel and Rodriguez-Lopez *et al*. have studied the effect of the size on the melting of the gold particles and found the reduction of melting temperature (T_m) as the particle reduces its size. The size of the particle plays a vital role on the stability and melting of a particular material. Although it is hard to determine or find the minima for small clusters few researchers have found that clusters with a few number of atoms or diameter are less stable [Michaelin *et al*. 1999, Nakamura *et al*. 2001, Doye and Wales 2001].

Nakamura *et al*. have found that wire orientation also plays a role in the stability of the clusters. They built structures of different shapes (zigzag, linear straight and rectangular) and found that the zigzag structure is more stable than structures that are linear and rectangular. The lower melting point in clusters is attributed to the higher proportion of surface atoms than larger particles. Surface atoms have fewer nearest neighbours and are more weakly bound and less constrained in their thermal motion than atoms in the body of a material [Schmidt *et al*. 1998]. Schmidt *et al*. have found that melting of sodium clusters occur on average 33% lower than the bulk material.

It is suggested that the catalytic properties of gold can be improved with the doping of transition metal [Chen and Yan, Yuan *et al.* 2005, Xiang *at al.* 2004]. In order to enhance the stability and improve their chemical activities, or examine the electronic shell structures in mixed gold clusters, many studies have been performed on impurity-doped or mixed gold clusters [Yuan *et al.* 2005]. Additionally, the dopant atom can modify and control the electronic structure of gold clusters, thus changing their chemical reactions for catalytic purposes through the increase of the electronic states around the Fermi level. It is also reported that the delocalization of s- and d-electrons of transition metal atoms considerably enhance the stability of gold (Au) or silicon (Si) clusters doped with transition metal (TM) atoms [Yuan *et al.* 2005]. These bimetallic clusters are particularly important in catalytic applications because of their unique catalytic selectivity, which originates from their unique structure due to the interactions between the two different elements and their composition. The platinum-gold (PtAu) bimetallic clusters (or alloys), which are important catalysts for alkane conversion, C-N coupling, isotope exchange, and NO reduction, were found to have enhanced catalytic activity [Tian *et al.* 2005].

Gold (Au) clusters (with up to seven atoms) were reportedly found to prefer low spin and planar geometry while platinum (Pt) clusters prefer high spin and three-dimensional (3D) structure [Tian *et al.* 2005, Tian *et al.* 2004]. This is attributed to the strong relativistic effect of gold in Au clusters and the involvement of platinum 5d and 6s atomic orbitals in bonding of Pt clusters. The substitution of an Au atom by a Pt atom in Au_7 cluster does not change the essential structure of the gold cluster, *i.e.* the preference for two-dimensional (2D) geometry and low spin, although 3D structures of Au_6Pt are stable. However, the electronic structure of Au_6Pt changes much upon the substitution of a Pt atom. The reactivity of Pt-doped gold cluster is much enhanced with respect to the pure Au cluster. In catalytic applications, Pt was found to be the essential catalytically active component in PtAu bimetallic catalysts [Tian *et al.* 2004].

Nanomaterials are exceptional materials because of their different properties and their special applications in technology. Many of the extraordinary properties attributed to nanotubes are their superlative resilience, tensile strength and thermal stability which have fed fantastic predictions of microscopic robots, dent-resistant car bodies and earthquake-resistant buildings [Collins and Avouris 2000]. Nanotubes have generated a strong interest in their possible applications in nano-electronic and nano-mechanical devises because they exhibit unique electronic and mechanical properties due to their curvature. Because of their very large surface area and curvature nanotubes can absorb large amounts of hydrogen and other species and this makes them the world's smallest gas tanks. Their large length/diameter enables them to be used in composite materials to obtain ultra strong materials. Nanotubes are chemically active materials, and can as such be functionalised with a wide variety of atoms and molecules and can be good transport materials.

Gold nanotubes in particular have attracted great interest because of their important applications in technology, telecommunications, satellites, and their ability to form covalent bonds to thiol–functionalised organic compounds make them an interesting subject of study [Bilalbegović 2003, Senger *et al*. 2004, Goring *et al*. 2004]. Because of their large non-linear optical properties and ultrafast response, gold and silver nanotubes improve optical limiter properties in carbon nanotubes [Chin *et al*. 2005]. Gold nanotube electrodes are used to detect hydrogen peroxide.

Nanowires have attracted a great deal of interest in the past few years because of their importance in fundamental physics and technological applications as molecular electronic devices [Bilalbegović 2000, Bilalbegović 2001, Bilalbegović 2003, Wang *et al*. 2001, Nakamura *et al*. 2001, da Silva *et al*. 2001, Novaes *et al*. 2001]. Nanowires are very important for the advances in various fields of technology and their electrical, thermal conductiveness, as well as mechanical properties are of great scientific and technological interest [Rubio-Bollinger 2001]. Nanowires have melting temperatures lower than the bulk but higher than those of nanoclusters [Bilalbegović 2000]. Several attempts were made on determining the stability and melting temperatures of gold nanowires [Bilalbegović 2000, Bilalbegović 2001, Wang *et al*. 2001, Bilalbegović 1998]. Wang *et al*. have found that nanowires become stable with the increasing wire size and that bigger nanowires behave similar to the bulk material, although some detail differences still exist. Bilalbegovic [Bilalbegović 2000, Bilalbegović 2002] and Wang *et al*. [Wang *et al*. 2002] have studied melting in nanowires extensively and found that nanowires show melting temperatures that are lower than the bulk melting.

The tight binding molecular dynamics (TB-MD) work by da Silva *et al.* [da Silva *et al.* 2001] show that nanowires break under tensile stress. The nanowires form a single five atom chain or necklace through pulling before breaking and the measured force is about 1.8 nN. The breaking of the nanowire shows an increase in the bond distances from ~3.1 Å to ~4.3 Å. Novaes *et al.* [Novaes *et al.* 2001] have done some ab initio work on the influence of impurities on the rupture of a gold nanowire. They found that the Au nanowire always breaks at an Au-Au bond, with a maximum bond length between 3.0 and 3.1 Å. They therefore concluded that the experimentally observed large Au-Au bonds before rupture of the nanowire (~3.6 Å) are probably due to the presence of light impurities (X) forming Au-X-Au bonds.

1.2. Structural Properties

In its bulk form gold is a soft gold and yellow metal with the highest ductility and malleability of any chemical element [Pudephatt 1978]. Figure 1.1 shows some gold nuggets as well as some examples of the applications of gold in jewellery and monetary systems. Gold is atom number 79 and falls under group eleven and period six on the periodic table of elements. The electronic configuration of gold is written as: $1s^2$ $2s^2p^6$ $3s^2p^6d^{10}$ $4s^2p^6d^{10}f^{14}$ $5s^2p^6d^{10}$ $6s^1$ or most commonly $[Xe].4f^{14}.5d^{10}.6s^1$ which then gives the valence of $5d^{10}.6s^1$. The electronic structure is shown in Figure 1.2. The atomic weight of metallic gold is 196.97 $g.mol^{-1}$ while the density and volume respectively are 19.32 $g.cm^{-3}$ and 67.9 Å at room temperature. The bulk gold melts at 1337 K and boils at 3080 K.

Gold crystallises into a face centred cubic (fcc) structure and has the lattice parameter of 4.08 Å (shown in Figure 1.3) and the atomic radius of 1.79 Å. The elecronegativity of the metal is given as 2.54 (Pauling) and 1.42 (Allrod Rochow). The bulk modulus of gold is 171 GPa and the Youngs modulus is 78.5 GPa. Figure 1.3 shows the lattice structure of gold. Gold has a thermal conductivity of 320 $W.m^{-1}.K^{-1}$, a coefficient of thermal expansion of 14.2 x 10^{-6} K^{-1}, enthalpy of fusion of 12.5 $kJ.mol^{-1}$, the enthalpy of vaporization is 330 $kJ.mol^{-1}$ and, its enthalpy of atomization is 368 $kJ.mol^{-1}$. Most of the mentioned bulk properties change drastically when we reach nanoscales, i.e. nanoclusters and nanotubes.

Figure 1.1. Gold nuggets are shown with the main picture showing a combination of those nuggets together with the application in jewellery and monetary systems [http://nevada-outback-gems.com/prospect/gold_specimen/Natural_gold.htm].

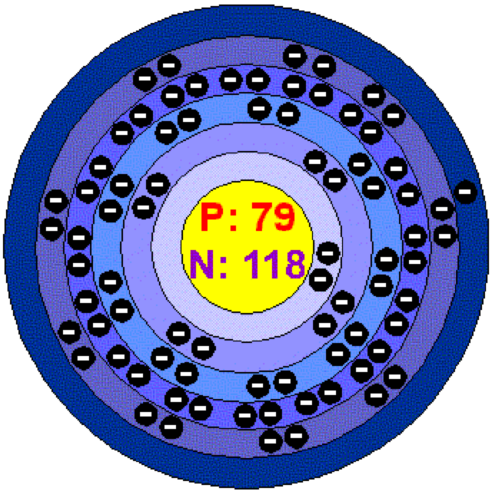

Figure 1.2. The electronic structure of gold is shown with six energy levels and one electron in the outer energy level. The atomic number of gold is shown as 79 (P =79), the number of neutrons is 118 (N = 118) [http://www.chemicalelements.com/elements/au.html].

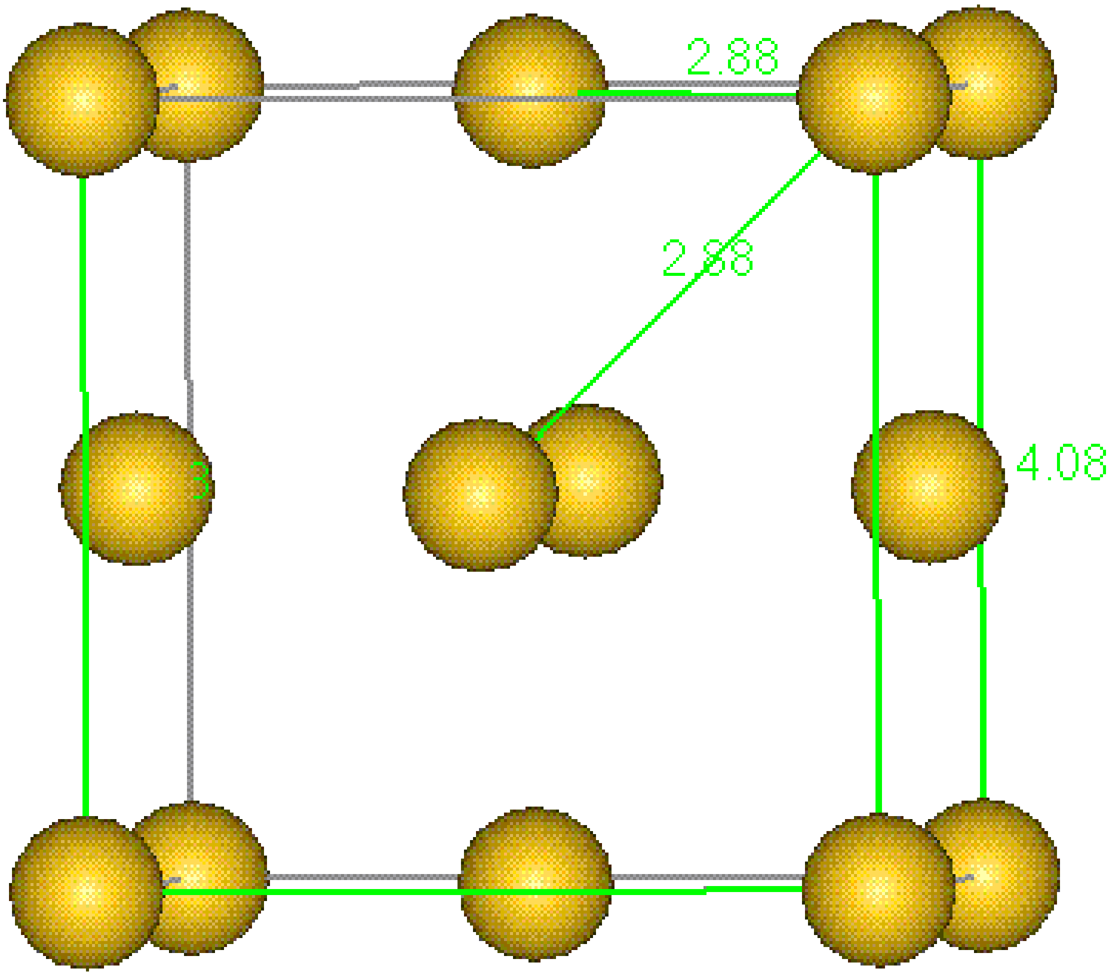

Figure 1.3. The structure of a simple face centred cubic (fcc) lattice of gold with four atoms is shown. The interatomic or bond length distance between the atoms is 2.88 Å with the lattice parameter of 4.08 Å.

The structural, physical, optical, chemical and mechanical properties of nanoclusters differ significantly from those of the bulk. Gold nanoclusters appear in different forms or shapes, e.g. they can be spherical, cylindrical, tetrahedral, octahedron, isocahedron, etc. The interatomic (bond) distance decreases or becomes small from that of the bulk, from 2.88 Å to 2.42 Å in a gold dimer. The structures of different clusters are shown in Figure 1.4. The experimental bond length for a Au dimer is 2.47 Å [Simard and Hackett 1990; Huber and Herzberg 1979] and compares well with our calculated value.

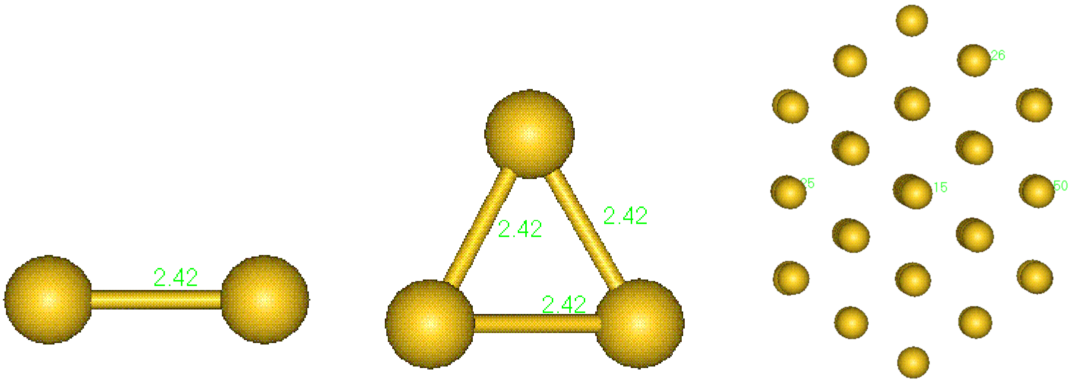

Figure 1.4. Gold nanoclusters are shown in different sizes. A dimer with a bond distance of 2.42 Å, a trimer and a bigger cluster with 55 (Au_{55}) atoms are shown from left to right.

Gold nanotubes and nanowires, on the other hand, assume a totally different structure from the bulk and clusters. The structure of a nanowire is an unbroken chain of atoms connected to each other. A nanotube structure is a continuous cylindrical shape with a hole. The structure of nanotube can be specified by a vector, (n, m), which describes how the graphene sheet is rolled up [Iijima 1991]. To produce a nanotube with the indices (6, 3), for example, the sheet is rolled up so that the atom labelled (0, 0) is superimposed on the one labelled (6, 3). A carbon sheet is shown in Figure 1.5 with the indices (n, m) well indicated.

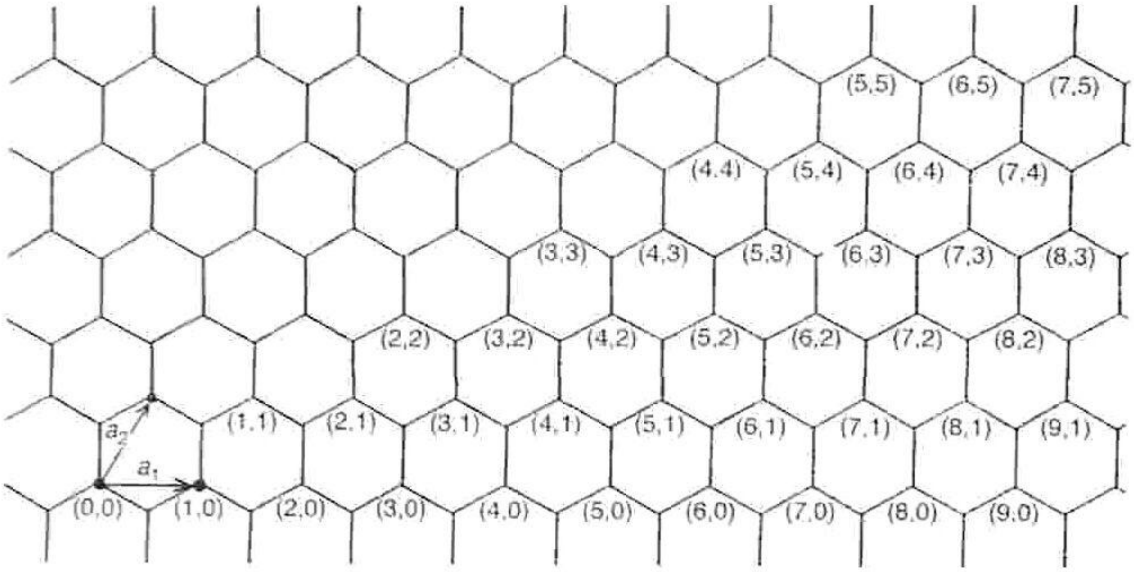

Figure 1.5. A carbon sheet with the hexagonal shapes clearly visible. The (n, m) indices are indicated for each hexagon [http://www.personal.reading.ac.uk/~scsharip/tubes.htm].

Different examples of single wall carbon nanotubes are shown in the figure below. Values for (n, m) are given after the grapheme sheet has been rolled. The bonding in carbon nanotubes is sp^2, with each atom joined to three neighbours, as in graphite. The tubes can therefore be considered as rolled-up graphene sheets (graphene is an individual graphite layer). There are three distinct ways in which a graphene sheet can be rolled into a tube, as shown in Figure 1.6 below.

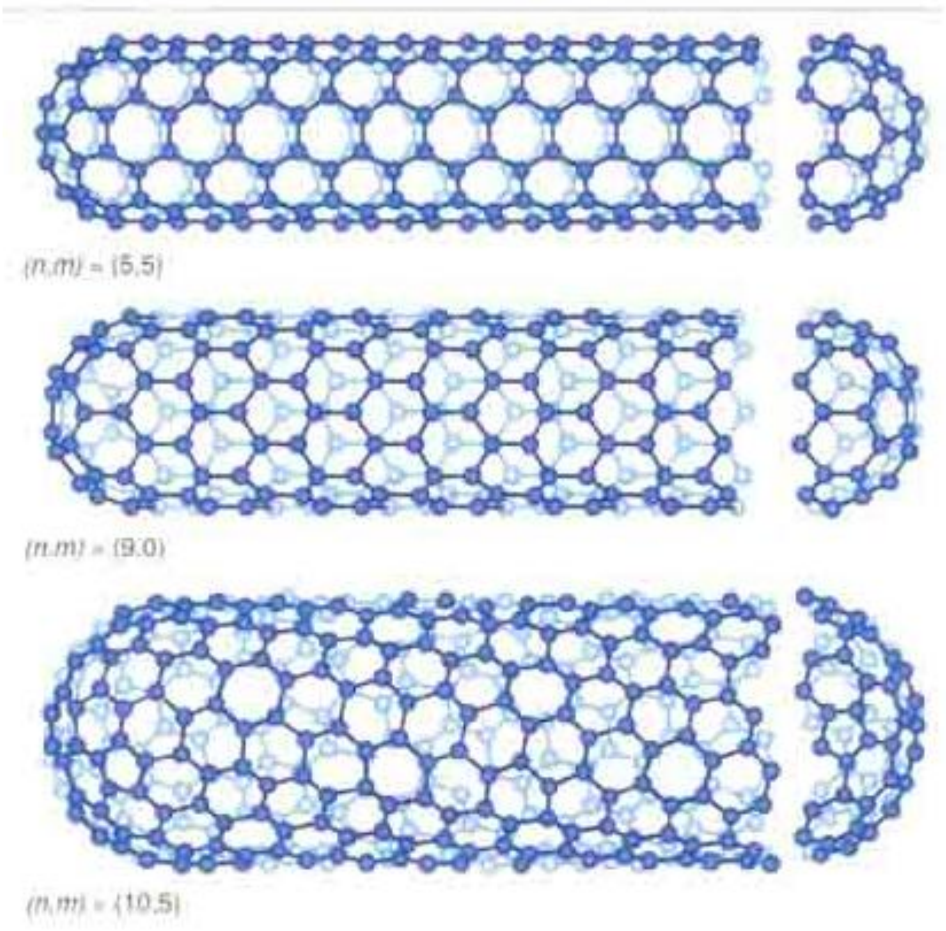

Figure 1.6 shows different (n, m) for sngle-wall carbon nanotubes with the specified values to give different sizes [http://www.personal.reading.ac.uk/~scsharip/tubes.htm].

Carbon nanotubes are most commonly known and studied after the discovery of helical microtubules of graphic carbon by Iijima [Iijima 1991, Iijima 1993]. They are reported to be the strongest materials around due to the strength of the sp^2 carbon-carbon bonds [Iijima 1991, Iijima 1993, Roth *et al*. 2001, Mizoguti 2000, Tans *et al*. 1997, Thelander *et al*. 2001]. Carbon nanotubes have hundred times the tensile strength of steel, thermal conductivity better than all but the purest diamond, and electrical conductivity similar to copper, but with the ability to carry much higher currents, [Thelander *et al.* 2001]. The electronic properties of carbon nanotubes are also extraordinary. Especially notable is the fact that nanotubes can be metallic or semiconducting depending on their structure. Thus, some nanotubes have conductivities higher than that of copper, while others behave more like silicon.

Carbon nanotubes can be applied in aerospaces and space elevators and because of their lightness are important transport materials [Thelander *et al.* 2001]. There are several areas of technology where carbon nanotubes are already being used. These include flat-panel displays, scanning probe microscopes, and sensing devices. The unique properties of carbon nanotubes will undoubtedly lead to many more applications. The discovery of carbon nanotubes has then prompted the study of nanotubes of other materials with gold taking as much attention [Nakamura *et al.* 2001, da Silva *et al.* 2001, Novaes *et al.* 2001, Rubio-Bollinger et al. 2001, Bilalbegović 1998, and Wang *et al.* 2002]. There has been a report of the evidence of a single wall platinum nanotube [Oshima *et al.* 2002] and structures of ultrathin copper nanotubes [Kang *et al.* 2002] has also been reported.

Nanotubes range from a single wall (SWNT) to multi wall (MWNT) as shown in Figure 1.7 where a single-wall and three-wall gold nanotubes can be seen. The structure of a nanotube can be likened to that of a chicken wire rolled to form a cylindrical shape with the hexagonal shapes noticeable in the structure.

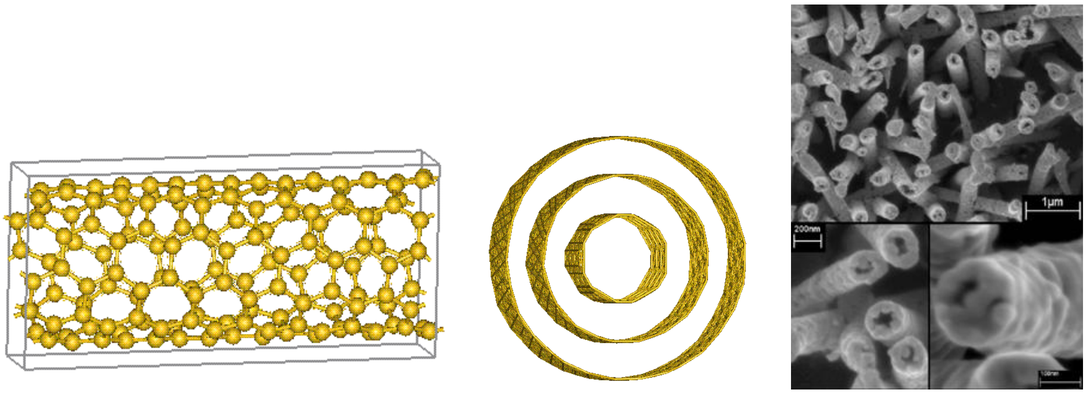

Figure 1.7. A single wall (SWNT) and a three wall nanotubes (TWNT) are shown. One ring makes a single wall nanotube, a combination of three rings constitute a three wall nanotube. Field emission scanning electron micrograph of gold nanotubes is shown on the far right [http://www.engr.wisc.edu/news/headlines/2004/Mar01.htm (2008/03/06), Roth *et al.* 2001].

1.3. Rationale of the Study

The importance of the metal gold is increasing every day. From the basic uses as a standard for monetary systems, in coinage and jewellery, gold was also found to be important for biological purposes, as in dentistry, treatment of cancer, arthritis, etc. [Pudephatt 1978, Schmidbaur and Chichester 2001]. The uses of gold for commercial purposes dominated the applications of gold in chemical processes because it was believed to be inert and therefore ineffective in chemical reactions because of its filled d-orbitals. Naturally, the relatively high price of this metal restricts its use to those applications where its unique properties make its use essential. Gold is not a threat to the environment and it is collected with great care because of its value.

In recent years, the world has focused on the use of gold at nanolevel (in nanotechnology). The importance of the nanoclusters, nanotubes and nanowires are special focus. Gold clusters are supported on materials such as TiO_2 to form the catalyst Au/TiO_2, which accelerates the rate of chemical reactions such as the oxidation of CO to CO_2. Nanotubes show potential application in technology, telecommunications, satellites, etc and their superlative resilience, tensile strength and thermal stability which have fed fantastic predictions of microscopic robots, dent-resistant car bodies and earthquake-resistant buildings have made them subject of great scientific interest.

In this work, we study the properties of both the clusters and nanotubes of gold in the classical molecular dynamics (MD) and electronic quantum mechanics (QM) in the density functional theory (DFT). The work in the MD consists of determining the properties of gold nanomaterials under different thermodynamic conditions using molecular dynamics simulation in the DLPOLY computer code. A many-body Sutton-Chen (SC) potential is employed to calculate the interactions between the atoms in the systems. Because of its simple form, its application to various types of structure and, its readily availability in the DLPOLY code, the Sutton-Chen potential is chosen for the simulations. The MD method gives an important advantage of determining different properties at different temperatures and the calculations are less expensive. Bigger structures with thousands, even millions of atoms can be well handled.

The calculations in quantum mechanics are performed on the gold clusters using density functional theory method in the DMOL^3 code. As opposed to thousands of atoms considered in the atomistic calculations, the electronic calculations will be limited to a few tens of atoms less than hundred. The generalised gradient approximation (GGA) is used to carry out the calculations on the clusters. A big advantage for using the DFT is that the results are more accurate and not reliant on any interatomic forcefield. Furthermore, doping of the gold clusters with different elements can be carried out.

1.4. Objectives of the Study

Our calculations are based on two different methods: classical mechanics (atomistic) and quantum mechanics (ab initio). To perform MD simulations under different thermodynamic conditions, we use a many-body Sutton-Chen potential in the DLPOLY code. The simulations are performed on different gold clusters and nanotubes under two conditions or ensembles, i.e. the constant NVT Berendsen and the constant NPT Berendsen ensembles. The potential is easy to use in DLPOLY code and owing to its simple form it can be applied in the calculations of alloys and in catalysis. Molecular dynamics will be used to determine the structures of the clusters and nanotubes at different temperatures from the radial distribution functions (rdfs). The melting temperatures will be estimated using the energy-temperature plot, the radial distribution functions and the density profiles.

In quantum mechanics, we will use the DFT in the GGA to perform geometry optimization calculations on different gold cluster sizes. We shall carefully note the changes in the bond distances after optimization of the structures. The total and binding energies will be determined during the simulations and we will use them to analyse the stability in the gold clusters. We will dope the gold clusters with different transition metals in order to further stabilise the clusters.

CHAPTER 2: Theoretical Background

2.1. Methodology

2.1.1. Historical Background

Computer simulation methods provide much insight into several structural, dynamical, and thermal properties of solids and liquids. Computational methods are particularly well suited to most systems, as well as the study of low-symmetry systems (such as those involving surfaces of defects), where the complexity of analytical treatments may become overwhelming, and of systems with finite temperature. Computer simulations, like experiments, can be used to investigate the properties of materials even to the electronic properties. They have a valuable role to play in providing essentially exact results for problems in statistical mechanics which would otherwise only be soluble by approximate methods, or might be quite intractable. The results of computer simulations can also be compared with those of real experiments. In the first place, this is a test of the underlying model used in a computer simulation. Eventually, if the model is a good one, the simulator hopes to offer insight to the experimentalist (as experiments have limits in that they cannot go to extremes of pressure and temperature), and assist in the interpretation of new results. The dual role of simulations, as a bridge between models and theoretical predictions on the one hand, and between models and experimental results on the other, is illustrated in Figure 2.1. Owing to the manner in which computer simulations are conducted and analysed, and as the word simulation means "mimic", these techniques are often termed "computer experiments" [Allen and Tildesley 1987].

Computer simulation provides a direct route from the microscopic details of a system (masses of the atoms, the interactions between them, molecular geometry, etc.) to macroscopic properties of experimental interest (the equation of state, transport coefficients, structural order parameter, and so on). In addition to being of academic interest, this type of information is technologically useful. It may be difficult or impossible to carry out experiments under extremes of temperature and pressure, while a computer simulation of the material in, say a shock wave, a high-temperature plasma, a nuclear reactor, or a planetary core would be perfectly feasible.

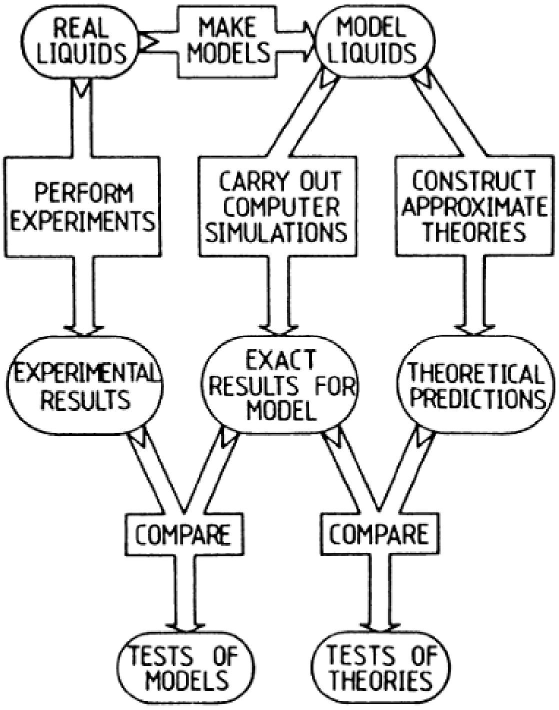

Figure 2.1. The connection between experiment, theory, and computer simulation [Allen and Tildesley 1987].

In computers physical systems are represented by models, which are then simulated using different techniques (maybe electronic or atomistic) on the computer. As a consequence of the developing technology, the capacity of computers has been upgraded significantly and computers can now handle systems with thousands and millions of atoms. Simulations can be performed classically (atomistic) or quantum mechanically (ab initio level). Both approaches can be used to perform a range of basic tasks including computation of the energy of molecules and solids and some methods can also predict properties related to the energy of the structure, geometry optimizations to find local energy minima for the specified starting structure as well as computation of vibrational frequencies resulting from interatomic motion within the molecule or solid. Quantum mechanical calculations are usually based on the density functional theory (DFT) or Hartree-Fock theory and deal mostly with the electronic properties while classical methods are mostly dependent on the interatomic forces or potentials and use the laws of classical physics to predict the structures and properties of molecules.

2.1.2. Classical Molecular Dynamics Method

2.1.2.1. Background

The molecular dynamics method was first introduced by Alder and Wainwright in the late 1950's (Alder and Wainwright, 1957, 1959) to study the interactions of hard spheres [Allen and Tildesley 1987, Leach 1996]. Many important insights concerning the behaviour of simple liquids emerged from their studies. The next major advance was in 1964, when Rahman carried out the first simulation using a realistic potential for liquid argon (Rahman 1964). Molecular dynamics calculates the real dynamics of the system, from which time averages of properties can be calculated. Sets of atomic positions are derived in sequence by applying Newton’s equations of motion. Molecular dynamics is a deterministic method, by which we mean that the state of the system at any future time can be predicted from its current state. The first molecular dynamics simulations were performed using very simple potentials such as the hard-sphere potential. The behaviour of the particles in this potential is similar to that of billiard or snooker balls. The particles move in straight lines at constant velocity between collisions. The collisions are perfectly elastic and occur when the separation between a pair of spheres equals the sum of their radii. In potentials such as the Lennard-Jones (LJ) potential the force between atoms or molecules changes continuously with their separation. By contrast, in the hard-sphere model there is no force between particles until they collide. The simulation of a realistic system was done by Rahman and Stillinger in their simulation of liquid water in 1974 (Stillinger and Rahman 1974). The number of simulation techniques has greatly expanded and there exists now many specialized techniques for particular problems, including mixed quantum mechanical-classical simulations that are being employed to study enzymatic reactions in the context of the full protein. Molecular dynamics simulation techniques are widely used in experimental procedures such as X-ray crystallography and NMR structure determination.

Molecular dynamics is the term used to describe the solution of the classical equations of motion (Newton's equations) for a set of molecules where their structures and properties can be predicted [Allen and Tildesley 1987, Leach 1996, Atkins 1998, Grant and Richards 1995] and uses assumptions like the Born-Oppenhiemer approximation [Atkins 1998] where it is assumed that the nuclei is fixed or stationery. Molecular dynamics is characterised or described by a forcefield (interatomic potential). A forcefield or interatomic potential comprises of a set of equations defining the variation of the potential energy of a molecule or a crystal with the locations of its component atoms, a series of atom types that define the characteristics of an element in a particular chemical context and one or more parameter sets that fit the equations and atom types to experimental data. The atoms type depends on hybridization, charge, and the types of the other atoms to which an atom is bonded. Parameter sets define force constants, and structural parameters such as bond lengths and angles.

Classical molecular dynamics methods do not consider the electrons in a molecular system explicitly. Instead, these calculations are based on interactions among the nuclei. Electronic effects are implicitly included in a forcefield via its parameterization. Such approximation makes molecular dynamics methods relatively inexpensive computationally and, hence, allows them to be used for very large systems containing up to millions of atoms. However, it also imposes limitations such as that, firstly a particular forcefield can achieve good results only for a limited class of molecules or solids, related to those for which it was parameterised, secondly, the results are as good as the forcefield used and thirdly, neglecting the electrons means that molecular dynamics methods cannot treat chemical problems in which electronic effects predominate.

Molecular dynamics simulation is used to compute the motions of individual molecules in models of solids, liquids, and gases. The key word is motion, which describes how positions, velocities, and orientations change with time. In effect molecular dynamics constitutes a motion picture that follows molecules as they dart to and fro, twisting, turning, colliding with one another, and, perhaps, colliding with their container. The usage is not unique as molecular dynamics may also refer to the motions of real molecules when studied primarily by molecular beam or spectroscopic techniques. The molecular dynamics simulation method is based on Newton's second law or the equation of motion written as:

$$\overline{F} = m\overline{a} \tag{2.1}$$

F is the force exerted on the particle, *m* its mass and ***a*** its acceleration (vector quantities are bolded). From the knowledge of the force on each atom, it is possible to determine the acceleration of each atom in the system. Integration of the equations of motion then yields a trajectory that describes the positions, velocities and accelerations of the particles as they vary with time. From this trajectory, the average values of properties can be determined. The force on a particular atom *i* can be written as:

$$\overline{F}_i = m_i \overline{a}_i \tag{2.2}$$

In the above equation ***F***, *m* and ***a*** respectively represent the force, mass and acceleration of the particle *i*. The force ***F*** can be evaluated directly from the derivative of the potential energy, *E*, with respect to the coordinates, *r*, and can be implemented in the Newton’s second law of motion to yield the equation:

$$-\frac{\partial E}{\partial r} = m\frac{\partial^2 r}{\partial t^2} \tag{2.3}$$

The acceleration is then given by:

$$\overline{a}_i = \frac{d^2 r_i}{dt^2} \tag{2.4}$$

There are many algorithms for integrating the equations of motion using finite difference methods, several of which are commonly used in molecular dynamics calculations [Leach 1996]. All algorithms assume that the positions and dynamical properties (velocities, accelerations, etc.) can be approximated as Taylor series expansions. The Verlet algorithm [Allen and Tildesley 1987, Leach 1996, Verlet 1976] is perhaps the most widely used method for integrating the equations of motion in a molecular dynamics simulation. The Verlet algorithm uses the positions and accelerations at time *t*, and the positions from the previous step, ***r***(*t-δt*) to calculate new positions at (*t+δt*), ***r***(*t+δt*). The following relationships between these quantities and the velocities at time *t* can be written as:

$$\bar{r}(t+\delta t) = \bar{r}(t) + \delta t\,\bar{v}(t) + \frac{1}{2}\delta t^2\,\bar{a}(t) + \ldots \tag{2.5}$$

$$\bar{r}(t-\delta t) = \bar{r}(t) - \delta t\,\bar{v}(t) + \frac{1}{2}\delta t^2\,\bar{a}(t) - \ldots \tag{2.6}$$

Adding these two equations gives

$$\bar{r}(t+\delta t) = 2\bar{r}(t) - \bar{r}(t-\delta t) + \delta t^2\,\bar{a}(t) \tag{2.7}$$

The velocities do not explicitly appear in the Verlet integration algorithm. The velocities can be calculated in a variety of ways, a simple approach is to divide the difference in positions at times t + δt and t – δt by 2δt:

$$\bar{v}(t) = \frac{\left[\bar{r}(t+\delta t) - \bar{r}(t-\delta t)\right]}{2\delta t} \tag{2.8}$$

Alternatively, the velocities can be estimated at the half-step, $t + \frac{1}{2}\delta t$:

$$\bar{v}(t + \frac{1}{2}\delta t) = \frac{\left[\bar{r}(t + \delta t) - \bar{r}(t)\right]}{\delta t} \qquad (2.9)$$

Implementation of the Verlet algorithm is straightforward and the storage requirements are modest, comprising two sets of positions (**r**(t) and **r**(t - δt)) and the accelerations **a**(t). The Verlet algorithm lacks an explicit velocity term in the equations and this makes it difficult to obtain the velocities, and thus the velocities are not available until the positions have been computed at the next step. Furthermore, it is not a self-starting algorithm which implies that the new positions are obtained from the current positions **r**(t) and the positions from the previous time step, **r**(t – δt). Therefore, several variations of the Verlet algorithm have been developed. The leap-frog algorithm [Hockney 1970] uses the following relationships:

$$\bar{r}(t + \delta t) = \bar{r}(t) + \delta t \bar{v}\left(t + \frac{1}{2}\delta t\right) \qquad (2.10)$$

$$\bar{v}\left(t + \frac{1}{2}\delta t\right) = \bar{v}\left(t - \frac{1}{2}\delta t\right) + \delta t \bar{a}(t) \qquad (2.11)$$

To implement the leap-frog algorithm, the velocities $\bar{v}(t + \frac{1}{2}t)$ are first calculated from the velocities at time $t - \frac{1}{2}\delta t$ and the accelerations at time *t*. The positions $\bar{r}(t + \delta t)$ are then deduced from the velocities just calculated together with the positions at time ***r(t)*** using the equation 2.10. The velocities at time *t* can be calculated from

$$\bar{v}(t) = \frac{1}{2}\left[\bar{v}\left(t + \frac{1}{2}\delta t\right) + \bar{v}\left(t - \frac{1}{2}\delta t\right)\right] \qquad (2.12)$$

The velocities thus ‘leap-frog’ over the positions to give their values at $t+\frac{1}{2}\delta t$ (hence the name). The positions then leap over the velocities to give their new values at $t+\delta t$, ready for the velocities at $t+\frac{3}{2}\delta t$, and so on. The leap-frog method thus has two advantages over the standard Verlet algorithm. It explicitly includes the velocity and also does not require the calculation of the differences of large numbers. The obvious disadvantage of the leap-from algorithm is that the positions and the velocities are not synchronised. This means that it is not possible to calculate the kinetic energy contribution to the total energy at the same time as the positions are defined (from which the potential energy is determined). The velocity Verlet method [Swope *et al.* 1982] therefore gives positions, velocities and accelerations at the same time and does compromise precision and the relationships are:

$$\bar{r}(t+\delta t)=\bar{r}(t)+\delta t\bar{v}(t)+\frac{1}{2}\delta t^{2}\bar{a}(t) \qquad (2.13)$$

$$\bar{v}(t+\delta t)=\bar{v}(t)+\frac{1}{2}\delta t\left[\bar{a}(t)+\bar{a}(t+\delta t)\right] \qquad (2.14)$$

The time dependence of the properties of the system can also be provided using molecular dynamics.

Suppose we wish to determine experimentally the value of a property of a system such as the pressure or the heat capacity. In general, such properties will depend upon the positions and momenta of the *N* particles that comprise the system. The instantaneous value of the property *A* can thus be written as $A\left(\bar{p}^{N}(t),\bar{r}^{N}(t)\right)$, where $\bar{r}^{N}(t)$ represent the *N* momenta and positions respectively at time t (i.e., $A\left(\bar{p}^{N}(t),\bar{r}^{N}(t)\right)\equiv A(p_{1x},p_{1y},p_{1z},p_{2x},...,x_{1},y_{1},z_{1},x_{2},...,t)$ where p_{1x} is the momentum of particle 1 in the *x* direction and x_1 it is coordinate. The experimentally measured value is the average of *A* over the time because the instantaneous value of *A* changes with time due to fluctuations as a result of interactions between the particles. As the time over which the measurement is made increases to infinity, so the value of the following integral approaches the true average value of the property:

$$A_{ave} = \lim_{\tau\to\infty}\frac{1}{\tau}\int_{t=0}^{\tau} A\left(\overline{p}^N(t),\overline{r}^N(t)\right)dt \tag{2.15}$$

Boltzman and Gibbs developed stastical mechanics in which a single system evolving is replaced by a large number of replications of the system that are considered simultaneously. The time average is then replaced by an ensemble average:

$$\langle A\rangle = \int\int d\overline{p}^N d\overline{r} A\left(\overline{p}^N,\overline{r}^N\right)\rho\left(\overline{p}^N,\overline{r}^N\right) \tag{2.16}$$

The angle brackets 〈〉 indicate an ensemble average, or expectation value, i.e. the value of the property *A* over all replications of the ensemble generated by the simulation. Equation 2.16 is written as a double integral for the convenience but in fact there should be 6*N* integral signs on the integral for the 6*N* positions and momenta for all the particles. $\rho\left(\overline{p}^N\overline{r}^N\right)$ is the probability density of the ensemble which refers to the probability of finding a configuration with momenta $\mathbf{p}^N$ and positions $\mathbf{r}^N$. The ensemble average of the property *A* is then determined by integrating over all possible configurations of the system. The ergodic hypothesis, which is one of the fundamental axioms of stastical mechanics, the ensemble average is equal to the time average. Under conditions of constant number of particles, volume and temperature, the probability density is the familiar Boltzmann distribution:

$$\rho\left(\overline{p}^N\overline{r}^N\right) = \frac{\left(\dfrac{\exp\left(-E\left(\overline{p}^N,\overline{r}^N\right)\right)}{k_BT}\right)}{Q} \tag{2.17}$$

In the above equation $E\left(\overline{p}^{N},\overline{r}^{N}\right)$ is the energy, Q is the partition function, k_B is Boltzmann's constant and T is the temperature. The partition function is more generally written in terms of the Hamiltonian, H, and for a system of N identical particles the partition function for the canonical ensemble is as follows:

$$Q_{NVT} = \frac{1}{N!}\frac{1}{h^{3N}}\int\int d\overline{p}^{N} d\overline{r}^{N} \exp\left[-\frac{H\left(\overline{p}^{N},\overline{r}^{N}\right)}{k_B T}\right] \qquad (2.18)$$

The canonical ensemble is the name given to an ensemble for constant temperature, number of particles and volume (NVT). Molecular dynamics is traditionally performed under conditions of the famous constant number of particles (N), volume (V), and energy (E). These conditions together form the microcanonical ensemble (NVE) [Allen and Tildesley 1987, Leach 1996, Atkins 1998, Grant and Richards 1995, Smith *et al*. 2006]. Also the following ensembles can be used in molecular dynamics: the canonical ensemble (the constant NVT), and the grand-canonical ensemble (the constant μVT), and many others derived from these basic three.

2.1.2.2. Setting up a MD Simulation

In setting and running a molecular dynamics simulation, the first task is to decide which energy model to use to describe the interactions within the system. Then the initial configuration has to be chosen in such a way that it favours the potential model used. In this work the many-body Sutton-Chen potential [Sutton and Chen 1990, Todd and Lyndell-Bell 1993, Mahladisa 2004] is employed to study properties of magic gold clusters and cylindrical gold nanotubes in molecular dynamics using the DLPOLY computer code. The first stage of molecular dynamics simulation is the equilibration phase; the purpose of which is to bring the system to equilibrium from the starting configuration. When these parameters achieve stable values, then the production phase can commence. It is during the production phase that the thermodynamic properties and other data are calculated. DLPOLY sums up all the steps at the end and gives the average results after the final step.

2.1.2.3. Interatomic Potentials

Potential models or interatomic potentials are used to describe the interactions between atoms in molecular dynamics and the choice of the potential model depends on the type of the system. We choose a many-body potential for metallic gold spherical nanoclusters and cylindrical nanotubes. The Sutton-Chen potential, which takes the general form of the Finnis-Sinclair potential [Finnis and Sinclair 1984], will be used in the DLPOLY [Smith *et al*. 2006] computer code to execute molecular dynamics simulations on gold clusters and tubes. The potential always favours fcc and hcp structures over the bcc structures and can always be compatible with the extended fcc structures like nanocluster and nanotubes. The potential is convenient for scaling properties of both length and energy, and a number of properties of the perfect crystal may be derived analytically.

Metallic systems require many-body potentials because of some shortcomings or failures of a two-body potential. A many-body potential is required because a two-body potential fails to deal with the complications in metals [Finnis and Sinclair 1984, Ercolessi *et al*. 1988, Daw and Baskes 1984, Holender 1990]. A two-body potential can model well the coordination of an ion which has nearly a constant coordination during the motion where the ion interacts with other ions. Motions which tend to change the coordination appreciably are greatly discouraged by their high energetic cost. Such motions occur easily in the proximity of surfaces or defects, and the extreme case consists of pulling an atom out of the system. This mechanism cannot be modelled by two-body forces, for one simple reason that a two-body scheme implies a linear dependence of the energy of an atom upon its coordination. A two-body force like the Lennard-Jones (LJ) potential gives a poor description of surface relaxation in metals and cannot account for the long range interactions. Another disadvantage of using a two-body force in the simulations of metals is that a two-body potential fails to simulate the electronic cohesion in metals and are not capable of describing rewarding atomic coordination. A many-body force gives rise to N-body interactions in the sense that the force exerted by one atom on another depends on the disposition of all neighbours to both atoms concerned. By contrast, a pair potential alone gives rise to a force that depends only on the separation of the atoms concerned and thus ignores the surrounding atoms. A pair-body potential gives the Cauchy relation between metals as $C_{12}=C_{44}$, which is seldom the case for real metals, for gold C_{12}/C_{44} is 3.7. In general, the pure pairwise-potential models do not work properly when the local environment differs from the uniform bulk.

2.1.2.4. The Sutton-Chen Potential

The Sutton-Chen potential has several advantages. Firstly, it provides a method for analysing trends in properties in different metals; secondly it is analytic and approximate expressions for various quantities may be obtained in terms of the potential parameters. Thirdly, it is particularly suitable for computer modelling, as they are efficient to evaluate. Lastly, that it is longer ranged than most semi-empirical potentials, a property that may be important for the correct modelling of surface phenomena.

The Sutton-Chen potential has the form:

$$E_{tot} = \varepsilon\left[\frac{1}{2}\sum_{i\neq}\sum_{j} V(r_{ij}) - c\sum_{i}\sqrt{\rho_i}\right] \tag{2.19}$$

The first term represents the repulsion between the atomic cores and the second term models the bonding energy due to the electrons. The first term is the two-body term which is purely repulsive and the second term deals with the many-body interactions and is totally cohesive. The electrons are not included explicitly, so the local density, ρ_i, in the second term is the local density of the atoms. The repulsion term is given by:

$$V(r_{ij}) = \left(\frac{a}{r_{ij}}\right)^{n} \tag{2.20}$$

The local density is given by:

$$\rho_i = \sum_{j \neq i} \left(\frac{a}{r_{ij}} \right)^m \tag{2.21}$$

In the above equations r_{ij} is the separation between atoms i and j, c is a positive dimensionless parameter, ε is a parameter with the dimensions of energy, a is a parameter with the dimensions of length, and n and m are positive integers. The three parameters, ε, C and a are not independent and are determined by the equilibrium lattice parameters and lattice energy of the face-centred lattice. The exponent pairs (n,m) are assigned for modelling different metals by fitting the elastic constants as closely as possible. For a given crystal structure, the Sutton-Chen potential is defined by the exponents n and m. That is because the equilibrium condition for a particular crystal structure fixes the dimensionless parameter c. If two metals, with the same crystal structures, may be represented by the same values of exponents, n and m, then the results obtained for one metal may be directly converted into the results of another simply by rescaling the units of energy and length. The relative stabilities that the potentials predict for the face-centred cubic (fcc) and body-centred cubic (bcc) crystal structures are also determined entirely by the exponents n and m. The ratio of the bulk elastic constant to the cohesive energy per unit volume is proportional to the product of the exponents. The exponents n and m in the potential for gold are given the values 10 and 8 respectively, while ε and c are given the values 0.0128 eV and 34.408 respectively. The lattice parameter a for gold is 4.08 Å. The force on each atom is written as a sum of a pairwise contribution. The force between two atoms i and j is described by the equation:

$$F = \sum_j F_{ij} \tag{2.22}$$

The pairwise form of the force between two gold atoms means that the interaction between the atoms ignores the surrounding atoms. The force will therefore represent the spring connecting two atoms.

2.1.2.5. Simulation Details

Molecular dynamics (atomistic) simulations were carried out on hexagonal (six corners) or spherical magic gold clusters ranging from 55 to 2214 atoms in size as well as cylindrical nanotubes of different number of atoms and different number of walls ranging from 24 to 1523. The exact numbers considered for Au clusters is 55, 149, 249, 309, 887, 1464 and 2214 and for the nanotubes we have considered structures with 24, 196, 364, 480, 541, 628, 1252 and 1523 atoms.

Different ensembles were used for the calculations on nanoclusters and nanotubes with the NPT Berendsen [Allen and Tildesley 1987, Leach 1996, Grant and Richards 1995, Smith *et al*. 2006] ensemble being the centre of focus. Other ensembles were used mainly for comparison with the NPT Berendsen ensemble. Each ensemble has its advantages due to different parameters controlled in each. The major reason for using the NPT conditions is that they give good results when determining the temperature effects, for example, the structural changes with temperature and melting points of these materials. The NVT or NVE ensembles do not give the much needed transition or jump in the energy-temperature plot and that is because the pressure is not closely controlled as in the NPT conditions. Furthermore, the NPT Berendsen ensemble allows simulations to be carried out at a chosen constant pressure and the temperature and pressure are controlled by the thermostat and the barostat relaxation times that are set to suit the simulation.

The constant-energy, constant-volume ensemble (NVE) is obtained by solving the standard Newton equation without any temperature and pressure control. Energy is conserved when this (adiabatic) ensemble is generated. The constant-temperature, constant-pressure ensemble (NPT) allows control over both the temperature and pressure. The unit cell vectors are allowed to change, and the pressure is adjusted by adjusting the volume (i.e., the size and also, in some programmes, the shape of the unit cell). The main difference between the two ensembles is that the NVE ensemble does not allow the size of the unit cell to change while the NPT ensemble allows the unit cell size to change either by contracting or expanding. The NPT Berendsen conditions allow the energy to change which abides well for the determination of the melting points through the energy-temperature plot (aided by the radial distribution function and the density profiles).

The Verlet algorithm, which uses acceleration, positions and time (*a, r, t*), at a previous step $r(t\text{-}\delta t)$ to calculate new positions at $(t+\delta t)$, $r(t+\delta)$, was used to integrate the equations of motion. This makes molecular dynamics to be systematic because if we know the acceleration, positions and time at the previous step we can predict the properties for the future step. No electrostatics interactions were taken into consideration since we have neutral systems [Leach 1996]. Periodic boundary conditions [Allen and Tildesley 1987, Leach 1996] were employed in most of our calculations. Periodic boundary conditions keep the number of atoms and the density in a simulation box constant throughout the simulation in that the central box is surrounded by neighbors such that when an atom leaves the box it is replaced by an image particle that enters from the opposite side.

The structures of gold clusters and tubes were first relaxed at T = 0 K before higher temperatures could be imposed on these nanostructures. Simulations were run for 6 x 10^4 MD steps with a time step of 5 ns. The simulation temperatures for the clusters ranged from as low as 100 K to as high as 2000 K depending on the resistance of the materials towards high temperatures. Au nanotubes do not show that much resistance as the clusters and the temperatures ranged from 100 K to 1400 K. Pressure was set to 0.0 kbar in the NPT Berendsen ensemble with the thermostat [Berendsen *et al.* 1984] and barostat [Evans 1983] relaxations times set at 0.4 ps and 0.5 ps respectively.

The annealing process was also performed on the selected gold clusters and nanotubes. Annealing is the process of heating a material to some high temperature and then slowly cooling down. In our calculations, we start from the point where melting has occurred and slowly cool down at intervals of 50 K until we get to very low temperatures, i.e. 50 K or 0 K. We have chosen the cluster with 309 atoms and the nanotube with 1252 atoms was considered assuming that the results are the same for other materials. The main purpose of this process is to test the possibility of regaining the initial structure after the structure has been deformed by temperature. We will also see if we indeed get stable structures by means of determining the energies at different stages.

2.1.3. The DLPOLY Computer Code

The DLPOLY code [Smith *et al*. 2006] is a parallel molecular dynamics simulation package developed at the Daresbury Laboratory by W. Smith and T.R. Forester in England in 1997. The code is issued free under license to academic institutions pursuing scientific research of a non-commercial nature. The purpose of the DL_POLY_2 package is to provide software for academic research that is inexpensive, accessible and free of commercial considerations. The users of the code have direct access to source code for modification and inspection. The code is a package of subroutines, programs, and data files, designed to facilitate molecular dynamics simulations of macromolecules, polymers, ionic systems, solutions, and other molecular systems on a distributed memory parallel computer. The DLPOLY code is capable of simulating the following molecular species:

1. Simple atomic systems and mixtures; e.g., Ne, Ar, and Kr,
2. Simple unpolarisable point ions ; e.g., NaCl, and KCl,
3. Polarisable point ions and molecules; e.g., MgO, and H_2O,
4. Simple rigid molecules; e.g., CCl_4, SF_6, and Benzene,
5. Rigid molecular ions with point charges e.g. KNO_3, $(NH_4)_2SO_4$,
6. Polymers with rigid bonds e.g. C_nH_{2n+2}
7. Polymers with rigid bonds and point charges; e.g., proteins
8. Macromolecules and biological systems
9. Molecules with flexible bonds
10. Silicate glasses and zeolites
11. Simple metals and alloys; e.g., Al, Ni, Cu, and Au,
12. Covalent systems; e.g., C, Si, Ge, SiC, and SiGe.

The code is capable of performing wide range of molecular dynamics simulations using different potential models, viz. the two-body potentials (Lennard Jones), many-body potentials (Sutton-Chen), etc. The Sutton-Chen potential is found readily available for use in the code. A range of properties like the total energy of the system, diffusion coefficients, pressure, volume, temperature, and lattice parameters, can be calculated using DLPOLY. The code uses different thermodynamic conditions such as different ensembles, and higher temperature can easily be carried out. The code can be used to investigate the melting temperatures, the change in the structure at different temperatures, and many thermodynamic properties.

Five input files which are equally valued in their different respect are required to initiate a DLPOLY simulation, viz. CONTROL, CONFIG, FIELD, TABLE and REVOLD files. The first three file are mandatory, while TABLE is used to input certain type of pair potential, and is not always required. REVOLD is required only if the job represents a continuation of a previous job. The FORTRAN written files must have their names written in capital letters for the code to recognise them. The files are interrelated and therefore one mistake in one file will lead to the termination of the simulation where an error message will be printed at the end of the OUPUT file.

2.1.3.1. The CONTROL Input File

The simulation is controlled in this file and is read by the subroutine SIMDEF. The file makes extensive use of directives and keywords. Directives are character strings that appear as first entry on a data record (or line) and which invoke a particular operation or provide numerical parameters. Also associated with each directive may be one or more keywords, which may qualify a particular directive by, for example, adding extra options. Directives have the following form:

keyword [*options*] {data}

The keyword and options are text fields, while the data options are numbers (integers or reals). Directives can appear in any order in the CONTROL file, except for the finish directive which marks the end of the file. Some of the directives are mandatory (for example the timestep directive that defines the timestep), some others are optional. The file is free-formatted, integers, reals, and additional keywords are entered following the keyword on each record. Real and integer numbers must separated by a non-numeric character (preferably a space or a comma) to be correctly interpreted. No logical variable appear in the CONTROL file. Comment records (beginning with a #) and blank lines may be added to aid legibility and the file is not case sensitive. The first record in the file is a header 80 characters long, to aid identification of the file and the last record is a finish directive which the end of the input data. A wide choice of control directives that are relevant to the simulation may be inserted between the header and finish directives. The CONTROL file in short contains all the parameters required to control a simulation, i.e., duration (number of steps), the job time and close time, the temperature, pressure, which properties to print during a simulation, the cut-off radius, the ensemble, etc.

2.1.3.2. The CONFIG Input File

This file contains the dimensions of the unit cell, the key for periodic boundary conditions and the atomic labels, coordinates, velocities and forces. The file is read by the subroutine SYSGEN (It is also read by the subroutine SIMDEF if the Ewald precision directive is used). The CONFIG file is where the structure is contained with the atoms and their specific positions or coordinates. The file has the same format as the output file REVCON. When restarting from a previous run, the CONFIG file must be replaced by the REVCON file, which is renamed as the CONFIG file and this, is done by the restart directive in the CONTROL file. The *copy* marco in the *executive* sub-directory of DLPOLY does this for the user. The first few records in a typical CONFIG file are shown below:

```
Sample of 5x5x5 unit cells of gold configuration
         2         3
       20.4800102205        0.0000000000        0.0000000000
        0.0000000000       20.4800102205        0.0000000000
        0.0000000000        0.0000000000       20.4800102205
AU               1
    0.7669999082E-01   -0.1800404519E-01    0.1559645479
   -0.6394637067        0.7191780488        0.3560873033
    -2617.585843       -6860.422622        -8329.447344
AU               2
    2.146807714         1.946505832         0.2320882471E-01
   -0.7201362964       -0.2587050489       -0.1215035490
   -6704.987987         3879.804010         332.7548383
AU               3
```

```
    2.056837622         -0.7392579524E-01     2.067636248
    0.3514962921         0.9539534229         0.2997429062
    264.0516524          9065.808543          4829.122639
AU               4
    0.3923468588E-02     1.960997966          2.043765690
   -2.540815867          0.6811282875         0.8479955133E-01
    1547.115607          9764.160026          302.7042774
etc.
```

The file is fix-formatted: integers as “i10”, reals as “f20.0”. The header record is formatted as 80 alphanumeric characters. The integer *2* means that coordinates, velocities and forces are included in the file. The integer *3* means that the parallelepiped periodic boundary conditions should be applied. The first *20.4800102205* is real and represents the x-component a cell vector, the second one gives the y-component and the third a z-component of the cell. The volume is thus determined from these three components which give the dimensions of the cell. The cut-off radius set in the CONFIG file should be less or equal to half of the smallest component, e.g. in this example the cut-off radius will be 10.0 Å or less but we have used 9.5 Å during our simulations and it worked very well. The next record start with an atomic label, Au for gold and its atom index will be one for the first atom, *2* for the second and etc. Each atom is described by the x-, y-, z-components of the coordinates, velocities and forces.

2.1.3.3. The FIELD Input File

The FIELD file contains the force field information defining the nature of molecular forces. It is read by the subroutine SYSDEF. This is where all the atomic interactions are dealt with the specification of the force-field or interatomic potential. The interactions between the atoms lead to the production of energy which is usually measured in electron volts (eV). The file is free formatted (though it should be noted that atom names are limited to 8 characters and potential functions keys are limited to only 4 characters). Additional information is associated with the directives and the file is not case sensitive. The file divides into three sections; i.e., general information, molecular description and non-bonded interaction descriptions, appearing in that order in the file. The first record in the FIELD file is the title and it must be followed by the units directive. Both of these are mandatory.

It is important to note that there is an organizational between the FIELD and the CONFIG file described earlier. It is required that the order of specification of the molecular types and their atomic constituents in the FIELD file follow the order in which they appear in the CONIFG file. Failure to adhere to this common sequence will be detected by DLPOLY and result in premature termination of the job. It is therefore essential to work from the CONFIG file when constructing the FIELD file. The entry of the molecular details begins with the mandatory directive:

molecules n

Here n is the integer specifying the number of different types of molecule appearing in the FIELD file. Once this directive is encountered, DLPOLY enters the *molecular description* environment in which only molecular keywords and data are valid. Immediately following the molecules directives are the records finding the individual molecules.

1. *name-of-molecule*

   which can be any character string up to 80 characters in length.(this is not a directive, just a simple character string).
2. *nummols n*

where *n* is the number of times a molecule of this type appears in the simulated system. The molecular data then follow in subsequent records.

3. *atoms n*

where *n* indicates the number of atoms in this type of molecule. A number of records follow, each giving details of the atoms in the molecule, i.e. site names, masses and charges. Each record carries the entries:

sitnam	a8	atomic site name
weight	real	atomic site mass
chge	real	atomic site charge
nrept	integer	repeat counter

ifrz	integer	‘frozen’ atom (if ifrx > 0)
igrp	integer	neutral charge/charge group number

These entries are order sensitive. Blank entries must not be left unless all parameters appearing after last specified are void. The integer need not be specified (in which a value of 1 is assumed). The number greater than 1 specified here indicates that the next (nrept - 1) entries in the CONFIG file are ascribed the atomic characteristics given in the current record. The sum of repeat numbers for all atoms in a molecule should equal the number specified by atoms directives.

4. *shell n m*

where *n* is the number of core shell units and *m* is an integer specifying which shell mode is required:

- m = 1 for adiabatic shell model;
- m = 2 for relaxed shell model;

Each of the subsequent n records contains:

index 1	integer	site index of core
index 2	integer	site index of shell
spring	real	force constant of core-shell spring

5. *finish*

This directive is entered to signal to DLPOLY that the entry of the details of a molecule has been completed. The entries for a second molecule may now be entered, beginning with the name-of-molecule record and ending with the finish directive. The cycle is repeated until all the types of molecules indicated by the molecules directive have been entered.

A complete FIELD file is shown below specifying all simulation requirements for a gold metal using the many Sutton-Chen potential. There is a good correlation between this file and the CONFIG file discussed earlier.

```
DL_POLY TEST CASE 2: Au Sutton-Chen forcefield
units ev
molecular types 1
Gold
nummols 1
atoms 55
AU   196.97   0.0      55
finish
vdw 1
AU  AU  stch   0.0204688  3.59   11.0  6.0  34.408
close
```

Metal potentials in DLPOLY are based on the Finnis-Sinclair model [Finis and Sinclair 1991]. The explicit form of the potential in DLPOLY is confined to the formulation of the Sutton and Chen [Sutton and Chen 1984] and Rafii-Tabar and Sutton [Rafii-Tabar and Sutton 1991]. These are non-bonded potentials and are characterized by atom types rather than specific atomic indices. The input of metal potential data is signaled by the directive:

metal n

where *n* is the number of metal potentials to be entered. There follows *n* records, each specifying a particular metal potential in the following manner (see Table 1):

atmnam 1	a8	first atom type
atmnam 2	a8	second atom type
key	a4	potential key
variable 1	real	potential parameter
variable 2	real	potential parameter
variable 3	real	potential parameter
variable 4	real	potential parameter
variable 5	real	potential parameter

The variables pertaining to each potential are described in Table 2.1. Any metal potential not specified in the FIELD file will be assumed to be zero. The Sutton-Chen will handle alloys, but care must be taken to enter the cross terms of the potentials explicitly. The rules for defining the cross terms of the potential are not usually the terms encountered in the Lennerd-Jones systems. A second potential is usually needed in alloys where the interactions between the two metals studied is taken care of by Sutton-Chen. The second potential model will handle the interactions between the different atomic species. However, the Sutton-Chen potential can be modified to suit such kind of calculations or the LJ potential can be modified through the use of the mixing rules.

Table 2.1. Definition of the metal potential functions and variables. This is exactly how the potential parameters are put in the FIELD file in DLPOLY as shown above.

key	potential type	Variables (1-5)					Functional form
stch	Sutton-Chen	ε	a	n	m	C	$U_i(r) = \varepsilon\left[\frac{1}{2}\sum_{j\neq i}\left(\frac{a}{r_{ij}}\right)^n - C\sqrt{\rho_i}\right]$ $\rho_i = \sum_{j\neq i}\left(\frac{a}{r_{ij}}\right)^m$

2.1.3.4. The REVOLD File

The file contains statistics array from a previous job. It is not required if the current job is not a continuation of a previous run (i.e. if the restart directive is not present in the CONTROL file). The file is unformatted and there not readable by a normal person. DLPOLY usually produces the file REVIVE at the end of a job which contains the statistics data. REVIVE should be copied to REVOLD before a continuation run commences. This may be done by the *copy* macro supplied in the *executive* sub-directory of the DLPOLY code.

2.1.3.5. The TABLE file

This file offers an alternative way of reading in the short range potentials – in tabular form. This is particularly useful if an analytical form of the potential does not exist or is too complicated to specify in the *FORGEN* subroutine. The TABLE file read by the subroutine *FORTAB.F* in the *VDW_TERMS.F* file.

2.1.4. THE DLPOLY OUTPUT FILES

The output file is where the output data produced from the input files is printed. DLPOLY produces up to seven output files: HISTORY, OUTPUT, REVCON, REVIVE, RDFDAT, ZDNDAT and STATIS. These respectively contains: a dump file of atomic coordinates, velocities and forces; a summary of the simulation; the restart configuration; statistics accumulators; radial distribution data; Z-density data and a statistical history. The REVCON and REVOLD files have been said about earlier.

2.1.4.1. The HISTORY file

The HISTORY file is a dump file of atomic coordinates, velocities and forces. Its principal use is for offline analysis. The file is written by the subroutine *TRAJECT* or *TRAJECT_U*. The control variables for this file are *ltraj*, *nstraj*, *istraj* and *keytrj* which are created internally, based on information read from the directive traj in the CONTROL file. The HISTORY file will only be created only if the *traj* directive appears in the CONTROL file. The file can be very large, especially if it is formatted. This file is particularly important if graphical processing of the data is required.

2.1.4.2. The OUTPUT File

The OUPUT file consists of eight or nine seven sections: Header; Simulation control specifications; Force field specification; Summary of the initial configuration; Simulation progress; Summary of statistical data; Sample of the final configuration; Radial distribution functions; and Density profiles. The printing of the radial distribution and density profiles is respectively executed by the inclusion of the directives *rdf* and *print rdf* and *zden* in the CONTROL file. The RDFDAT file (for the radial distribution functions) is written from the subroutine *RDF1* while the ZDNDAT file (for the density profiles) is written by *ZDEN1*.

2.1.4.3. The STATIS File

The file is formatted with integers as “i10” and as reals “e14.6”. It is written by the subroutine *STATIC*. It consists of two header records followed by many data records of statistical data. The STATIS file is appended at intervals determined by the *stats* directive in the CONTROL file. The complete structure of both the input and output DLPOY files is Figure 2.2.

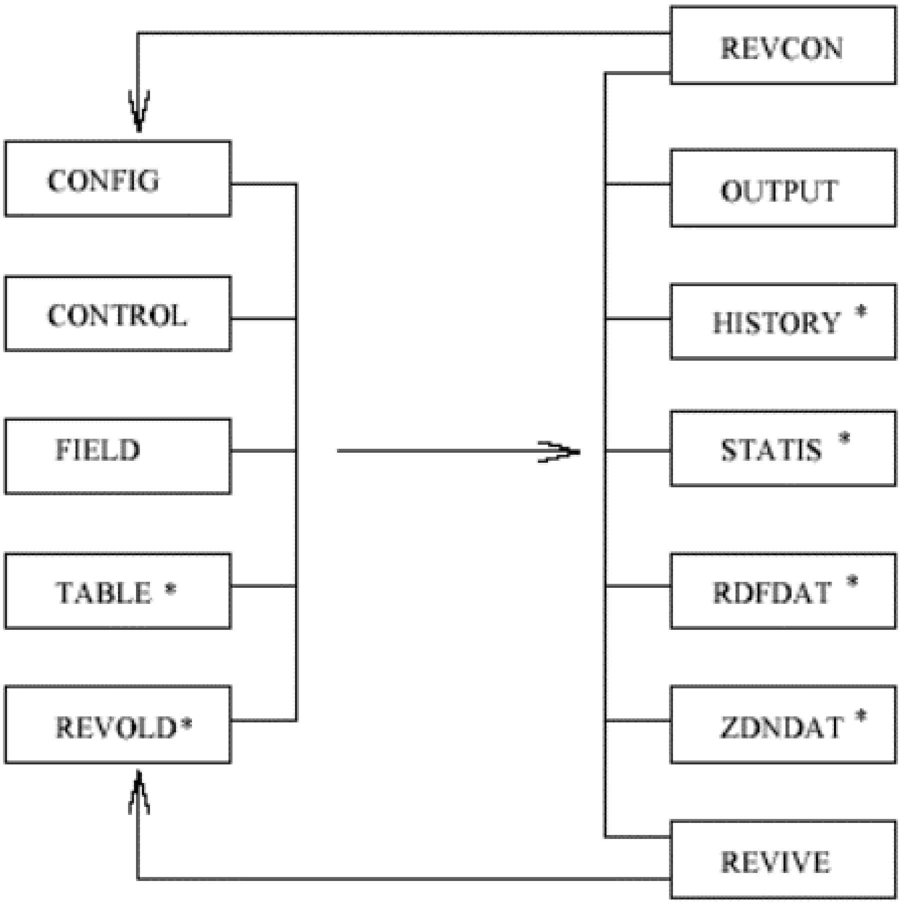

Figure 2.2. The scheme illustrating the DLPOLY input (left) and OUTPUT (right) files. Files marked with an asterisk are non-mandatory.

2.1.5. Calculated Parameters

A wide variety of thermodynamic properties can be calculated from computer simulations and molecular dynamics is just one technique to carry out that job. Simulations give results that can be compared with the experiments to quantify the potential model used as well as to validate the obtained results.

2.1.5.1. The Energy

The internal energy is easily obtained from a simulation as the ensemble average of the energies of the states that are examined during the course of the simulation. The equation for the energy can be written as:

$$U = \langle E \rangle = \frac{1}{M} \sum_{i=1}^{M} E_i \tag{2.23}$$

The average potential energy V is obtained by averaging its instantaneous value, which is obtained at the same time as the force computation is made. Thus, the potential energy is given by:

$$V(t) = \sum_{i} \sum_{j>1} \phi\left(\left| r_i(t) - r_j(t) \right| \right) \tag{2.24}$$

The kinetic energy is given by:

$$K(t) = \frac{1}{2} \sum_{i} m_i \left[\bar{v}_i(t) \right]^2 \tag{2.25}$$

where m_{i} is the mass of atom i and $\mathbf{v}_i$ is the velocity of atom i. The total energy of the system can be represented as the sum of the kinetic energy and the potential energy and, the total energy of the system with a given set of positions and velocities is represented by:

$$T_{tot} = K(t) + V(t) \tag{2.26}$$

2.1.5.2. The Pressure

The pressure is usually calculated in a computer simulation via the virial theorem of Classius. The virial is defined as the expectation value of the sum of the products of the coordinates of the particles and the forces acting on them. This is usually written $W = \sum x_i \bar{p}_{xi}$ where x_i is a coordinate (e.g. the x or y coordinate of an atom) and $\bar{p}_{xi}$ is the first derivative of the momentum along that coordinate ($\bar{p}_i$ is the force, by Newton's second law). The virial theorem states that the virial is equal to $-3Nk_BT$. In an ideal gas, the only forces are those due to interactions between the gas and the container and it can shown that the virial in this case equals $-3PV$, the results which can be obtained directly from $PV = Nk_BT$. Forces between the particles in a real gas or liquid affect the virial, thence the pressure. The pressure is then written as:

$$P = \frac{1}{V}\left[Nk_BT - \frac{1}{3k_BT}\sum_{i=1}^{N}\sum_{j=i+1}^{N} r_{ij}\, f_{ij} \right] \tag{2.27}$$

The forces are calculated as part of molecular dynamics simulation, so little additional effort is required to calculate the virial and thus the pressure. The pressure can be kept constant depending on the type of ensemble used. In the NPT isorthermal-isothermic ensemble the total pressure of the system is constant. In the microcanonical ensemble, however, the pressure will fluctuate throughout the simulation.

2.1.5.3. The Temperature

The temperature, like the pressure, depends on the type of ensemble used for a particular simulation. In a canonical ensemble the total temperature is constant whereas it is allowed to fluctuate in the microcanocial ensemble. The temperature is directly related to the kinetic energy of the system as follows:

$$K = \sum_{i=1}^{N} \frac{\left|\overline{p}_i\right|}{2m_i} = \frac{k_B T}{2}\left(3N - N_c\right) \tag{2.28}$$

In the above equation, $\boldsymbol{p}_i$ is the total momentum of particle i and m_i is its mass and N_c is the number of constraints on the system. Each degree of freedom contributes $k_BT/2$ according to the theorem of equipartition of energy. If there are N particles, each with three degrees of freedom, then the kinetic energy should equal $3Nk_BT/2$.

2.1.5.4. The Radial Distribution Functions (RDFs)

Radial distribution functions are a useful way to describe the structure of a system, particularly of liquids. Consider a spherical shell of thickness δr at a distance r from a chosen atom. The volume of the shell is given by:

$$\begin{aligned} V &= \frac{4}{3}\pi\left(r + \delta r\right)^3 - \frac{4}{3}\pi r^3 \\ &= 4\pi r^2 \delta r + 4\pi r \delta r^2 + \frac{4}{3}\pi \delta r^3 \approx 4\pi\delta^2 \delta r \end{aligned} \tag{2.29}$$

If the number of particles per unit volume is ρ, then the total number in the shell is $4\pi\rho r^2\delta r$ and so the number of atoms in the volume element varies as r^2. The pair distribution, $g(r)$, gives the probability of finding an atom (or molecule, if simulating a molecular fluid) a distance *r* from another atom (or molecule) compared to the ideal gas distribution. *g(r)* is thus dimensionless. Higher radial distribution functions (e.g. the triplet radial distribution function) can also be defined, but are rarely calculated and so references to the radial distribution function are usually taken to mean the pairwise version. In a crystal, the radial distribution function has a multiple number of sharp peaks whose separation and heights are characteristic of the lattice structure. The radial distribution function of a liquid is intermediate between the solid and the gas, with a small number of peaks as short distances, superimposed on a steady decay to a constant value at longer distance. The radial distribution functions can in short be used to differentiate between solids, liquid and gas phases. Furthermore, the radial distribution functions can be used in calculations where we are able to notice a change in the phases; i.e., starting from a solid structure we can be able to see the structure change to a liquid phase and then to a gaseous one as shown in Figure 2.3.

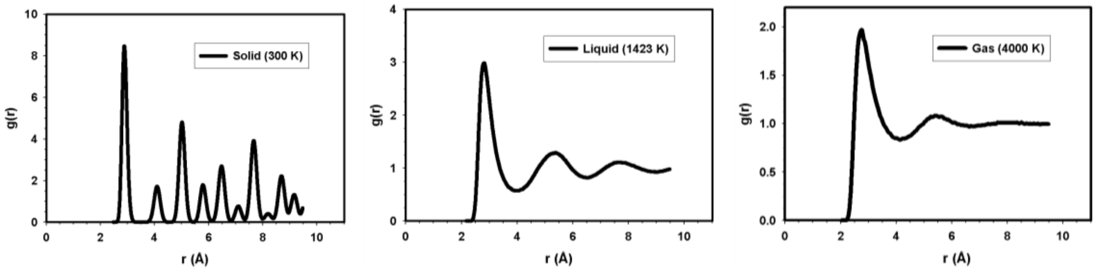

Figure 2.3. The rdfs for gold bulk are shown, starting from a solid crystal on the left, the system reaches melting in the central figure and on the right the gaseous system can be observed. The number of peaks decreases and the broadening of the peaks is quite noticeable.

2.1.5.5. The Density Profiles

The density profiles show less dense structures at melting by a decrease in the number of peaks and a sudden change in the peak pattern. Figure 2.4 shows a change in the peak patterns of the density profiles as we move from a solid to a liquid phase. The behaviour of the density in the system can be described using the density profiles when it changes by the changing pressure or temperature. The increasing pressure always increases the density of a material while the increasing temperature decreases the density.

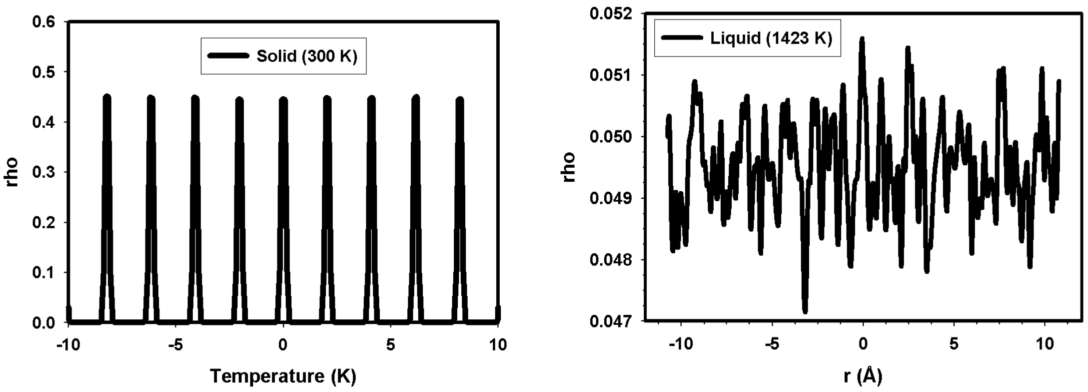

Figure 2.4. The density profiles are plotted for the bulk Au at solid and liquid phases. The peak patterns in the liquid structure change quite significantly from that of the solid structure.

2.1.5.6. Melting Temperature (T_m)

Melting temperature is defined as the temperature at which, under a specific pressure, the liquid and solid phases of a substance coexist in equilibrium. At melting the systems appear disordered and molecular diffusion can occur and it is a high pressure case. At low temperatures systems are ordered with little molecular motion and that occurs at low pressures. The melting temperature of most substances is the same as their freezing temperature because the substance melts at a similar temperature as that at which it freezes. The example is that of the most interesting liquid, water, which melts very close to 0 ^{0}C (273.15 K). Coexistence is easily achievable in larger systems in two dimensions [Atkins 1998].

Unlike the boiling point, the melting temperature is relatively insensitive to pressure. Meting points are often used to characterise organic compounds and ascertain the purity. The melting point of a pure substance is always higher and has a smaller range than the melting point of an impure substance. The more impurity is present, the lower the melting point and the broader the range. The chemical element with the highest melting point is tungsten which melts at 3695 K (3422 ^{0}C) making it excellent for use in light bulbs. Platinum, with the melting point of 1772 ^{0}C (2045.15 K), has the highest melting point amongst the precious metals while metallic gold melts at 1064 ^{0}C (1337 K). Computationally we are able to keep the pressure and temperature constant while allowing the energy to fluctuate until a stable value is reached.

Not only is heat required to raise the temperature of the solid to the melting point, but the melting itself requires heat called the heat of fusion. From thermodynamics, at the melting point the change in Gibbs free energy (ΔG) of the material is zero, because the enthalpy (H) and the entropy (S) of the material are increasing (ΔH, $\Delta S > 0$). Melting phenomena happens when the Gibbs free energy of the liquid becomes lower than the solid for that material. Carnelley's rule established in 1882 by Thomas Carnelley states that high molecular symmetry is associated with high melting point. A good example is that of three structural isomers with molecular formula C_5H_{12} where the melting point increases in the series: isopentane 113 K, n-pentane 143 K and nenopentane 255 K. Pyridine has a lower symmetry than benzene hence its lower melting point.

A high melting point results from a high heat of fusion or low entropy of fusion or a combination. In highly symmetrical molecules the crystal phase is densely packed with many efficient intermolecular interactions resulting in a higher enthalpy change on melting.

The melting temperature for spherical particles of radius R is obtained phenomenologically by equating the Gibbs free energies of solid and liquid spherical clusters, assuming constant pressure conditions:

$$\frac{T_m^b - T_m(R)}{T_m^b} = \frac{2}{\rho_s L^b R}\left[\gamma_{sv} - \left(\frac{\rho_s}{\rho_l}\right)^{\frac{2}{3}} \gamma_{lv}\right] \qquad (2.30)$$

where ρ_s and ρ_l are the solid and liquid densities, L^b is the bulk latent heat of melting, and γ_{sv} and γ_{lv} are the solid-vapour and liquid-vapour interface energies, respectively. The surface energy anisotropy of the solid is not taken into account, and the possibility of inhomogeneous phases (such as a liquid skin wetting the solid cluster) is also neglected. For a wire, following a similar procedure, the Gibbs free energies per unit length of the solid and liquid wires at constant pressure and temperature equate to,

$$G_s = N\mu_s + 2\pi R\gamma_{sv} \tag{2.31}$$

and

$$G_l = N\mu_l + 2\pi R\gamma_{lv} \tag{2.32}$$

where N is the number of atoms per unit length, μ_s and μ_l are the chemical potentials of the solid and liquid phases, respectively, R is the wire radius. Since near bulk melting temperature, T_m^b,

$$N(\mu_s - \mu_l) = V\rho_s L^b \frac{(T - T_m^b)}{T_m^b} \tag{2.33}$$

we obtain for the melting temperature $T_m(R)$ of a thin wire,

$$\frac{T_m^b - T_m(R)}{T_m^b} = \frac{1}{\rho_s L^b R}\left[\gamma_{sv} - \left(\frac{\rho_s}{\rho_l}\right)^{\frac{1}{2}}\gamma_{lv}\right] \tag{2.34}$$

Hence, the melting temperature of a wire should be depressed by approximately half the corresponding amount for a spherical cluster. The definition of the surface atoms plays an important role in melting of materials. A wire has clearly defined surface atoms than a spherical cluster while it is difficult to locate such atoms in the bulk. In this simple model the latent heat of melting per atom (averaged on all atoms) decreases with exactly the same law when the size is decreased:

$$\frac{L^b - L(R)}{L^b} = \frac{1}{\rho_s L^b R}\left[\gamma_{sv} - \left(\frac{\rho_s}{\rho_l}\right)^{\frac{1}{2}} \gamma_{lv}\right] \tag{2.35}$$

These relations imply the existence of a critical radius,

$$R_c = \frac{\left[\gamma_{sv} - \left(\frac{\rho_s}{\rho_l}\right)^{\frac{1}{2}} \gamma_{lv}\right]}{\rho_s L^b} \tag{2.36}$$

Corresponding to

$$T_m R_c = 0, L(T_c) = 0 \tag{2.37}$$

Below this condition the wire is not stable.

2.1.5.7. Periodic Boundary Conditions

Periodic boundary conditions enable a simulation to be performed using a relatively small number of particles, in such a way that the particles experience forces as if they were in bulk fluid. Imagine a cubic box of particles which is replicated in all directions to give a periodic array. A two-dimensional box is shown in Figure 2.5. In the two-dimensional example each box is surrounded by 8 neighbours, in three dimensions each box would have 26 nearest neighbours. The coordinates of the particles in the image boxes can be computed simply by adding or subtracting integral multiples of the box sides. Should a particle leave the box during a simulation then it is replaced by an image particle that enters from opposite side, as illustrated in Figure 2.5. The number of particles within the central box thus remains constant and so is the density at particular thermodynamic conditions. Periodic boundary conditions are indicated by a number 3 at the top of the CONFIG file.

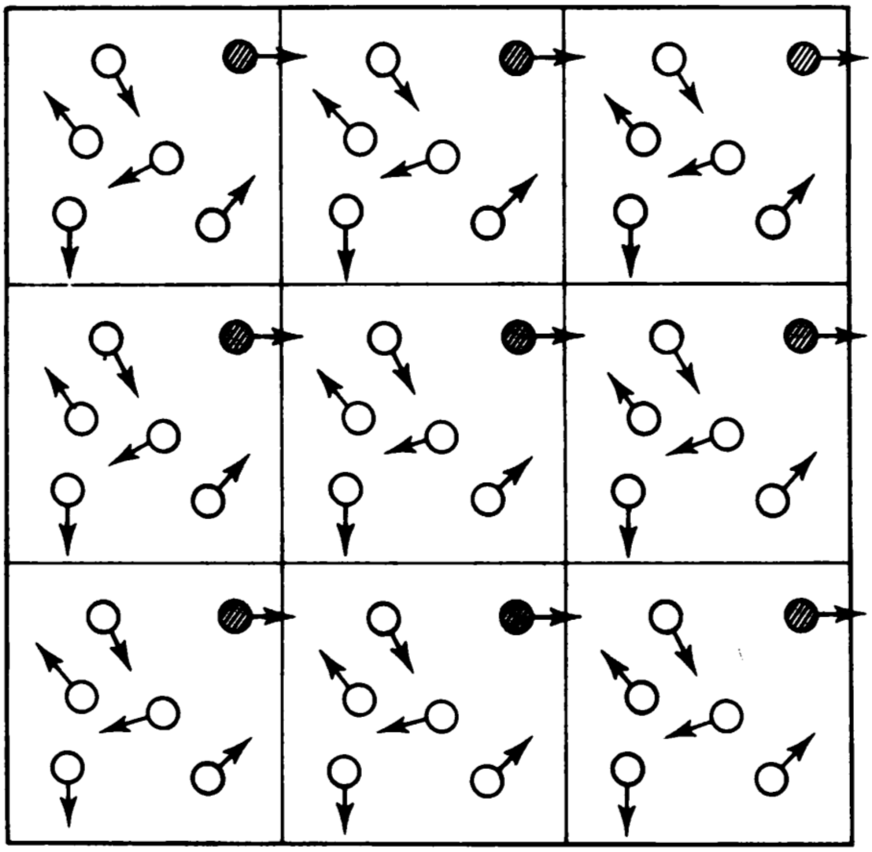

Figure 2.5. Periodic boundary conditions are shown in two dimensions [Allen and Tildesley 1987; Leach 1996].

2.1.5.8. The Heat Capacity at constant Volume and Pressure

The internal energy of a substance increases when its temperature is raised. The increase depends on the conditions under which the heating takes place, and for the calculation at a constant volume we suppose that the sample is confined to that volume. The internal energy is then plotted against temperature and the slope thereof at any temperature is called the heat capacity of the system at that temperature. The heat capacity at constant volume is denoted C_v and is defined formally as:

$$C_v = \left(\frac{\partial U}{\partial T}\right)_v \tag{2.38}$$

where U is the internal energy of the system and T is the temperature. The heat capacity is an extensive property, i.e. 100 g of water has 100 times the heat capacity of 1 g of water and therefore requires 100 times the heat to bring about the same rise in temperature. The heat capacity is then calculated as a change in the energy over the change in temperature at constant volume.

In the same way the energy of a substance changes, the enthalpy increases as the temperature is raised. The relation between the increase in enthalpy and the increase in temperature depends on the conditions, for example, constant pressure or volume. The most important condition in this case is constant pressure, and the slope of the graph of enthalpy against temperature at constant pressure is called the heat capacity at constant pressure, denoted C_p, and given by:

$$C_p = \left(\frac{\partial H}{\partial T}\right)_p \tag{2.39}$$

Here H is the enthalpy of the system. For a constant pressure of 0.0 kbar we find that the enthalpy of the system equals to the energy as the term pV becomes zero ($H = U$). The heat capacity at constant pressure is then calculated as the change in the energy over the change in temperature at constant pressure.

Most systems expand when heated at constant pressure. Such systems do work on the surroundings and some of the energy supplied to tem as heat escapes back to the surroundings. As a result, the temperature of the system rises less than when the heating occurs at constant volume. A smaller increase in temperature implies a larger heat capacity, so it can be said that in most cases the heat capacity at constant pressure of a system is larger than its heat capacity at constant volume. The relation between the two heat capacities for any pure substance is the written as:

$$C_p - C_v = \frac{\alpha^2 TV}{\kappa_T} \tag{2.40}$$

T is the temperature, V the volume, α the expansion coefficient and κ_T is the isothermal compressibility defined as:

$$\kappa_T = -\frac{1}{V}\left(\frac{\partial V}{\partial p}\right)_T \tag{2.41}$$

2.1.5.9. Diffusion Coefficient

Diffusion is the phenomena of random motion causing a system to decay towards uniform conditions. For example, diffusion of particles causes a net movement of particles from areas of high concentration to areas of lower concentration until equilibrium is reached. Diffusion is a spontaneous process more familiarly known as a passive form of transport, rather than active and affects a variety of different quantities. Spontaneous processes are not reversible. Examples of diffusion include diffusion of concentration, heat, or momentum. Diffusion increases entropy, decreasing Gibbs free energy, and therefore is thermodynamically favourable.

In all cases of diffusion, the flux of the transported quantity (atoms, energy, or electrons) is equal to a physical property (diffusivity, thermal conductivity, electrical conductivity) multiplied by a gradient (a concentration, thermal, electrical field gradient). Diffusion in this type of molecular dynamics simulations is calculated as the slope of the graph of mean square displacement as a function of time.

2.1.5.10. The Coefficient of Thermal Expansion

During heat transfer, the energy stored between the intermolecular atoms changes. When the stored energy increases, so does the length of the molecular bond. As a result, solids typically expand as a response to heating and contract on cooling and this response to temperature change is expressed as its coefficient of thermal expansion. The coefficient of thermal expansion is used in two very close ways, firstly as a volumetric expansion coefficient and secondly as a linear thermal expansion. The volumetric expansion coefficient can be measured for all substances of condensed matter (liquids and solids) while the linear thermal expansion can only be measured in the solid state and is common in engineering applications. Some substances have a negative expansion coefficient and will expand when cooled, e.g. freezing water.

Thermal expansion is used in mechanical applications to fit parts over one another; e.g., a bushing can be fitted over a shaft by making its inner diameter slightly smaller than the diameter of the shaft, then heating it until it fits over the shaft, and allowing it to cool after it has been pushed over the shaft, thus achieving a 'shrink fit'. The thermal expansion coefficient is calculated between three different volumes using the formula below:

$$\alpha = \frac{1}{3V}\frac{\Delta V}{\Delta T} \tag{2.42}$$

V is the volume and *T* is the temperature. A large value of thermal expansion means that the volume of the sample responds strongly to changes in the temperature.

2.1.6. Annealing Process

Annealing is a heat treatment in which a material is exposed to an elevated temperature for an extended time and then slowly cooled down. It is regarded as the toughening process and prevents the creation of defects in the atomic scale as defects like vacancies, misplacement, etc. can really hurt the strength of material. In the glass factory it is extremely important to anneal the glass before it is ready or else it will be very fragile and even removing it from its mould will be impossible. Glasses which are not properly annealed will contain stress which may result in breakage before or at any time subsequent to their removal from the kiln. Annealing is critical to the longevity of glass.

Annealing is also used as an optimisation tool in finding the global minima. Another important application is to relieve internal stress, refine the structure and improve cold working properties. There are three stages in the annealing process, with the first being the recovery phase, which results in softening of the metal through removal of crystal defects and the internal stresses which they cause. The second phase is recrystallization, where new grains nucleate and grow to replace those deformed by internal stresses. If annealing is allowed to continue once recrystallization has been completed, grain growth will occur, in which the microstructure starts to coarsen and may cause the metal to have less than satisfactory mechanical properties. The high temperature of annealing may result in oxidation of the surface of the metal, resulting in scale. If scale is to be avoided, annealing is carried out in an oxygen, carbon, and nitrogen free atmosphere. In thermodynamics annealing occurs by diffusion of atoms within a solid material, so that the material progresses towards its equilibrium state. Annealing process is depicted in Figure 2.6.

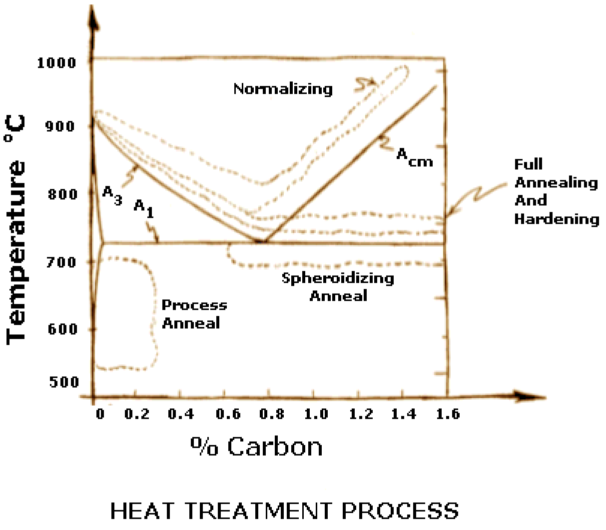

Figure 2.6. The different processes of annealing are illustrated, special attention to full annealing [http://www.efunda.com/processes/heat_treat/softening/annealing.cfm].

2.1.7. Quantum Mechanics

2.1.7.1. Historical Overview

Quantum mechanics deals with the behaviour of subatomic particles, particularly electrons. Quantum mechanics differs from classical mechanics (where Newton's laws of motion are solved) in that matter has wave-like character, i.e. instead of particles and waves having distinct entities, particles have some of the properties of waves and waves have some of the properties of particles.

It is not possible to obtain the exact solutions to the Schrödinger equation for any but the smallest, totally symmetric systems. Quantum mechanics methods are characterised by their various mathematical approximations to its solutions. The fundamental section of quantum mechanics is the ab initio methods. The aim of an ab initio method is to find the solution to the many-body Schrödinger equation for the system being studied. The behaviour of N electrons in a system is described by the many-body wavefunction Ψ, which is an anti-symmetric function of the electron coordinates, $\{r_i \; i = 1....N\}$. For convenience, one can write such a wave function in the form of a product of individual particle functions (leads to the so-called Slater determinant [Slater 1951]):

$$\Psi(x_1, x_2, ..., x_N) = \chi_1(x_1) \cdot \chi_2(x_2) \cdot ... \cdot \chi_N(x_N) \quad (2.43)$$

This wavefunction satisfies the many-body Schrödinger equation written as:

$$\mathrm{H}E = E\Psi \quad (2.44)$$

where

$$\mathrm{H} = -\frac{\hbar^2}{2m}\sum_i \nabla^2_{r_i} + V_{ext}(\{r_i\} + V_{e-e}\{r_i\}) \quad (2.45)$$

and the eigenvalue E is the total energy of the system. The potential V_{ext} consists of the external potential imposed on the electrons by the nuclear configuration {R$_I$} and V$_{e\text{-}e}$ is the electron-electron interaction given by the Hartree term $\sum_{j>i}\frac{e^2}{|r_i - r_j|}\cdot i$ denotes the Cartesian coordinates and the spin coordinates of each electron. In principle this equation can be solved to arbitrary accuracy by representing the Ψ as a direct product of the wavefunction and diagonalizing the Hamiltonian. However, the cost of this calculation scales exponentially with the number of electrons in the system and is intractable for all but the smallest of systems. The variational principle shows that the ground state energy can be found by minimizing the quantity

$$E[\Psi] = \frac{\langle \Psi | \mathrm{H} | \Psi \rangle}{\langle \Psi | \Psi \rangle} \tag{2.46}$$

over all possible $\Psi(\{r_i\})$. The variational principle states that the expectation value of the total energy using any approximate many electron wavefunction such as a Slater determinant is an upper bound for the exact total energy. Therefore by varying each electron wavefunction such that it minimizes the total energy

$$\frac{\delta \mathrm{E}}{\delta \varphi_i} = 0 \quad , \tag{2.47}$$

one obtains conditions for each wavefunction in the form of one-electron wave functions. The functions are known as the Hartree-Fock (HF) equations expressed as:

$$\left[-\frac{\hbar^2}{2m}\nabla^2 + V_{ext} + V_x^i \right]\varphi_i = \varepsilon_i \varphi_i \tag{2.48}$$

The ab initio methods use no experimental computations unlike the classical mechanics or the semi-empirical quantum mechanical methods. The computations in ab initio are based solely on the laws of quantum mechanics and on the values of a small number of physical constant like, the speed of light, masses of charges of electrons and nuclei, and Planck’s constant. Ab initio methods provide high-quality quantitative predictions for a broad range of systems. These methods are not limited to a specific class of systems and nowadays handle large systems of up to 100 atoms as compared to previous times where they were very much limited to small systems. The ab initio and atomistic methods are both important and some programs like QMERA combine them together. Since the formation of quantum mechanics in the 1920’s, two major theoretical approaches or electronic structures have emerged; namely, the Hartree-Fock (HF) theory [Hartree 1928, Fock 1930] and the density functional theory (DFT) [Hohenberg and Kohn 1964, Kohn and Sham 1965].

The quality and reliability any electronic structure theory of solids, surfaces and molecules hinges on the ability to describe the many-body interactions accurately enough to allow quantitative predictions of physical properties. A useful theory has to allow practical calculations with a reasonable computational effort on systems which are large enough to represent realistic models. The balance between accuracy and speed is intimately linked to the theoretical approach as well as to the computational implementation. Figure 2.7 shows a comparison for the methodology for solving the many-body Schrödinger equation and the effective one-electron Kohn-Sham equations.

Owing to its applicability to a wide range of systems including metallic, semiconducting and insulating materials and its good balance between accuracy and compute efficiency, the density functional theory has become the dominant approach for calculations of solids and surfaces of different sizes and dimensions. However, for organic molecules the Hartree-Fock based approaches have been very successful in describing the electronic structures, binding energies, vibrational frequencies and other molecular properties [Thomas 1926]. The problem with the Hartree-Fock methods is that they are computer intensive and thus are limited to relatively small systems. Furthermore, problems can arise if one tires to use the HF theory for metallic systems. An overview of the difference between the Hartree-Fock (HF) and the density functional theory (DFT) is shown in Figure 2.8.

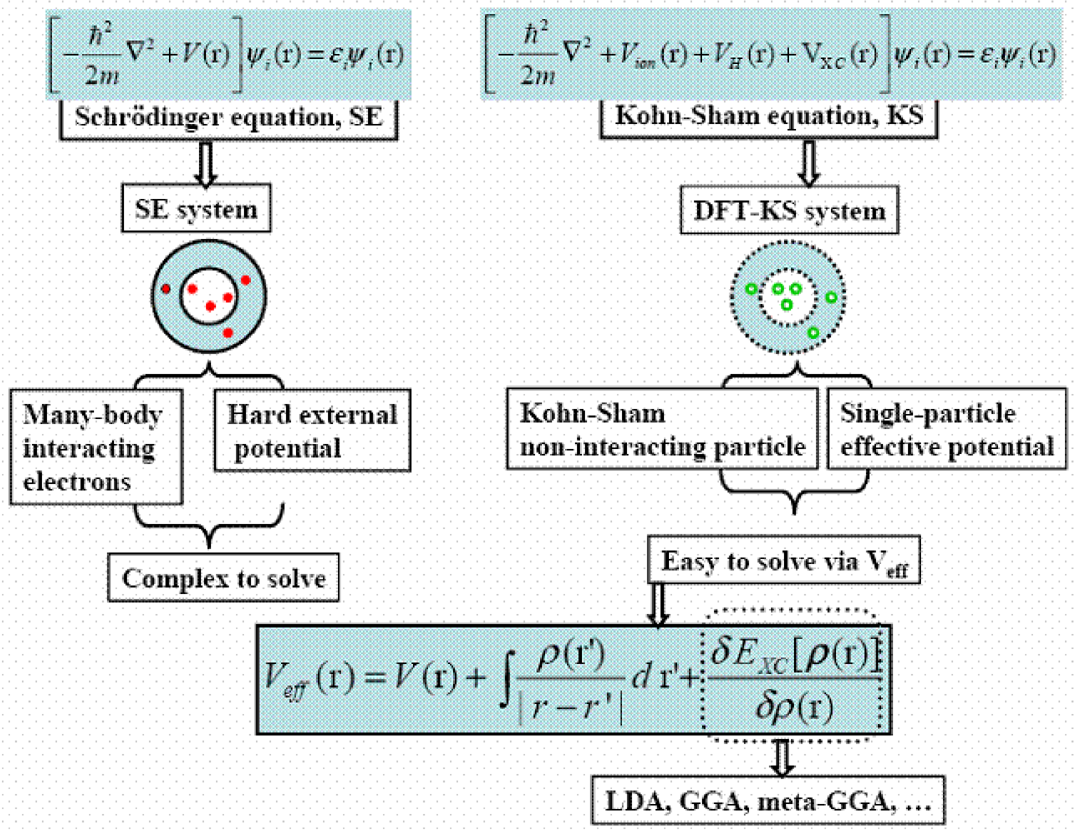

Figure 2.7. The difference between the Schrödinger and Kohn–Sham equations is illustrated [Wimmer 1998].

2.1.7.2. The Density Functional Theory (DFT)

The density functional theory is the quantum mechanical method used in physics and chemistry to investigate the electronic structure of many-body phases, in particular molecules and the condensed phases. DFT is among the most popular and versatile methods available in condensed matter physics (computational physics) and computational chemistry.

The predecessor to the density functional theory was the Thomas-Fermi model, developed by Thomas and Fermi in 1927 [Thomas 1926, Fermi 1928]. They calculated the energy of an atom by representing its kinetic energy as a function of the electron density, combining this with the classical expressions for the nuclear-electron and electron-electron interactions (which can both be represented in terms of the electron density).

Hartree-Fock (1928,1930)	Density Functional (1964,1965)
$\Psi(1,2,...N) = \Psi_1(1)\cdot\Psi_2(2)\cdot ...\cdot\Psi_N(N)+...$ $E = E[\Psi]$ $E[\Psi] = \frac{\int \Psi^* H\Psi d\tau}{\int \Psi^*\Psi d\tau}$ $\frac{\delta E}{\delta \Psi_i} = 0$ $\Downarrow$ $\left[-\frac{1}{2}\nabla^2 + V_c + \mu_x^i\right]\Psi_i = \varepsilon_i\Psi_i$ **Hartree-Fock equations**	$\Psi^*\Psi = \rho(r) = \sum_i \Psi^*\Psi$ $E = E[\rho]$ $E[\rho] = T_0[\rho] + U[\rho] + E_{xc}[\rho]$ $\frac{\delta E}{\delta \Psi_i} = 0$ $\Downarrow$ $\left[-\frac{1}{2}\nabla^2 + V_c + \mu_{xc}\right]\Psi_i = \varepsilon_i\Psi_i$ **Kohn-Sham equations**

Figure 2.8 shows the Hartree-Fock and density functional theory schemes on the left and right respectively in quantum mechanics. The DFT leads to the Kohn-Sham equations [Wimmer – Electronic Structure Methods, NATO Series].

Although this was an important first step, the Thomas-Fermi equation's accuracy was limited because it did not attempt to represent the exchange energy of an atom predicted by the Hartree-Fock theory. An exchange energy was added by Dirac in 1928. The Thomas-Fermi-Dirac theory remained rather inaccurate for most applications. The largest source of error was in the representation of the kinetic energy, followed by the errors in the exchange energy, and due to the complete neglect of the electron correlation.

The density functional theory is an approach to the electronic structure of atoms and molecules which has enjoyed a dramatic surge since the 1980s [Leach 1998, Parr 1983, Wimmer 1991]. The density functional theory is based on a rather remarkable theorem which states that the total energy of a system such as a bulk solid or a surface depends only on the electron density of its ground state [Hohenberg and Sham 1964, Wimmer 1991, MedeA User's Guide]. The Hohenberg-Kohn theorem [Leach 1996, Wimmer 1991] thus enables us to write the total electronic energy as a function of the electron density:

$$E[\rho] = T_o[\rho] + U[\rho] + E_{XC}[\rho] \tag{2.49}$$

$T_o[\rho]$ is the kinetic energy, U$[\rho]$ is the Coulombic energy, and $E_{XC}[\rho]$ contains the exchange and correlation contributions. All of the electron-electron interactions are thus contained within the E_{XC} term. A crucial conclusion from the Hohenberg-Kohn theorem is that the ground-state properties of a system are determined by the density. An incorrect density gives energy above the true energy. To perform a density functional calculation it is necessary to write the various terms in equation (2.49) in terms of the density and then optimise the energy with respect to the density, subject to any constraints on the system. The starting point is a wavefunction that is taken to be antisymmetrised product of molecular orbitals which are both real and orthonormal. The charge density at a point r can then be written as the sum over occupied molecular orbitals of ψ^2:

$$\rho(r) = \sum_i n_i \left|\psi_i(r)\right|^2 \tag{2.50}$$

The kinetic energy $T_o[\rho]$ of all effective electrons in the system is given by:

$$T_o[\rho] = \sum_i n_i \int \psi *_i (r) \left[-\frac{\hbar^2}{2m} \nabla^2 \right] \psi_i(r) dr \tag{2.51}$$

In the above equation n_i denotes the number of electrons in state *i*. By construction, dynamical correlations between the electrons are excluded from the $T_o[\rho]$. The Coulomb energy term $U[\rho]$ is purely classical and contains the electrostatic energy arising from the Coulombic attraction between electrons and nuclei (U_{en}), the repulsion between all electronic charges (U_{ee}), and the repulsion between nuclei (U_{nn}):

$$U[\rho] = U_{en} + U_{ee} + U_{nn} \tag{2.52}$$

with

$$U_{en} = -e^2 \sum_{\alpha} Z_\alpha \int \frac{\rho(r)}{|r - R_\alpha|} dr \tag{2.53}$$

$$U_{ee} = e^2 \int\int \frac{\rho(r)\rho(r')}{|r - r'|} drdr' \tag{2.54}$$

$$U_{nn} = e^2 \sum_{\alpha\alpha'} \frac{Z_\alpha Z_{\alpha'}}{|R_\alpha - R_{\alpha'}|} \tag{2.55}$$

where *e* denotes the elementary charge of a proton and Z_α is the atomic number of atom α at position R_α. The summations extend over all atoms and the interactions over all space. The exchange-correlation energy E_{XC} includes all remaining complicated electronic contributions to the energy. The most important of these contributions is the exchange term. The next step is the derivation of equations that can be used for practical density functional calculations. Equations (2.49) to (2.55) introduce one-particle wave functions and a change of these wave functions corresponds to a variation in the electron density. The procedure leads to the following equations which include the exchange-correlation term:

$$\left[-\frac{\hbar^2}{2m}\nabla^2 + V_C(r) + \mu_{XC}\left[\rho(r)\right]\right]\psi_i(r) = \varepsilon_i\psi_i(r) \qquad (2.56)$$

with

$$V_{eff} = V_C(r) + \mu_{xc}[\rho(r)] \qquad (2.57)$$

Equations (2.56) are called the Kohn-Sham equations. The electron density, which corresponds to these wave functions, is the ground state density which minimizes the total energy. The Coulomb or electrostatic potential $V_C(r)$ at point r is generated from the electric charges of all nuclei and electrons in the system. It can be evaluated directly in space:

$$V_C(r) = -e^2\sum_\alpha \frac{Z_\alpha}{|r - R_\alpha|} + e^2\int \frac{\rho(r')}{|r - r'|}dr' \qquad (2.58)$$

The electronic structure calculation is shown in Figure 2.9.

The solutions of the Kohn-Sham equations form an orthornomal set, i.e.

$$\int \psi *_i (r)\psi_j(r)dr = \delta_{ij} \qquad (2.59)$$

The exchange-correlation potential is related to the exchange-correlation energy by:

$$\mu_{xc} = \frac{\partial E_{xc}[\rho]}{\partial \rho} \tag{2.60}$$

The equation above is formally exact in the sense that it does not contain any approximations to the complete many-body interactions.

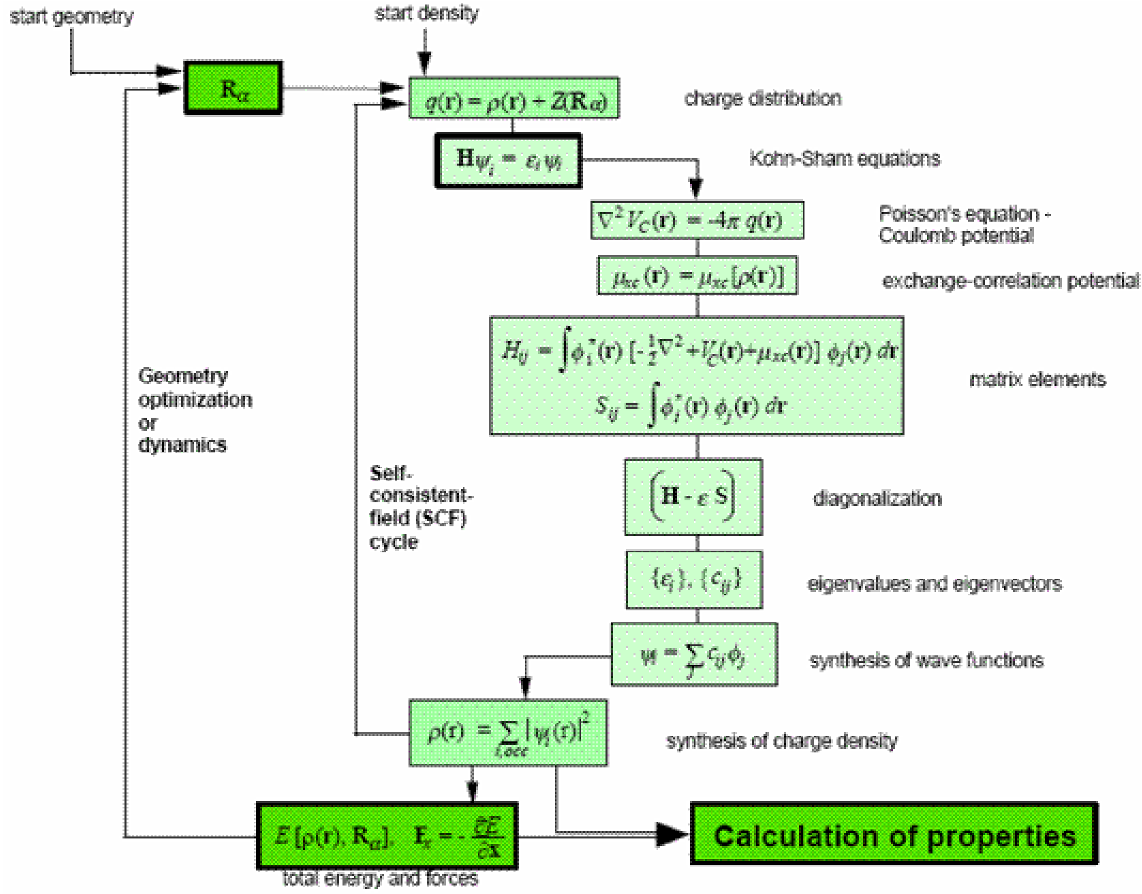

Figure 2.9 shows the structure of a typical electronic structure calculation [Dreizler and Gross 1990; Perdew and Yang 1992; Freeman and Wimmer 1995].

2.1.7.3. Solution to the Kohn-Sham equation

By standard mathematical techniques for solving eigenvalue problems, expansion can be made to the unknown solutions $\Psi_i(\mathrm{r})$ in a set of known functions, $\Phi_j(\mathrm{r})$, with unknown linear coefficients, c_{ij}

$$\Psi_i(r) = \sum_j c_{ij}\Phi_j(r) \tag{2.61}$$

These coefficients are determined through a variational procedure which leads to the solution matrix problem

$$(\mathrm{H} - \varepsilon S)c = 0 \tag{2.62}$$

H and S are the so-called Hamiltonian and overlap matrices with the following matrix elements

$$\mathrm{H}_{ij} = \int \Phi_i(r)\left[-\frac{\hbar^2}{2m}\nabla^2 + V_c(r) + \mu_{xc}(r)\right]\Phi_j(r)dr \tag{2.63}$$

$$S_{ij} = \int \Phi_i \Phi_j(r)dr \tag{2.64}$$

ε represents an eigenvalue and c are the coefficients of a solution denoted as a column vector.

2.1.7.4. The Local Density Approximation (LDA)

As a consequence of the Kohn-Sham theorem, the exchange-correlation energy depends only on the electron density. As a simple and, as it turns out, surprisingly good approximation, one can assume that the exchange-correlation energy depends only on the local electron density around each volume element *dr*. This is called the local density approximation (LDA):

$$E_{xc}[\rho] \approx \int \rho(r)\varepsilon_{xc}^0[\rho(r)]dr \tag{2.65}$$

The basic idea of the LDA is illustrated in Figure 2.10. In any atomic arrangement such as a crystal, a surface, or a molecule, there is a certain electron density ρ(r) at each point *r* in space. The LDA then rests on two basic assumptions. Firstly that the exchange and correlation effects come predominantly from the immediate vicinity of a point *r* and secondly that these exchange and correlation effects do not depend strongly on the vibrations of the electron density in the vicinity of a point *r*. If conditions of the two assumptions are reasonably well fulfilled, then the contribution from volume element dr would be the same as if this volume element were surrounded by a constant electron density to the same value within dr. This is an excellent approximation for metallic systems, but represents quite a significant simplification in systems with strongly varying electron densities.

A system of interacting electrons with a constant electron density is called a homogeneous electron gas. The exchange-correlation energy per electron of a homogeneous electron gas, $\varepsilon^{0}_{xc}[\rho]$, has been calculated by several approaches. As a result, $\varepsilon_{xc}[\rho]$, is quite accurately known for a range of densities. For practical calculations, $\varepsilon_{xc}[\rho]$ is expressed as an analytical function of the electron density. There are various analytical forms with different coefficients in their representation of

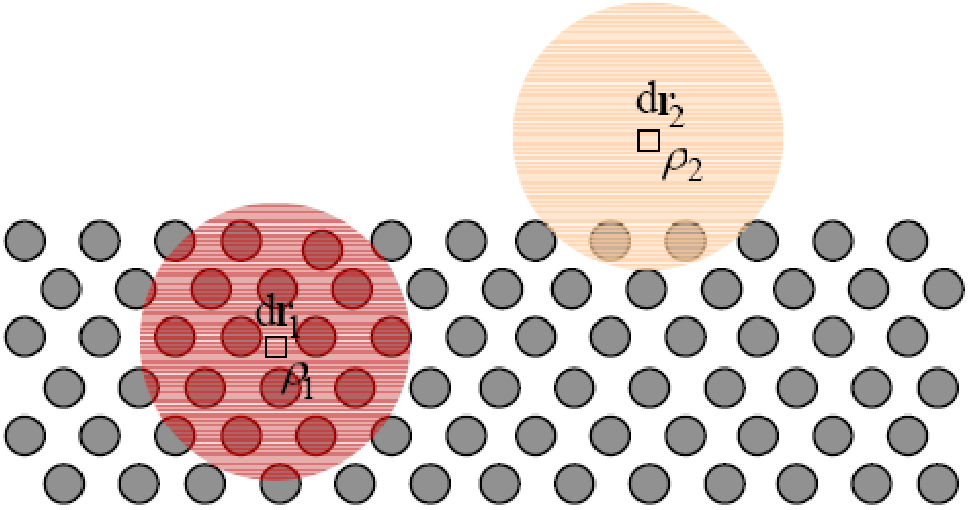

Figure 2.10 shows the illustration of the local density approximation. For the purpose of computing the exchange-correlation energy in a volume element dr_i, the electron density ρ_i around point r_i is assumed to be constant in the near surrounding. The value of ρ_i is different in each volume element.

the exchange-correlation terms. These coefficients are not adjustable parameters, but rather they are determined through first-principles theory. Hence, the LDA is a first principle approach in the sense that the quantum mechanical problem is solved without any adjustable, arbitrary, or system dependent parameters.

There are two types of exchange-correlation terms, one for the energy and one for the potential. The energy, ε_{xc}, is needed to evaluate the total energy and the potential term, μ_{xc}, is required for the Kohn-sham equations. The two terms are related by:

$$\mu_{xc} = \frac{\partial[\rho\varepsilon_{xc}(\rho)]}{\partial\rho} \tag{2.66}$$

Using the explicit formulas given in Table 2.2, one can evaluate the exchange-correlation potential for any electron density ρ(r).

Table 2.2. Explicit forms for the local density approximation, originally given by Gôspôr [Gôspôr 1954] and Kohn and Sham [Kohn and Sham 1965]. Correlation terms are according to Heidin and Lundvist [Heidin and Lundvist 1972]. Exchange and correlation energies per electron are denoted by ε and the corresponding potentials by μ. Both quantities are given in Hartree atomic units (1 Hartree = 2 Rydberg = 27.21165 eV).

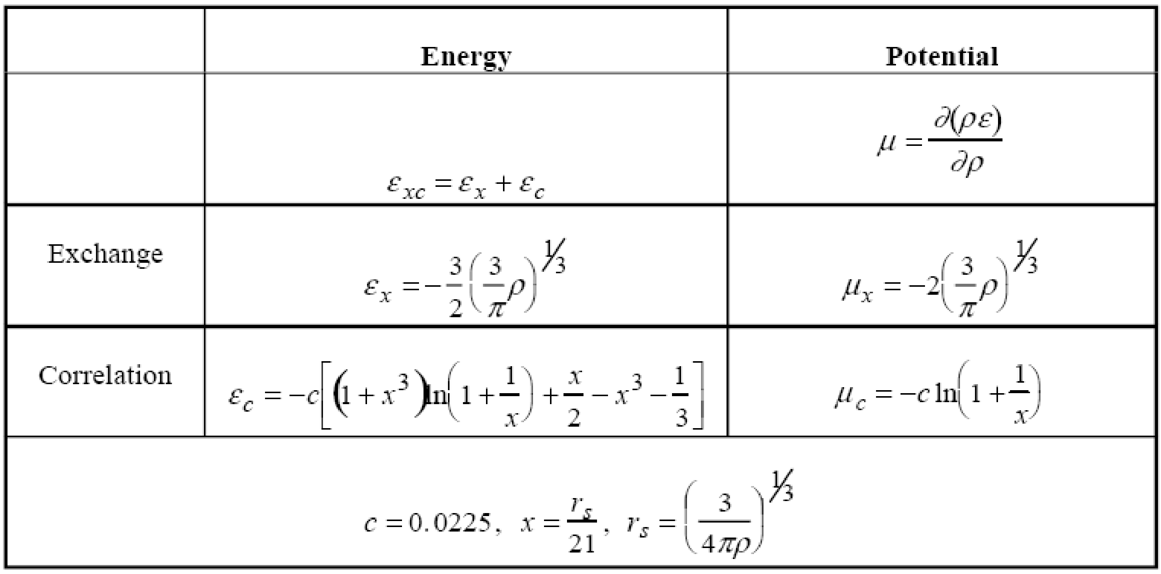

	Energy	**Potential**
	$\varepsilon_{xc} = \varepsilon_x + \varepsilon_c$	$\mu = \frac{\partial(\rho\varepsilon)}{\partial\rho}$
Exchange	$\varepsilon_x = -\frac{3}{2}\left(\frac{3}{\pi}\rho\right)^{1/3}$	$\mu_x = -2\left(\frac{3}{\pi}\rho\right)^{1/3}$
Correlation	$\varepsilon_c = -c\left[\left(1+x^3\right)\ln\left(1+\frac{1}{x}\right)+\frac{x}{2}-x^3-\frac{1}{3}\right]$	$\mu_c = -c\ln\left(1+\frac{1}{x}\right)$
$c = 0.0225,\ x = \frac{r_s}{21},\ r_s = \left(\frac{3}{4\pi\rho}\right)^{1/3}$		

2.1.3.5. The Generalised Gradient Approximation (GGA)

The development of non-local exchange and correlation functions challenges for the need to improve the LDA when coming to the bond energies of molecules, the cohesive energies of solids, and the energy barriers of molecular reactions. A large number of total energy calculations have shown that LDA gives interatomic bond lengths within ± 0.05 Å of experiment or better for a great variety of solids, surfaces and molecules. However, two systematic trends have been found, that is that the weak bonds are too short and binding energies calculated with the LDA are typically too large [Wimmer 1998]. The generalized gradient approximation (GGA) [Yang *et al*. 1990, Perdew 1991] is then employed to deal with the failures of the local density approximation. The local density approximation can be considered to be the zeroth order approximation to the semi-classical expansion of the density matrix in terms of the density and its derivatives [Dreizler and Gross 1990].

A natural progression beyond the LDA is thus to the gradient expansion approximation in which first order gradient terms in the expansion are included. This results in an approximation for the exchange hole which has a number of unphysical properties which does not normalise to -1 and it is not negative definite and contains oscillations at large separation distance (u) [Yang *et al*. 1990]. In the generalized gradient approximation a function form is adopted which ensures the normalisation condition and that the exchange hole is negative definite. This leads to an energy function that depends on both the density and its gradient but retains the analytic properties of the exchange correlation hole inherent in the LDA. The typical form for a generalized gradient approximation (GGA) function is:

$$E_{xc} \approx \int \rho(r)\varepsilon_{xc}(\rho,\nabla\rho)dr \tag{2.67}$$

The GGA improves significantly on the LDA's description of the binding energy of molecules. It was this feature that led to the very wide spread acceptance of the DFT in the chemistry community during the early 1990. Figure 2.11 shows the density functional theory methods implementation with the entire link from LDA to GGA.

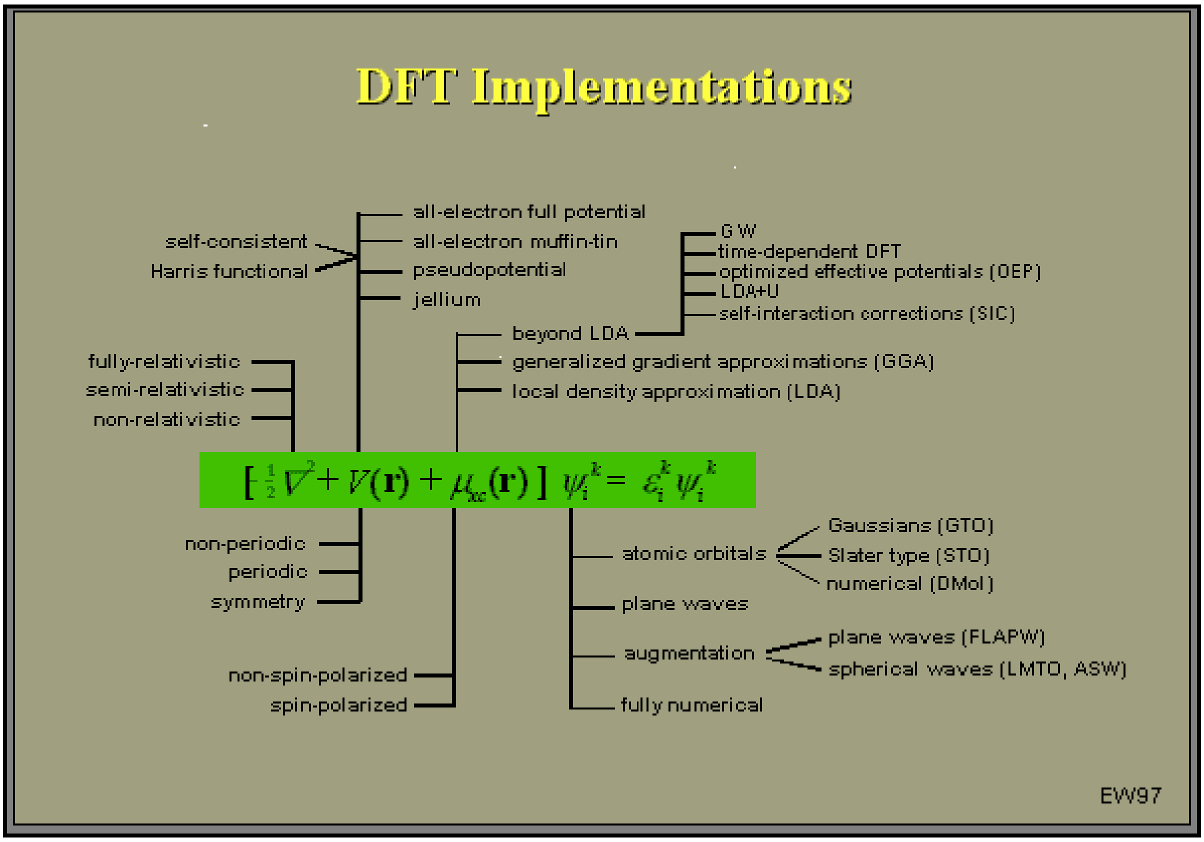

Figure 2.11. Overview of the theoretical and computational choices for the solution of the density functional one-particle equations [Yang et al. 1990; Freeman and Wimmer 1995] is illustrated.

2.1.8. The DMOL^3 Code

DMOL^3 [Delley 1990, Delley 2000] computer code allows the simulations or modelling of the electronic structure and energetics of the molecules, solids, and surfaces using the density functional theory (DFT). A broad range of systems, including organic and inorganic molecules, molecular crystals, covalent solids, metallic solids, and infinite surfaces of a material can be studied using the DMOL^3 computer code and then the structure, reaction energies, reaction barriers, thermodynamic properties and vibrational spectra can be predicted. DMOL^3 uses the DFT to produce highly accurate results while keeping the computational cost fairly low for an ab initio method. The code is capable of performing quite a few different tasks such as:

- Single-point energy calculations
- Geometry optimization
- Molecular dynamics
- Transition-state search
- Transition-state optimization
- Following a reaction path.

Each of these calculations can be set up so that it generates specified chemical and physical properties. A number of properties are calculated by a DMOL^3 job including the total energy, binding energy, density of states (both total and partial), population analysis, etc. The code performs calculations on molecules and three-dimensional periodic structures (crystals) as well as non-periodic systems but cannot work on structures with two-dimensional periodicity such as surfaces. Molecular dynamics in total energy DFT schemes is implemented in essentially the same way as in conventional force-field methods with the main difference being the atomic forces which are derived by solving the DFT equations rather than being derived from the empirical potentials of interatomic interactions.

The DMOL^3 calculation dialog contains the following tabs:

- Setup: Allows the choice of the type and quality of calculation that the code will perform along with other basic input options, such as the basis set, DFT functional, spin state, and the total charge.
- Electronic: Allows the setting of the parameters that control the details of the energy evaluation including the integration accuracy and the SCF convergence.
- Properties: Allows the selection of the properties that will be computed by the code which include the volumetric visualizations (such as charge density and molecular orbitals) and electronic properties.
- Job Control: Allows the specification of the job settings for the DMOL^3 calculation.

2.1.8.1. Simulation Procedure

Three-dimensional structures of the Au_N (N = 2, 4, 13, 19, 38, and 55) clusters of different number of atoms were built to favour the code used for this work. Geometry optimization was then performed on different clusters to search for minimum energy structures. The overall quality of the DMOL^3 calculation affects the basis set, k-point and SCF convergence. We have chosen medium which is regarded as the high quality level for the geometry calculations on metallic gold clusters. The electron density functional is treated by the gradient-corrected generalised gradient approximation (GGA) [Yang *et al*. 1990, Perdew 1991] with the exchange-correlation potential parameterized by Perdew and Wang (PW91) [Perdew and Wang 1992]. The DNP or DND basis set was used.

The calculations were performed using the same orbitals for alpha and beta spins by choosing the spin-restricted option. The medium convergence threshold was chosen to set the quality of the geometry optimization for energy, maximum force and maximum displacement between optimization cycles. The values for the energy, maximum force and maximum displacement in the medium convergence threshold respectively are 2 x 10^{-5} Ha (2.72 x 10^{-3} eV), 0.004 Ha/Å^{-1} (0.1088 eV/Å^{-1}) and 0.005 Ha (0.136 eV). Maximum number of geometry optimization cycles was specified by selecting maximum number of iterations and was set at 100 which proved enough to give good results. The maximum step size is set at 0.3 Å. This number determines the length of the simulation and once it is reached the calculation will stop, even if the convergence criteria are not satisfied.

The quality of the k-point sampling is particularly important for metallic systems, where rapid changes in electronic structure may occur along the energy band that crosses the Fermi level. The default settings used by DMOL^3 are designed to give accurate sampling for metallic systems. The integration accuracy, SCF tolerance and orbital cutoff quality were set to medium with the smearing set at 0.05 Ha (1.360 eV) and the all-electron core treatment was used. The total energy, binding energy, density of states, etc. were calculated during the simulations. The quality of the k-points is tested in the convergence of the energy during a simulation.

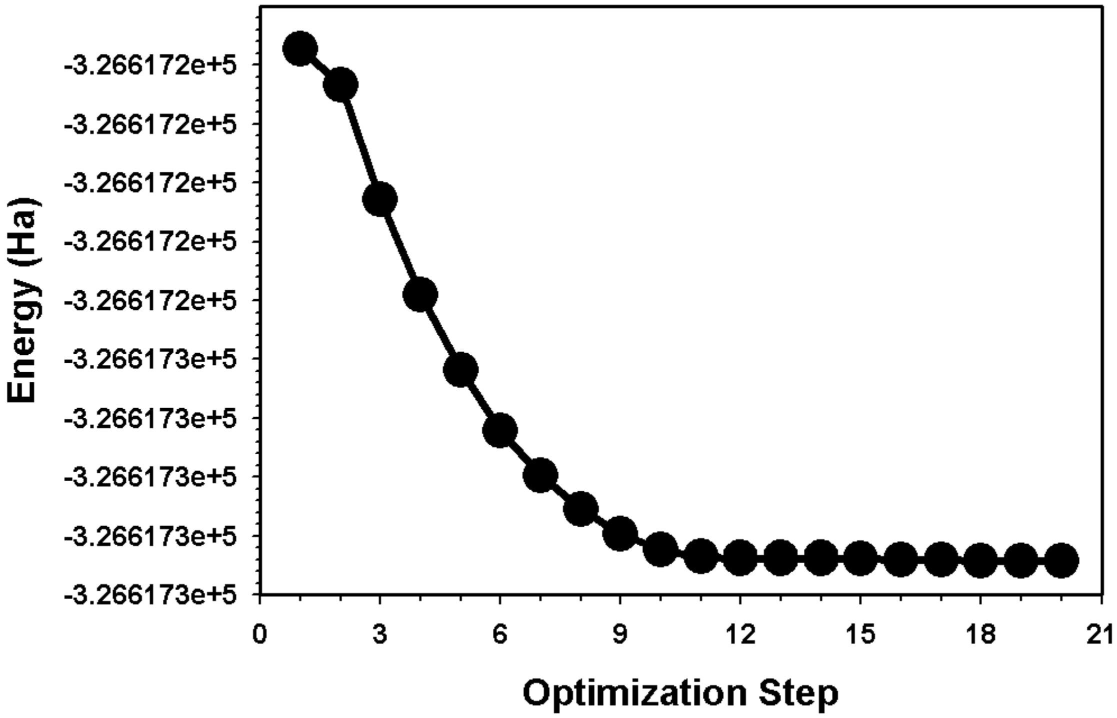

Figure 2.12 shows energy as a function of optimization steps for a DMOL^3 geometry optimization calculation.

Figure 2.12 shows a typical energy convergence in a DMOL^3 geometry optimization simulation. The energy starts at less negative values and goes down exponentially from the first step to step number 11. The energy then stabilizes and becomes constant from step 12 to step 20 at a value of -326617.3284 Ha. The stabilized energy signifies a good optimized structure and that will further imply a well run calculation. It is always good to check the convergence of few parameters even though the OUPUT file gives a successful completion message.

2.1.9. QMERA (QM/MM)

QMERA [Sherwood *et al.* 2003] is a program that allows combined quantum mechanical (QM) and molecular mechanics (MM) forcefield calculations on nonperiodic systems to be performed using the ChemShell [Sherwood and de Vries 1997-2000] environment. ChemShell is a computational chemistry environment, based on the Tcl (Tool Command Language) interpreter that takes over the communication and data handling for hybrid QM/MM calculations leaving the time-consuming energy evaluations to specialized external codes.

Mixed quantum mechanical molecular mechanics (QM/MM) calculations involve the division of a system into two parts: the central chemically active QM region ("*I*") and the surrounding outer MM region ("*O*"). Treating the central part of the system quantum mechanically allows the electronic structure and its changes (e.g. bond breaking and formation in a chemical reaction) to be modelled in a concise way. The remaining portion of the system is described using molecular mechanics with the two regions being allowed to interact through the use of appropriate potentials. The combination of the speed and efficiency of the MM forcefield calculations for the bulk of the system with the versatility and precision of the QM method for the important reactive zone allows the reactions in large systems to be studied in a more realistic manner than would be possible using either QM or MM alone.

QMERA provides both mechanical and electronic embedding schemes for treatment of the QM/MM interactions. Dangling covalent bonds between the QM and MM regions are capped with hydrogen link atoms. Geometry and transition state optimization in QMERA can be carried out using a range of minimizers, including a linear-scaling delocalized coordinate algorithm. QMERA employs DMOL3 as the QM server and GULP for the MM calculations.

2.1.9.1. Tasks in QMERA

The QMERA module allows you to perform calculations on nonperiodic systems. QMERA can currently perform three different tasks:

- Single-point energy calculation
- Geometry optimization
- Transition state optimization

A QMERA job initiates with the definition of the structure which should be a nonperiodic three-dimensional (3D) atomistic document that contains the system of interest. The second step is to select the type of calculation to be performed and set the associated parameters. We have in our work, performed simple single-point energy calculations before we could run geometry optimization calculations. The calculation is then run by selecting the server on which the calculation will take place. The final step after a geometry optimization calculation will be to analyse the results when the job is complete. The files are returned to the user and where appropriate, displayed in the Project Explorer dialog.

2.1.9.2. Simulation Details

We have performed QM/MM geometry optimization calculations on the interactions between a graphite surface and a gold atom. The geometry optimization task allows for the refine of the geometry of a structure in order to obtain a stable structure. This is achieved by carrying out an iterative process in which the coordinates of the atoms are adjusted at each step so that the total energy of the structure is minimized. Geometry optimization is based on reducing the magnitude of calculated forces until they become smaller than defined convergence tolerances. The process of geometry optimization results in a structure that closely resembles the real structure.

The quantum mechanical (QM) region was first selected by highlighting the central atoms which we need to fall in that region and then click select and add. The program indicates the selected atoms by naming them QuantumAtoms. Geometry optimization calculations were then performed for 500 maximum iterations and the step size was set at 0.3 Å. With the quality set to medium we have used the energy of 2 x 10^{-4} Ha (5.4 x 10^{-3} eV) to specify the convergence threshold for the maximum energy change. The maximum force of 0.004 Ha/Å (0.11 eV/Å) to specify the convergence threshold for the maximum force, and the maximum displacement is 0.005 Å for the convergence threshold for the maximum displacement were also used. The BFGS pseudo-Newton minimization with BFGS update of the inverse hessian was used. The DMOL^3 code was used as the server for QM interactions while GULP was used as the

MM server. The electron density exchange-correlation functional for the QM server was handled by the generalized gradient approximation (GGA-PW91). The GGA functional yields more reliable results and is relevant for any calculations involving comparison of energies. In the molecular mechanics (MM) server GULP, we used the Dreiding forcefield to handle the interactions between the outer carbon atoms. The electronic embedding scheme was employed and the model to disperse the boundary charge was included. The program is then able to calculate the electron density, frequency, population analysis and Muliken charges. The total and the binding energies are given in the output file while the optimized structure is updated every step of the calculation.

2.1.10. COMPUTER SPECIFICATIONS FOR CALCULATIONS

The atomistic (MD) simulations on nanoclusters, nanotubes and nanowires were carried out on the ORIGIN 2000 Silicon Graphics Incorporated (SGI) UNIX machine which uses the IRIX 6.5 operating system. The access to the SGI machine is through a remote login from a workstation. Because of the capacity of the SGI machine and, depending on the size of the system, calculations on the nanoclusters, nanotubes and nanowires took on average 4 hours to two days to complete. A calculation on the nanocluster with 55 atoms would take about 8 hours to complete while the smallest nanotube calculation would only take about 4 hours to complete. However, the calculation on the nanocluster with 2214 atoms would on average require two days to complete while that one on a multi-wall nanotube would complete after one and a half days. The nanowire took one day to complete.

The ab inito calculations were performed on the HP Compaq Windows XP Service Pack 2 desktop computer. The Materials Studio Version 4.2 operating system was used to run the DMOL^3 calculations on different nonperiodic nanoclusters. The smallest cluster took two days to complete while the biggest nanocluster with 55 atoms would take almost the whole week to converge. The structures from both the MD and ab initio calculations were then viewed using the weblab viewer program and sigmaplot program was used to plot different graphs.

CHAPTER 3: Semi-Empirical Results

3.1. Introduction

In this section we will show results from the molecular dynamics (MD) atomistic simulations. Gold nanoclusters and nanotubes consist of atoms from tens up to a thousand or more atoms. The MD work will focus on the temperature effect on the clusters by discussing the melting temperatures as well as the structural behaviour at different temperatures. The temperature was increased in small intervals until a sudden jump in the energy is obtained. The total energy plotted against temperature shows a jump in the transition of the material from solid to liquid. The radial distribution functions (rdfs) are a useful way of describing the structure at different thermodynamic conditions while the density profiles help in validating the prediction the total energy curve and the rdfs. The change in the structure in terms of the bond distances will be dealt with. Diffusion coefficients and the annealing process are discussed in details.

3.1.1. Molecular Dynamics (MD)

The total energy, radial distribution functions (rdfs) and the density profiles will be the centre of discussion in this part. The total energy shows a jump in the transition of the material from a solid to a liquid phase. The radial distribution functions differentiate between solid, liquid and gas phases of materials. The solid features in the rdfs are characterised by a multiple number of well defined peaks in the structure, the liquid phase will show few well-defined peaks and the gas state will have more long range interactions. The density profiles on the other hand show a decrease in the number of peaks and a change in the pattern when a particular material gets to a liquid state.

We shall therefore combine the three methods in estimating the melting temperatures in different materials (clusters and tubes) considered in this work. Melting in the clusters can be sufficiently predicted as three methods mentioned above can be satisfied. Contrary to the nanoclusters, gold nanotubes do not show the necessary discontinuity in the total energy curve which is essential in the estimation of the melting temperature. We shall therefore show where melting occurs in the nanotubes with the help of the radial distribution functions as well as the density profiles.

We will also plot the diffusion coefficients as a function of temperature for some materials. The heat capacity at constant volume and pressure will be discussed and then compared to that of the bulk. The structural evolution of the nanomaterials will be shown at different temperatures. The annealing process in which materials are cooled from a high temperature to lower temperatures will be studied for the cluster with 309 atoms and the nanotube with 1252 atoms.

3.1.1.1. Gold Clusters

We commenced simulations at very low temperatures and increased the temperature in the steps of 50 K, 100 K or 200 K until the total energy shows a jump or a sudden increase in the slope. The use of a change in the total energy slope as signal of melting temperature in materials is quite common [Gülseren et al. 1995, Ercolessi *et al.* 1991, Wang et al. 2004, Rodriguez-Lopez *et al.* 2003]. However, we prefer to couple this method with changes in the radial distribution functions (rdfs) as well as the density profiles to further validate our predictions of the melting points. The number of atoms in the gold clusters ranges from 55 to 2214 in order to study the impact of the system size on the physical properties. The cluster with 2214 atoms is sufficiently large enough to yield most details concerning the cluster behaviour and could also depict some bulk properties. The magic number clusters considered in this work are Au_{55}, Au_{147} and Au_{309}.

3.1.1.1.1. The Au_{55} Cluster

We now show the total energy, in the NPT Berendsen ensemble at 0.0 kbar, for the Au cluster with 55 atoms. The energy curve plotted in Figure 3.1 depicts a linear increase in the energy with temperature up to 1200 K. The jump or discontinuity in the energy is not clear but observable. This makes the use of radial distribution functions and density profiles more necessary as will be noted in Figures 3.2 and 3.3. There is a significant change in total energy from 1600 K to 1700 K. The value of the total energy at 300 K is -3.09 eV/atom which is less negative when compared to the bulk cohesive energy of -3.78 eV/atom [Sutton and Chen 1990], hence the cluster will be less stable than the bulk at 300 K.

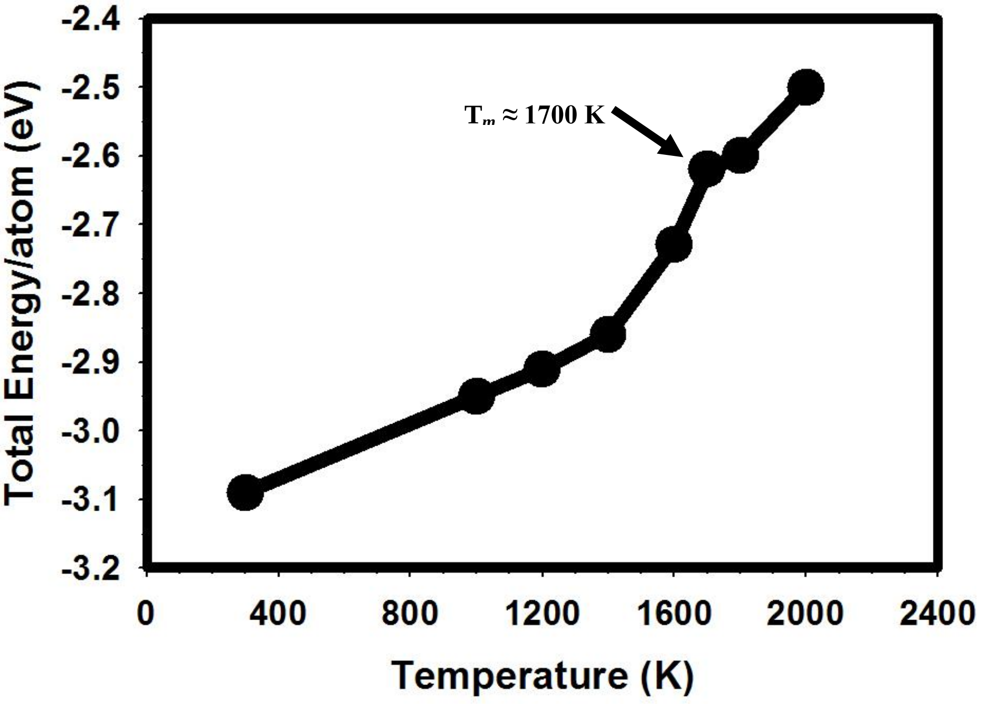

Figure 3.1. The energy is plotted against temperature in the constant pressure and temperature conditions. The estimated melting temperature is shown by the arrow in the inset.

The radial distribution functions at different temperatures, depicted by Figure 3.2, show more structure at 300 K where many periodic peaks can be observed. The number of peaks has decreased dramatically at 1400 K but some solid features are still present. However, the peaks have lost the order of arrangement that was seen at 300 K. The graph at 1700 K shows two well defined peaks which have dropped in peak heights. The behaviour of the peaks at 1700 K signifies a liquid structure and, the trend is further continued at 1800 K.

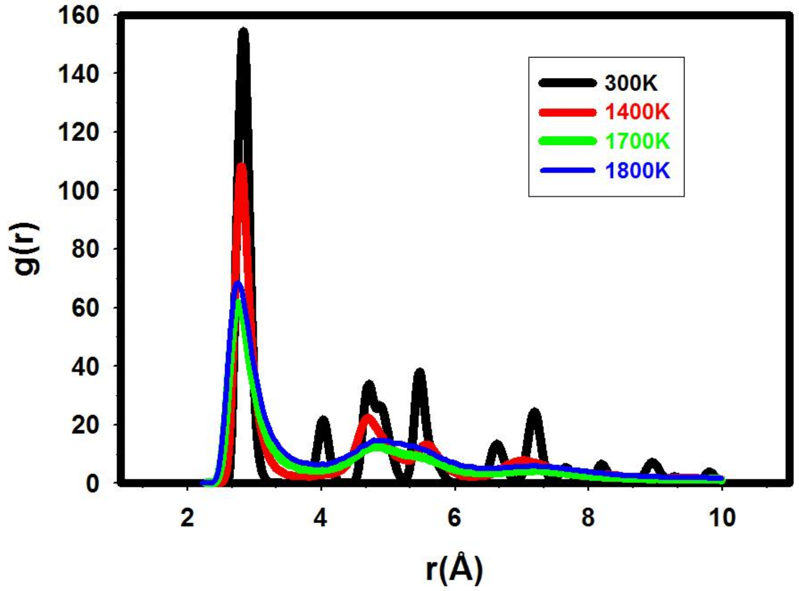

Figure 3.2. The radial distribution functions in the constant pressure and temperature conditions are shown for the Au_{55} magic cluster

We now look at Figure 3.3 where the density profiles for the cluster are shown. The structure is dense and follows a circular pattern which gives a distinct peak height at 300 K. There is continuity at 1000 K with the only difference being the decrease in the denseness. However, the plot at 1600 K shows a slight change in the behaviour of the graph. The peak at 1600 K starts to broaden and covers a larger area with a further decrease in the peak height. The noise that represents the denseness in the structure disappears gradually as the temperature is raised. The peak then collapses with a dramatic change in the peak pattern at 1700 K. The dramatic change in the pattern of the peak is a clear indication of a change in the phases. The peak at 1600 K can be taken to be representing a transition temperature as it shows a different behaviour from the ones at 300 K and 1700 K. The temperature just above the melting temperature shows a continuation of the melting process and the same trend was seen in the rdfs.

It therefore argues well to say that the energy plot, the radial distribution functions, and the density profiles concur well in showing the melting behaviour in the cluster. We are satisfied with the results of these three methods and can therefore estimate the melting temperature of the cluster. We deduce the melting temperature of the Au_{55}

cluster to be 1700 K which is several Kelvins above the bulk melting points. The fact that gold undergoes reconstruction at its three low index surfaces {(100), (110) and (111)} might give an indication of a reconstructing cluster. The process of reconstruction makes materials to adopt their most compact structures which results in the reduction in the interatomic distances and tensile stress.

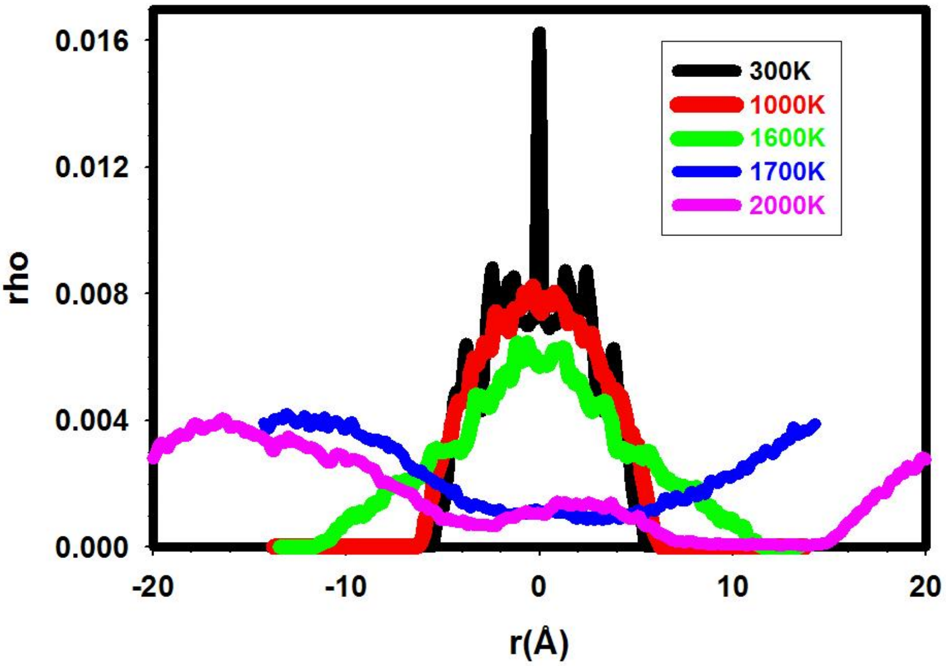

Figure 3.3 shows the density profiles in the Au_{55} cluster. We note the different volumes occupied at various temperatures.

Furthermore, a Au(111) surface has shown melting above the bulk [Carnevali *et al*. 1987] and solid tin clusters (Sn) above the bulk tin have also being reported [Shvartsburg and Jarrold 2000]. The reasoning behind the high melting of the materials expected to show melting that is below the respective bulk material is much attributed to the reconstruction in the effort to relieve some stress. The simulated annealing embedded atom potential Monte Carlo work on the different face-centred cubic (fcc) metal clusters with 55 atoms has shown that palladium (Pd), gold (Au), and platinum (Pt) clusters do not show the discontinuity in the energy at least until 1600 K [Vlachos *et al*. 1993]. Figure 3.4 shows the energy versus temperature plot for different clusters as well as the heat flow in the Al-Cu-V compounds. The transition before 1600 K is only observed in the case of silver (Ag) and nickel (Ni) clusters. The transmission electron microscope experimental work by Singh and Tsai [Singh and Tsai 2003] also uses the discontinuity in the energy to determine melting temperatures (see Figure 3.4b). The heat flow is plotted as a function of temperature for Al-Cu-V nanomaterials and the sudden change in the pattern is considered the point of melting initiation. Also Figure 3.4(b) shows the different namomaterials melt lower than the respective bulk materials.

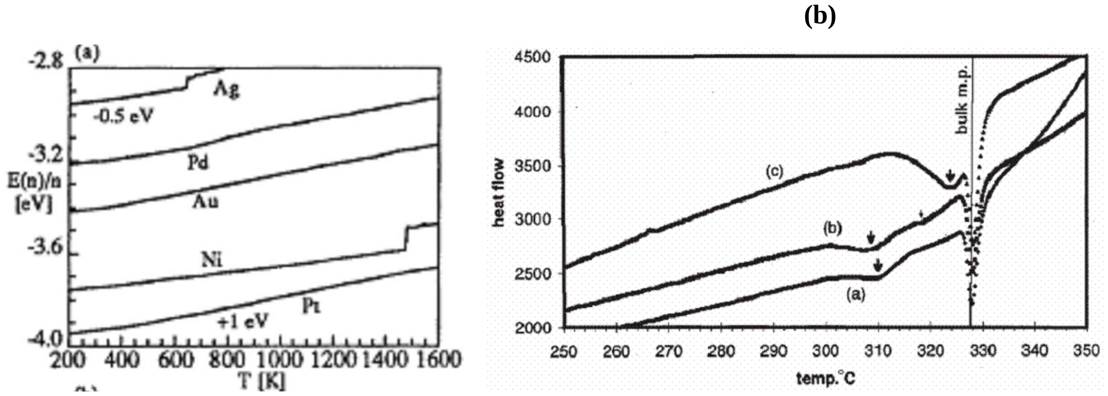

Figure 3.4 shows the energy E(n)/n as a function of temperature for different face-centred cubic (fcc) metals [Vlachos *et al.* 1993] on the left (a) and on the right (b) the heat flow versus temperature in the Al-Cu-V nanomaterials [Singh and Tsai 2003].

The structure of the Au_{55} cluster is shown at the starting configuration and at the melting point in Figure 3.5. The cluster assumes a well ordered near spherical shape at the initial configuration, and then dismantles itself into a disordered structure at 1700 K. The bonding distances do not conform into any particular pattern at 1700K as some increase while others decrease as they deviate from 2.77 Å noted at 0 K.

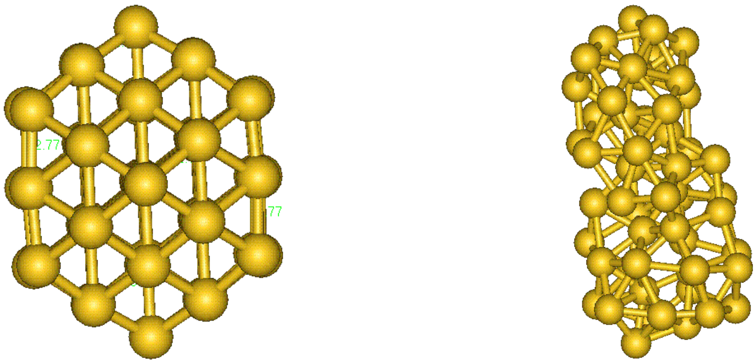

Figure 3.5. The starting configuration of the Au_{55} cluster is on the left. On the right we show the structure at melting (1700 K). The bond distances are 2.77 Å at the initial configurations.

3.1.1.1.2. The Au_{147} Cluster

The gold cluster with 147 atoms was also studied and its melting behaviour the NVT Berendsen ensemble was investigated. An important contribution from these simulations is the step by step illustration of the procedure towards melting by means of the radial distribution functions (rdfs). We will also show the changes in the structure at the corresponding temperatures as in the rdfs.

The plot for the radial distribution functions in Figure 3.6 shows that the cluster reaches its melting temperature at 850 K. The cluster achieves more peaks at 300 K, and that depicts strong crystalline features. At 800 K some solid features are still notable with reduced number of peaks, and in particular the shoulder and the splitting are much visible.

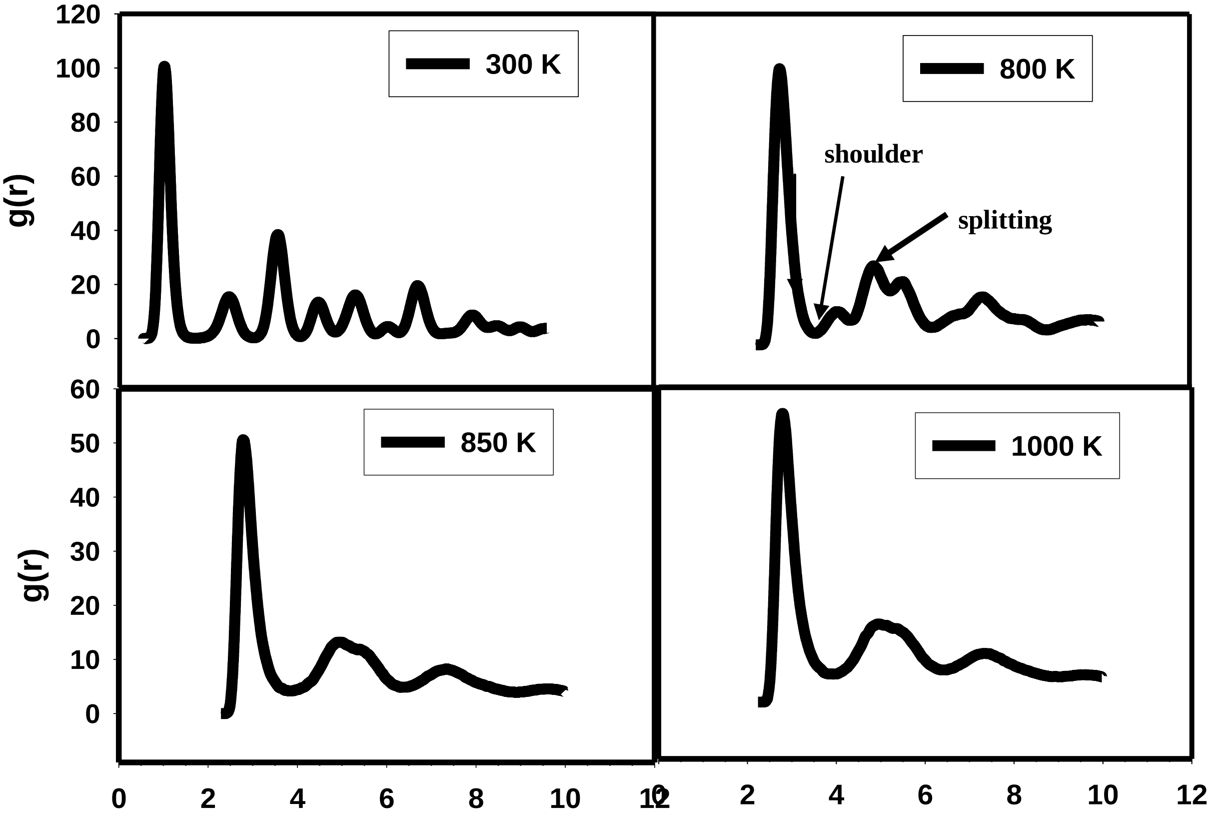

Figure 3.6. Rdfs for the Au_{147} cluster at different temperatures are shown as melting is approached.

The appearance of the shoulder will, therefore, imply the presence of a solid while the splitting signifies the initiation of melting. The cluster is melted at 850 K with the rdf plot showing three ordered peaks. The same peak pattern is again noted at 1000 K. As observed and expected, the predicted melting temperature of the Au_{147} cluster is lower than that of the bulk.

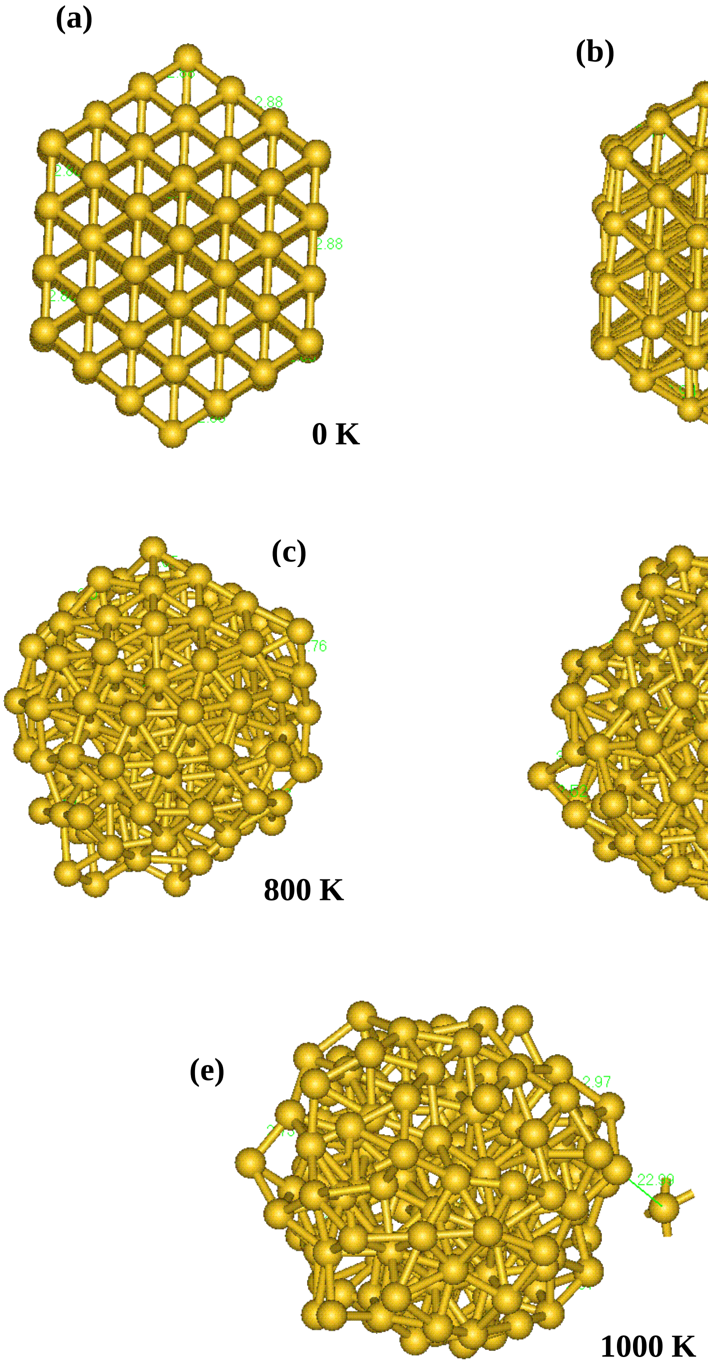

Figure 3.7. The structural evolution of the Au_{147} cluster at different temperatures and constant volume is illustrated in the figure. The initial configurations are represented by (a) and (b).

The cluster before and after simulations is shown in Figure 3.7. The atoms in the cluster at the starting configuration form a hexagonal or spherical pattern and the bonds are defined (Figure 3.7a). The interatomic bond distance is the same as in the bulk gold, i.e. $r \approx 2.88$ Å. It is interesting to note that atoms start to stretch at 300 K as we find an irregular change in the bond distances. However, as depicted by the rdfs the structure is very much a crystal at 300 K (Figure 3.7b) and the atoms and the bond distances are well ordered.

The cluster changes to a significant level at 800 K (Figure 3.7c), where the corners are destroyed and it assumes a convincing round shape. Further collapse in the structure is observed at 850 K (Figure 3.7d), a temperature determined to be the melting of the cluster. The structure begins to disintegrate at 1000 K and a single atom is seen to be breaking away as shown by Figure 3.7e. The structural evolution illustrated in Figure 3.7 further validates the results from the rdfs. The bond distance change from 2.88 Å at the starting configuration to 2.73 Å, 2.93 Å, 3.93 Å, 2.89 Å, 3.92 Å, etc. at 300 K, to 2.70 Å, 2.85 Å, 2.77 Å, 2.86 Å, etc. at 800 K, to 2.80 Å, 2.79 Å, 2.91 Å, 2.82 Å, etc., and finally to 2.79 Å, 2.58 Å, 3.03 Å, 2.66 Å, 2.90 Å, etc. at 1000 K. The change becomes more irregular at 1000 K where distances as low as 2.58 Å and the one as high as 3.03 Å are obtained.

3.1.1.1.3. The Au_{249} Cluster

The different gold clusters come in different sizes and one way to increase the size is to increase or change the number of atoms in the system but still keeping the size at the nanometer level. It has been said in one of the previous sections (Introduction) that the size of material has some impact on its melting. In general, under ideal conditions, the melting temperature of a substance is supposed to increase with size. It implies that the melting in the bulk materials should be higher than the melting temperatures at the nano level. We will show the total energy curve, the radial distribution functions (rdfs), and the density profiles at different temperature in our underlying discussions. The total energy as a function of temperature is plotted in Figure 3.8.

A linear increase of the total energy with temperature for the cluster with 249 atoms is evident in Figure 3.8. A notable change in the slope of the energy occurs at 1000 K. The graph becomes linear again above 1050 K. The radial distribution functions are then plotted in Figure 3.9 to check the structural evolution into melting and to further ascertain the predictions of the total energy curve. It can be observed from the comparison of clusters with a few atoms (e.g. Au_{55}) and a larger one (Au_{249}) that the latter reflect a clear jump in the energy, which then makes prediction of the melting temperature using the total energy curve more reliable.

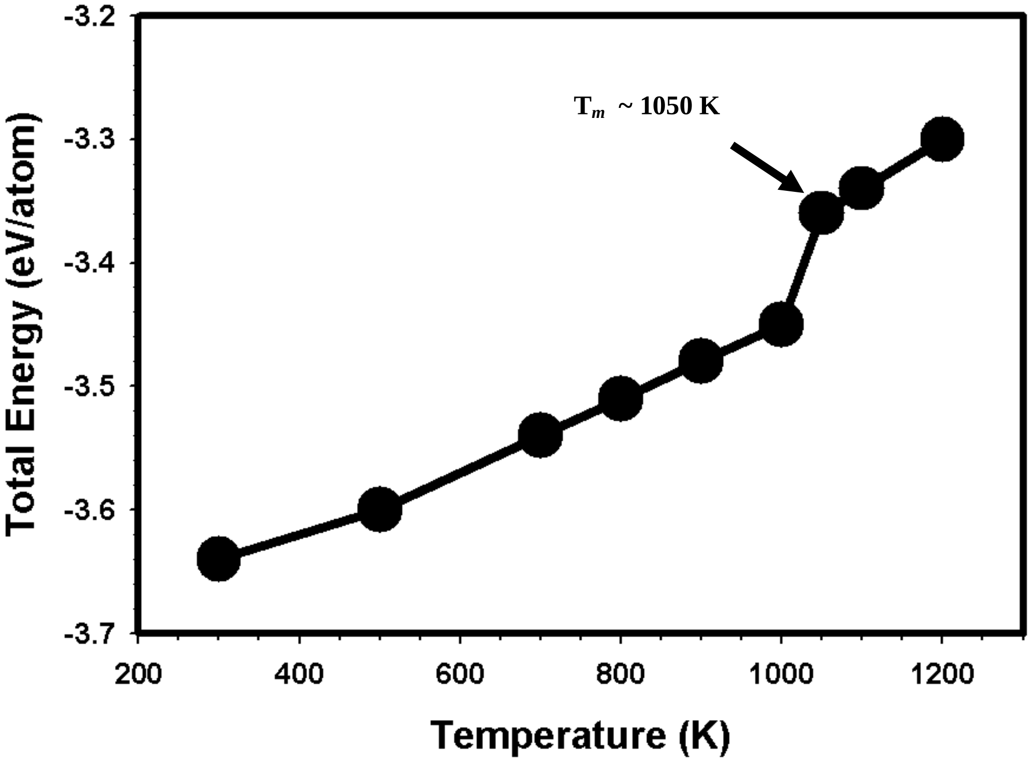

Figure 3.8. The change in the total energy with temperature for the Au_{249} cluster is shown.

In Figure 3.9 the structure possesses more peaks which are well ordered at 300 K signifying more interactions between the atoms in the system. The structure quickly loses the long range interactions at 800 K (the cluster becomes amorphous) and melting is attained at 1050 K. The melting process continues to show at 1200 K where a molten state is being approached. g(r) is zero for short distances less than the atomic diameter (from 0.0 Å to 2.6 Å) due to the strong repulsive forces. The first and the maximum peak at 300 K occurs at $r \approx 2.88$ Å with g(r) having a value of 6.8. The highest peak reduces to $g(r) \approx 3.4$ in the molten phase with the same value of r. The implication of g(r) in the liquid phase is that the chances of two molecules having the separation of r ≈ 2.88 Å are more than three times. The radial distribution function passes through a minimum value around r ≈ 3.5 Å at 300 K which then shifts to r ≈ 3.6 Å at 800 K, and r ≈ 4.0 Å at 1050 K as the peaks broaden with the increase in temperature. This means that the chances of finding two atoms with these separations are less than for the ideal gas. At long distances, g(r) tends to the ideal gas value, indicating that there is no long-range order.

The significant decrease in the peak height very much justifies an idea that interactions between the atoms in the solids are stronger than those in the liquid due to the difference in the bond distances. The interatomic distances usually increase in the liquid because of the gain in the energy which accelerated the atomic vibrations and this weakens the van der Waals forces that act between the atoms.

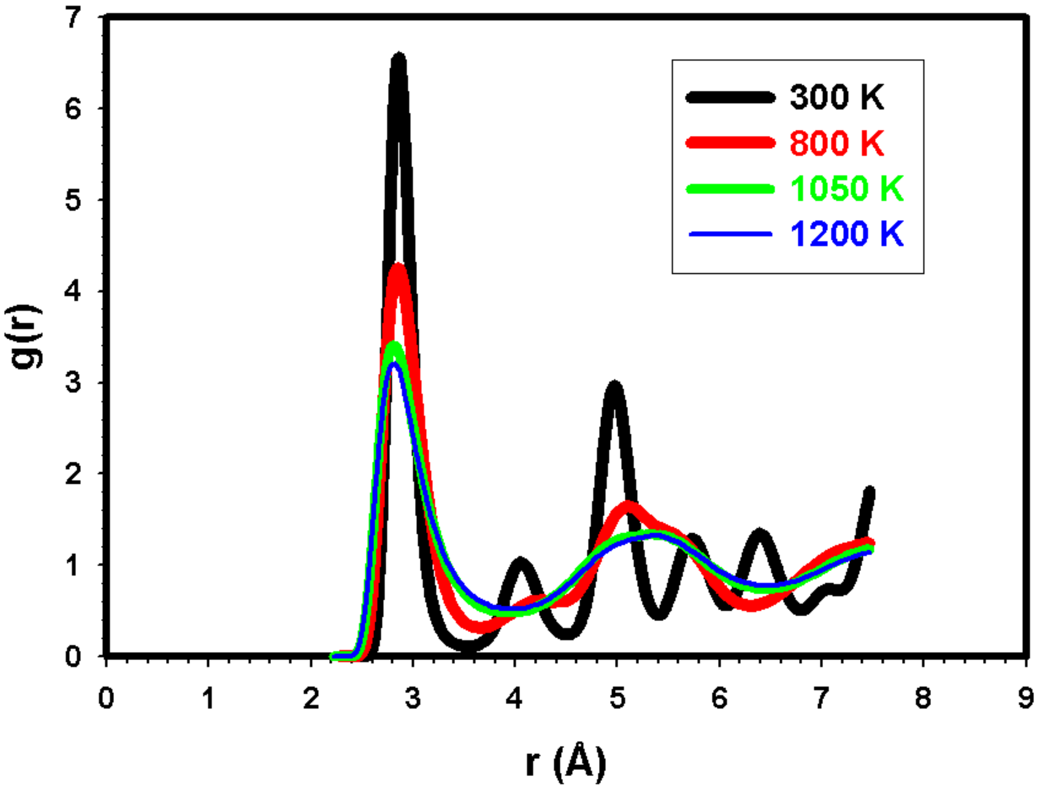

Figure 3.9. The radial distribution function of Au_{249} cluster at various temperatures where a transition into melting can be followed.

The density profiles are plotted in Figure 3.10 at four different temperatures. The simulations start with a solid crystal at 300 K and transform into a liquid structure at 1050 K, the process which is illustrated in the figure above. The system is more dense at 300 K where multiple peaks are evident. The system then looses much denseness at 800 K but still maintaining some regular pattern which seems to elapse at 1050 K. The peaks have even smaller heights at 1200 K and it is interesting to note that the density fluctuates along the same boundaries or r for various temperatures. The density profiles stretch from a minimum value of r ≈ -8.0 Å to a maximum value of r ≈ +8.0 Å.

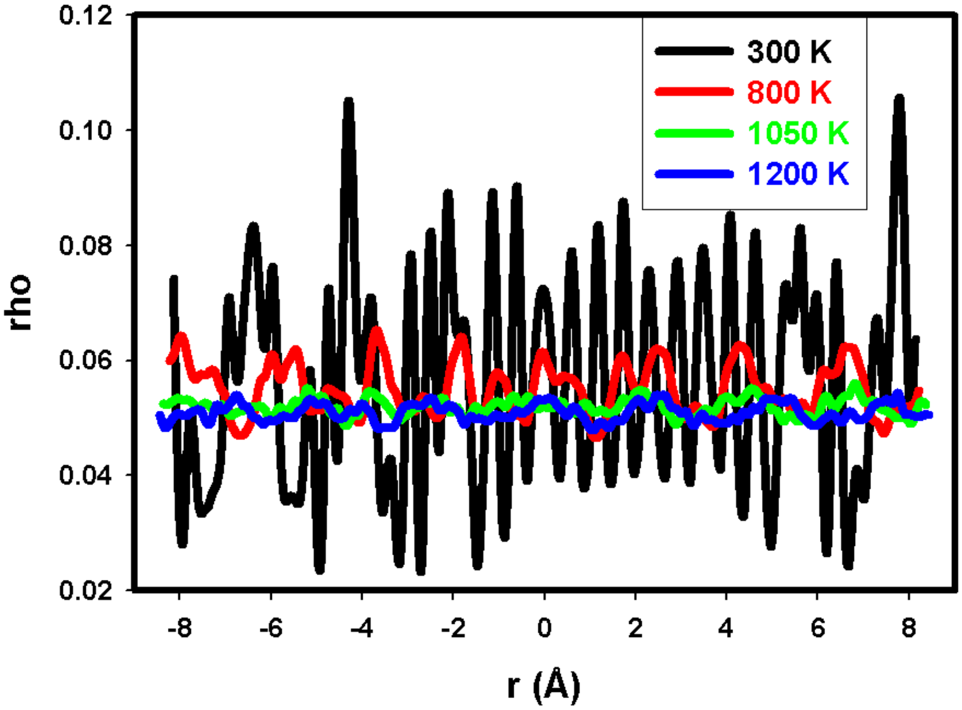

Figure 3.10. The density show the behaviour in the solid and the liquid state of the Au_{249} cluster and the cluster is melted at 1200 K.

We show the cluster at its initial configurations with a spherical morphology depicted by Figure 3.11. The interatomic distance is found to be 2.88 Å. The simulated structured at the melting temperature is also shown by Figure 3.11. The structure appears molten and some atoms have bigger separations between them. The bond distance of 2.88 Å at the initial configurations changes to, for example, 2.70 Å, 3.02

Å, 2.61 Å, at 1200 K. The change in the bond distances is irregular leading to the gaps being created as some bonds stretch.

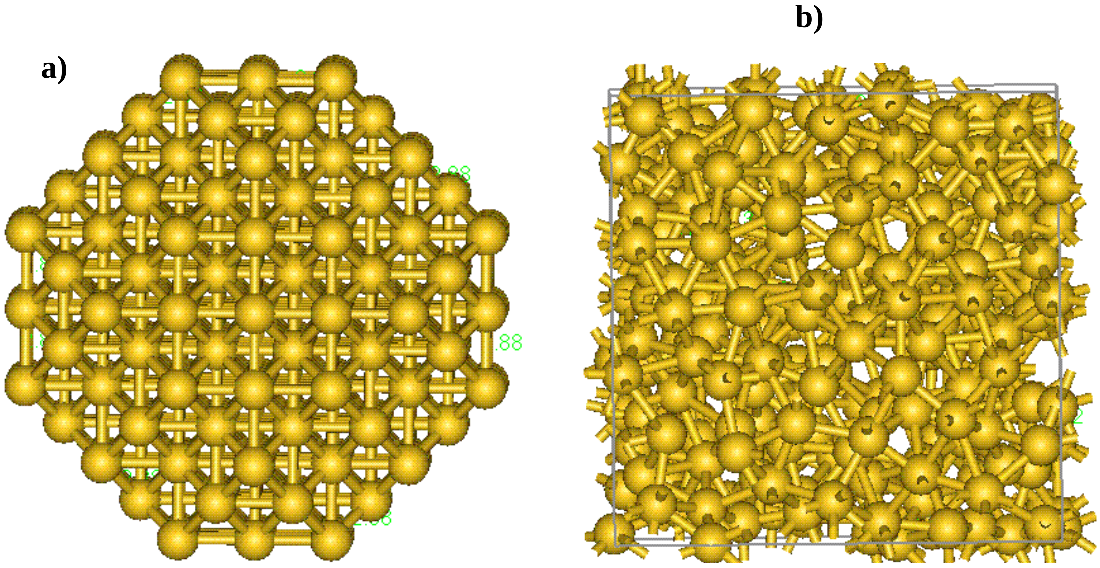

Figure 3.11. The well ordered structure of the cluster is shown by a) at the starting configurations with the bond distance of 2.88 Å. The configurations at 1200 K are shown by b).

3.1.1.1.4. The Au_{309} Cluster

The total energy curve related to the Au_{309} cluster can be divided into four regions as shown in Figure 3.12. In region 1 the cluster is solid and diffusion is either non-existent or very low. Region 2 (transition temperature) exhibits an upward curvature and the increase in the total energy which is associated with the loss of solid rigidity and onset of diffusion at the cluster surface. Region 3 is the estimated melting point of the cluster and region 4 shows complete melting where the energy starts increasing linearly. The estimated T_m is 1000 K which lies below the bulk melting temperature of Au.

Contrary to the magic cluster with 55 atoms the total energy curve for this magic cluster shows a clear jump towards melting. The energy shows an upward increase between 950 K and 1000 K which then tends to level off afterwards. It is also interesting to note that the four sections in the energy curve are clearly distinguishable. We attribute this to the added number of atoms as we move from 55 atoms in the cluster to 309 atoms. The total energy shows the same increasing behaviour in the solid and liquid phases. It is apparent that the energy becomes less negative as the temperatures is increased, making the cluster less stable as atoms gain kinetic energy.

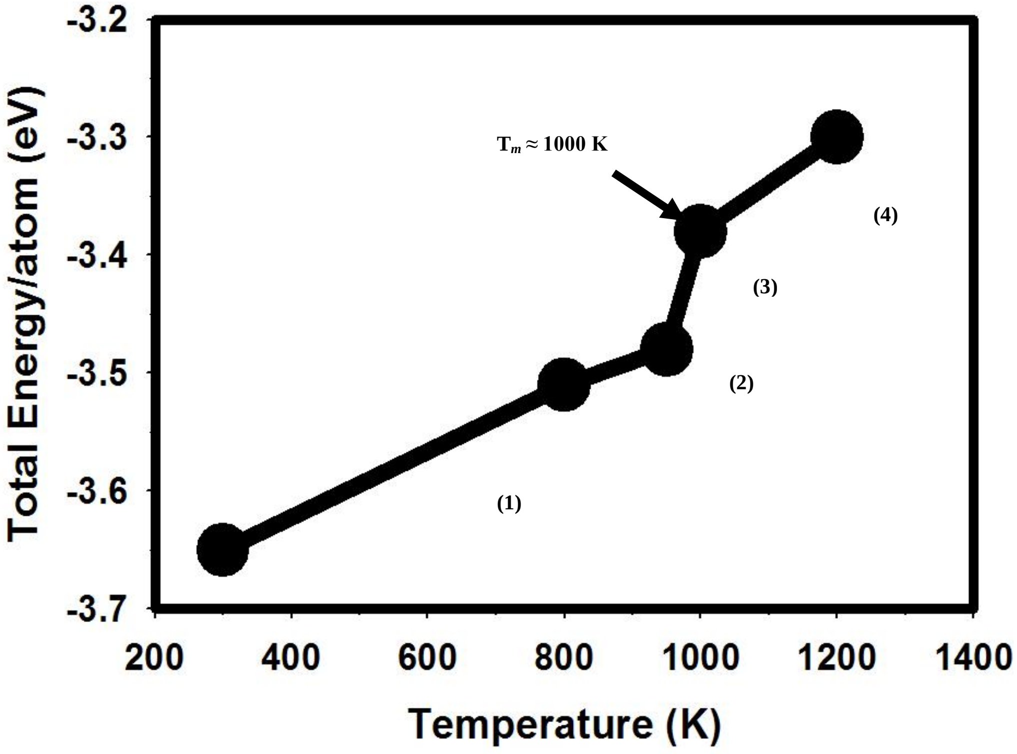

Figure 3.12 shows the total energy in the Au_{309} cluster. The bulk melting temperature of our model is 1320 K (experimental value is 1337 K).

The radial distribution functions for the Au_{309} cluster at various temperatures are depicted in Figure 3.13. There is an early onset of instability in the cluster at 300 K indicated by the peaks which do not follow any particular trend as observed in the case of the Au_{55} and Au_{249} clusters. However, we are able to see the transition the cluster undergoes as the temperature is enhanced. The plot at 950 K shows a very unstable structure with the immediate appearance of the shoulder and the splitting. A shoulder shows between two peaks characterizing a crystal while splitting is a result of the number of peaks decreasing and this behaviour usually emerges at the transition temperature. The shoulder and the splitting vanish immediately on melting. Fewer and ordered peaks are obtained at 1000 K. The structure of the Au_{309} cluster starts at a distance r ≈ 2.65 Å. The first and the maximum peak occurs at r ≈ 2.88 Å and the corresponding g(r) ≈ 6.2. Broadening and reduction of the peak heights with increasing temperature is observed.

The density profiles for the Au_{309} cluster at different temperatures are shown in Figure 3.14. The density profiles plotted at different temperatures show many peaks following a specific trend at 300 K which is further visible at 800 K. The peaks then show a sudden decrease in their number and denseness at 950 K. As expected the density profiles show a different change in the pattern of the peaks at 1000 K, then 1200 K. Hence the density profiles show less dense structures at melting by a decrease in the number of peaks and a sudden change in the peak pattern.

There is a good agreement between the total energy curve, the radial distribution functions as well as the density profiles. As estimated by the energy plot and the rdfs, the density profiles confirm the melting temperature for the Au_{309} cluster to be ~ 1000 K. The density profiles show that the more atoms we have in a system the more peaks we can generate as seen in the case of the bigger cluster with 309 atoms. The density profiles extend over the same area from low to high temperatures and r ranges from -9.0 Å to 9.0 Å.

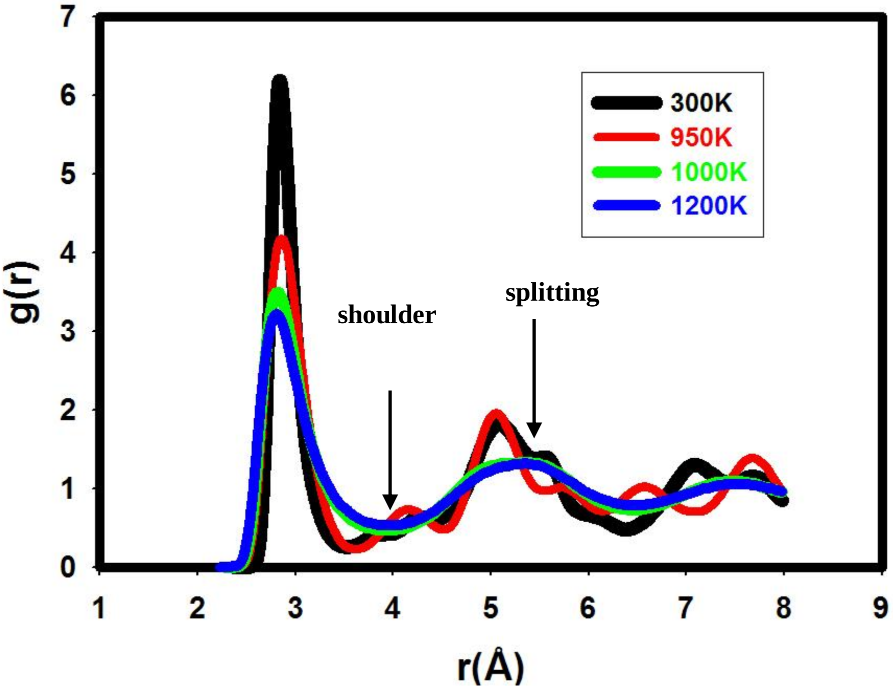

Figure 3.13. The rdfs in the Au_{309} cluster at different temperatures. The cluster show unstable peaks at 300 K.

The transition temperature occurs very close to the melting and that is clearly shown by the graph at 950 K. The peaks indicate certain features associated with the crystal (300 K) and some of the characteristics of melting are also present. The decrease in the denseness of the system is also depicted by the structure plotted at a higher temperature which will be shown in Figure 3.15.

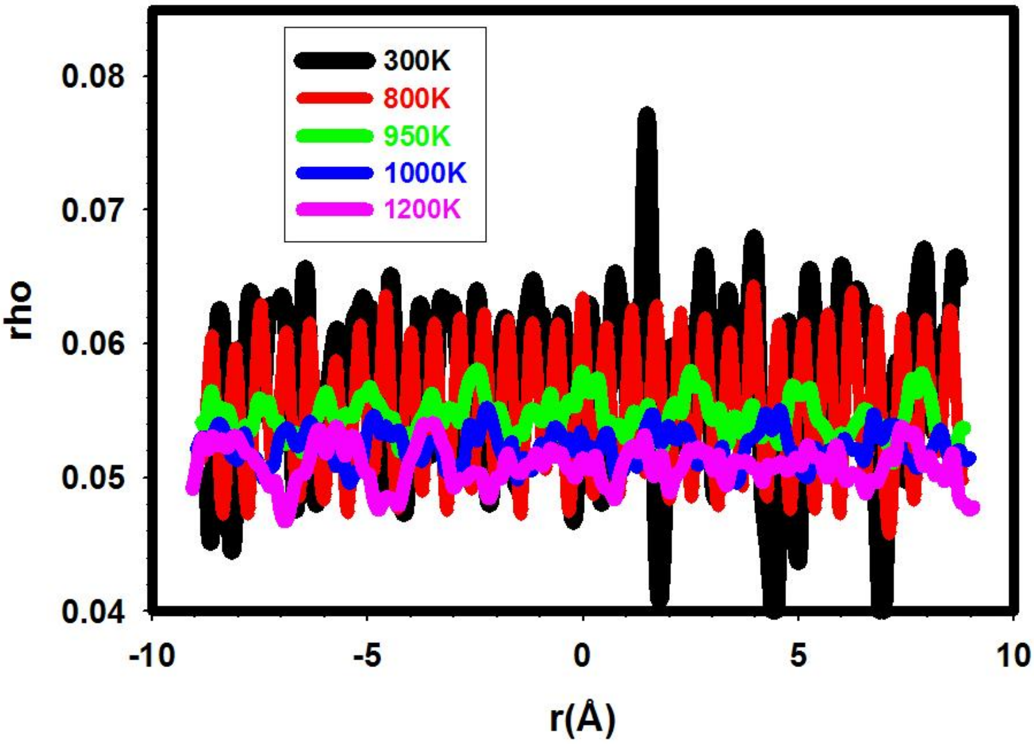

Figure 3.14. Density profiles in the NPT Berendsen conditions for the Au_{309} cluster are represented at different temperatures.

We now look at the structures of the gold cluster with 309 atoms before and after simulations. The structures are shown by Figure 3.15. A well ordered cluster with atoms regularly arranged into a spherical or hexagonal shape is shown in Figure 3.15(a). The bond distance at the initial configurations is 2.88 Å, which is the same as in the bulk gold. The Au_{309} cluster deforms into a disordered tetragonal (four-cornered structure) shape at 1000 K (Figure 3.15b). The structure become loosely compact at 1000 K and voids can be noted where one is able see through the structure. The voids are generally associated with the increasing bond distances although some show a decrease. We also observe the change from a hexagonal to a tetragonal shape.

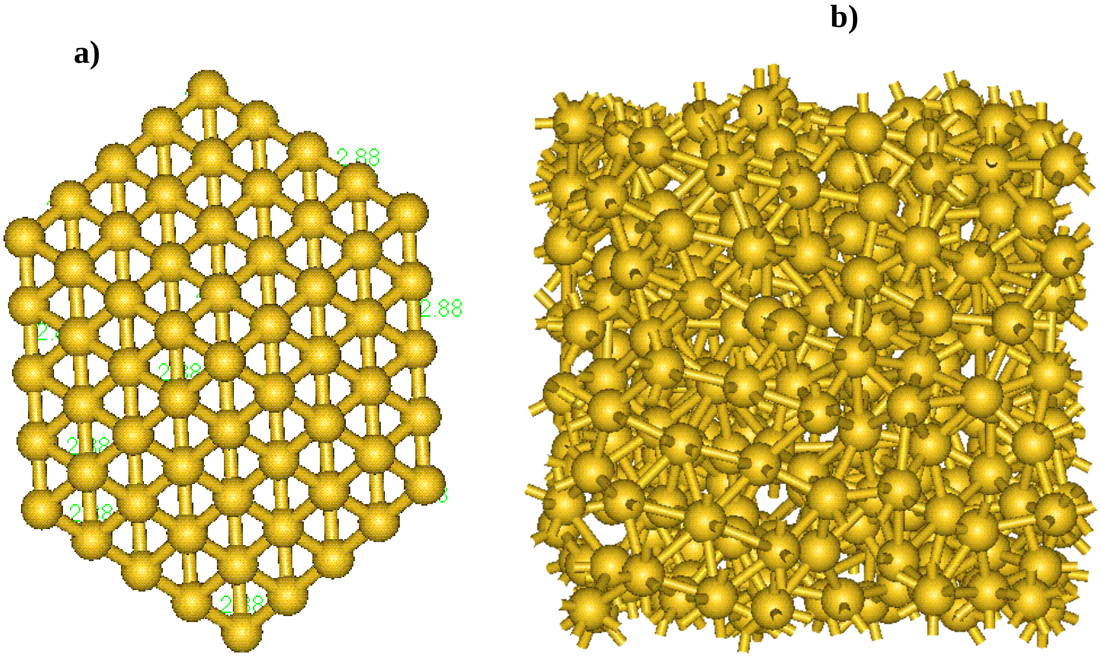

Figure 3.15. A well ordered structure before calculations is shown by a) while disoriented structure is a melted one at 1000 K shown by b).

3.1.1.1.5. The Au$_{887}$ Cluster

We show some results from the total energy, the radial distribution functions and the density profiles. We show the energy curve first. The number of atoms in the cluster or the size of the material does not quantify a structure to be of nanometre level. If a material, however big it may be, behaves like a nanocluster in all respects that material will automatically be called a nanocluster. We increase the number of atoms in our nanoclusters and compare the change in the behaviour relative to the bulk material. The fact that the melting temperature increases with the increasing size should mean that this cluster will show melting above 1000 K because the previous cluster (Au$_{309}$) has shown melting at 1000 K.

The radial distribution functions, on the other hand, are related to more atoms and hence the interactions between the atoms will be more characterised by the increased number of peaks. The density profiles also show good increased number of peaks which will change by decreasing when the liquid structure is attained. It is satisfying that the transition from solid to liquid is clearly indicated by the rdfs and the density profiles.

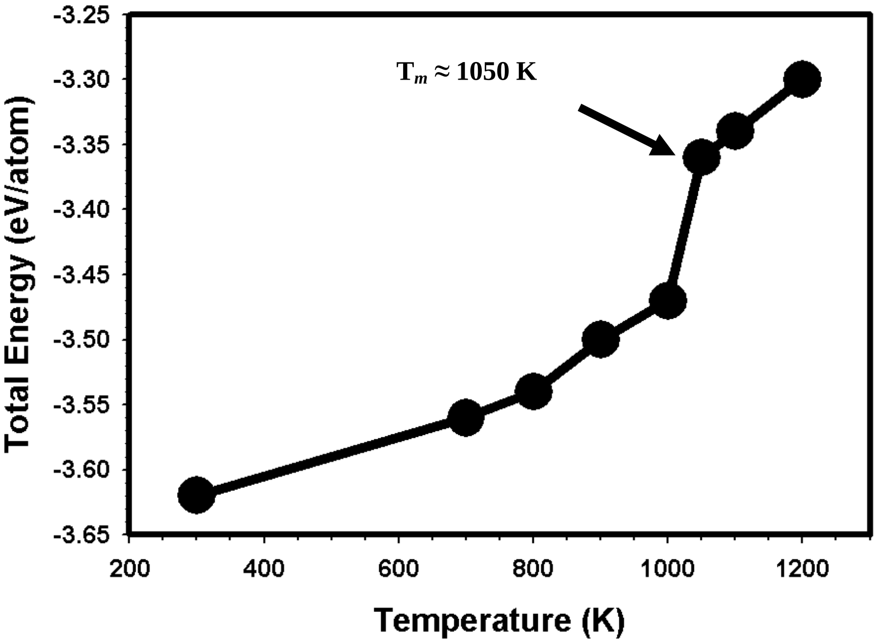

Figure 3.16 shows the change in the total energy of the cluster with 887 atoms at changing temperatures.

The total energy plotted, in Figure 3.16 for the cluster with 887 atoms, shows an increase in the solid right into the liquid phase with a sudden increase occurring in the region where melting is approached. The transition temperature occurs in well defined crystal materials as some known materials such as glass do not show this behaviour. The Au_{887} cluster, which is a clearly defined crystal at lower temperatures, shows a clear jump in the energy between 1000 K and 1050 K. The energy shows a linear behaviour in both the crystal and the molten phases of the nanoclusters. This observation highlights the fact that atoms in a particular phase have an average energy.

The radial distribution functions are shown in Figure 3.17 where a crystal structure is depicted at 300 K and melting occurs at 1050 K. The plot at 1200 K shows a slight decrease in the peak height while keeping the same trend implying that melting in this cluster is a slow process. Melting will, in most instances, commence at the outer atoms or at those atoms near the surface.

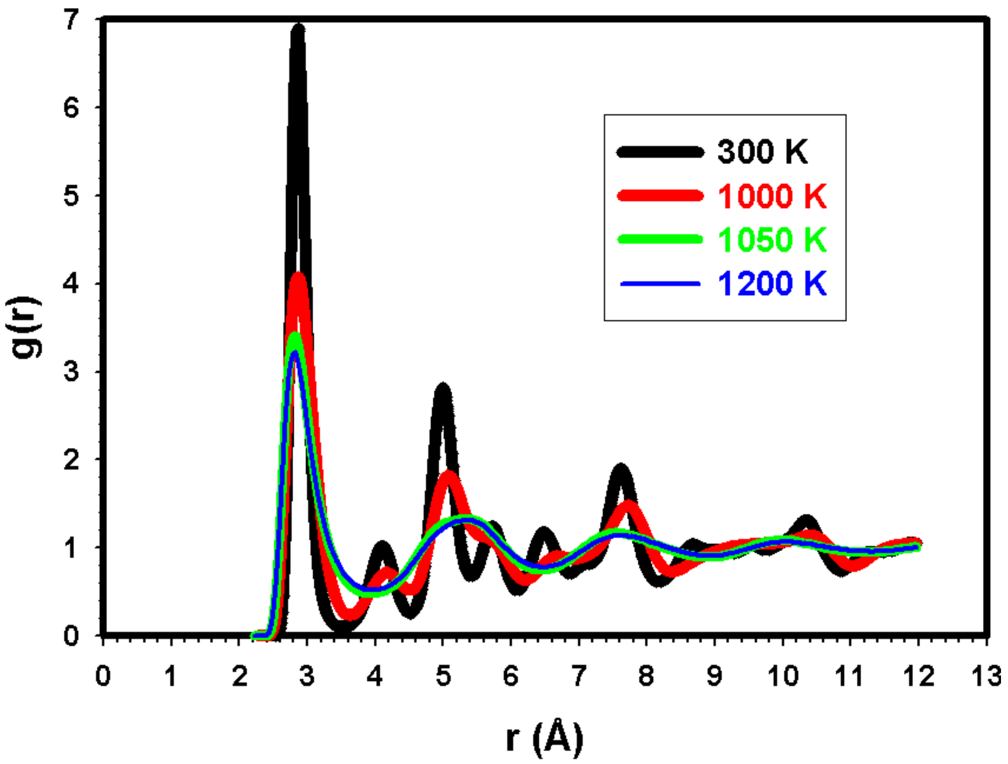

Figure 3.17. The rdfs for the Au_{887} cluster are shown. Different colours indicate different temperatures.

The density profiles for the Au_{887} cluster are shown by Figure 3.18. The system is much denser at 300 K through the multiple peaks which have arranged themselves in a particular pattern. Similarly to previously studied clusters, we are able to achieve a change in the pattern of the profiles when the temperature exceeds 1000 K. The order of the peaks at 1000 K remains the same as those at 300 K but a decrease in the heights is noted. The plot at 1050 K is further reduced and the pattern has faded. The density profile at 1200 K becomes flat denoting a much decrease in the denseness of the system. The density profiles, like the radial distribution functions show broadening of the peaks due to the increasing vibrations as temperature is raised. It is gratifying that the three methods discussed, concur well in the estimation of the melting temperatures of the various clusters. The estimate of the melting temperature of the Au_{887} cluster is 1050 K. The melting of the cluster initiates change in the shapes of the cluster, as observed in smaller clusters, from more spherical to tetragonal shapes (Figure 3.19).

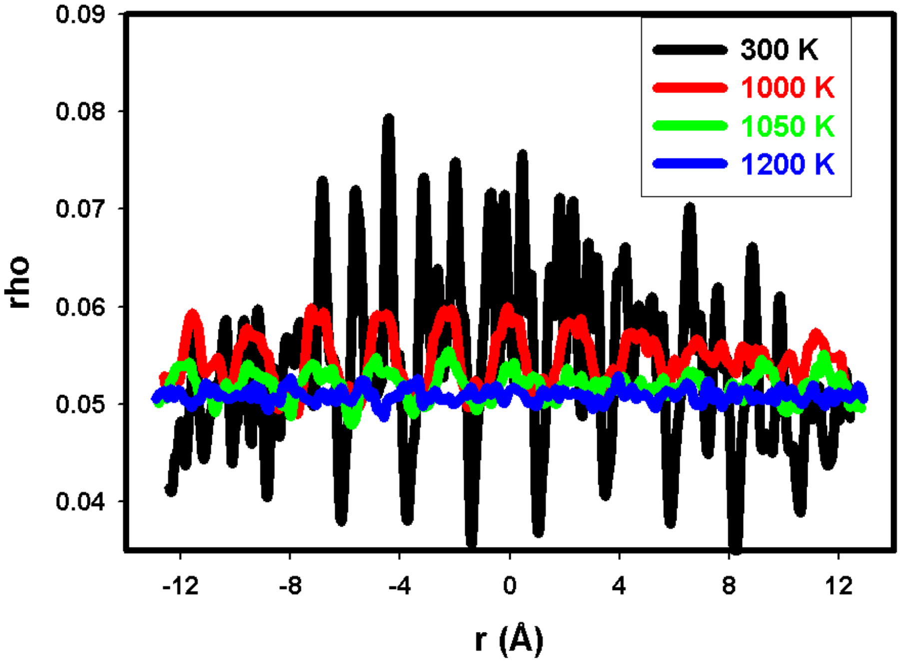

Figure 3.18 shows the density profiles for the Au_{887} cluster. The density profiles go between -12 Å and +12 Å. There are almost no peaks to talk of at 1200 K.

The bond distance in the spherical clusters at lower temperatures is 2.88 Å, as has been from the cluster with 249 atoms. The reduced peaks in the rdfs and the density profiles justify larger separation of atoms at higher temperatures.

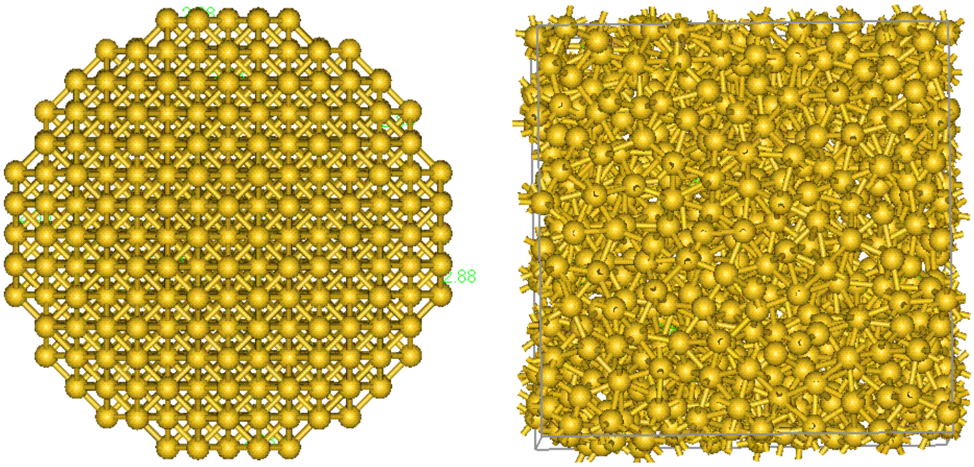

Figure 3.19 shows a spherical Au_{887} cluster before melting on the left and a melted structure of the cluster at 1200 K on the right.

3.1.1.1.6. The Au_{1464} Cluster

We now study a bigger cluster with more than a thousand atoms. The total energy curve is shown in Figure 3.20. The four regions of interest explained earlier, are clearly shown as the cluster slowly changes from a solid to a liquid phase. The variation of energy with temperature is not convincingly linear in region 1 which suggests that the atoms are showing significant vibrations. There is a marked change or jump in the energy between 1000 K and 1100 K.

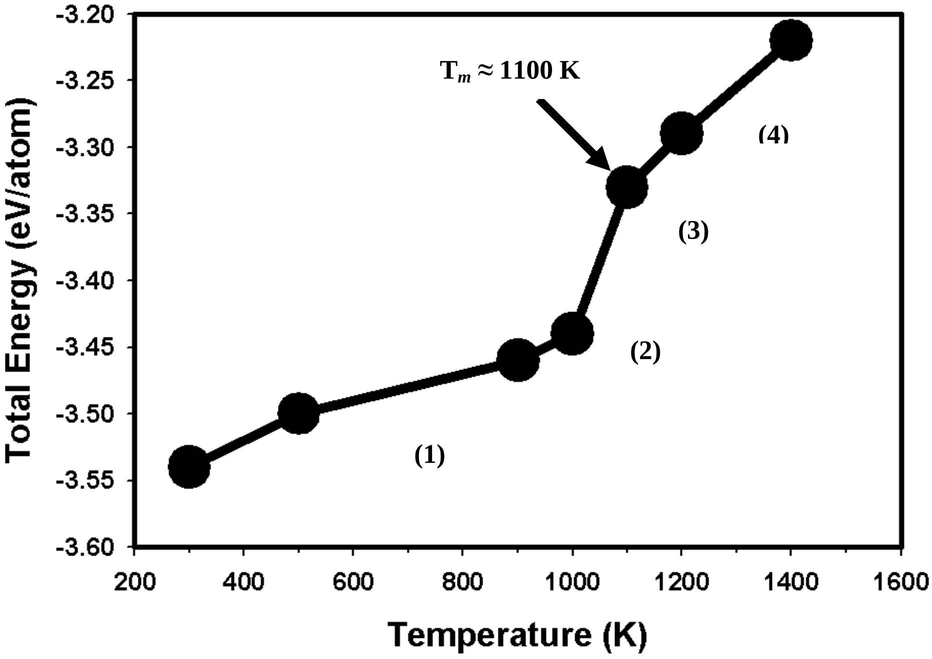

Figure 3.20. The variation of the total energy with temperature in the cluster with 1464 atoms in the NPT Berendsen ensemble is illustrated.

The total energy commences from more negative values signifying a stable structure and increase steadily with temperature. The cluster gives a total energy of -3.54 eV/atom at 300 K and it is less negative compared to the bulk total energy of -3.78 eV/atom at the same temperature.

The radial distribution functions are shown in Figure 3.21 from 300 K to 1400 K. The structure at 300 K represents a clear crystal behaviour with distinct peaks, starting with a large peak followed by a smaller ones. The first and the maximum peak occurs at g(r) ≈ 12.5 and r ≈ 2.9 Å while the plot runs up to 12.0 Å. We notice a reduction in the number of peaks at 1000 K, but no melting is depicted at this temperature. The cluster has melted at 1100 K. The melted structure at 1100 K shows three broad peaks with fewer long range interactions. Melting in the cluster continues to show at 1400 K where we expect higher atom diffusion since the cluster is molten. There is a consistent pattern in the reduction of the rdf peak heights as temperature is raised. The melting temperature estimated from the total energy curve is in line with what is shown by the rdfs.

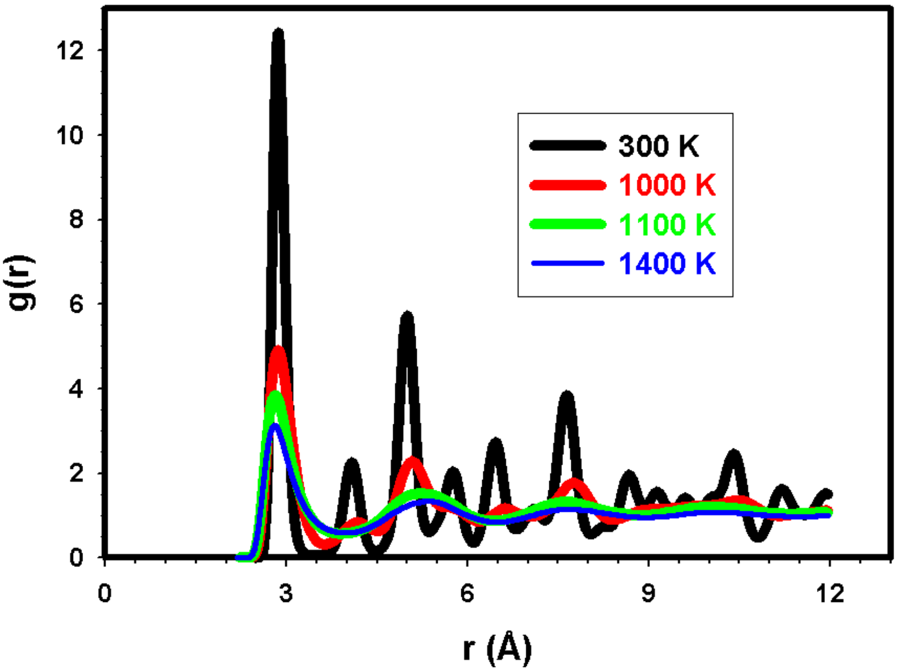

Figure 3.21 shows the radial distribution functions of the Au_{1464} cluster. Different temperatures are indicated by the corresponding colours.

The density profiles of the Au_{1464} cluster are reflected in Figure 3.22, and are a way of further validating the results from the total energy curve and the radial distribution functions. The density profiles show a regular pattern of many peaks that extend from r ≈ -15.0 Å to r ≈ +15.0 Å. The pattern of the peaks changes dramatically at 1000 K with a small upward curvature. The behaviour of the density profiles change slightly at 1100 K towards achieving a flat shape. The plot becomes flat at 1400 K which is higher than the bulk melting temperature. The energy curve, the radial distribution functions and the density profiles show the transition temperature of the Au_{1427} cluster to be at 1000 K and melting is attained at 1100 K. The transition or intermediate temperature is defined as the temperature which lies between the solid and the liquid phase of a material and it is achieved when there is a transformation from a solid to a liquid phase.

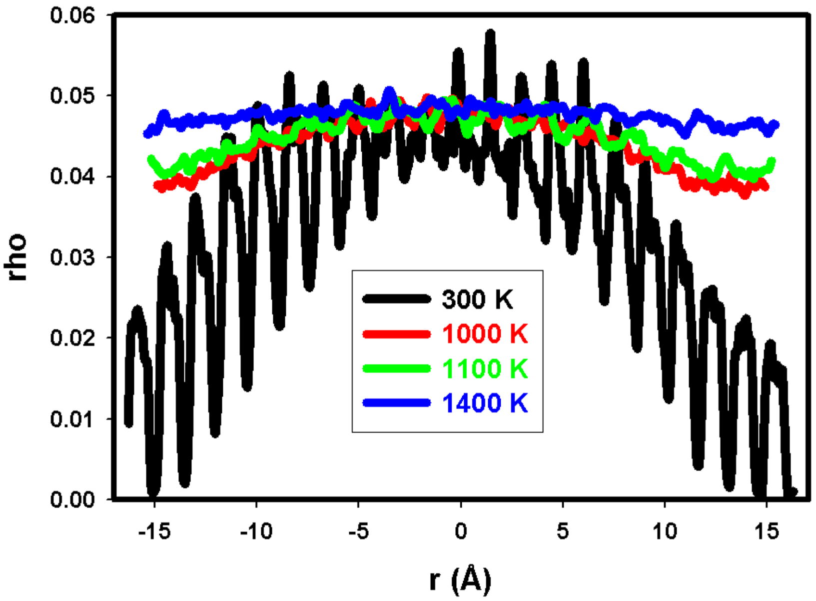

Figure 3.22. The density profiles show a total different behaviour in different phases, solid and liquid phases.

We would also like to explore the change in the structure of the cluster as the temperature is enhanced. Figure 3.23 (a and b) shows the starting structure of the Au_{1464} cluster in different forms, the ball and stick and cpk respectively. The bond distance in the cluster is uniform and equals 2.88 Å at the initial configurations. The structure of the cluster deforms into a tetragonal shape which is also a face-centred cube at the temperature before melting, 1000 K. Figure 3.23c depicts the ball and stick model representing the structure just before melting at 1000 K. Although the cluster has lost its spherical shape at 1000 K, the compactness is still visible. The structure after melting (at 1200 K) is illustrated by Figure 3.23d where voids are seen with the reductions in the interactions between the atoms. It remains to be seen if the predicted melting temperature is directly proportional to the size of the cluster. Thus far, with the exception of the Au_{55} cluster, melting of the nanoclusters is below the bulk melting.

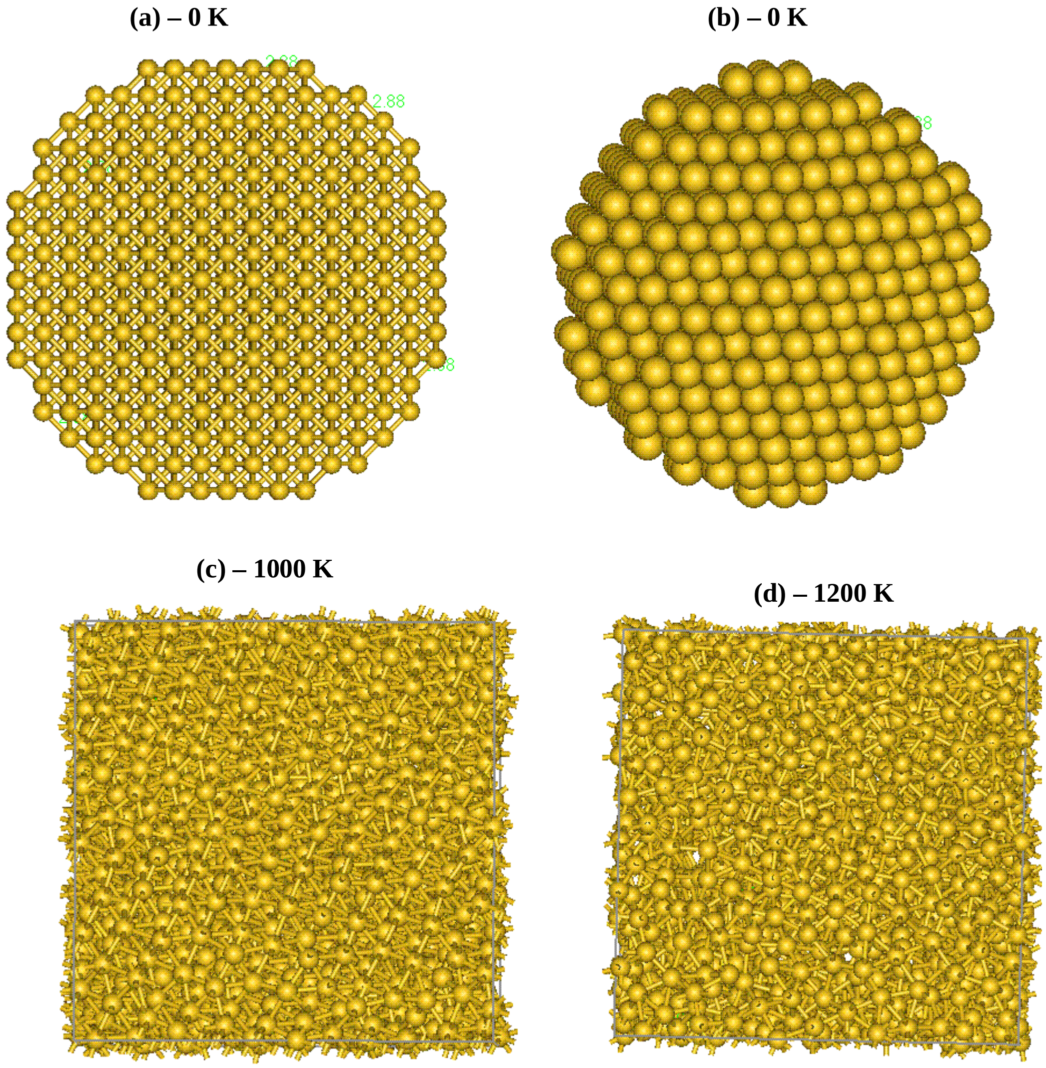
(a) – 0 K

(b) – 0 K

(c) – 1000 K

(d) – 1200 K

Figure 3.23. The structure of the Au_{1464} is shown at different stages of the MD calculations in terms of temperature.

3.1.1.1.7. The Au_{2214} Cluster

Discussions on the Au_{2214} cluster are similar to the preceding ones. We look at the total energy as we vary the temperature in the NPT Berendsen ensemble at a constant pressure of 0.0 kbar. The radial distribution functions tell us about the change in the structure as the temperature is raised and the density profiles show how the denseness of the system varies with temperature.

The total energy depicted in Figure 3.24 shows a jump between 1000 K and 1200 K after which a linear increase is noticed.

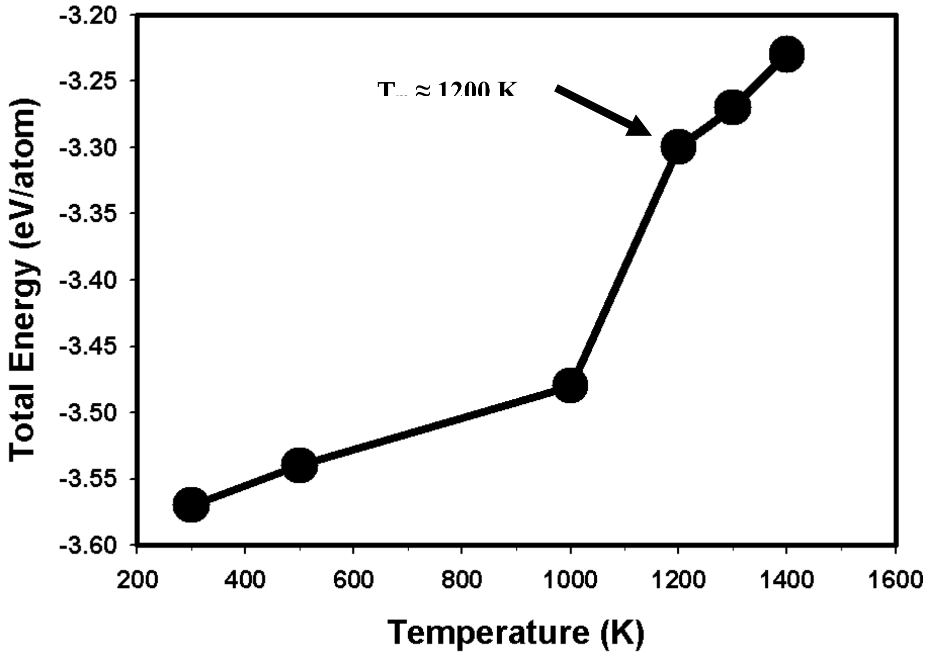

Figure 3.24. The variation of the total energy with temperature in the Au_{2214} cluster is illustrated.

The radial distribution functions for the cluster are shown in Figure 3.25. The structure starts from a well defined crystal and very close to the melting temperature of the cluster a molten system is shown by the red colour at 1100 K. This is the intermediate temperature where the solid and liquid phases co-exist. At this temperature, 1100 K, the number of peaks and the peak heights in the system decrease drastically and the behaviour is very close to that of the liquid structure but the peaks are not well defined. The cluster reaches melting at 1200 K with broad peaks and that continues to show at 1400 K. The structure in the cluster starts at ≈ 2.5 Å while the first and maximum peak occurs at g(r) ≈ 10.2 and the corresponding distance r ≈ 3.0 Å and then terminates at 12.0 Å.

The density profiles validate the results of the total energy curve and the radial distribution functions, and further shed insights on the change on the denseness with temperature. The density profiles plotted in Figure 3.26 depict a decrease in the denseness at higher temperatures and follow the same trend as those of the Au_{1464} cluster. The 1100 K plot shows a similar behaviour to the one at 1200 K. The plot at 1400 K depicts a small change in comparison to the plot at 1200 K but the peaks deep downwards. There is quick change between phases in the Au_{2214} cluster.

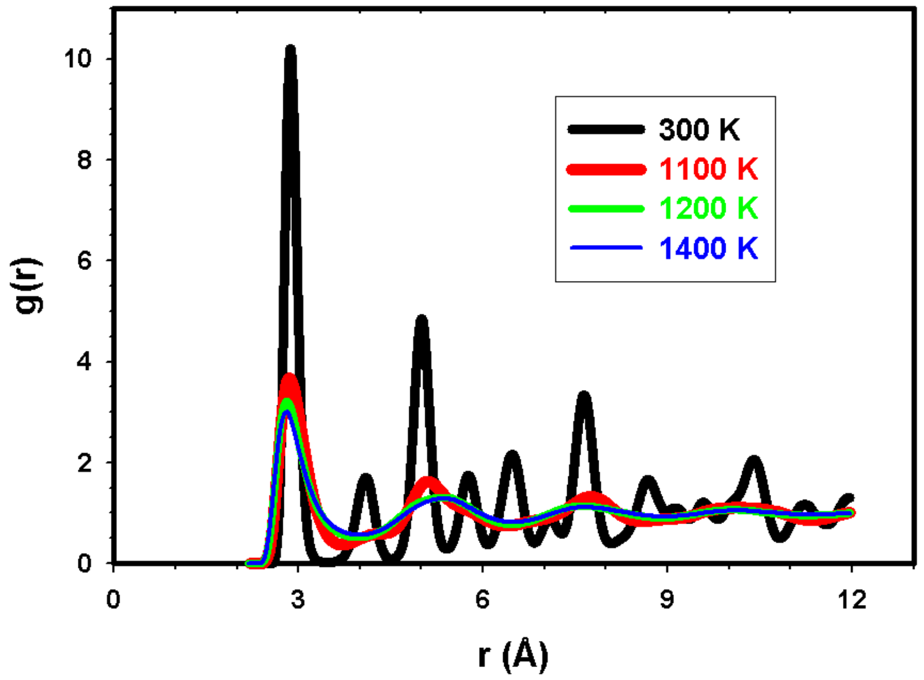

Figure 3.25. The rdfs for the Au_{2214} are shown from 300 K to 1400 K. The plot shows more regular peaks at 300 K just like in the bulk.

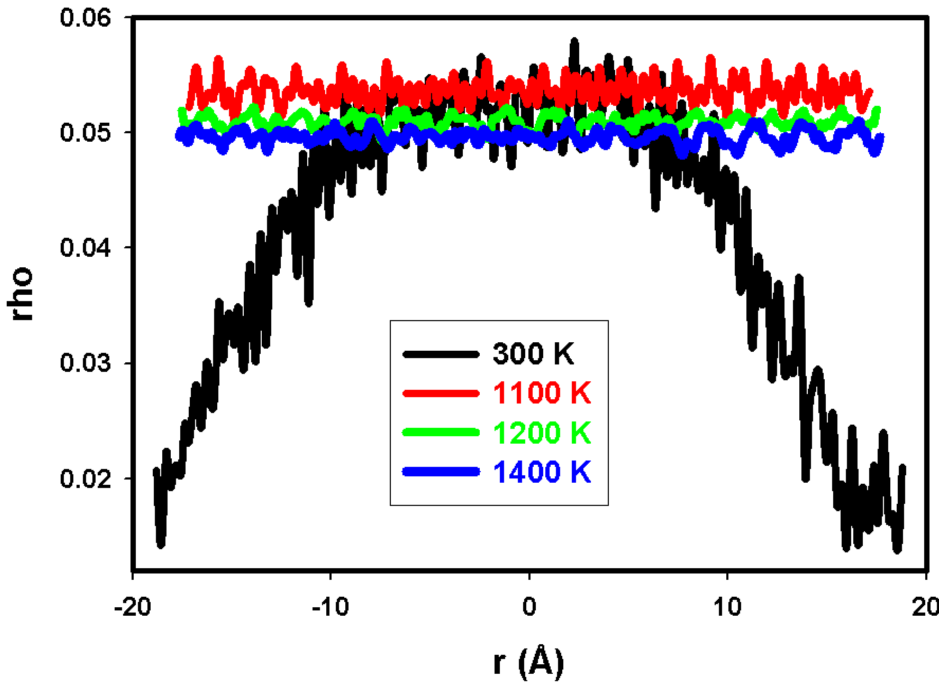

Figure 3.26. The change in the behaviour of the density profiles for the cluster with 2214 atoms is illustrated.

3.1.1.2. The Platinum Magic Clusters

We have also carried out some molecular dynamics work on platinum clusters and found the Pt_{55} cluster to behave similarly to the Au_{55} cluster. Platinum shows the similar behaviour to gold from bulk to the surface properties [Sutton and Chen 1990, Todd and Lyndell-Bell 1993], and together with gold are the only metals whose three low index surfaces {(110), (100), (111)} reconstruct [Ravelo and El-Batanouny 1989, Hakkinen *et al*. 1991, Ravelo and El-Batanouny 1993]. Since the metals have the same crystal structures, they are represented by the same values of m and n, the results from one metal can be directly converted into results of the other by simply rescaling the units of energy and length.

The Pt_{55} cluster shows melting at higher temperatures as compared to the Pt_{309} cluster. The energy plots for platinum clusters are shown in Figure 3.27. The total energy per atom at 300 K is -4.81 eV/atom and -5.71 eV/atom for the Pt_{55} and Pt_{309} respectively. The total energies for the clusters at 300 K are less negative when compared to the bulk platinum cohesive energy of -5.86 eV/atom [Sutton and Chen 1990].

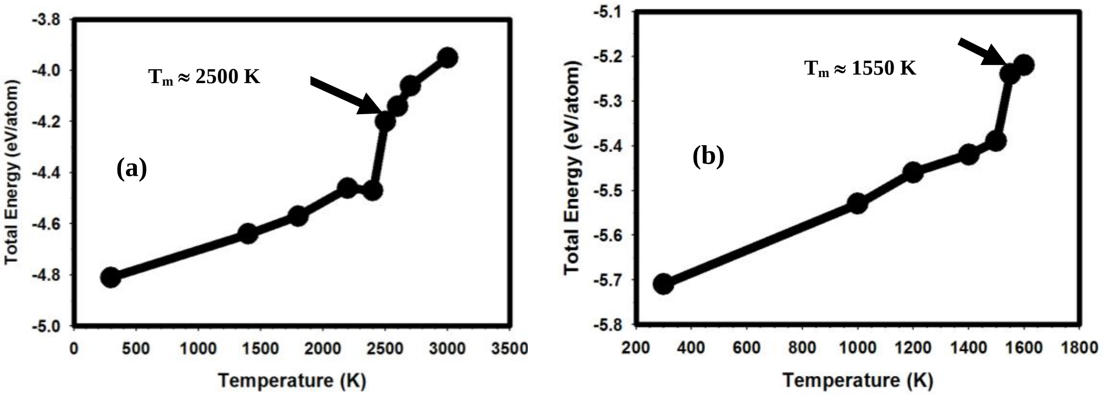

Figure 3.27. The energy is plotted against temperature for the two clusters of platinum where (a) shows the Pt_{55} cluster and (b) the Pt_{309} cluster. The Pt_{309} cluster shows a good jump as compared to Pt_{55} cluster.

The energy curve for the Pt_{55} cluster plotted in Figure 3.27(a) shows some ambiguity next or around the transition and melting temperatures. The Pt_{309} cluster shows a good transition into melting, as reflected in Figure 3.27(b). The rdfs for the platinum clusters are plotted in Figure 3.28. We have estimated melting temperatures for the two clusters using the total energy plotted as a function of temperature in conjunction with the rdfs and the density profiles. The estimated melting temperatures for the Pt_{55} and Pt_{309} clusters were then respectively found to be 2500 K and 1550 K. The melting temperature of bulk platinum is 2045.15 K and clearly the Pt_{55} cluster shows melting at a temperature higher than the bulk while the Pt_{309} cluster melts below the bulk.

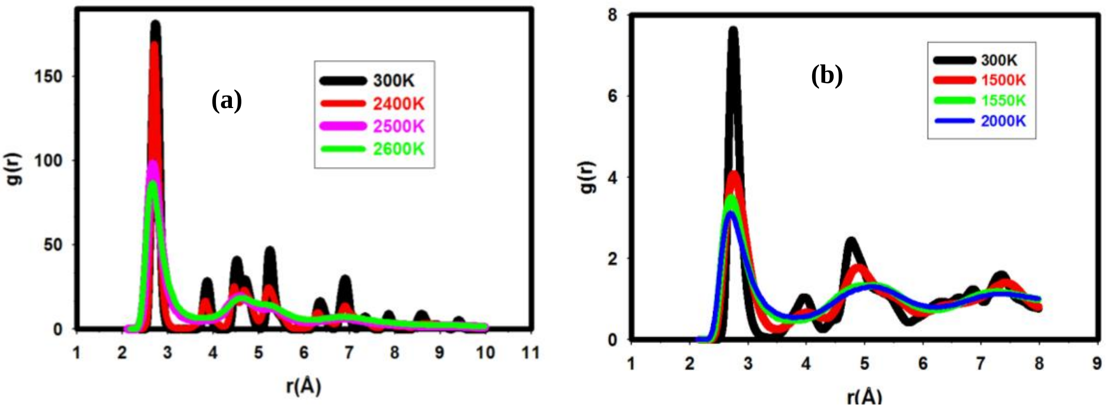

Figure 3.28 (a and b) show the rdfs in the Pt_{55} and Pt_{309} clusters respectively. The Pt_{55} cluster shows more peaks at 300 K as compared to the Pt_{309} cluster. The Pt_{309} cluster looks less stable at 300 K.

The density profiles for the two platinum clusters are shown in Figure 3.29. The behaviour is the same as in gold clusters. The Pt_{55} cluster is shown in Figure 3.29(b) where a change in the pattern of the peaks changes and levels off at 2500 K. The drastic change in the density profiles in the Pt_{309} cluster is observed at 1550 K.

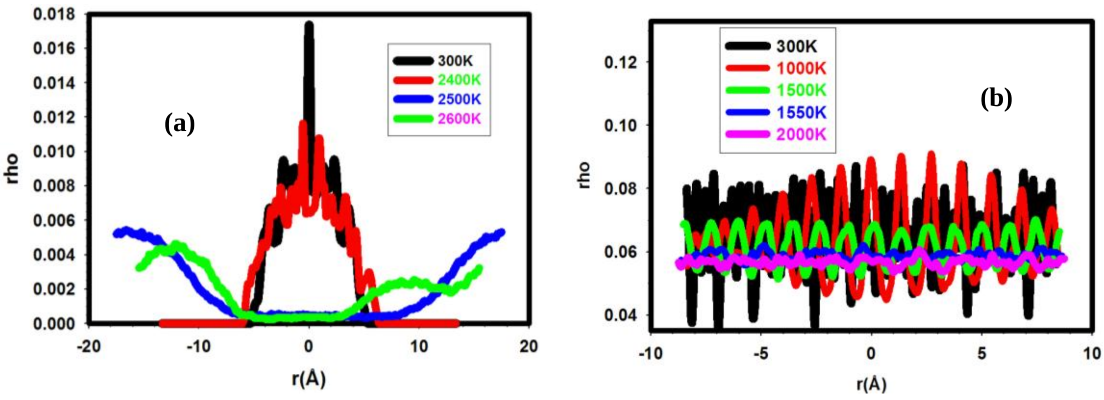

Figure 3.29. Density profiles for Pt_{55} and Pt_{309} clusters are shown by (a) and (b) respectively. Similar behaviour to the gold nanoclusters is observed.

3.1.1.3. The Cohesive Energy at 300 K

The material with the lowest energy at a specified temperature is usually the most stable under those conditions. The stability of the surfaces is determined by the value of their surface energies and the one with the lowest surface energy is always the most stable surface. We noted from our previous work on the bulk and surface properties of gold [Mahladisa 2004, Todd and Lyndell-Bell 1993] that the most stable surface of gold is the close-packed (111) surface which reconstruct into 23 x √3 layers. Furthermore, a material with the highest energy is usually the most reactive. It is well-known that gold, in its bulk form does not react with almost all materials including the highly reactive oxygen and sulphur. In fact gold is the most inert of all transition metals.

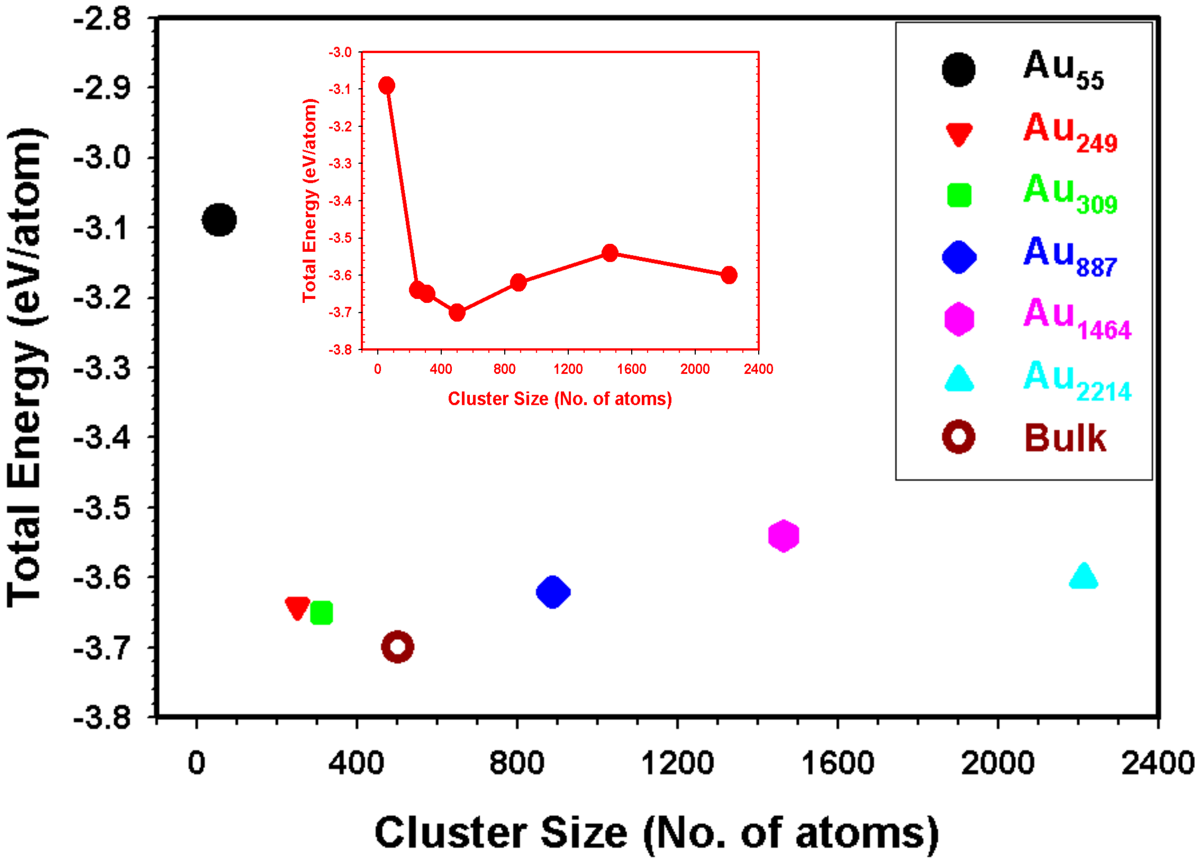

Figure 3.30. The cohesive energies of the nanoclusters at 300 K are shown with comparison made to the bulk gold at the same temperature. The cohesive energy illustrates the stable nature of bulk gold and the fact that the smallest cluster depicts lower stability as expected.

The cohesive energy of a metal discloses the strength of the metallic bond. The decreasing cohesive energy of a nanoparticle implies the decreasing strength of the corresponding metallic bond and so the metallic bond will be broken much easier which will then lead to the decreasing melting point of the nanoparticle.

Figure 3.30 shows the cohesive energy in the different clusters at 300 K and comparison is made with the bulk gold. The insert shows a line joining the points. The Au_{55} cluster depicts the highest cohesive energy while the clusters with the lowest energies are found to be the Au_{249} and Au_{309} clusters. In fact the two clusters showing the lowest cohesive energies are very close, in value being -3.64 eV/atom and -3.65 eV/atom for Au_{249} and Au_{309} respectively. The energy for the Au_{55} cluster is -3.09 eV/atom. The bulk material, which has 500 atoms, as expected, depicts the lowest energy equalling to -3.70 eV/atom. In the previous work it was shown that the many-body Sutton-Chen potential gives the bulk cohesive energy as -3.78 eV/atom at 0 K which agrees perfectly with the experimental value of -3.78 eV/atom [Miedema 1978]. The energy in the figure above does not follow any trend with the increasing size but rather only irregular pattern is noticeable. The bigger clusters (Au_{1464} and Au_{2214}) which exceed a thousand atoms in their size are actually the ones showing higher cohesive energies. We also have to highlight the fact that gold is very reactive at a nano level and we can notice in this case that the energy in the clusters increases quite significantly compared to the bulk. We find the energy of the Au_{55} cluster at 300 K (-3.09 eV/atom) to be higher than the energy of the bulk at 1773 K (-3.16 eV/atom).

We have plotted the total energy for different magic gold clusters with the size ranging from 13 to 55 atoms at different temperatures. Figure 3.31 shows that the energy in different systems increases with increasing temperature. An interesting phenomenon observed in the plot is that the energy becomes more negative with the increasing cluster size. The smallest cluster with 13 atoms has the highest energies at different temperatures while the biggest cluster with 55 atoms has more negative energies. The results below show that the cluster with the highest number of atoms is the most stable and more good is that the stability is kept that way at temperatures as high as 1000 K. The energy increases as the atoms feel some heat and therefore begin to vibrate with the frequent vibrations showing at higher temperatures as a result of the increase in the kinetic energy.

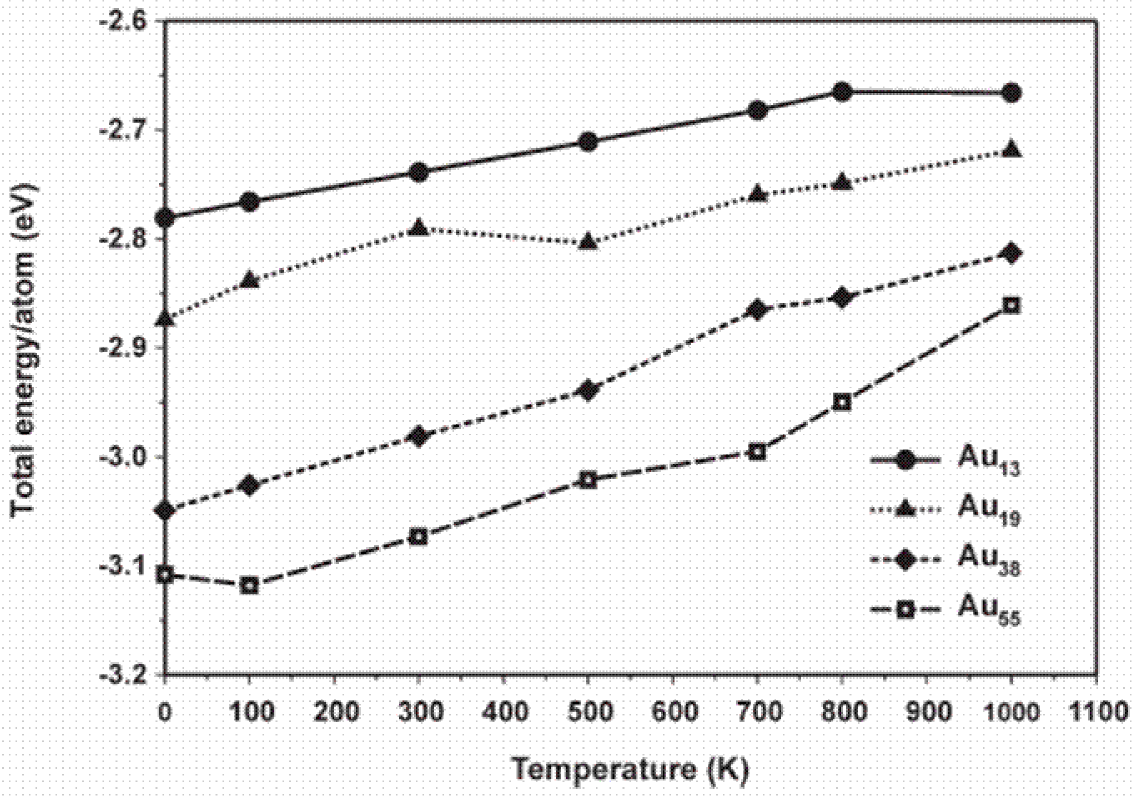

Figure 3.31. The total energy for different clusters is plotted at various temperatures. The size of the clusters ranges from 13 atoms to 55 atoms. The circles with a solid line represent the Au_{13} cluster, the triangles up with a dotted line show the Au_{19} cluster, the diamonds with dashed line represent the Au_{38} cluster while the squares with a white fill and long dashed line show the Au_{55} cluster.

3.1.1.4. The Behaviour of the Melting Temperature

The materials at a nano level are expected to show a significant drop in the melting temperature when compared to their respective bulk materials. In addition, we have found that surfaces of gold show melting temperatures that are well below the bulk melting. We have therefore plotted the melting temperatures for the different gold clusters against the size of the clusters in Figure 3.32. Melting in a material initiates at the surface and melting in nanoclusters is below the respective bulk melting because nanoclusters have clearly defined surfaces. The spherical shapes of these structures also an important role.

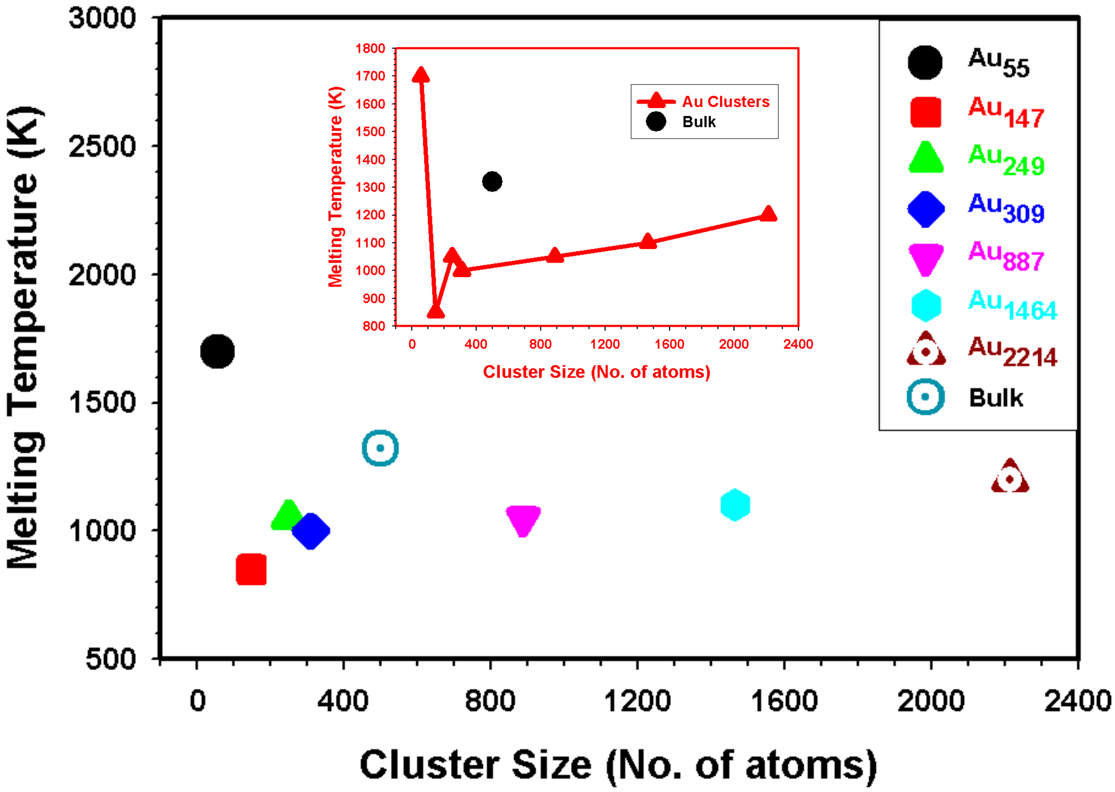

Figure 3.32 shows the behaviour of the melting temperature in the different Au clusters in the NPT Berendsen ensemble at 0.0 kbar. The melting temperature of the bulk is indicated by an open circle.

The Au_{55} cluster shows the highest melting temperature and it is well above the bulk material. The bulk melting temperature for the potential model we use in this work is 1320 K which is in good agreement with the experimental value of 1337 K. The cluster with the second smallest number of atoms has the lowest melting temperature of 850 K. It is quite intriguing to note that the biggest cluster considered in this work shows the highest melting temperature at 1200 K with exception of the Au_{55} cluster. Although the melting temperature fluctuates with cluster size it can be noticed that there is an increase from the cluster with 309 atoms up to the cluster with 2214 atoms as shown in Figure 3.33.

The reason behind the high melting temperature found in the Au_{55} cluster is assumed to be the reconstruction that the cluster might undergo. The fact that all low index surfaces of gold reconstruct provides a reasonable basis for cluster showing melting that is well above that of the bulk.

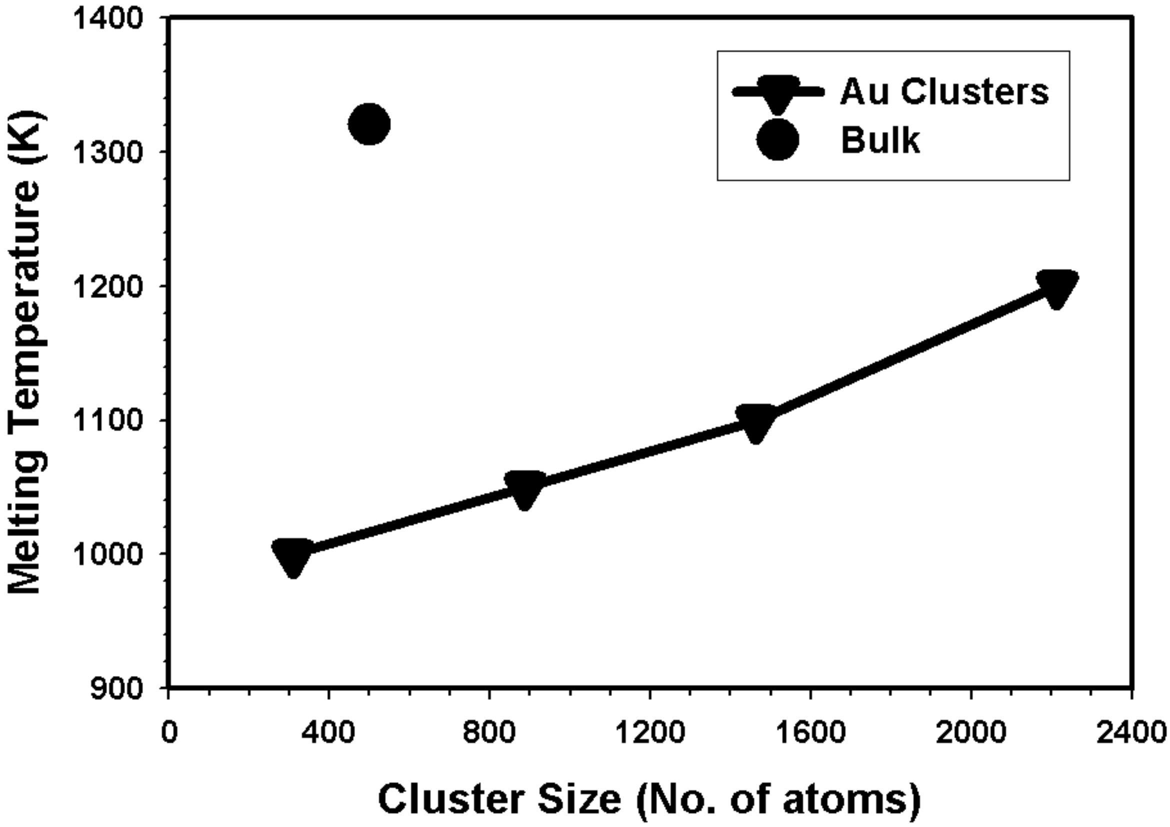

Figure 3.33. The melting temperature is shown from the cluster with 309 atoms to the Au$_{2214}$ cluster with the bulk shown by a circle lying well above all.

In addition, the temperature simulations on the Au(111) surface have shown that the reconstructed surface melts at 100 K or 150 K above the bulk melting temperature as opposed to the unreconstructed one which melts below the bulk by 1250 K [Carnevali *et al*. 1987]. The high melting in the Au(111) surface might be a contribution of the denseness of the first-layer packing in the surface or might be the effect of the many-body forces.

In the experimental work by Shvartsburg and Jarrold (2000) the different tin clusters ranging from 10-30 atoms in size have shown melting to occur at least 50 K above the bulk tin, and the latter has a melting temperature of 505 K. The elevation of the melting points in the small clusters is, in certain instances caused by the impurities.

However, this was not the case with the tin clusters and for our computational work we are well aware that no impurities can exist unless introduced by hand. Another factor is the indirect involvement of the change in the chemical bonding through differences in coordination numbers, directionality and rigidity. It is therefore suggested that if the physical basis for the elevated melting points in small tin clusters is their heavily reconstructed geometries, then the same phenomenon may occur for other clusters that are heavily reconstructed. The Carr-Parrinello ab initio molecular dynamics study by Lu and co-workers [Lu *et al.* 2000] shows that the melting points calculated for the silicon and germanium clusters exceed the melting points of the respective bulk elements by a smaller margin. It can therefore be assumed that the "reconstructed" silicon and germanium clusters may show melting points that are well above their respective bulk forms.

It is understood that nanoclusters will show melting that is lower than the bulk material but melting does not necessarily increase or decrease with the size of the clusters (see Figure 3.31). Schmidt and co-workers [Schmidt *et al.* 1998] as well as Kusche and co-workers [Kusche *et al.* 1999] have studied melting in different sodium clusters ranging from 55 to 200 atoms. It is found that sodium clusters melt reasonably below the bulk sodium melting temperature (by about 33%) with the smallest clusters (Na_{55} and Na_{59} clusters) depicting highest melting temperatures. However, the melting points of these Na clusters show large variations with changing cluster size, rather than any gradual trend.

The behaviour of the melting process in the bulk gold is shown by Figure 3.34. The caloric curve shows a clear description of the transition from a solid to a liquid through the well defined jump in the energy. The relation between temperature and energy, $U = U(T)$, is called the caloric curve and its derivative is the heat capacity, C_p or C_v, depending on the conditions under which the calculations are performed. The energy becomes more negative with the increasing size. The bulk shows a linear increase in the energy before and after melting. The sudden jump in the energy is well defined. The energies in the solid are obviously lower than those in the liquid and this is clearly shown by all the results in Figure 3.34. The model we are using for the calculations in this work estimates the melting of the bulk gold very well. The value for $T_m \approx 1320$ K compares fairly well with the experimental value of 1337 K. The results from total energy for the bulk, just like in the nanoclusters, was complemented by the radial distribution functions and the density profiles and a concurrence was found.

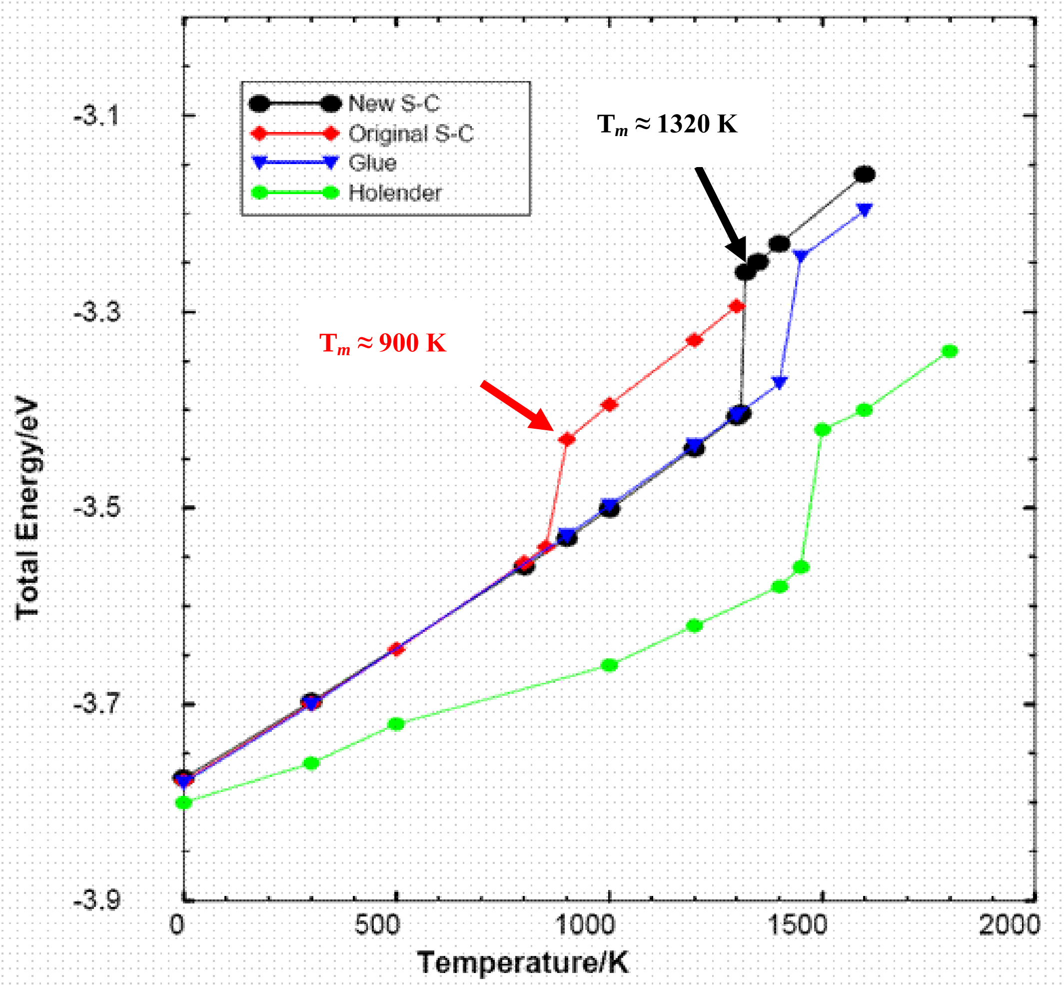

Figure 3.34. The bulk melting temperature calculated from our previous work [Mahladisa 2004] is shown. Comparison of the Sutton-Chen model is made with the glue model as well as results from Holender [Holender 1990].

3.1.1.5. Diffusion Coefficients (D)

Molecular dynamics simulation provides a good way of investigating dynamic processes on the picoseconds time scale. Where atomic diffusion occurs at liquid-like or near liquid-like rates it can be observed and measured in the simulations. The effects of diffusion in a system are shown by the irregular arrangement of peaks in the density profiles. Diffusion in the bulk materials initiates at the surface atoms as that is where melting also commences. The onset of diffusion in a material signals the instability of that particular system.

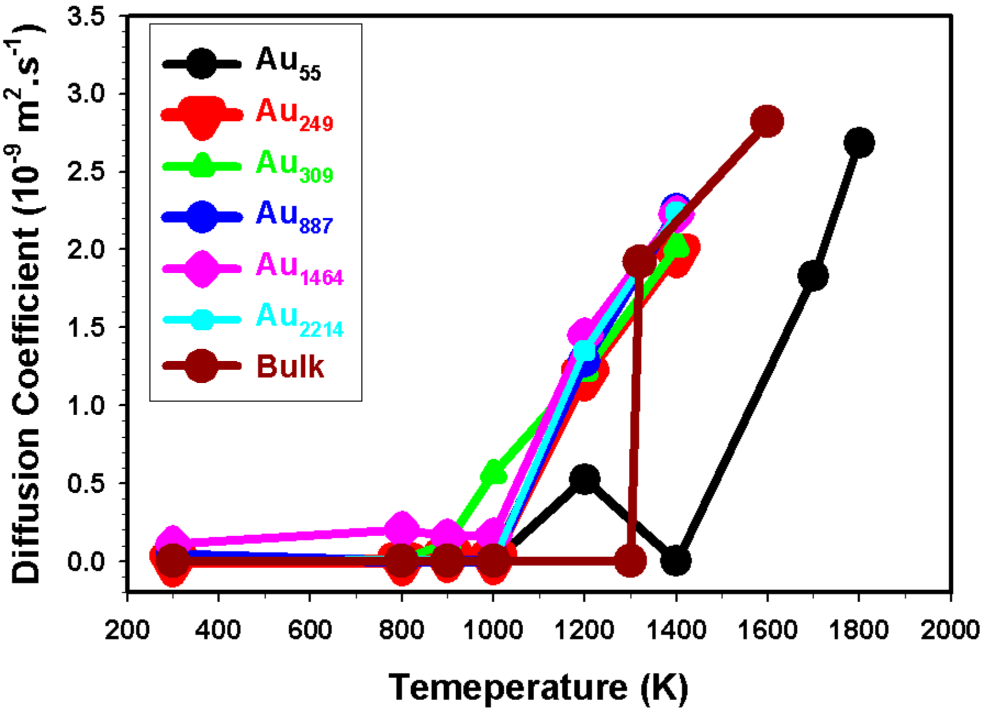

Figure 3.35. The diffusion coefficients are show for different clusters at different temperatures. Diffusion is also plotted for the bulk for comparison.

Diffusion coefficients for different clusters and the bulk are plotted at various temperatures in Figure 3.35. Diffusion is zero or very minimal at 300 K for all the clusters as well as the bulk. In fact no diffusion is noted until 1000 K for all the clusters except for the Au_{309} cluster. The Au_{309} cluster has some significant diffusion values of more than 5.0 x 10^{-10} $m^2.s^{-1}$ at 1000 K. All the clusters depict substantial improvement at 1200 K with the values higher than 1.5 x 10^{-9} $m^2.s^{-1}$. The diffusion increases further at 1400 K for all clusters. The bulk material on the other hand only starts to show the onset of diffusion at 1320 K which tends to be the melting temperature.

It was previously shown that among the clusters plotted in Figure 3.33, the Au_{309} cluster shows the lowest melting at 1000 K. The other clusters have their melting temperatures starting from 1050 K to 1200 K. The Au_{55} cluster, owing to its high melting temperature, starts to show diffusion at 1400 K. It should then be expected that at 1000 K the radial distribution functions and the density profiles will show significant instabilities, as we have observed.

There is a relation between the inter-atomic potential and the structural changes around the melting temperatures and the phase transition size. The molecular dynamics work by [Ercolessi *et al*. 1991] on different gold clusters shows the same behaviour in the mobility where it is found that no significant amount of diffusion can be seen at temperatures from 0 K to 1000 K. They observe substantial leaps in diffusion once 1000 K is exceeded. Wang *et al*. [Wang *et al*. 2004] found the same results on icosahedra gold clusters where the onset of diffusion shows only after 1000 K. Different observations are noted on the work by Rodriguez-Lopez *et al*. [Rodriguez-Lopez *et al*. 2003]. They have studied different concentrations of gold-copper (AuCu) alloys and calculated the diffusion coefficients of individual atoms in the alloys. They are able to see notable values of diffusion at temperatures as low as 550 K. However, their calculated melting points for the alloys were found to be around 550 K.

Our results show that diffusion is much reliant on the size of clusters and that high values are obtained when the melting is approached. The materials with the lowest melting points show higher diffusion.

3.1.1.6. The heat capacity at constant pressure (C_p)

The heat capacities of selected Au clusters are shown in Table 3.1 and the bulk and experimental values are included for comparison. The heat capacities for the cluster and the bulk were calculated at the same temperature interval, i.e. between 900 K and 800 K for better reference. The estimation of the bulk heat capacity at 3.37 is fairly comparable to the experimental value of 3.06 [Evans 1983]. We cannot as much compare the numbers of this parameter for the bulk and the clusters because of the different scales.

Table 3.3. Heat capacities for different clusters are shown. The value in the bulk is also shown with the experimental value taken from [Evans 1983]. The heat capacity is multiplied by the Boltzmann constant (k_B = 1.380 x 10^{-23} J.K^{-1}) to make it dimensionless.

Cluster (No. of atoms)	C_p	Bulk	Experimental
249	3.30	3.37	3.06
309	2.33		
1464	3.87		
2214	2.33		

Gold nanoclusters in Table 3.1 are lower than the bulk except for the cluster with 1464 atoms. The trend of the heat capacity in the clusters follows an irregular pattern as the size increases. The biggest cluster in our study together with the Au_{309} cluster shows the lowest heat capacities while the small cluster (Au_{249}) shows a value close to the bulk. The Au_{249} cluster has a heat capacity C_p = 2.30 which is close to C_p = 3.37 in the bulk.

The results discussed with respect to the different nanoclusters show that most parameters calculated and discussed are distinguishable to those of the bulk material, the most crucial one being the melting temperature. It has already being mentioned that if a material, no matter what the size, behaves like a nanoclusters, that material is called a nanocluster. The melting temperatures of the materials discussed are below the bulk, the structures show less peaks in the rdfs and the density profiles compared to the bulk, the density is significantly lower than the in the bulk and the atomic diffusions are higher than in the bulk. The diffusion coefficients and the energies in the nanoclusters are significantly higher than in the bulk and this further proves that nanoclusters are less stable than the bulk material. The bond distances in the nanoclusters are lower than 2.88 Å for the small clusters and matches that of the bulk as the size of the clusters increases. This confirms the fact that big nanoclusters will carry some characteristics that are similar to the bulk.

3.1.2. Gold Nanotubes

We shall look at the structural behaviour of gold nanotubes defined by (*n, m*) at different temperatures and try to estimate their melting temperatures. We shall refer to the radial distribution functions (rdfs) and the density profiles for the discussions of our results. We will try to show how the structure changes with temperature. The energy curves for the nanotubes, contrary to what we have observed with different Au nanoclusters, do not show the necessary jump or discontinuity as we have noticed with the clusters and we shall omit them for the discussions in this regard. This is owing to the nanotubes having small radii of the order of 1.0 nm (10.0 Å) and are close to one-dimensional systems for which the strict phase transitions do not exist [Bilalbegović 2000, Bilalbegović 2003]. The nanotubes will be divided into two categories, i.e. single wall (SWNT) and multi-wall (MWNT). A single wall nanotube is a single cylindrical shape with a hole allowing us to peep through while a multi wall nanotube is a combination of single walls and ranges from two walls to as many as possible (to four in this work). Different sizes of nanotubes will be considered for each class. The multi wall nanotubes will have two, three and four walls. We present our results under two different ensembles, the NVT and NPT Berendsen ensembles and the results will thereof be compared.

3.1.2.1. Single Wall Nanotubes (SWNT)

The radial distribution functions will be shown first under two conditions; we follow with the density profiles, the diffusion coefficients and then the changes in the structures at different temperatures will be shown. The size of the nanotubes start from 24 atoms and will go up to 1523 atoms.

3.1.2.1.1. The Au24 (6, 6) nanotube

We start by showing a small nanotube with 24 atoms where we illustrate how the details of the structure change as the number of atoms increases in the systems. The radial distribution functions give limited details in the structures containing slightly few atoms associated with few peaks (one peak) that will be detected. The number of peaks increases significantly with the increasing number of atoms. The simulations in this nanotube were carried out only under conditions of the constant volume and temperature (NVT).

The radial distribution functions (rdfs) as well as the density profiles of the nanotube with 24 atoms are shown in Figure 3.36. The structure shows only one peak at 300 K and the increasing temperature only decreases the height of the peaks. Obvious broadening of the peak is visible as the interactions between the atoms weaken. The density profiles show a well shaped curve at 300 K. The curves at 700 K and 1000 K become smooth and shift to the right. The rdfs in this regard cannot show a well melted structure because there cannot be few well ordered peaks since there is only peak depicted by the nanotube. However, it may be surmised that the much observed fall in the peaks signifies melting in the nanotube.

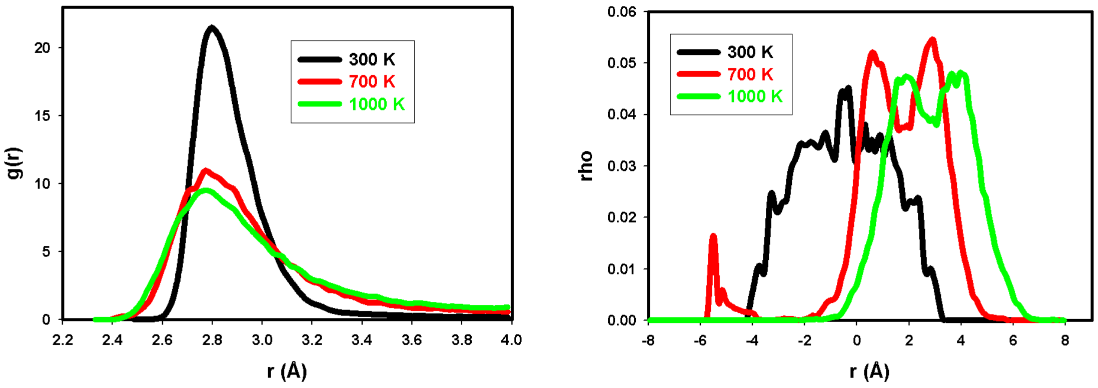

Figure 3.36 shows the Au24 nanotube where the radial distribution functions at different temperatures are depicted by the picture on the left and the density profiles are on the right.

The starting configurations of the nanotube with 24 atoms are shown from different directions in Figure 3.37. The interatomic distances, which do not differ much from those of the bulk gold, are noted to be 2.83 Å and 2.84 Å (the interatomic distance in the bulk is 2.88 Å). The atomic arrangement depicted on the left of Figure 3.37 follow the ring pattern. The atoms are nicely packed and although there are no clear hexagonal patterns, the building of such patterns can be witnessed. However, the nanotube shows a good cylindrical shape.

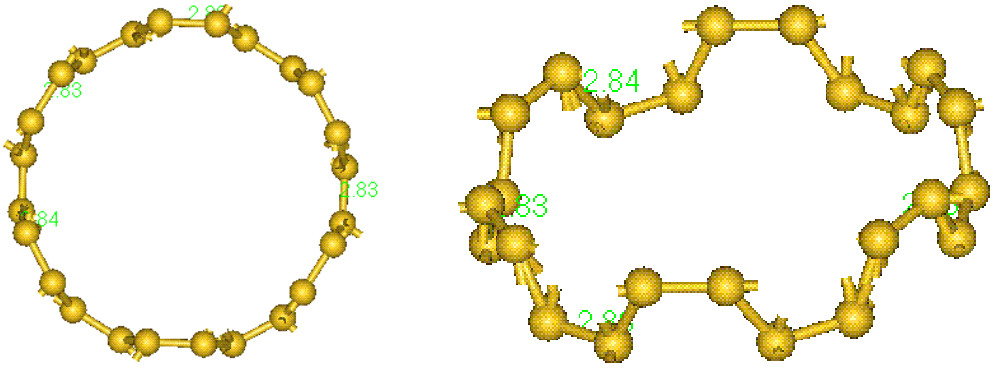

Figure 3.37 shows the structure of the Au24 nanotube before simulations viewed straight and along a the z-direction. The tube has the diameter of D = 8.14 Å and length L = 4.92 Å.

The nanotube looses the ring shape at 700 K and form a single structure. At 1000 K a longer bond of 3.00 Å formed and atoms start to break away from the structure. There is an irregular pattern in the change of the bonds. The bond distances change from 2.83 Å and 2.84 Å to 2.84 Å, 2.74 Å, 2.86 Å and 3.00 Å. The resulting structures at 700 K and 1000 K are shown in Figure 3.38. The increase in the bond length weakens the interaction between the atoms resulting in some atoms breaking away from the rest.

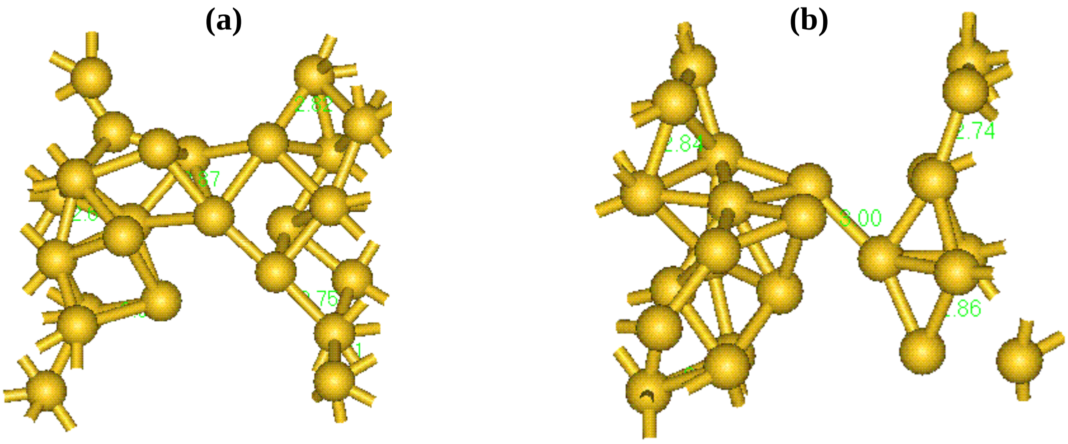

Figure 3.38. The simulated structures of the nanotube are shown at 700 K on the left and at 1000 K on the right.

3.1.2.1.2. The Au196 (5, 3) nanotube

The radial distribution functions depicted by Figure 3.39 show that the NVT conditions reflect more structure than the NPT condition due to a number peaks observed. The peaks show a lot of instabilities at room temperature as they follow no particular pattern. The nanotube is approaching a liquid phase at 700 K where a second peak starts to assume a round shape.

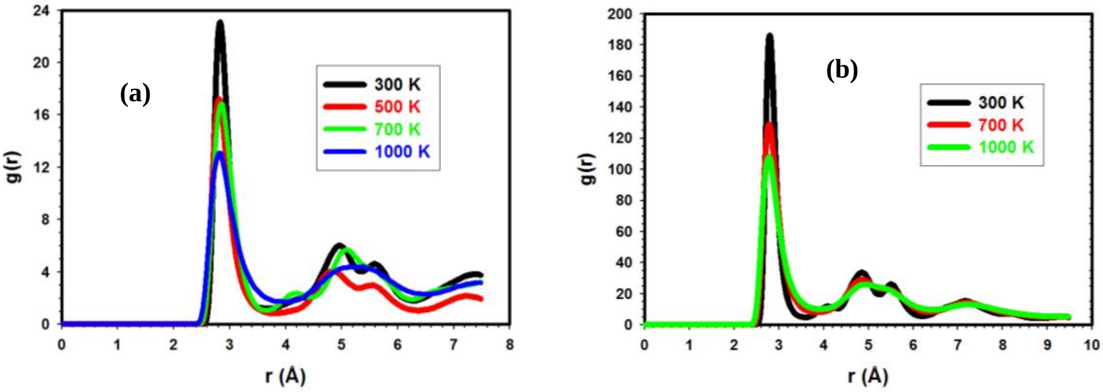

Figure 3.39 shows the rdfs in the NVT (left) and NPT (right) Berendsen ensembles at various temperatures.

The melted structure of the Au196 nanotube under the two ensembles is observed at 1000 K with well defined two peaks. Similarities in the two rdfs are that the structures start at ≈2.8 Å and the first and the maximum peak occurs at ≈3.0 Å. The rdf peaks broaden and decrease in peak height as the temperature rises.

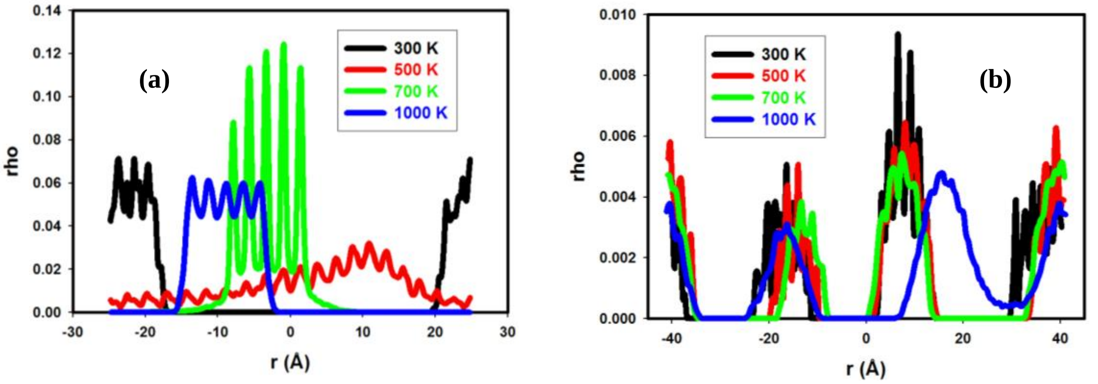

Figure 3.40. The density profiles for the Au196 nanotube at different temperatures from left to right in the NVT and NPT conditions.

The density profiles plotted against the distances r, at different temperatures are shown in Figure 3.40. The NVT Berendsen ensemble performs the simulation at a fixed volume throughout the calculations. The NPT Berendsen ensemble fixes the pressure and temperature while the volume is allowed to change, either by expanding or contracting. The density profiles on the left in Figure 3.40 for the NVT conditions show the plots to be dense at a particular area (around -10 and 10) with a shift with a temperature change. The NPT conditions show the plots to extend over a considerable distance and noticeable denseness in the system is at four regions. The density profiles show more dense systems at 300 K in both conditions. The order followed by the peaks in the density profiles is completely lost at 1000 K. The NPT, which shows clear plots in this regard, depicts a decrease both in the number of peaks as well as the peak heights. The structure in the NPT ensemble is dense at 300 K and 500 K. A reasonable decrease in the density of the system occurs at 700 K although some noise can still be detected. The peaks are very smooth at 1000 K where the nanotube is already melted. The peaks in the NPT follow the same behaviour throughout which gives a good transition from a solid to a liquid phase.

We now look at the structure of the nanotube plotted at different temperatures in the two ensembles. Figure 3.41 shows the starting structure. As opposed to the nanotube with 24 atoms we are able in this regard to see the hexagonal patterns with atoms connecting to form a long and stretching shape (Figure 3.41 (a)). Figure 3.41 (b) shows a different orientation where a hole is depicted.

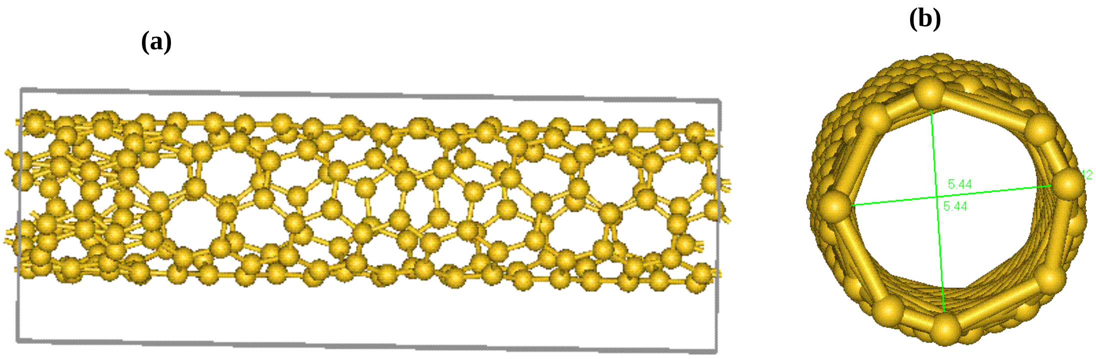

Figure 3.41 shows the structure of the Au196 nanotube before simulations. The hexagonal shapes are easily spotted in the left orientation, and on the right we show a hollow in the nanotube. The diameter D of this nanotube measures to 5.48 Å while the length L = 29.82 Å. This is the experimentally observed chiral gold nanotube.

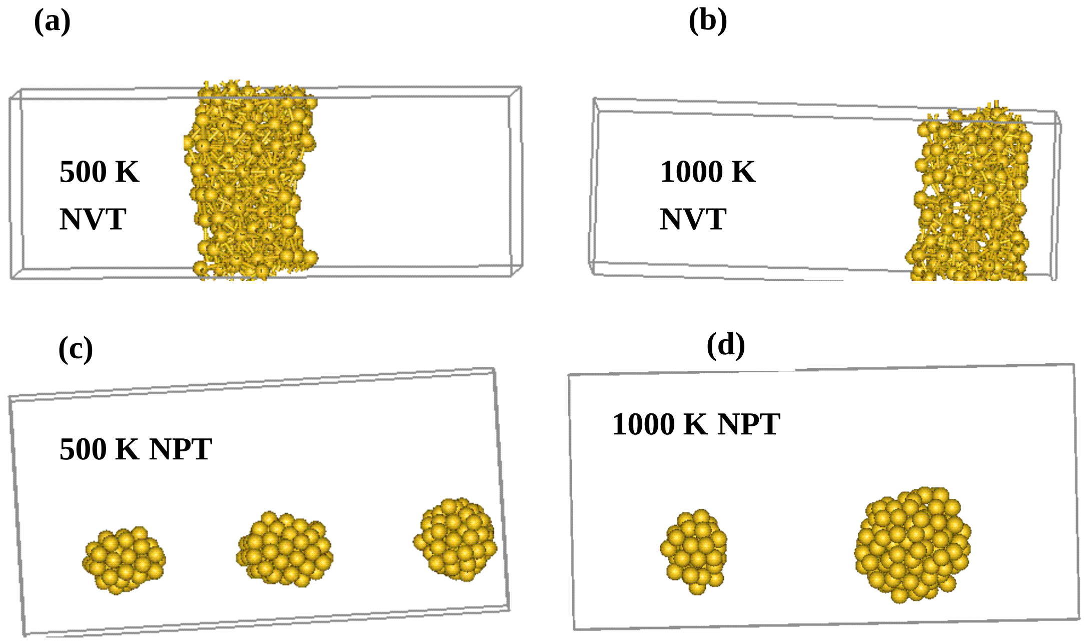

Figure 3.42. The Au196 nanotube is shown in the NVT and NPT conditions at two different temperatures, i.e. 500 K and 1000 K. (a) and (b) show the nanotube in the NVT while (c) and (d) the NPT structures. Different temperatures give different atom mobilities.

Figure 3.42 shows the nanotube under the NVT and NPT conditions at 500 K and 1000 K. Figure 3.42 (a) and (b) show the NVT structures while Figure 3.42 (c) and (d) show the NPT ones. The NVT conditions attain a single structure with some tubular features still visible at both 500 K and 1000 K. The nanotube stays at the centre of the simulation box at 500 K (Figure 3.42a) and then moves to the bottom at 1000 K (Figure 3.42b) and this is what the density profiles have shown where the plot changed positions with the changing temperature. The NPT structures shown by Figure 3.42 (c) and (d) depict different structures at the two temperatures. The nanotube splits into three clusters at 500 K but two of the three clusters merge to form one cluster. Two clusters of different sizes are then obtained at 1000 K. The effects of different volumes are shown in the behaviour of the nanotube at higher temperatures.

3.1.2.1.3. The Au364 (6, 5) nanotube

The obvious difference between the Au196 and Au364 nanotubes is the number of atoms each one consists of. The number of atoms in a structure, sometimes, plays an important role in certain structural properties such as melting. The melting temperature of a material decreases when the size of the material decreases and nanomaterials show melting temperatures that are below their respective bulk materials. The interatomic distances in the nanomaterials also decrease with the size. The Au-Au interatomic distance in the Au196 nanotube is 2.42 Å and in the Au364 is 2.82 Å.

The radial distribution functions for the Au364 nanotube in the NVT and NPT ensembles in Figure 3.43 show melted structures at 850 K and 750 K respectively. The rdfs start at 2.82 Å with instability clearly showing at 300 K. The plots show increased number of peaks since there are more atoms than in the tube with 196 atoms.

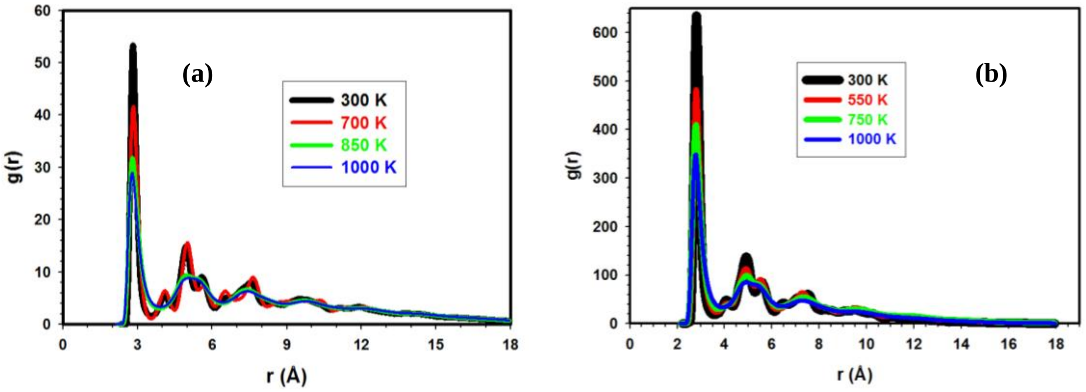

Figure 3.43. The radial distribution functions for the gold naotube with 364 atoms in the NVT and NPT Berendsen ensembles.

The density profiles are plotted in Figure 3.44. The NVT plot becomes dense within a small distance range and shifts to the left at higher temperatures of 850 K and 1000 K. The plots show some decrease in the denseness as high temperatures are reached. The NPT plot shows quite a wide range with noise fading as the temperature is increased. The plots are smoother and peak heights decrease and change the initial pattern at 1000 K.

The ball and stick and stick models of the starting configurations of the Au364 structure are shown in Figure 3.45.

The bond distance in the nanotube is 2.82 Å which slightly differ with 2.89 Å of the bulk gold.

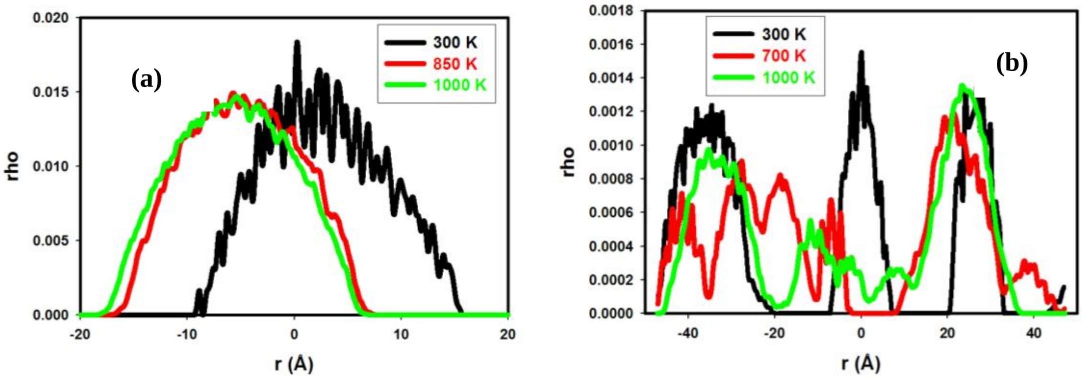

Figure 3.44 shows the density profiles for the Au364 nanotube in the NT and NPT shown respectively by (a) and (b).

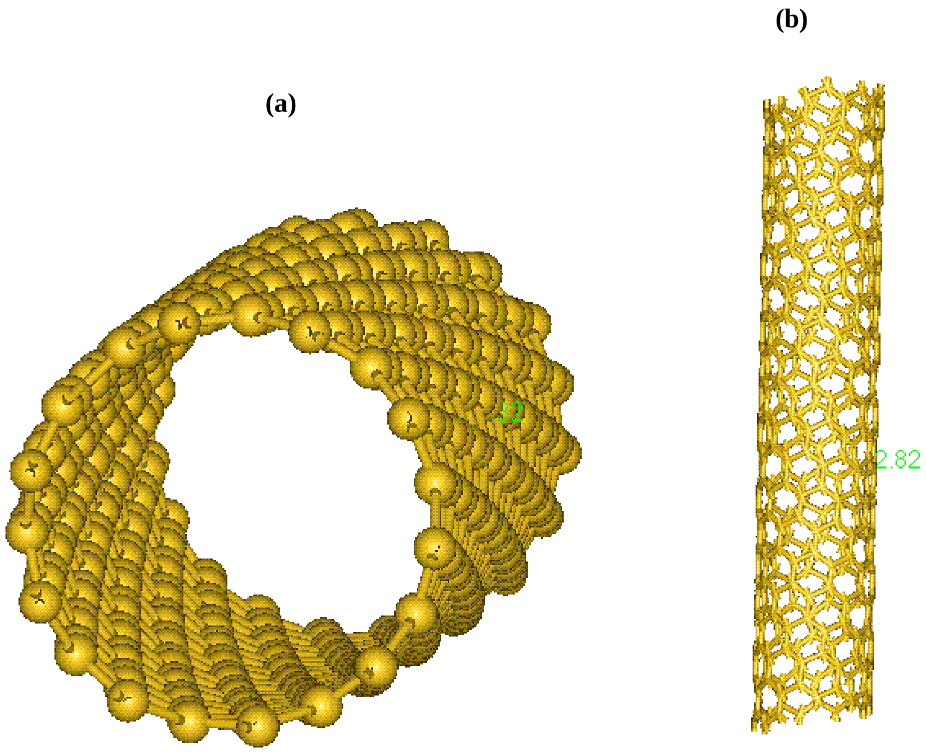

Figure 3.45. The starting structure of Au364 nanotube with the bond distance at 2.82 Å and the diameter D is 7.47 Å. The length L measures to 81.28 Å.

The structures are shown at 500 K and 1000 K, in the NVT and NPT ensembles, in Figure 3.46. The first two structures on the left represented by Figure 3.46 (a) and (b) show the NVT conditions where single clusters are obtained. Figure 3.46 (a) shows the Au364 deforming into a single cluster at 500 K and the cluster assumes a more spherical shape at 1000 K. The NPT nanotube deforms into four clusters varying in sizes at 500 K (Figure 3.46c). The nanotube at 1000 K depicted by Figure 3.46 (d) then forms two big clusters and one small one. The tube feels early heat at 500 K and forms many clusters, but adjustment is made when the temperature is raised and then the number of clusters decrease. The phenomenon of temperature is known to increase the kinetic energy in a system. The structures in the NPT show that the kinetic energy, under such conditions, increases at 500 K and then reduces at 1000 K where the atoms come together again after separating in patches. The nanotube breaks into clusters which prefer spherical shapes at higher temperatures. The shape of the clusters is always spherical since that is how nanoclusters and nanotubes prefer to configure at melting.

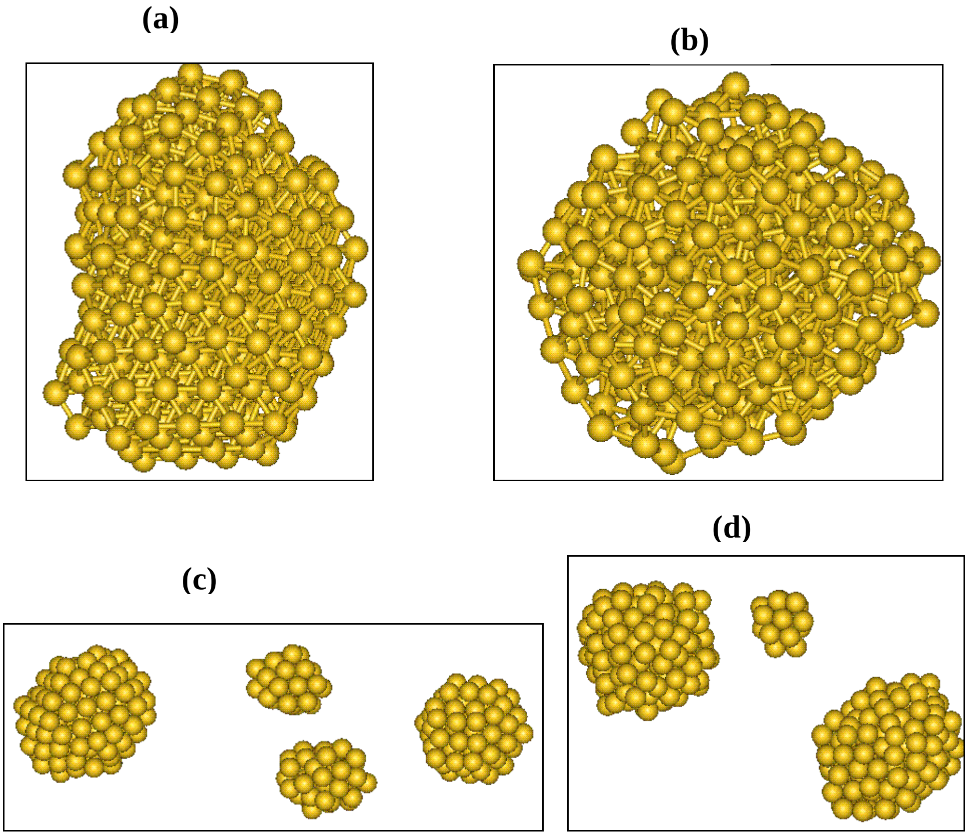

Figure 3.46. The NVT structures are depicted by a at 500 K and b at 1000 K. c and d show the structure under the NPT conditions, c shows four clusters at 500 K, d consists of three clusters at 1000 K.

3.1.2.1.4. The Au628 (7, 3) nanotubes

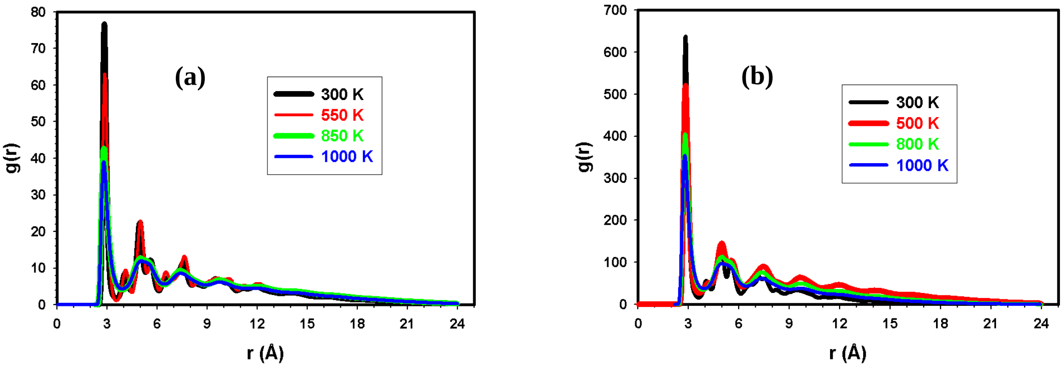

Figure 3.47. The rdf for the Au624 are shown in the NVT in (a) and NPT in (b).

The rdfs for the gold nanotube with 624 atoms are shown in Figure 3.47. The graphs show melting at 850 K in both ensembles. The rdfs start at the point corresponding to the interatomic bond distance for a particular nanotube and terminates at the cut-off radius used for the calculations. The three nanotubes studied so far, the Au196, Au364 and Au624 show their rdf plots to respectively start at 2.42 Å, 2.82 Å and 2.83 Å which are their corresponding bond distances. All nanotubes show strong repulsive forces at short distances less than the atomic radius and g(r) is zero. The plot for the density profiles in Figure 3.48 further justifies the melting behaviour of the Au624 nanotube at 850 K. The graph for the nanotube at 850 K loses the animosity and becomes smoother. There is a shift to the left in the plots in the NVT conditions as the melting temperature is approached. The graphs at 700 K and 1000 K in the NPT conditions reduce the number of peaks as well as the peak heights.

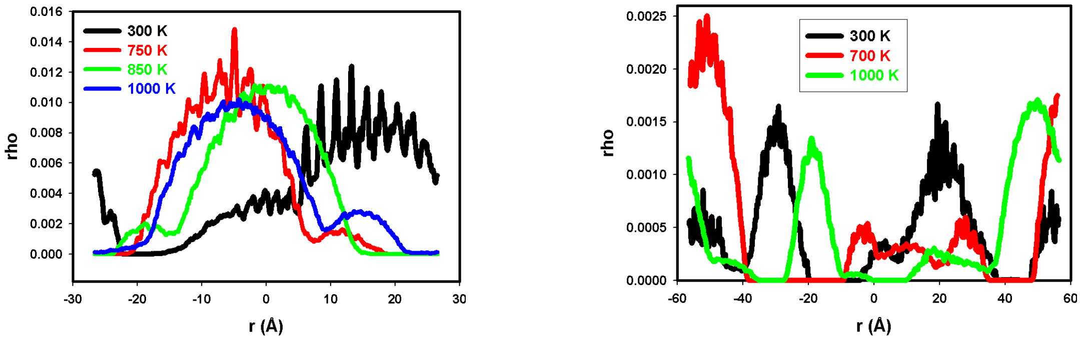

Figure 3.48. The density profiles for the Au624 are shown. The left plot will indicate the constant volume conditions and the right one will indicate the NPT ensemble.

The structure of the nanotube at the starting configuration is shown in Figure 3.49. The interatomic distance in the nanotube is found to be 2.83 Å before simulations. The simulated nanotubes show different results from the other two nantoubes above in the NVT conditions. The Au624 nanotube does not form a spherical cluster at 500 K, rather a shape with a chain-like end. The tube then forms a big spherical cluster and some patches can be observed on the sideways at 1000 K.

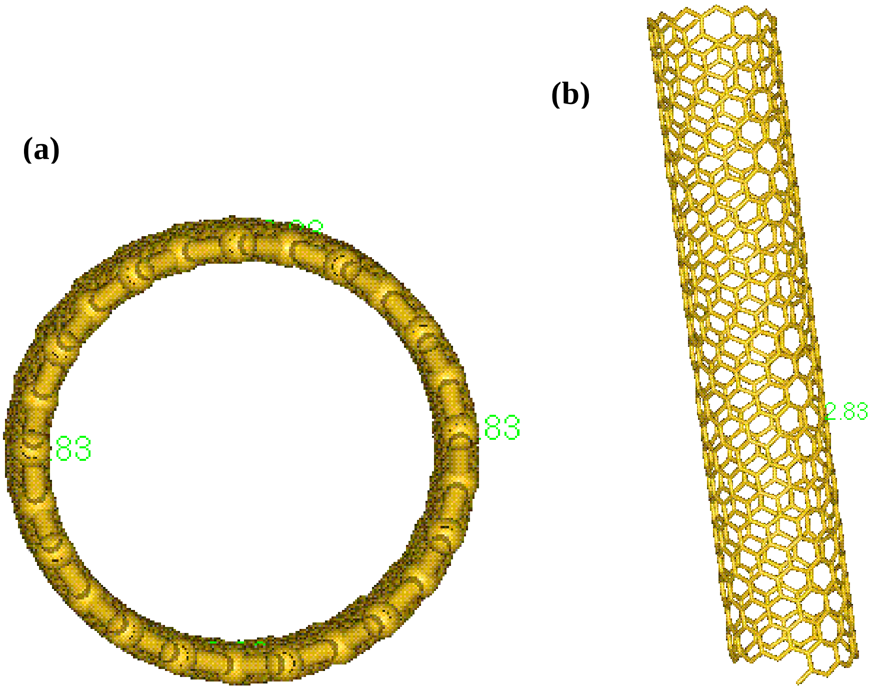

Figure 3.49. The starting configurations of the Au628 nanotube. The bond distances are found to be 2.83 Å. The diameter of this nanotube measures to 6.96 Å.

The work by da Silva and co-workers [da Silva et al. 2004] have shown that a nanotube stretches into a mono chain before breaking. The cause of the breakage is found to be the stress applied or experienced by the nantoube. Bilabegović [Bilalbegović 2001] has studied the stress effect on the gold nanotubes using the embedded atom method (EAM) in molecular dynamics. The results found show that applying certain stress on a nanotube deforms the structure to such an extent that the initial structure cannot be recovered by removing the stress. The stress can be in the form of applied pressure, temperature, etc. The NPT conditions show similar effects to the previous nanotubes where the nanotube disintegrate into four clusters, two big and two small clusters at 500 K and later forming three spherical clusters at 1000 K. The simulated structures of the Au628 nanotube are shown in Figure 3.50.

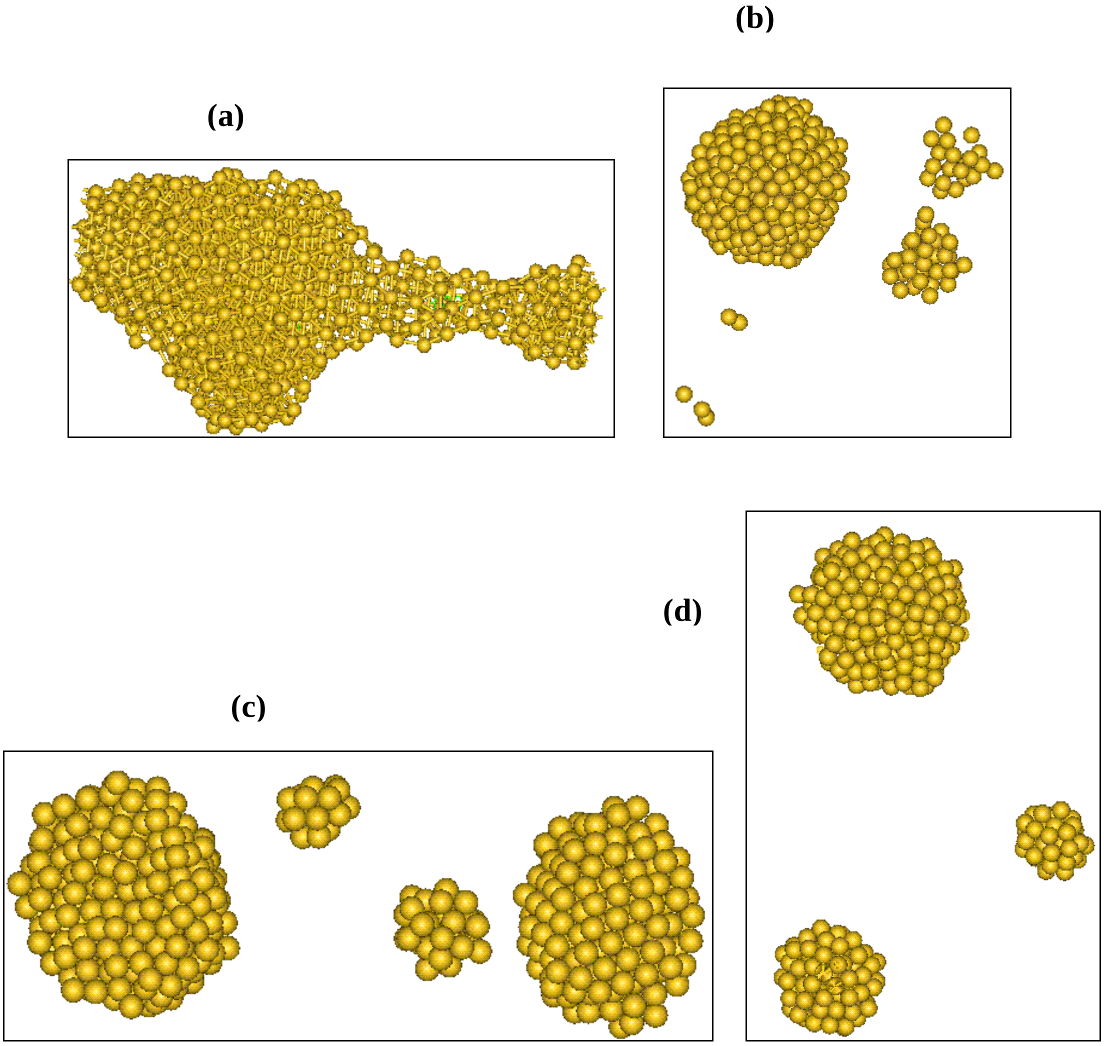

Figure 3.50. The structures of the Au628 nanotube simulated at 500 K and 1000 K under the NVT (a and b) and NPT (c and d) conditions.

3.1.2.1.5. The Au1252 (8, 7) nanotube

In this nanotube we move from a hundred of atoms in the structures and consider a nanotube with over a thousand atoms. The rdfs in Figure 3.51 show more long range interactions in the structure of the nanotube. The structure at 300 K shows much instability due to lack of multiple peaks in the rdfs, but strong solid features exist. The structure of this nanotube is less characterised by the rdfs as we have seen with the case of the nanotube with 624 atoms. The contributing factor is the much volume accorded to the atoms and hence the long range interactions. We are however, still able to observe a structure described by a few well defined peaks at 1000 K in both ensembles which signifies the melting in the nanotube.

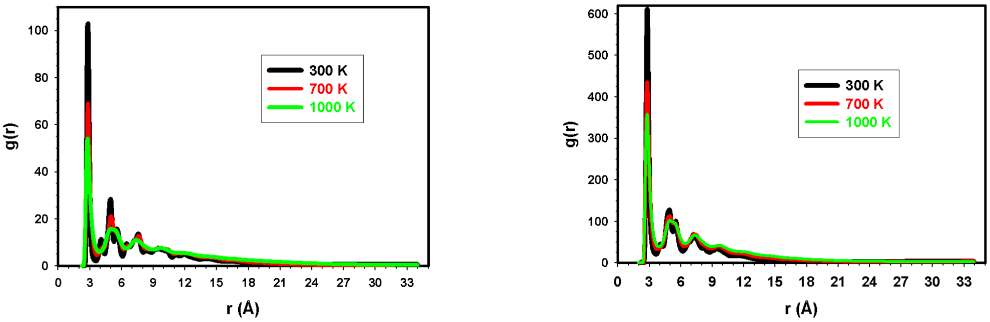

Figure 3.51. The radial distribution functions for the Au1252 nanotube extracted at different temperature in the two ensembles.

The graph for the density profiles for the Au1252 nanotube depicted in Figure 3.52 gives less dense systems at 300 K. The NVT conditions show only one complete peak at r ≈ 0.0 Å with some noise contrary to the multiple peaks observed in the NPT conditions. The plots become smooth at 700 K and continue to smoothen further at 1000 K. Once again the difference in the volume in the two ensembles can be noticed. The graphs in the NVT ensemble go from r ≈ -35 Å to r ≈ 35 Å while the NPT ensemble has -70 Å ≥ r ≤ 70 Å as the range of the distance. Transition for a solid to a liquid phase is well established from the rdfs and the density profiles. The density profiles show, through the NVT and NPT ensembles, what difference the volume can make in the movement of the atoms.

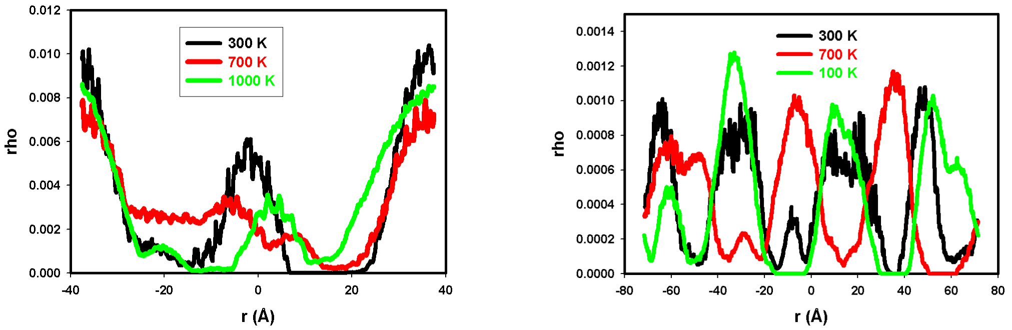

Figure 3.52. The graph on the left shows the density profiles in the NVT and the right graph shows the NPT ensemble.

The starting configuration of the nanotube is shown in Figure 3.53 with the hollow in the nanotube clearly shown. As one of their potential uses, nanotubes can be used as transport materials where a fluid can be allowed to pass through the nanotube from one end to the other. The process allows the fluid to be passed from source to the other. The initial configurations of the nanotubes show well ordered structures with the cylindrical shapes well appreciated.

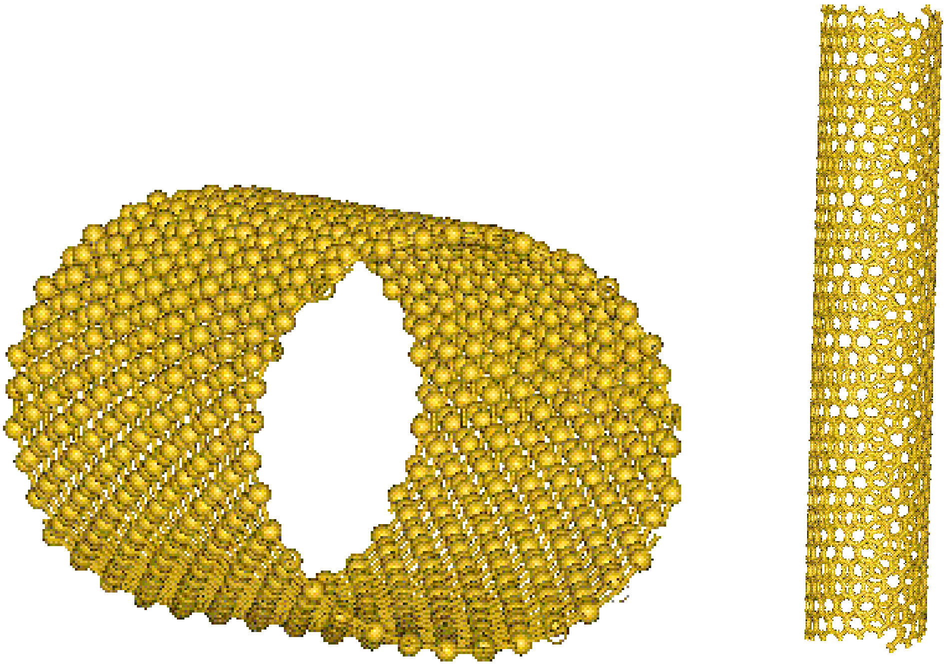

Figure 3.53. The different view of the starting configurations of the Au1252 nanotube with the diameter of 10.18 Å and length 110.76 Å is shown.

The process of heating different structures at various temperatures yields different results for each particular system. The number of atoms in a system plays some significant role as has been observed with different results for the nanotubes. The general agreement generated from imposing temperature on different nanotubes is that the initial cylindrical shapes of these nanomaterials collapses at temperatures as low as 300 K. Figure 3.54, which shows the nanotube with 1252 atoms, clearly shows the role played by a number of atoms in a system. The Au1252 nanotube collapses into multiple clusters at 500 K which then merge or coalesce and form three spherical clusters at a higher temperature of 1000 K under both conditions.

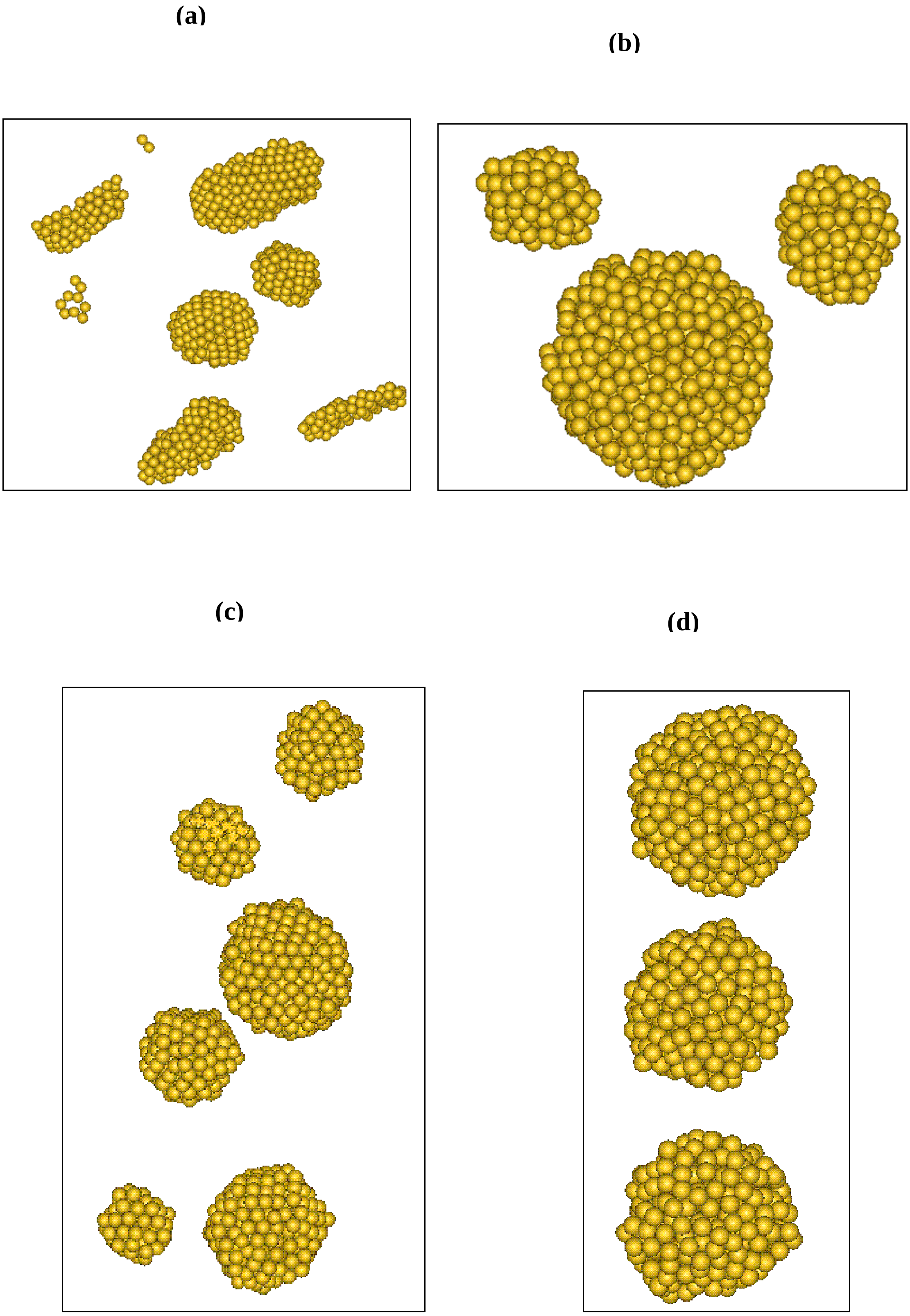

Figure 3.54 shows the structure of the Au1252 nanotube at 500 K and 1000 K in the NVT (a and b) and NPT Berendsen (c and d) ensembles.

The mechanism followed during the collapse of the nanotubes is that the atoms break away from each other forming patches or groups of clusters and remain bonded in those small clusters. The bond distances in the heated structures are found to be different with others preferring to contract and others increasing. The clusters formed under the NPT conditions seem to assume a more spherical shape while those in the constant volume and temperature show some inconsistency. The constant pressure and temperature conditions form exactly six clusters at 500 K which are able to converge to form three clusters of comparable sizes. The constant volume-temperature conditions depict three clearly visible clusters which are not convincingly spherical with some small structures on the side. However, three near spherical shapes are obtained at 1000 K although the sizes are not as comparable as those in the NPT.

3.1.2.2. Multi-Wall Nanotubes (MWNT)

The significant question arising from studying these types of nanotubes is whether melting starts from the inside layer or the outside one. We hope we will be able to address that problem in the underlying discussions. Wang *et al*. [Wang et al. 2002] and Bilalbegović [Bilalbegović 2000] have reported some results on the effect of temperature on the multi wall nanotubes. We shall consider three different nanotubes under this topic, viz. double wall, three wall and four wall nanotubes. We are following the discussion underlined in the single wall nanotubes sections where we shall focus on the radial distribution functions (rdfs), the density profiles as well as the structures at various temperatures. The molecular dynamics simulation studies of CuNi alloys by Kazanc [Kazanc 2006] and Zhou and Gao [Zhou and Gao 2005] follow the same procedure as ours where the radial distribution functions are used in differentiating between different phases. The studies clearly show crystal structures of the alloys and gold nanowires transforming from a liquid phase to a solid, going through the transition. Bilalbegović [Bilalbegović 2000] shows that multi wall nanotubes are very solid at lower temperatures which then loose their crystalline structures faster than the bulk material. The loss of the tubular structure is further confirmed by the semi-empirical tight-binding work at different temperatures by Delogu [Delogu 2007].

3.1.2.2.1. Au Double Wall (6, 3) nanotube (DWNT)

The radial distribution functions, in Figure 3.55, for this nanotube clearly show the difference between the constant number of atoms (N), constant volume (V) and constant temperature (T), the NVT Berendsen ensemble, and constant number of atoms (N), constant pressure (P) and constant temperature (T), the NPT Berendsen ensemble. That difference is much noticeable at 300 K where the NVT conditions show more structure which gives a clear face-centred crystal (fcc) structure. The fcc structure is characterised by the multiple number of peaks in the rdfs. The NPT conditions on the other hand show an unstable fcc structure at 300 K and splitting appears at the peak located at $r \approx 5.5$ Å. The instabilities in the structure at a room temperature are caused by the fact that in the NPT conditions, due to constant pressure, the system feels heat quicker and hence lattice vibrations occur earlier. However, the behaviour of the structure in the two ensembles is found to be the same at 700 K where a shoulder is observed at $r \approx 4.2$ Å.

The graphs for the rdfs in Figure 3.55 show melted structures at 1000 K where two smooth and well defined peaks are seen. The premelting (melting below the bulk T_m) behaviour in the nanotubes is a clear indication that the cylindrical and spherical shapes of these materials provide a good surface as melting initiates at surface atoms. It may be argued that that the nanotubes have an enhanced free energy at the surface atoms which is generated from the liquid-vapour interface free energy being much lower than the average solid-vapour interface free energy, which in turn increases the surface to volume ratio. In such shapes there appears to be no or very few bulk atoms owing to the instability that they show at low temperatures. The radial distribution functions, as expected show more structure under the NVT conditions although both ensembles show well melted structures at 1000 K.

A nanotube is in general round in shape and the hexagonal patterns of atoms stimulate the melting in these materials. The double wall nanotube significantly gives an increased number of atoms and, as we expect depicts a good number of clearly defined peak at room temperature. This fact leads to well ordered peaks at melting to clearly show a molten nanotube structure.

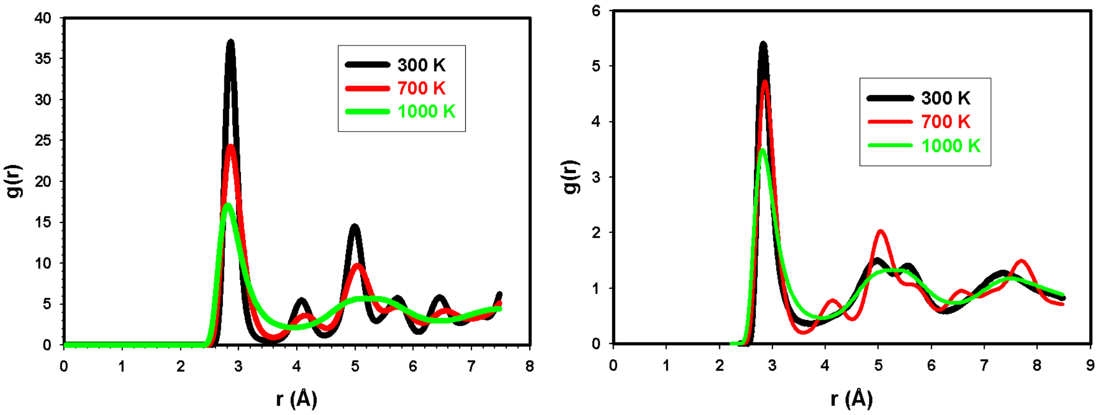

Figure 3.55. The radial distribution functions under the NVT and NPT Berendsen conditions for the Au double wall nanotube.

The density profiles are plotted in Figure 3.56 for the Au double wall nanotube. The graph on the left shows a more dense system at 300 K with the distance r ranging from -10 Å to 10 Å. The plot at this temperature consists of an infinite number of peaks signifying the solid behaviour in the system. The graph changes dramatically at 700 K, the number of peaks has decreased significantly. The system at 1000 K shows a flat graph compared to the other two temperatures which confirms the results from the rdfs. The NPT system shows stability up to 700 K where a multiple number of well defined peaks are observed. The system at 300 K is not as dense as the one in the constant volume and temperature conditions as the peaks have some good separations. The number of peaks decreases at 700 K and then the plot similarly flattens as in the NVT at 1000 K.

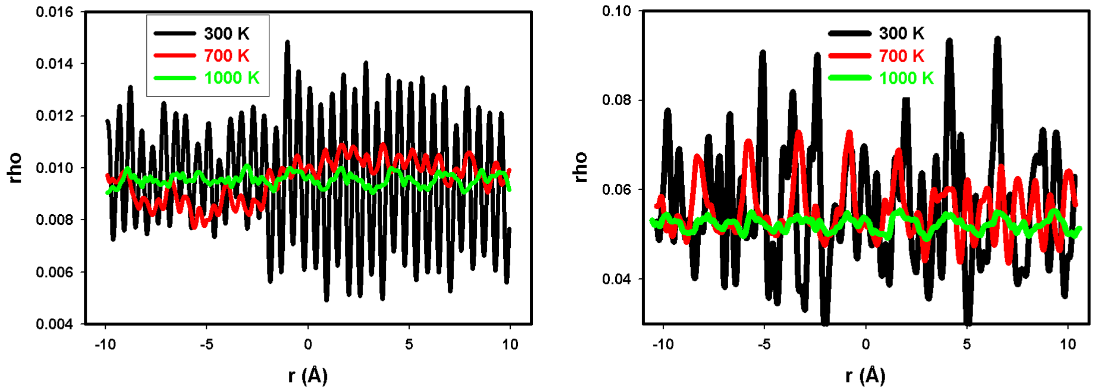

Figure 3.56 shows the density profiles under two conditions for the double wall nanotube. The left graph always represents the NVT conditions and the right graph is for the NPT ensemble.

The initial configuration of the Au double wall nanotube is shown in Figure 3.57. The separation distance between the walls in the nanotube is found to exceed 3.347 Å. This separation is good enough to make sure the walls do not appear to be one thing and remain separated until a high temperature in imposed on the nanotubes. The bonding distances are the same as in the bulk gold, r = 2.88 Å. This double wall nanotube consists of 480 atoms.

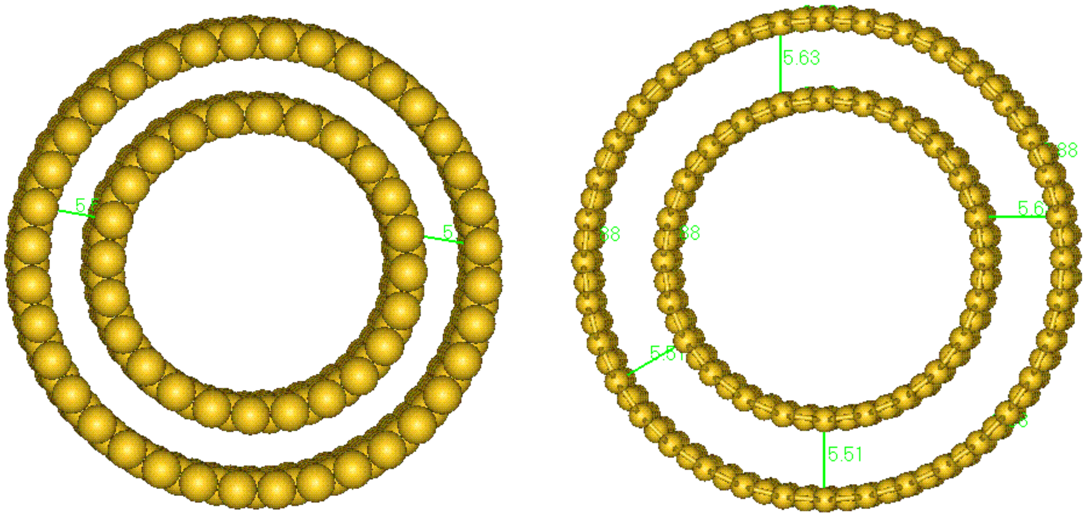

Figure 3.57 shows the nanotube with two walls. The nanotube spots two shells or walls which are separated by a distance of more than 5.50 Å. The interatomic or bond distance in the nanotube is 2.88 Å.

The simulated configurations are shown by Figure 3.58. The single wall nanotubes studied in previous sections show the same trend on increasing temperature. They (single nanotubes) prefer to form patches of clusters differing or equal in their sizes. The double wall nanotube shows a totally different morphology when subjected to the same conditions. The NVT conditions show the nanotube deforming into a tetragonal shape at 500 K and then a spherical cluster is attained at 1000 K. The nanotube in the NPT conditions on the other hand undergoes only one phase change which is from two cylindrical shapes to a tetragonal one. The nanotube deforms into a tetragonal structure at 500 K, and keeps the same structure at 1000 K but with more separations between the atoms. The NPT conditions deform the nanotube into a face centred cubic structure resembling the surface structure of gold. The structures at 1000 K under both conditions show some visible gaps. The density profiles have shown that the denseness in the systems decreases quite significantly at 1000 K. In this type of a nanotube we observe that heating occurs simultaneously in the two walls leading to a total collapse in the structure. The rdfs and density profiles have shown melted structures at 1000 K and the difference is noticeable in the structures between 700 K and 1000 K.

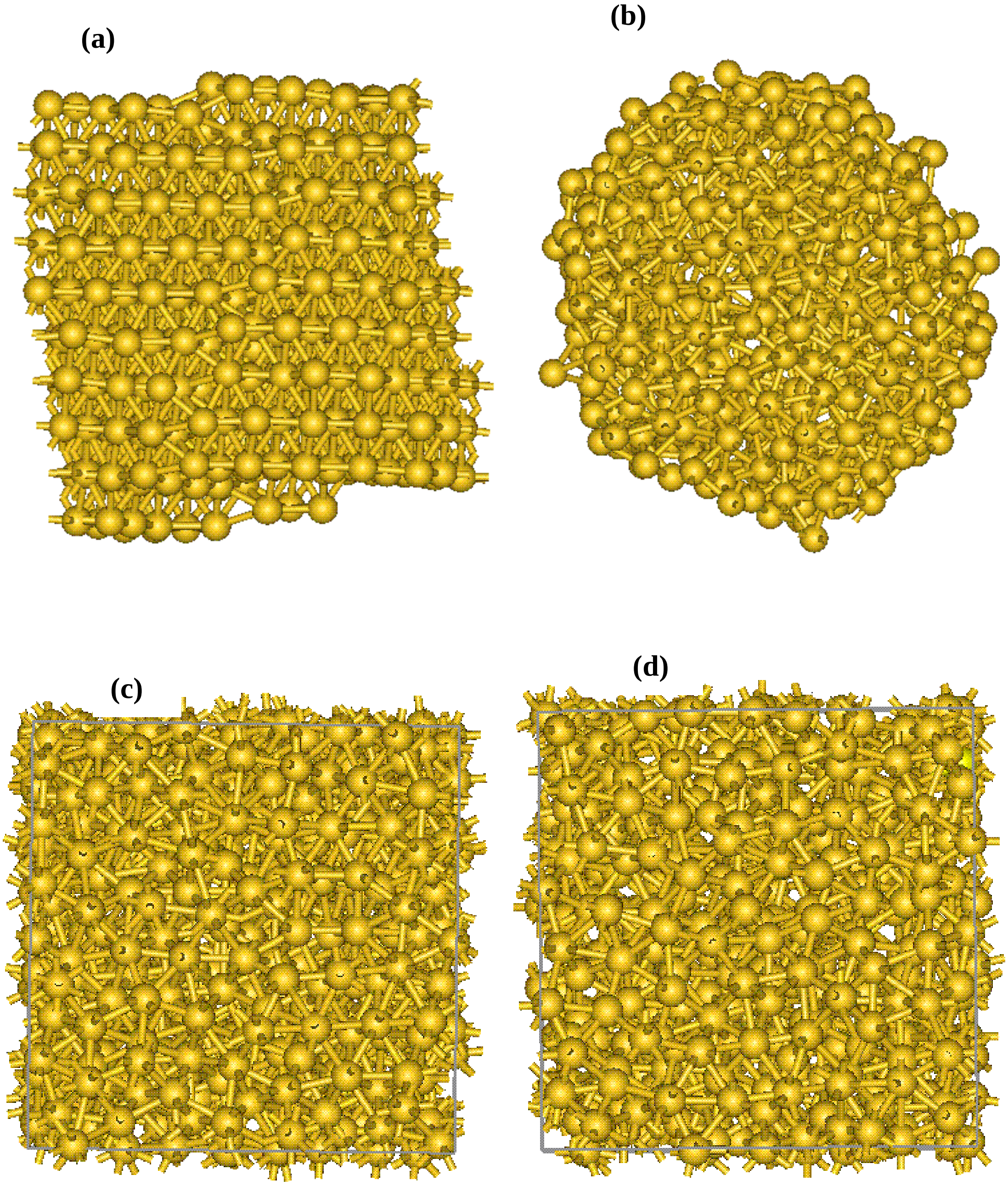

Figure 3.58. Simulated structures of the Au double wall nanotube are shown. (a) and (b) are the NVT configurations at 500 K and 1000 K respectively while (c) and (d) represent the NPT structures at 500 K and 1000 K.

The structural transformation in the nanotubes starts with the breaking of the walls that form the cylindrical shapes. The atoms break away from their curved bonding, forming a shape like a flat sheet and depending on the restrictions the structure is subjected to, one or a number of clusters are formed. The two walls in the double wall nanotube are destroyed completely once the temperature is introduced and the atoms will rearrange and form single structures. The nanotubes collapse under high temperatures and are not able to retain their tube structure. The bond distances are found to follow no particular order during the destruction of the nanotube, some bonds do increase while others decrease from the original distances.

3.1.2.2.2. Au Three Wall (6, 4) Nanotube (TWNT)

The increasing number of walls or shells will obviously increase the number of atoms in a nanotube. As the number of walls increases the inner wall becomes further rooted into the interior of the structure. This poses two possibilities when the system is heated. Firstly, as in the case of the double wall, the heating of the three walls in the nanotube might be simultaneous and could therefore lead to the collapse of the cylindrical nanotube structure. The second possibility is that heating might occur wall by wall where outer shells might experience more heat than the inner ones. If the second possibility holds, it could be suggested that the nanotubes are important materials for storage under hot conditions.

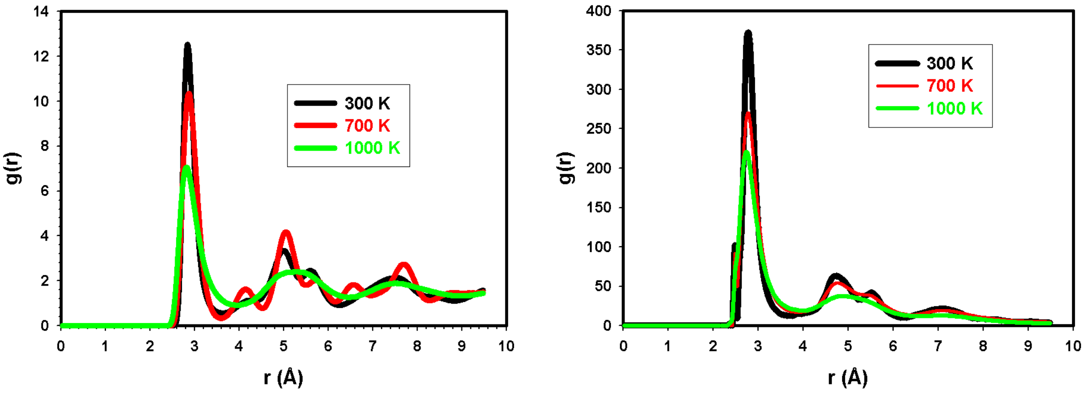

Figure 3.59. The radial distribution functions in a three walled nanotube with 541 atoms. The left plot show the NVT ensemble while the on the right we exhibit the NPT ensemble.

Figure 3.59 depicts the radial distribution functions of the nanotube under the NVT (left graph) conditions showing an unstable structure at room temperature. The peaks do not follow any particular pattern, with the first and maximum peak occurring at r ≈ 3.0 Å and g(r) ≈ 12.5. The structure shows more instability at 700 K and melting reflected at 1000 K. The peak height drops in the first and maximum peaks. The structure under the NPT conditions shows more instability with splitting already occurring at 300 K. The structure is molten at 700 K, and a liquid structure is depicted at 1000 K. The nanotubes have even more clearly defined surfaces than in the nanoclusters and all atoms seem to be at surfaces already and therefore difficult to separate bulk atoms from those at the surface. Melting in the nanotubes seems to involve all atoms contrary to the clusters where surface atoms are where melting initiates.

The density profiles for the nanotube are shown in Figure 3.60 where the NVT conditions are shown on the left and the NPT conditions are on the right. The structure of the nanotube is better represented in the left plot where many peaks signify the denseness of the system. At 1000 K a horizontal line is noted, quite different from the many peaks observed at 300, 500 K and 700 K. The NPT density profiles cover more volume as compared to the NVT ones. Although not as dense as the structure in the NVT case, the NPT conditions show progressive difference from 300 K and 1000 K. The structure starts with certain peaks at 300 K which decrease in height at 700 K and then followed by a smooth peak at r ≈ 20 Å at 1000 K. The results follow the same trend as in the previous discussions where the density profiles validate the findings from the radial distribution functions.

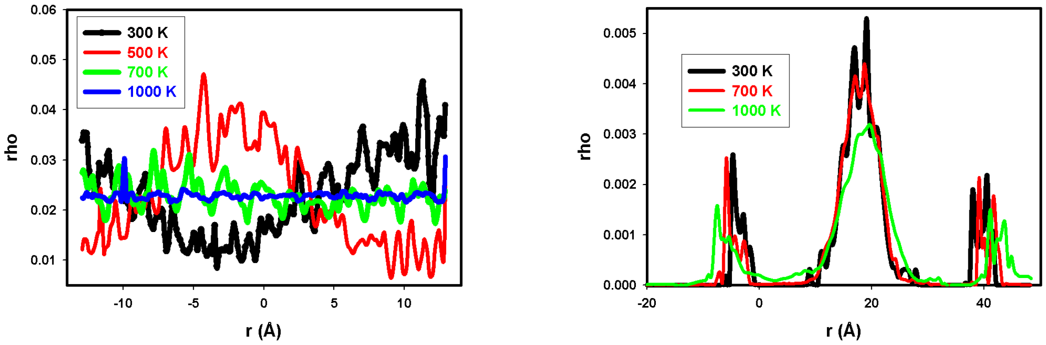

Figure 3.60. The density profiles are shown. Many peaks in the plot signify the denseness.

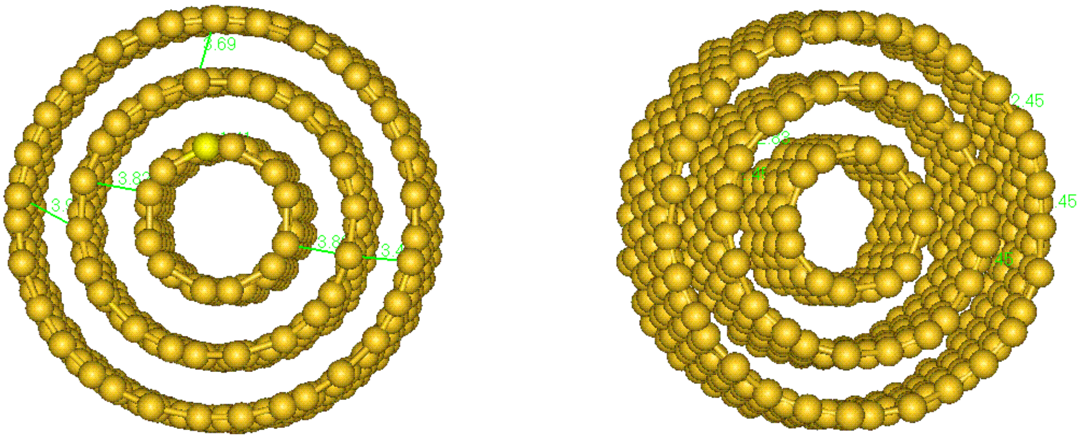

Figure 3.61. The starting structure of the Au three wall nanotube is shown from different angles. the inner nanotube is always the smallest.

The starting configurations of a gold nanotube with three walls and 541 atoms are shown in Figure 3.61. Bonding in this nanotube is different in the three walls or shells. The interatomic distance in the outer shell is found to be 2.45 Ǻ. The central wall shows higher interatomic distances of 2.83 Ǻ, where the bond distance in the interior and smallest wall is 2.78 Ǻ. The separation between the exterior wall and the second one is about 3.94 Ǻ and the central and the inner shell are separated by approximately 3.82 Ǻ.

Figure 3.62 shows the evolution of the nanotube structure with temperature in the NVT and NPT ensembles. The NVT structures are shown by Figure 3.62 (a, b and c) at 300 K, 500 K and 1000 K respectively. The nanotube looses the cylindrical shape at 300 K with one or two atoms breaking away from the rest. However, the atoms are still arranged in the form of a tube pattern. The deformation of the structure continues at 500 K where a near spherical shape is attained. Finally at 1000 K the structure converges to form a face centred cubic structure showing more holes implying that most bond distances have increased. We have noticed in the previous nanotubes that at lower temperatures the structure of the nanotube collapses and some atoms break away. However, the atoms then come together at a higher temperature of 1000 K and form one structure, a fcc structure in case of the larger nanotubes.

In Figure 3.62 (d, e and f) we show the evolution of the structure in the NPT Berendsen ensemble. Melting process of a crystalline material is known to start from the surface layer and propagates into the interior. Thus, the atoms in the outer shell of the nanotube should show lower melting than the interior shell due to their large surface-to-volume ratio. The NPT conditions preserve the cylindrical walls of the nanotube throughout, even up to higher temperatures. The outer and central walls deform into patches of clusters forming rings, but the three shells are still identifiable at 300 K. The walls of the nanotube are more homogenous at 500 K than at 300 K. The inner wall remains intact with a small cluster inserted inside. The interior wall continues to be visible and can still be noticed at 500 K and 1000 K while the other two walls form patches of clusters that surround the inner shell. Our results show that heating in the nanotube commences at the outer walls, which have lower melting temperature as compared to the inner wall. The outer wall is then seen as the one providing more surface atoms and the inner one providing the most part of the bulk.

Bilalbegović [Bilalbegović 2000], in the MD study of multi-walled nanotubes using the embedded atom method (EAM), has also found that as the multi wall nanotube is heated, the walls become homogenous with a thin filled interior core. Bilalbegović however, reported that melting occurs simultaneously in the nanotube. Gülseren *et al.* [Gülseren *et al.* 1995] on the other hand reported that the atomistic work using a many-body potential on lead (Pb) nanowitres show melting to be preceded by surface melting effects of the outer skin or shell. The MD work by Delogu [Delogu 2007] on Au nanotubes in the NPT ensemble using tight-binding band energy semi-empirical interatomic potential shows that nanotubes form fcc structures first before breaking and this study shows a good agreement with our observations. We have noted different results in our study thus far where a double wall nanotube behave similarly to the results of Bilalbegóvic and the three walled nanotube show similar results, under the NPT conditions, to those of Gülseren *et al.* The emerging assumption is that melting in the multi-wall nanotubes starts from the outer wall or that the structure can collapse leading to simultaneous melting. It is intriguing to note that the two ensembles show different results in the melting behaviour of the three wall Au nanotube.

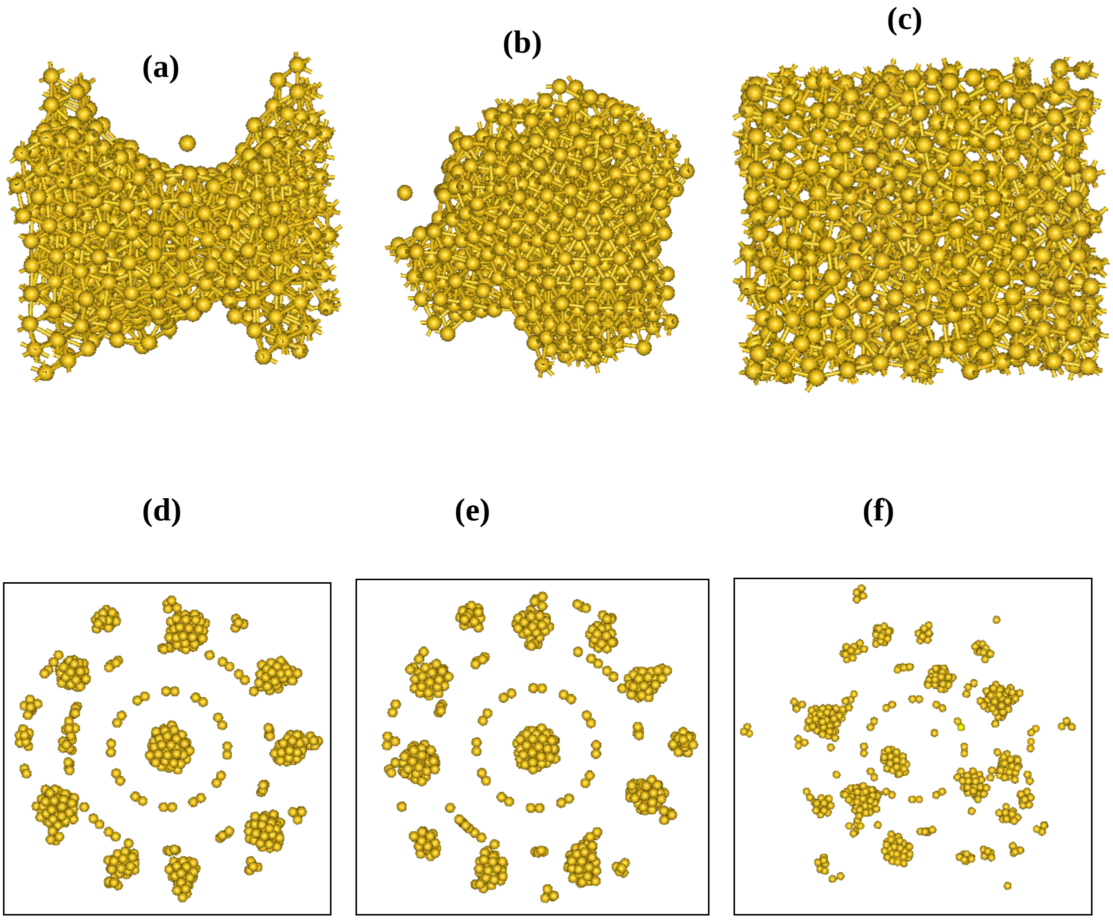

Figure 3.62. Different temperature configurations are shown. The top three structures represent the NVT ensemble. The bottom configurations are the structures in the NPT ensemble. (a) and (d) show the NVT and NPT structures respectively at 300 K, (b) and (e) show the 500 K and (c) and (f) are the 1000 K configurations.

3.1.2.2.3. Au Four Wall (6, 3) Nanotube

The structure of the Au four wall nanotube is characterized by four rings forming circles that will eventually form one structure. The number of atoms in the chosen nanotube is of 1523 atoms. The increased number of atoms in a system should increase the number of peaks in the plot for the radial distribution functions and therefore the possibility of finding an atom or a group of atoms within a particular distance range. On comparing the structures of various nanotubes, we realise that as the size, in terms of the number of atoms and walls, increases the behaviour towards that of the bulk.

The radial distribution functions of the nanotube with four walls are depicted in Figure 3.63. The plot for the NVT conditions start at 800 K due to some technicalities experienced in the calculations. The structure of the nanotube shows strong solid features at 800 K with many unstable peaks depicted. The melted structure occurs at 900 K and that continues at 1000 K. The NPT conditions on the other hand show a stable structure at 300 K which resembles that of the bulk gold. The well ordered peaks follow a particular order where the first and maximum peak is located at g(r) ≈ 7.0 and r ≈ 3.0 Å. Melting occurs at 1000 K. Although the structure is much crystalline at 300 K in the NPT conditions, onset of instabilities is already noticed.

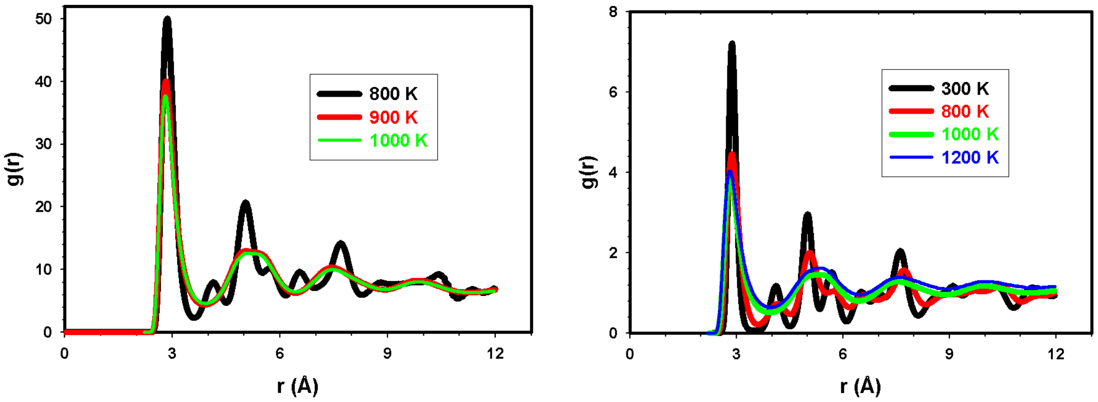

Figure 3.63. The structural evolution of the nanotube with temperature is depicted. The constant pressure simulations are performed at 0.0 kbar. The NVT conditions are shown on the left and the NPT on the right.

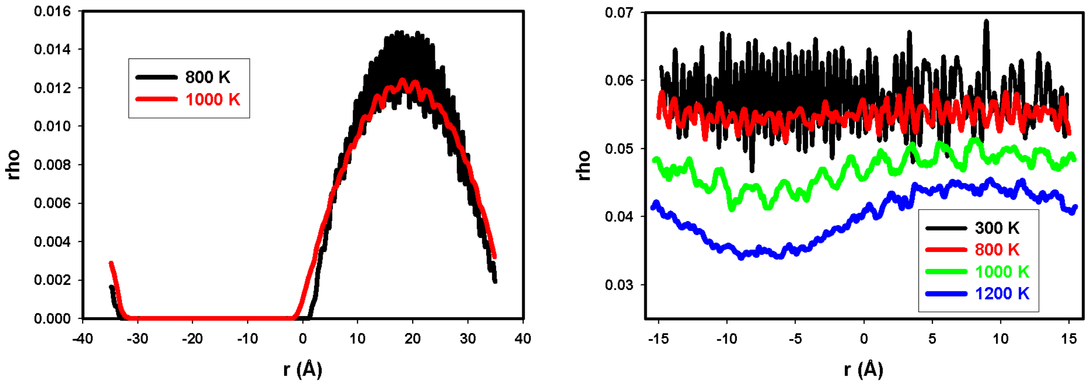

Figure 3.64. We are able to show two temperatures on the left figure in the NVT conditions as explained earlier. More details can be observed in the NPT ensemble.

The density profiles under the two conditions are shown by Figure 3.64. The NVT conditions show less structure but a dense system is seen at 800 K through a congested peaks at 5.0 Å ≤ r ≤ 35.0 Å. The denseness in the system fades at 1000 K where a smooth graph is depicted. The NPT conditions show a good representation of the crystal structure at 300 K with uncountable number peaks going over a large distance range. However, the number of peaks as well as the peak heights drops at 800 K. The density profiles at 1000 K show a change in the pattern where a curvature filled with peaks is noted. The 1000 K and 1200 K graphs are further down from the rest implying strong liquid features. The density profiles validate the results from the radial distribution functions.

We further observe changes in the nanostructure at various temperatures. Figure 3.65 show the starting configurations for the nanotube with four walls and 1523 atoms. Each wall contributes a certain number of atoms towards the total number. The bond distances are the same in the four walls and are equal to 2.84 Å. The spacing of the walls are different. The outer wall is ≈ 7.84 Å from the third one, the third one ≈ 6.99 Å from the second and the second wall is ≈ 7.61 Å from the inner wall. The four-wall nanotube is essentially the continuation of a three-wall nanotube by simply adding another wall, just like the three-wall being the continuation from a double-wall nanotube.

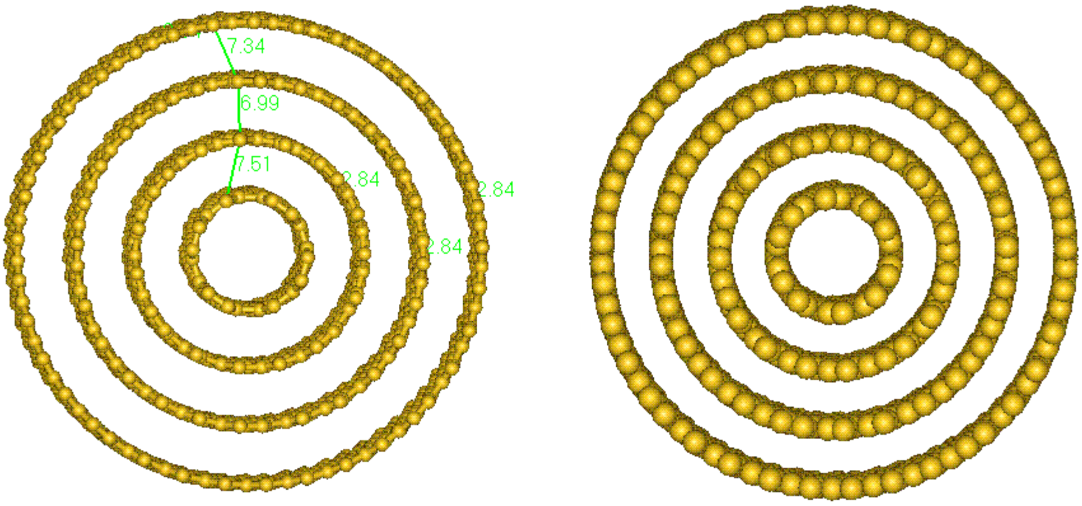

Figure 3.65 shows the starting configuration of the Au four wall nanotube. The bond distance is 2.84 Å. The separation between the walls is about 3.347 Å.

In Figure 3.66 we show how the structure of the nanotube evolves with temperature in the NVT and NPT Berendsen ensembles. Under the NVT, the nanotube collapses into a spherical cluster at 500 K which has varying bond distances, and atoms are attached to each other. The structure at 1000 K also shows a spherical cluster but some atoms are detached from the larger structure. The NPT conditions reflect a compact face centred cubic (fcc) structure at 500 K. The fcc structure is further attained at 1000 K though the atoms are not as closely packed as in the case of 500 K.

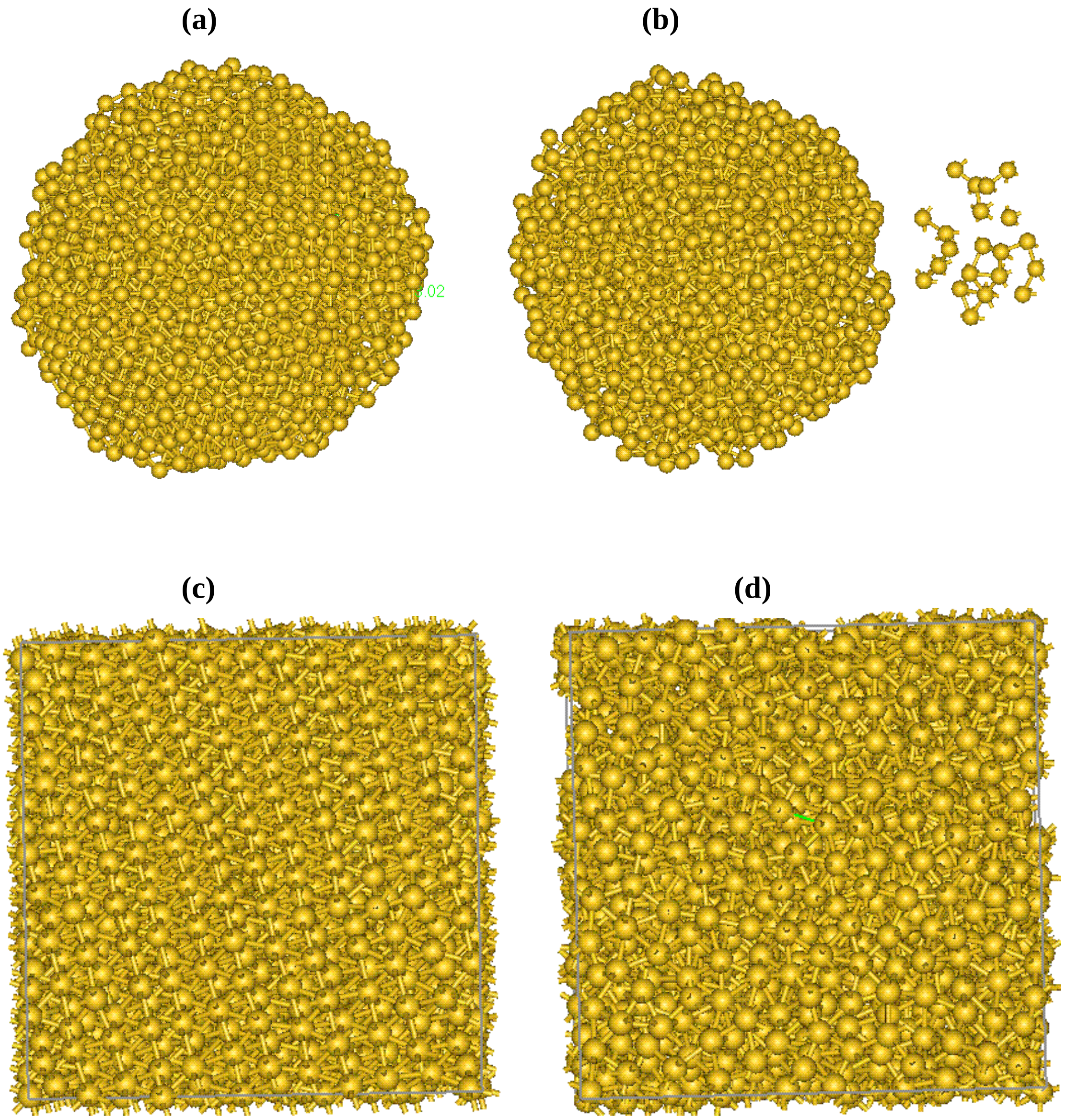

Figure 3.66. The structural evolution of the four wall nanotube is shown. The NVT conditions are represented by a) 500 K and b) 1000 K while c) 500 K and d) 1000 K show the NPT conditions.

3.1.2.3. Diffusion Coefficients

It is expected that heavier molecules should diffuse slower in a system. Heat is needed to increase the rate of diffusion by providing the energy needed to break and form new bonds. The diffusion coefficients of different gold nanotubes under the constant pressure conditions are shown in Figure 3.67.

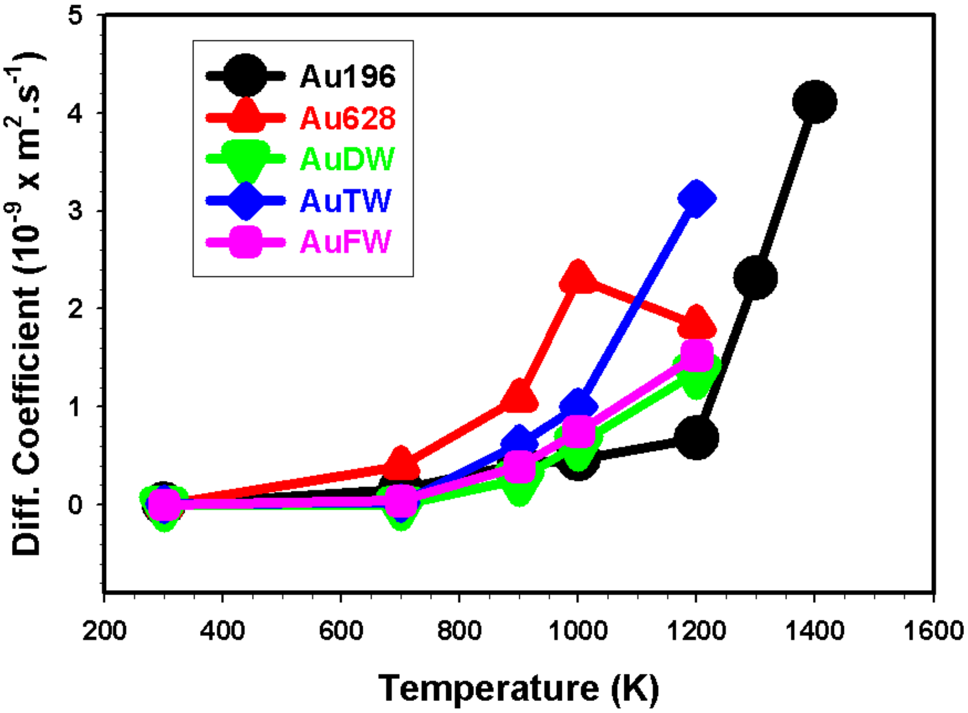

Figure 3.67. The diffusion coefficients of different nanotubes are shown in the NPT conditions. The double-wall nanotube consists of 480 atoms, the three-wall nanotube 541 atoms and the four-walled nanotube has 1523 atoms.

The single-wall nanotube with 628 atoms shows higher values of diffusion at respective temperatures with the value of more than 1.0 x 10^{-9} $m^2.s^{-1}$ obtained at 900 K. The multi-walled nanotubes show zero diffusion at least until 700 K and start to show appreciable values at 1000 K. The three-wall nanotube, with 541 atoms, shows higher values of diffusion coefficient compared to the Au double-wall and four-wall nanotubes. The four-wall nanotube at higher temperatures reflects slightly higher diffusion coefficients to the double-wall nanotube. However, the single-wall nanotube with 196 atoms depicts very low diffusion remaining below 1.0 x 10^{-9} $m^2.s^{-1}$ at temperatures as high as 1200 K. The diffusion in this nanotube only exceeds 2.3 at 1300 K and then increases to 4.1 x 10^{-9} $m^2.s^{-1}$ at 1400 K.

3.1.2.4. The Heat Capacity

The heat capacity of a material depends on the enthalpy and therefore the total energy of the system plays a crucial role in determining this property. The good linear behaviour of the energy will determine the good values for the heat capacity as was shown with the bulk and clusters. The total energy in the nanotubes does not depict neat (in terms linearity) behaviour with temperature and therefore do not provide a good slope of the plots.

Table 3.2 shows the heat capacities (C_p and C_v) in the two ensembles used for the calculations on different gold nanotubes.

Nanotube Size and Type	C_p	C_v
196 (Single-Wall)	4.65	2.33
628 (Single-Wall)	2.33	5.82
480 (Double-Wall)	4.65	3.49
541 (Three-Wall)	6.98	4.65
1252 (Single-Wall)	6.98	3.49
1523 (Four-Wall)	2.33	4.65

Table 3.2 shows values for the heat capacity under constant pressure and volume conditions for different nanotubes. The change in the heat capacity does not reflect any trend in both ensembles, whereas some values are below the bulk value of 3.37 and others are well above that. The NVT conditions give consistent values of C_v if we consider the same types of structures. As an example, the double-wall nanotube has the smallest value of 3.49 as compared to the three-wall and four-wall nanotubes which have the same C_v of 4.65.

The fluctuations of the heat capacity can be best shown graphically in Figure 3.68. The black triangles represent the values of C_v and the red circles show those for C_p.

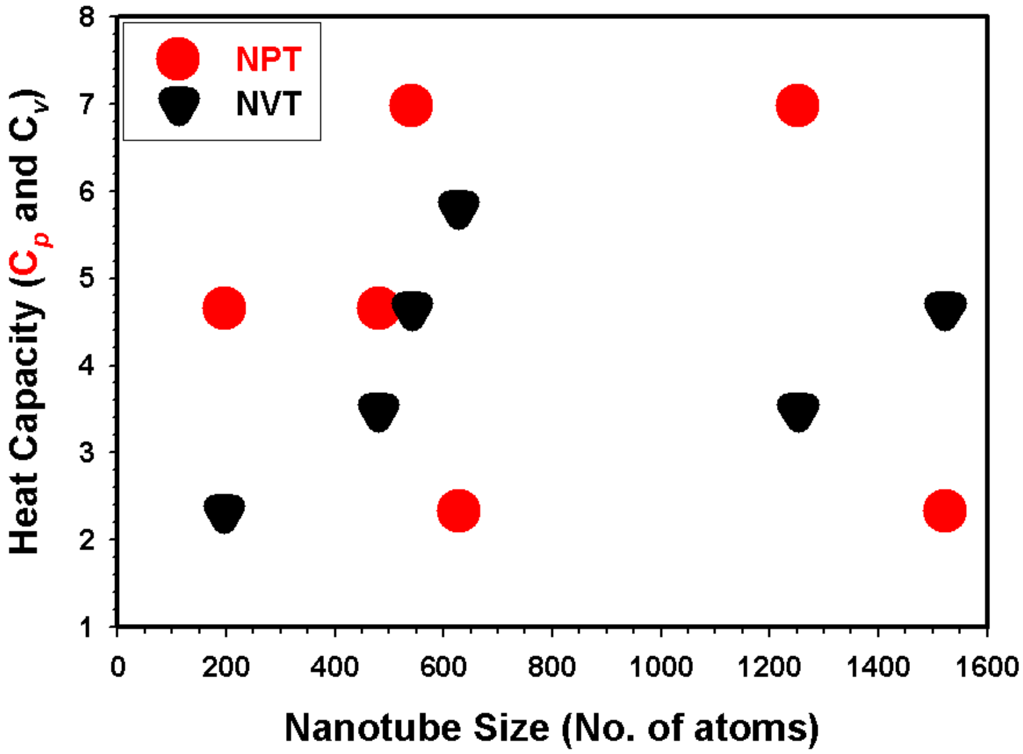

Figure 3.68 shows the heat capacities for the gold nanotubes in the constant volume (NVT) and pressure (NPT) conditions. The values here are the same as those in Table 3.2 above. The heat is multiplied the Boltzmann's constant (k_B) to make it dimensionless.

The two conditions show fluctuating values with increasing number of atoms of the nanotubes. However, the values in the NVT ensemble fluctuate from just above 2.0 to slightly below 6.0 while those in the in the NPT ensemble shows large differences with the values commencing from 2.0 and ending with 7.0. The same fluctuations were however also found in the nanoclusters and indeed some clusters depicted values above those of the bulk. It is good to compare the values of the heat capacities among the same kind of nanotube rather than the bulk. The values show that nanotubes are very instable materials. And because they loose their structures at every low temperatures, it is not a surprise to get high values of the heat capacities, especially in the NPT ensemble.

3.1.3. The Annealing Process

Annealing occurs by the diffusion of atoms within a solid material, so that the material progresses towards its equilibrium state. The movement of atoms has the effect of redistributing and destroying the dislocations in metals and (to a lesser extent) ceramics. This alteration in dislocations allows metals to deform more easily, so increases their ductility. The annealing process reduces the amount of process-initiating Gibbs free energy in a deformed metal and this (reduction of Gibbs free energy) in turn causes “stress-relief”. The relief of internal stress is a thermodynamically spontaneous process at higher temperatures.

Annealing is simply a method used to toughen materials and is important in preventing the creation of defects (like vacancies and misplacements) in the atomic scale. The process is carried-out by heating the material to some temperature, a melting temperature in this work which is 1000 K, and then slowly cooling the structure down to the most possible lower temperature. The configurations are always taken from the previous temperature; i.e., we perform a simulation at a temperature of 900 K and the final configurations are taken to perform a simulation at 850 K and the trend continues in that manner. The annealing process was carried out in the NPT Berendsen ensemble for the Au_{309} clusters and in the NVT Berendsen ensemble for the Au1252 nanotube.

We will discuss this process through the illustration of the total energy when the temperature is raised, and when the temperature is slowly reduced. The radial distribution functions and the density profiles will be used to show the evolution of the structure from one phase to the other. The atomic structures will be shown at different temperature from the starting configurations to the final image. We will measure a few bond distances and with the help of the volume change will determine whether the reduction of the applied heat can relieve stress from the structures. Using the results from the above-mentioned calculated parameters we hope to address the questions of whether annealing really makes the structure stable and if it is possible to move from a liquid phase and then slowly back to the solid phase and if the initial structures before any temperatures could be applied can be restored.

3.1.3.1. The Energy

The structure with the lowest total energy at respective temperatures is regarded as the most stable. The total energy under both methods (straight calculations where we start from 0 K and annealing) is therefore plotted at various temperatures.

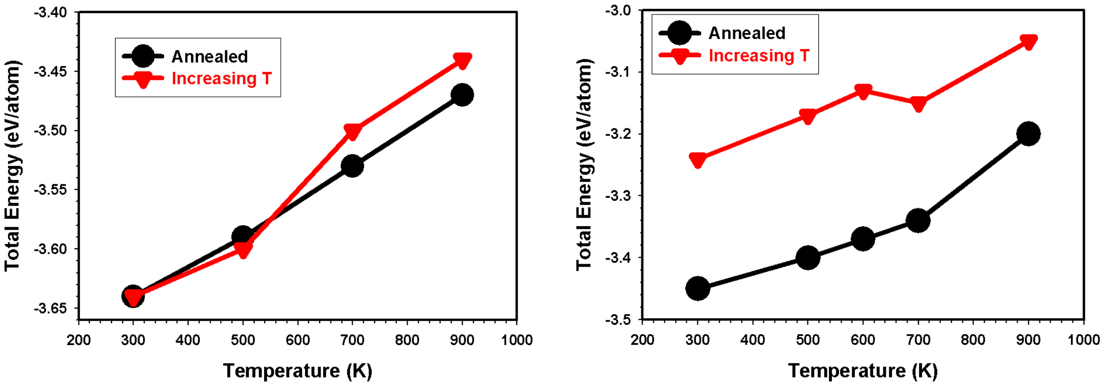

Figure 3.69. The total energy is shown in for the Au_{309} cluster in the NPT Berendsen ensemble on the left and in the Au1252 nanotube in the NVT Berendsen ensemble on the right.

The total energy for the Au_{309} cluster does not show major differences between the two methods. The annealed structure however, shows lower energies at higher temperatures before the structures start to show the same values at a lower temperature. The energy, in the case of the increasing temperature is lower at 500 K, a good indication that the cluster is stable at lower temperatures. The small difference in the energy in the cluster between the two methods tells us that the cluster retains its cluster structure even at higher temperatures. The nanotube shows significant differences between the annealed structure and the heated one. The annealed structure clearly depicts lower energies at all temperatures. The big difference in the energy in the nanotube clearly shows the change in the structure at higher temperatures as we have shown in the previous section on nanotubes. The higher energies depict the unstable nanotube while the lower energies show the stable cluster (the nanotube deforms into clusters at elevated temperatures). The two graphs in Figure 3.69 illustrate the fact that annealing structures to lower temperatures make them more stable.

3.1.3.2. The radial distribution functions (rdfs)

The rdfs for the Au_{309} cluster and Au1252 nanotube are shown by Figure 3.70. The starting point is a high temperature point where the structures are molten. The rdfs for the Au_{309} cluster on the left show two or three well ordered peaks at 1000 K which are rapidly increased at 500 K and many more peaks are attained at 50 K. The rdfs for the Au1252 nantoube on the right show a liquid structure at 950 K and the solid structure is visible at 0 K. The annealing method allows the transformation of the structure from liquid to solid and hence stable structures are also obtained. The annealing process does not restore the initial or same crystal structures but rather more stable solid structures.

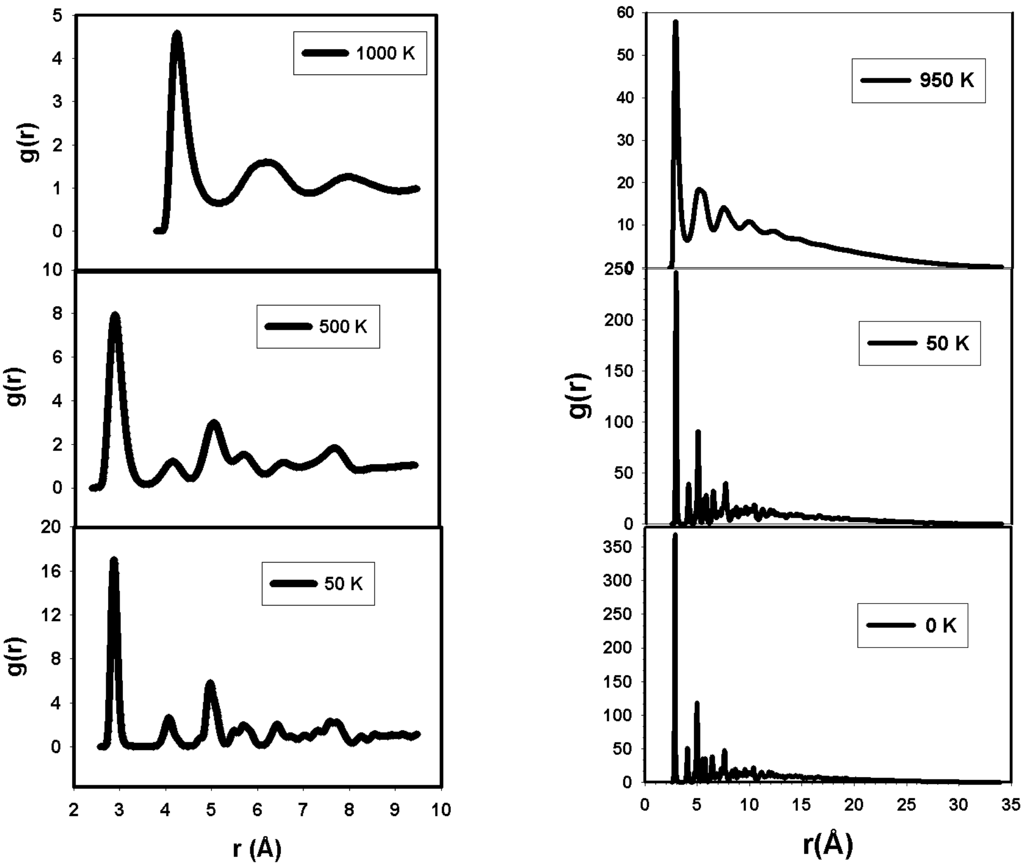

Figure 3.70. The radial distribution functions are shown starting from a high temperature of 1000 K or 950 K and then slowly getting lower temperatures, 50 K or 0 K. The left plot shows the Au_{309} cluster and the right represent the Au1252 nantoube.

3.1.3.3. The Density Profiles

The density profiles, like the radial distribution functions, increase the number of peaks when in a solid phase. The density profiles for the Au_{309} cluster and the Au1252 nanotube are illustrated by Figure 3.71. The plots for the density profiles for the Au_{309} cluster are on the left in Figure 3.71 where few peaks depicting some good separations between them are shown at 950 K. The number of peaks increases at 500 K and numerous peaks are attained at 50 K. The density profiles for the Au1252 nanotube are shown on the right of the figure. The nanotube only shows one peak. The peak is very smooth at 900 K. The noise starts to show at 500 K and some more is generated at 50 K. The density profiles agree with the results from the radial distribution in that starting from few peaks at elevated temperatures we are able to generate more peaks at lower temperatures signifying solid structures.

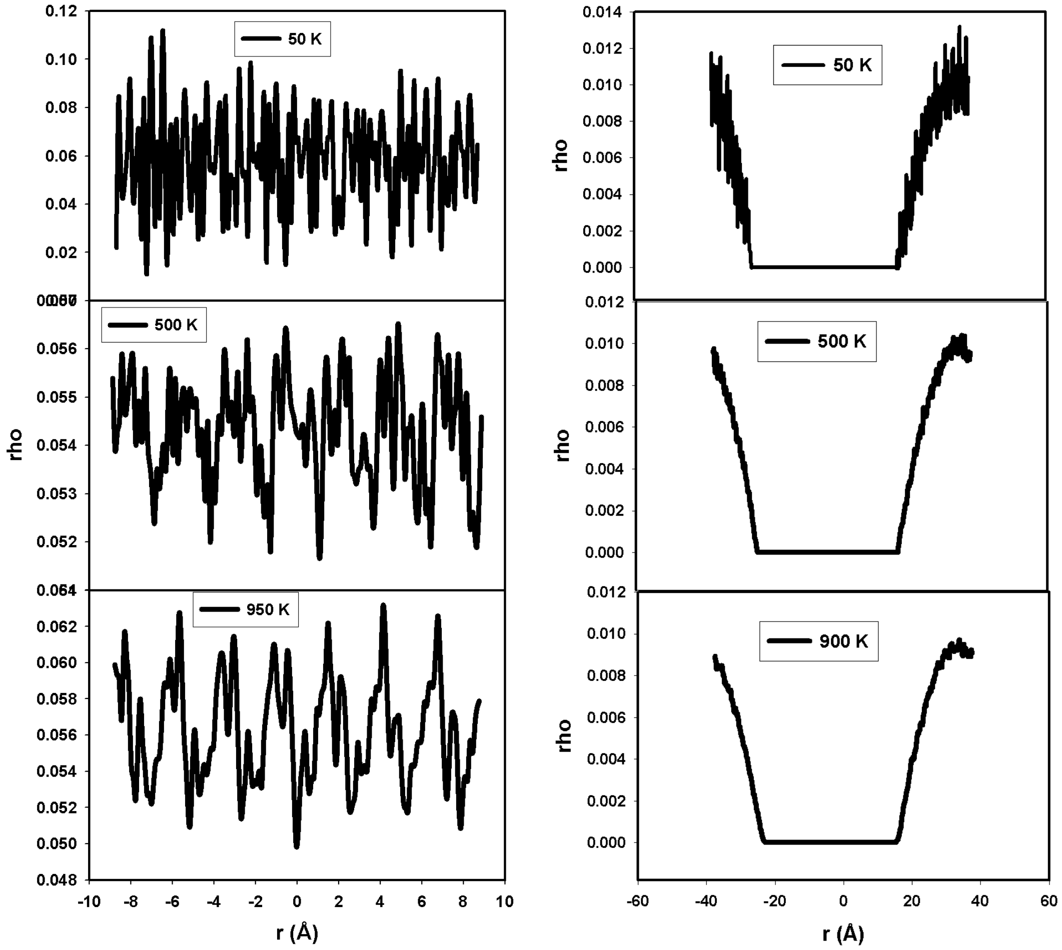

Figure 3.71 shows the density profiles for the Au_{309} cluster on the left and Au1252 nanotube on the right.

3.1.3.4. The Structural Configurations

We show the configuration at different stages to check if initial structures can be restored through the annealing method. Figure 3.72 shows the structure at high temperatures on the left (a and c) and the annealed structures are on the right (b and d) in the figure. The three cluster merge to form one shape in case of the nanotube while the more compact structure in the cluster is formed but the shape does not change.

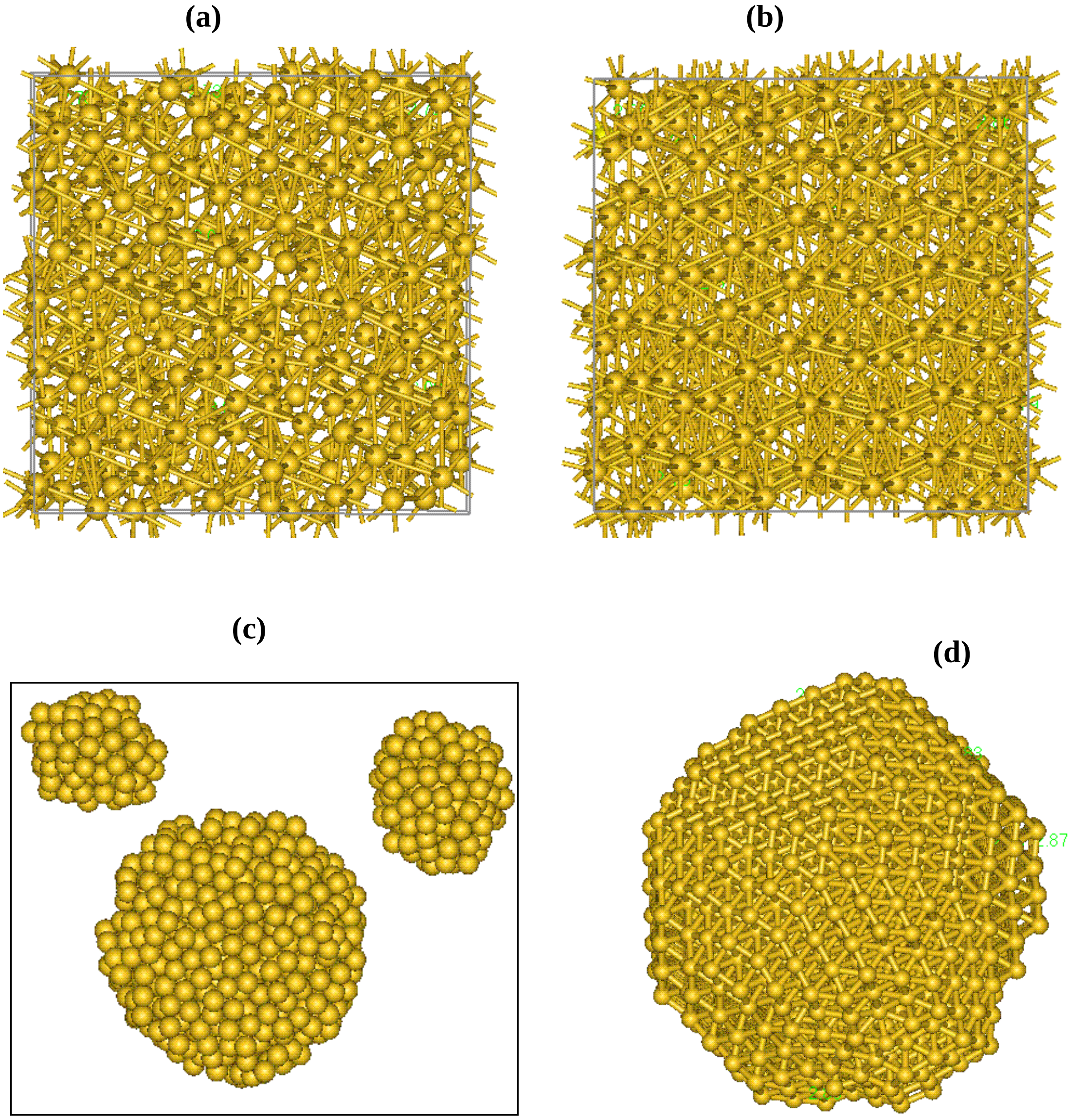

Figure 3.72. The structures of the Au_{309} cluster and the Au1252 nanotube are shown at different stages of the calculations. (a) and (c) show the melted structures of the cluster and nanotube (the starting configuration in the annealing process) respectively while (b) and (d) show the configuration at 50 K.

We would like to further show or compare with the results from the bulk material. In Figure 3.73 we show the total energy of the bulk with one case starting from low temperatures and the other plot shows the energy starting from high values and then decreasing gradually. There is some discrepancies in the two plots where the decreasing temperature shows high energies which reduce towards those of the increasing temperature. The two plots highlight the difference in the values of the energy in the solid and liquid phases.

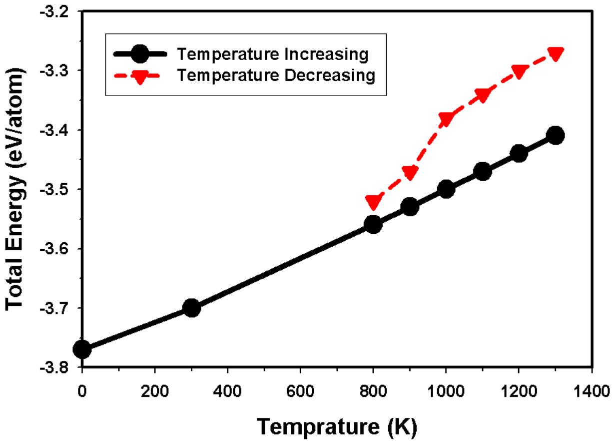

Figure 3.73 illustrates the difference in the behaviour of the total energy of the fcc bulk lattice with 500 atoms in the NPT Berendsen ensemble.

The configurations in Figure 4.74 show the well ordered pattern of atoms in the starting structure on the left and then the atoms are highly disordered after melting. Furthermore, in the bulk, the bond lengths show increasing trends although there are certain sporadic decreases. Some holes can be seen in the melted structure.

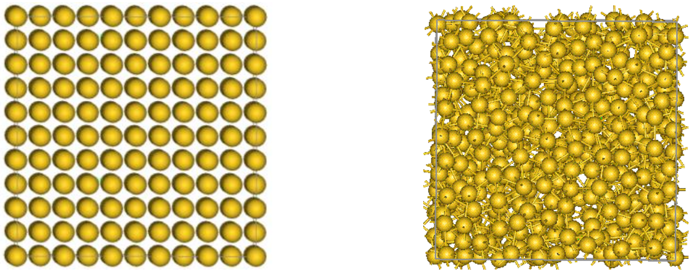

Figure 3.74. The initial and high temperature (after melting) configurations are depicted for the bulk gold 500 atoms.

3.1.4. Model Nanowires

A nanowire is a connection of atoms to form a continuous straight line as opposed to the nanotubes where there is no hole and there are no hexagonal shapes. A nanowire is shown in different orientations in Figure 3.75. The wire forms a stacking pattern of atoms with some steps meaning that it is not a uniform continuous arrangement of atoms.

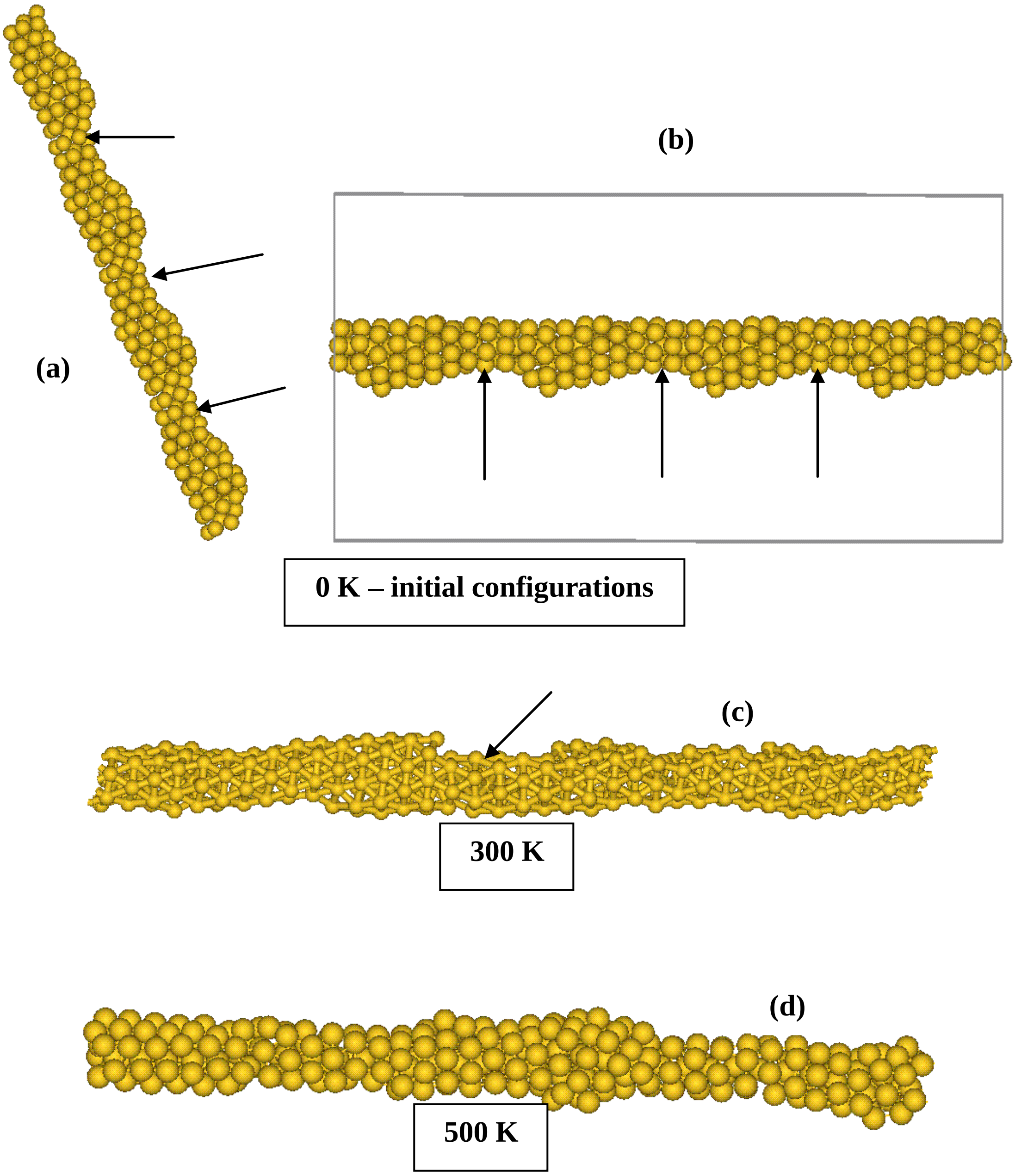

Figure 3.75. We show the structures of the nanowire with 288 atoms at different temperatures in the NVT Berendsen ensemble.

We have used the NVT Berendsen ensemble with the temperature controlled by the thermostat at 0.04 ps and the calculations were run for 6 x 10^4 MD steps. The simulated structures of the nanowire at higher temperatures are depicted in Figure 3.75(c and d). The atomic movements were given freedom in the z-direction. The dimensions of the wire are as follows: x = 46.2968 Å, y = 46.2912 Å and z = 89.5416 Å while the angles are: $\alpha = 90.0635^0$, $\beta = 89.7416^0$ and $\gamma = 89.7269^0$. Although we could only manage a temperature raise to 500 K, we are able to see significant changes in the structure. The pointing arrows in Figure 3.75(a and b) show the steps in the nanowire resulting in the hills being formed. The temperature simulated structures show the atoms to move from areas of high concentration (the hills) to the valley sites. Figure 3.75(c) depicts only one small kink or step site at 300 K as pointed by the arrow. The kinks disappear at 500 K (Fig. 3.75d) with high concentration of atoms in the centre of the wire.

The radial distribution functions as well as the density profiles for the nanowire are shown in Figure 3.76. The rdfs depict the wire structure that is already approaching melting at 300 K. A decrease in the peak height is depicted by the 500 K plot showing amorphous state of the wire. The density profiles plot shows many peaks with some low concentrations in certain areas. The denseness in the structure decreases at 500 K as compared to that at 300 K. The middle peaks in the density profiles are very dense with virtually no spacing between them and, separations are noted between the ones on the extreme left and right.

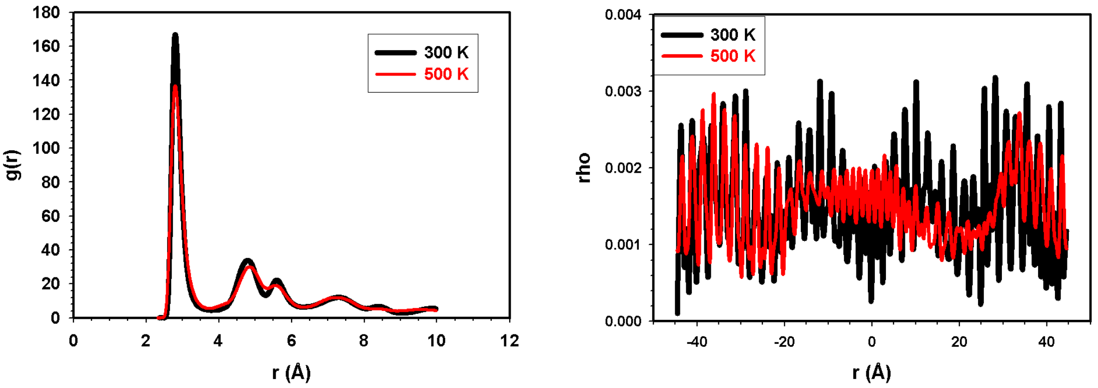

Figure 3.76 illustrates the radial distribution functions (rdfs) as well as the density profiles for the Au288 nanowires in the constant volume and temperature conditions.

CHAPTER 4: Quantum Mechanical Results

4.1. Introduction

This section deals with the interaction of atoms at electronic level where the density functional theory (DFT) method was executed in the DMOL^3 code. Different clusters with the size ranging from 2 atoms up to 55 atoms will be discussed. We will look at the optimised structures of the clusters, their binding energies as well as the effect of the dopant atom (platinum, palladium, titanium and zinc) on the properties of different gold clusters. We will study the individual clusters separately and we shall refer to the structural changes with respect to the bond distances, the binding energies and effect of the number of atoms on different properties for our discussions.

4.1.1. The Density Functional Theory (DFT)

The density functional theory does the calculations at the electronic level without using any experimental data but only some constants such as the Planck's constant. The DFT method tries to find the solution to the Schördinger (or rather the Kohn-Sham) equation. This method is applicable to a wide range of materials including metallic, semiconducting and insulating materials and has a good balance between accuracy and computational efficiency and that make the density functional theory the dominant approach for electronic structure calculations of solids and surfaces. In the DFT, the total energy of a system such as a bulk solid or a surface depends only on the electron density of its ground state.

The understanding and quantitative prediction of the electronic structure takes a central and fundamental role in today's concept of materials science. We therefore look for the changes of the structure after optimisation in terms of the change in the bond distances and the total energy of the system thereof. The binding energy and the number of atoms also help in the description of the behaviour of the different gold clusters. The total and the binding energies tell us about the stability of the clusters as the size is increased. The stable atoms or nuclei have the highest binding energies. The density of states if calculated, tell if the clusters behave like metals, semiconductors, or insulators through the presence or absence of the energy gap. We have, starting from the face centred cubic (fcc) bulk lattice of gold with four atoms, built the spherical clusters using the Materials Studio interface. The number of atoms in each particular cluster is determined by the chosen radius. We have built non-periodic spherical models for the clusters as the DMOL^3 code allows to build such structures and gives the binding energy in its output file.

4.1.1.1. Smaller Non-spherical Gold Clusters

We have started our DFT calculations from a small structure; i.e., from a dimer (two atoms) to try and reproduce the Au-Au interatomic distance. The size of these structures goes from 2 atoms to 43 atoms. All the DMOL^3 clusters are non-periodic with different symmetry patterns.

4.1.1.1.1. The Au_2 cluster

This cluster is essentially made by joining two gold atoms with a string called a bond distance thereby forming a dimer. We show the configurations of the cluster at the start and after optimisation in Figure 4.1. The cluster has a D_{infh} symmetry with a centroid of 1.1834, 1.1837, 0.0001.

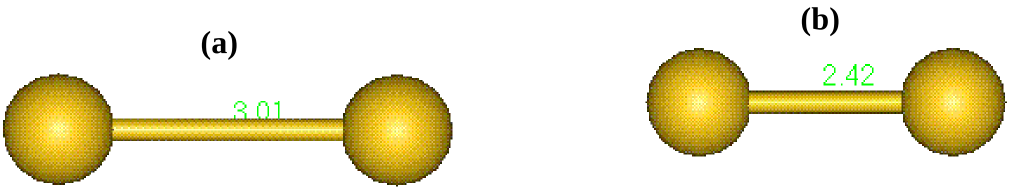

Figure 4.1 shows the structure of the Au_2 nanocluter with two atoms at the starting (on the left) and final (on the right) configurations. The interatomic distance in the starting structure is 3.01 Å which then reduces to 2.42 Å after optimisation.

The bond distance in the Au-Au dimer from our geometry optimization calculations is obtained to the value of 2.42 Å (Figure 4.1). It compares well with the experimental value of 2.47 Å [Simard and Hackett 1990; Huber and Herzberg 1979] which validates our approach we have chosen to study small clusters and this verifies the fact that we have the correct structure. Other density functional studies [Chen and Yang, Yuan *et al*. 2005, Sankaran and Viswatharan 2006, Joshi *et al*. 2006] have been performed on this cluster in trying to reproduce the experimental bond length and different values are reported.

The DMOL^3 work by Chen and Yan [Chen and Yang] reports a value of 2.49 Å while the Amsterdan density-functional calculations [Yuan *et al*. 2005], gives a value of 2.52 Å. The Au-Au bond length in the bulk is 2.89 Å. The optimized bond length found by [Joshi *et al*. 2006] as well as [Sankaran and Viswatharan 2006] in their density functional theory (DFT) Lee-Yan-Parr correlation function (B3LYP) in the Gaussian 03 program is 2.57 Å. The geometry of the cluster is not altered in any way through the optimization cycles, except for the bond length.

Different geometries of nanoclusters are illustrated in Table 4.1 with symmetry operations in brackets. The letter *n* in Au_n indicates the number of atoms in that nanocluster. The bond length of 2.42 Å from the dimer is further maintained in the clusters with three (Au_3) and four (Au_4) atoms and the change in the bond distance in the two clusters is uniform. The nanocluster with five atoms (Au_5) shows an increase in the bond length to the value of 2.49 Å. This value matches the experimental bond length in the dimer, but cannot be as such compared as there is a factor of the surrounding atoms as well as the size. A further slight increase to 2.50 Å is obtained with the Au_6 nanocluster. The increase in the bond length remains steady as the Au_8 cluster shows a value of 2.52 Å. The cluster with nine atoms (Au_9) has a bond length of 2.78 Å. The bulk bond length is matched by the cluster with fifteen atoms, having a value of 2.88 Å. We have plotted the bond length as a function of cluster size in Figure 4.2 in order to asses if this parameter changes linearly with the size of the clusters. The nanoclusters in consideration validate the fact that these small materials show some properties different to the bulk, with the bond length being an example in this case.

Table 4.1. Different gold nanoclusters are illustrated starting from a dimer. Symmetries are shown in brackets for each cluster and the subscript numbers indicate the size of the nanocluster in terms of the number of atoms.

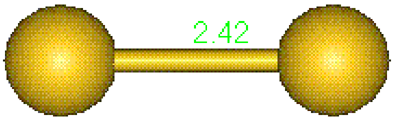 **Au$_2$ *(Dinfh)***	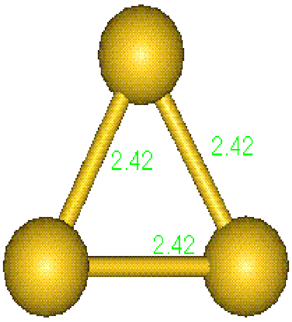 **Au$_3$ (*D3h -6 m 2*)**	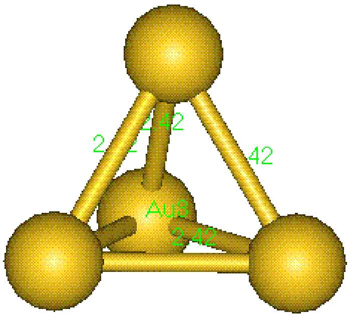 **Au$_4$ (*Td – 4 3 m*)**
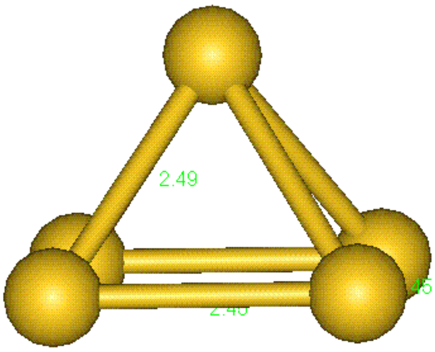 **Au$_5$ (*C2v 4 m m*)**	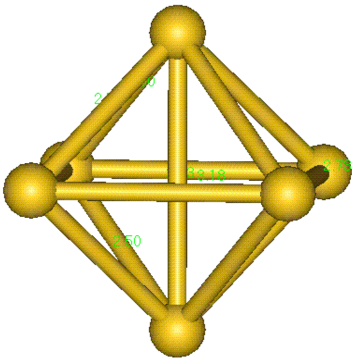 **Au$_6$ (*D4h 4/m m m)***	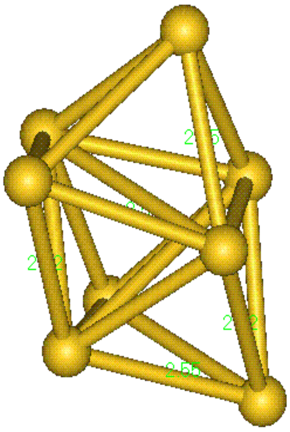 **Au$_8$ (*D2d -4 2 m)***
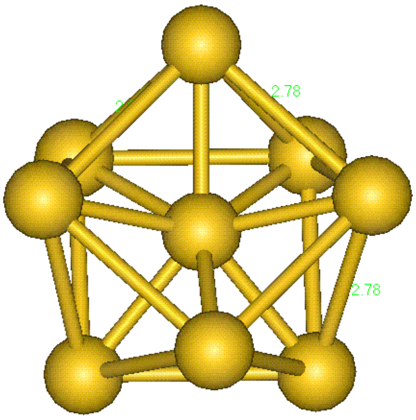 **Au$_9$ *(D4d)***	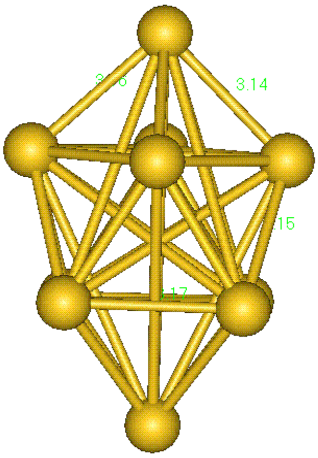 **Au$_{10}$ *(D4d)***	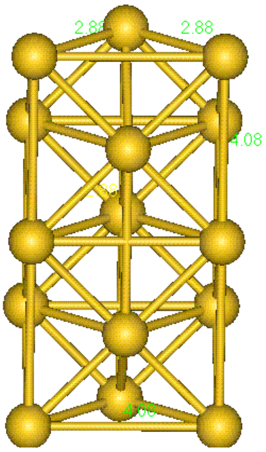 **Au$_{15}$ (*C2v m m 2)***

The average bond lengths, in Figure 4.2, as a function of cluster size show somewhat linear increase from the dimer to the cluster with eight atoms, i.e. from 2.42 Å to 2.52 Å. There is a significant increase in the parameter at nine atoms (Au_9) which is further enhanced at ten atoms (Au_{10}). The bond length reduces at the Au_{12} cluster causing some fluctuations from Au_9 to Au_{15} nanoclusters. Although the bulk bond length is matched for the cluster with fifteen atoms, it is obvious that the Au_{10} and Au_{12} nanoclusters show the bond distances that are well above the bulk. The increasing bond lengths in the clusters imply the reduction in the strength of interactions between atoms as the neighbours move slightly away from the central atom. As already indicated, the smaller distances were obtained for clusters consisting of two and four atoms.

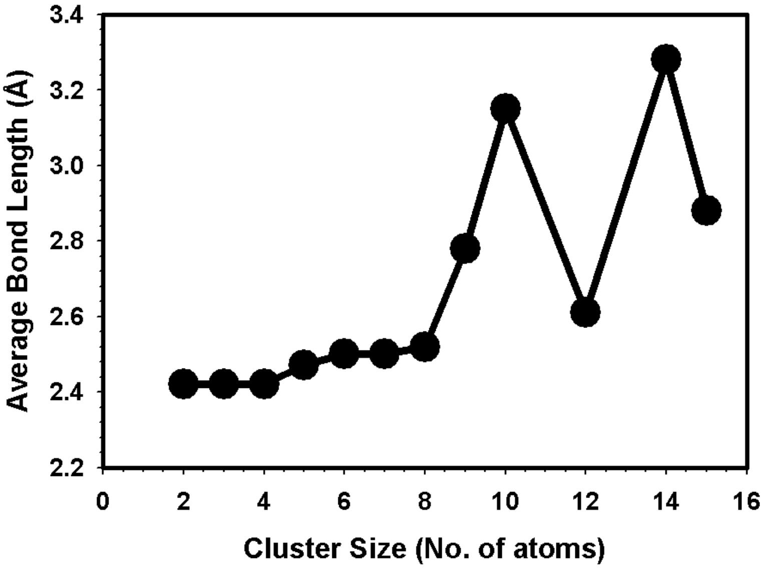

Figure 4.2 shows the average bond length in the gold nanoclusters up to the size of 15 atoms. The bond lengths are measured between atoms.

4.1.1.2. The Binding Energy of the Small Non-spherical Clusters

The binding energy is a useful property for determining the stability of materials especially nanomaterials. It is defined as the energy required to decompose a molecule, an atom, or a nucleus into its components or alternatively the energy required to separate a particle from a system of particles or to disperse all the particles of a system. The increasing binding energy usually signifies the increase in the stability of the particular material. The binding energy is calculated from the formula:

$$E_B = \frac{\left[E_T - nE_{atom}\right]}{n} \tag{4.1}$$

E_T is the total electronic energy of the cluster, E_{atom} the total electronic energy of a single gold atom and n is the number of atoms.

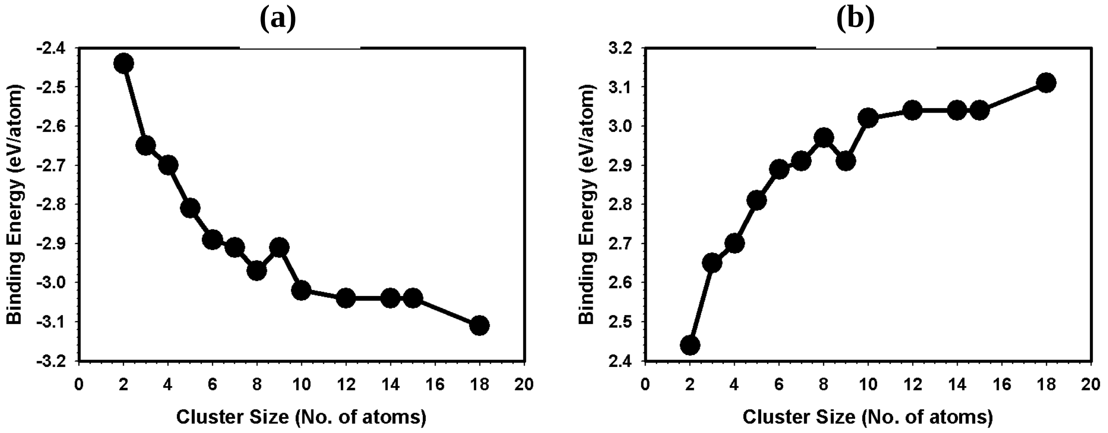

Figure 4.3. The binding energy (E_B) per atom is plotted with (a) the negative values and (b) the positive values. The size of the clusters starts from two (2) to eighteen (18) atoms.

The binding energy of the pure gold nanoclusters, in Figure 4.3(a) starts from a less negative value with the dimer and gradually continues to move towards more negative values until the cluster with 18 atoms. The plot in Figure 4.3(b) illustrates the increasing values more and clearly the difference between the clusters is not large. The binding energy increases with cluster size due to the increase in the average number of nearest neighbours per atom and this promotes greater average number of interactions per atoms. There is a change in the trend at the Au_9 nanocluster which might suggest the probability of an unstable structure. Although the binding energy increases with cluster size and the difference is significant between Au_2 and Au_{18} structures, the values are still far from bulk cohesive energy. The binding energies for the Au_2 and Au_{18} are -2.44 eV/atom and -3.11 eV/atom respectively while the bulk value is known to be -3.78 eV/atom. It should be mentioned that the binding energy does not necessarily indicate which cluster is the most stable; however, this is provided by the second energy difference. The second energy difference is calculated using the relation:

$$\Delta_2 E_B(n) = \left[E_B Au_{n-1} + E_B Au_{n+1} - 2E_B Au_n\right] \tag{4.1}$$

where E_B is the binding energy of the cluster and n the size of the cluster. $\Delta_2 E_B$ is plotted in Figure 4.4 for the structures of size n = 2 – 14. In cluster physics, the quantity $\Delta_2 E_B$ is very sensitive and can be used to represent the relative stability of a cluster with respect to its neighbours.

In fluctuations (Figure 4.4) on this parameter ($\Delta_2 E_B$) two different patterns are observed. For the smaller clusters (n = 2 - 5) we notice even-odd staggering pattern where the odd numbered structures show high peaks. The clusters with the size (n = 6 - 10) show the oscillations resulting in the high peaks given by the even numbered clusters. The high peaks are obtained for the Au_3 and Au_8 nanoclusters with Au_3 showing the highest peak at 0.16 eV/atom. We therefore find the Au_3 and Au_8 structures to be more stable with the Au_6 cluster also depicting some peak. The lowest peak is depicted by the Au_9 structure and to a lesser degree the Au_4 cluster. The plot of the binding energies has also shown the Au_9 cluster to be less stable in agreement with the $\Delta_2 E_B$.

Chen and Yan [Chen and Yan] show the even numbered cluster to be the most stable but they have also observed a staggering pattern for clusters which break in the middle and initiates again at a little bigger cluster. On the other hand, Zhao *et al.* [Zhao *et al.* 2001] show that for titanium clusters the odd numbered clusters are the stable ones. The self-consistent-field (SCF) electronic structure calculations [Jain 2005], in Q-Chem package, show high peaks for Au_8 and Au_{10} clusters. The odd-even oscillations are however not clearly defined. In good agreement with our work, Jain [2005] also found the Au_9 cluster to depict less stability.

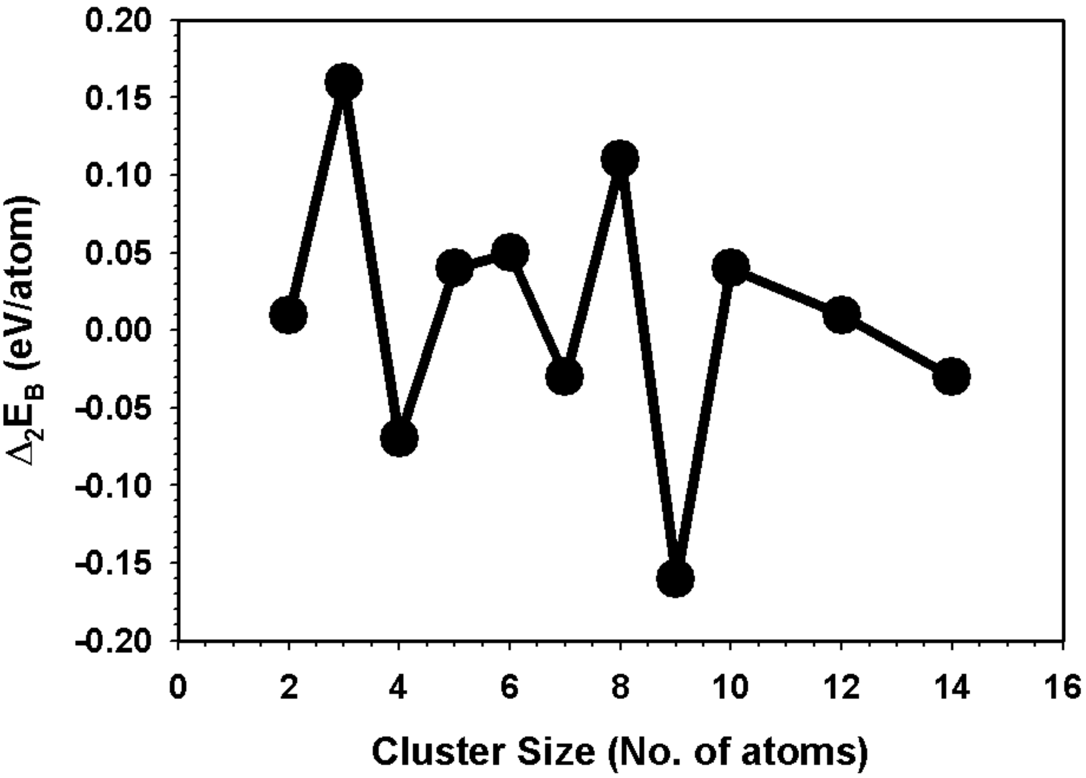

Figure 4.4. The second change in the binding energy differences are shown for the pure gold nanoclusters.

4.1.1.3. Doped Gold Clusters

Doping of gold clusters of various sizes can be expected to show different results from pure clusters with respect to geometry, stability, bond lengths, etc. Different dopants, depending on their electronic structure configurations, might show varying effects on different properties for gold clusters. We have doped different gold clusters with impurities, platinum (Pt), titanium (Ti), zinc (Zn) and palladium (Pd). The doping process is done by substituting one gold atom with one of the impurities for different sizes of the Au nanoclusters. In our results we will discuss the geometry, show the binding energies; and stability of clusters will be checked with the help of the second energy differences. The stability of a material plays an important role in the chemistry of that material since less stable materials with defined surfaces are the more reactive ones. The binding energy shows that the size of cluster increases its stability but that the atomic coordination is the last determining factor.

Table 4.2. We show selected Pt-, Ti-, Zn-, and Pd-doped gold clusters at different sizes. Some bond lengths are indicated with different colours showing different impurities.

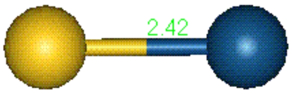 **Au_1+Pt_1**	 **Au_1+Ti_1**	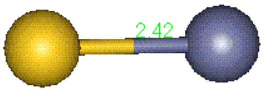 **Au_1+Zn_1**	 **Au_1+Pd_1**
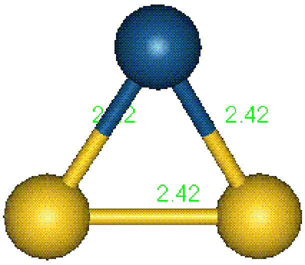 **Au_2+Pt_1**	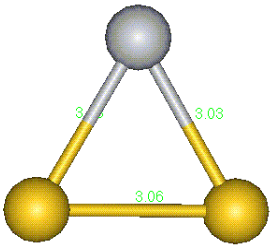 **Au_2+Ti_1**	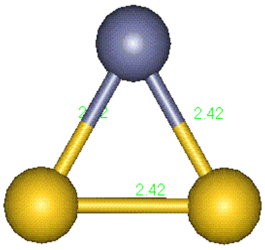 **Au_2+Zn_1**	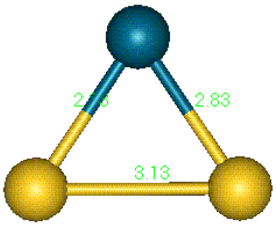 **Au_2+Pd_1**
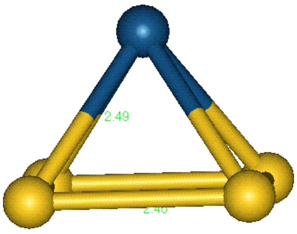 **Au_4+Pt_1**	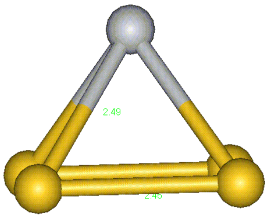 **Au_4+Ti_1**	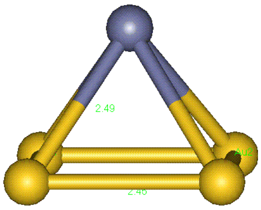 **Au_4+Zn_1**	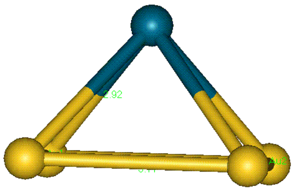 **Au_4+Pd_1**
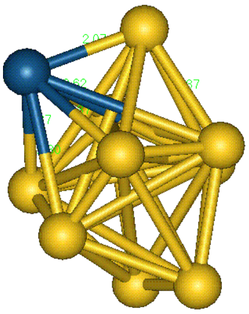 **Au_9+Pt_1**	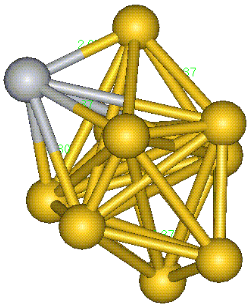 **Au_9+Ti_1**	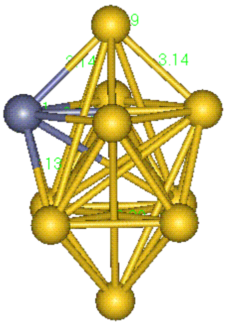 **Au_9+Zn_1**	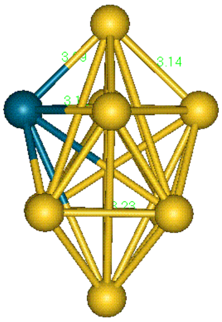 **Au_9+Pd_1**

Doped gold nanoclusters are illustrated in Table 4.2. The optimized bond length for the diatomic molecule where platinum, titanium and zinc are dopants is 2.42 Å. This value is the same as the one for Au-Au interatomic distance. The Pd-doped cluster does, however, show a different result, with a value of 2.97 Å. The results clearly indicate that palladium makes a longer bond with gold as compared to the pure cluster and other dopants such like Pt, Ti and Zn. The strongest bond in the investigated diatomic systems occurs in the Au-Ti structure and has a higher binding energy of -5.90 eV/atom. Au-Pt bond (-3.41 eV/atom) is the second on the list and the weakest bond is realised in the zinc doped nanocluster (-1.82 eV/atom). Changes are noticed at the cluster with three atoms where a uniform bond length of 2.42 Å is only retained in the Pt- and Zn-doped clusters. In the case of titanium a bond length of 3.03 Å is noted between gold and titanium while the Au-Au distance is 3.06 Å. The Pd-doped cluster with three atoms makes Au-Pd bond length of 2.83 Å while Au-Au distance is 3.13 Å. The bond length between the gold and the impurity atoms continues with the increasing trend with palladium leading the pack. We have to, however, allude to the fact that the geometry of the clusters thus far does not differ from that of the pure Au clusters, except for the bond lengths in certain instances.

There is no change in the structural configuration for the doped gold clusters when compared to the bulk up to the size of nine atoms. We observe different geometries with regard to the different dopants at the Au_{10} nanocluster. The structural configurations are illustrated in Figure 4.5. The pure Au_{10} cluster is shown for reference and initial structures have the same configuration. The optimized structures of the Pt-and Ti-doped nanocluster give different geometries. The initial configurations show the well ordered pattern where five atoms arrange themselves at the top and the other five do so at the bottom. There is one atom at the peak and one at the bottom and these atoms have four atoms next to them. Geometry optimization results for platinum and titanium impurities show random arrangement of atoms and no ordered atom arrangement at the top and bottom is noted as in the initial structures. For the Au_{10} nanocluster, Pt and Ti atoms show greater effects and our findings presumably suggest that the initial configurations are not their preferred geometry. Zn- and Pd-doped clusters show no differences from the Au pure cluster geometry and the bond lengths in all the structures including the Au_{10} nanocluster exceed 3.0 Å.

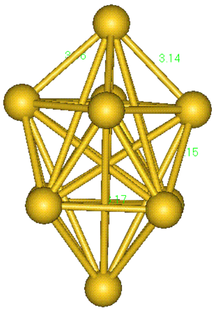

Au_{10}

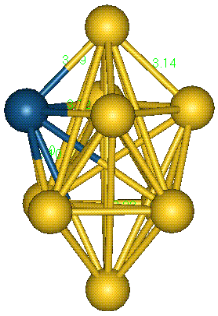

Au_9+Pt_1 Initial

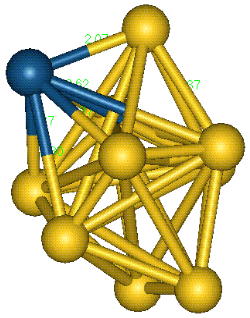

Au_9+Pt_1 Optimized

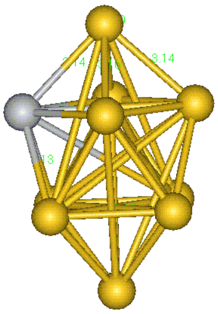

Au_9+Ti_1 initial

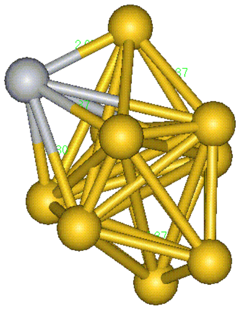

Au_9+Ti_1 Optimized

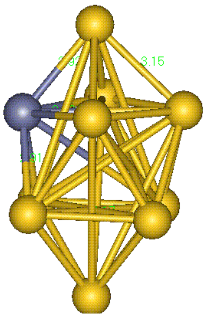

Au_9+Zn_1 initial

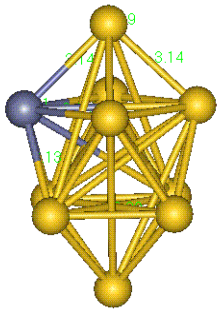

Au_9+Zn_1 Optimized

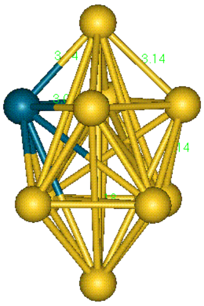

Au_9+Pd_1 initial

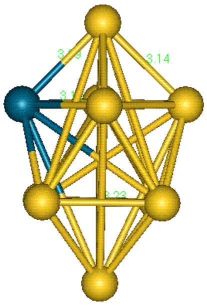

Au_9+Pd_1 Optimized

Figure 4.5 illustrates the doped gold cluster with ten atoms. The first structure at the top left is the pure Au10 cluster for comparison.

4.1.1.3.1. The Binding Energy of the Doped Clusters

The dopant atoms are expected, in one or the other, to show a change in the binding energy relative to the pure gold nanoclusters. Pure gold nanoclusters have shown their stability to increase with size where the binding energy became more negative as the number of atoms increased.

Figure 4.6 shows the binding energy of pure gold clusters as well as that of the doped clusters. The binding energies for platinum and titanium show the same pattern where they start from more negative values and steadily converge to -3.32 eV/atom for platinum and -3.68 eV/atom for titanium. We have already mentioned that the titanium dopant forms the strongest bond with gold at the diatomic level. Zinc-doped nanoclusters give the binding curve that depicts the same behaviour as that of pure Au clusters. Zinc-doped nanoclusters start from the less negative values of the binding energy and move to more negative values as in the pure Au nanoclusters. The numerical values of the binding energy for zinc dopant are close to those of pure gold clusters although slightly lower at smaller clusters from two until seven atoms. The values merge with those of pure Au clusters at 12 atoms. The palladium impurity has binding energies that are more negative with some fluctuations between six and ten atoms. The binding energies in the Ti-doped clusters remain higher throughout. The plots in Figure 4.6 show stable values of the binding energy between 12 and 18 atoms.

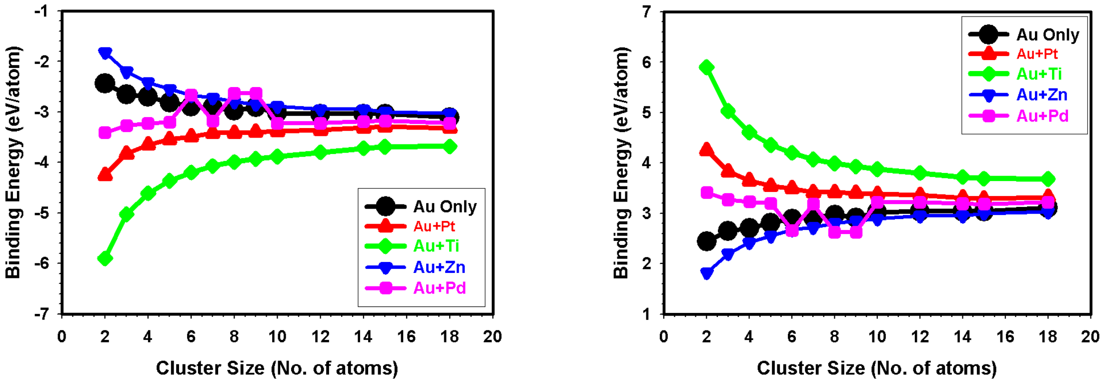

Figure 4.6 shows the binding energies of the pure god clusters compared to those of the doped clusters. Different colours show different impurities.

Figure 4.7 shows the second difference in the binding energy for the different impurities or dopants. Pure gold nanoclusters have shown even-odd alterations and we were able to determine the stable clusters and the Au_3 and Au_8 clusters are the most stable because we observed two patterns in the oscillations depending on the cluster sizes. The second change in the binding energy was calculated using the formula:

$$\Delta_2 E_B(n) = \left[E_B\left(Au_{n-1}X\right) + E_B\left(A_{n+1}X\right) - 2E_B\left(Au_n X\right)\right] \tag{4.3}$$

where E_B is the binding energy, n the number of atoms, and X is the impurity element and in this work it will be one of Pt, Ti, Zn or Pd.

The platinum-doped gold clusters are plotted in the upper curve of Figure 4.7. The change in the binding energy increases from n = 2 - 4, then shows an even-odd oscillations between the clusters with four and nine atoms. The odd numbered clusters show higher peaks with the Au_4Pt (n = 5) and Au_6Pt (n = 7) clusters indicating higher stabilities. The lower peak is depicted by the Au_5Pt (n = 6) cluster. The effect of a titanium impurity on gold clusters shows a smooth increasing trend from n = 2 - 5. The highest peak is obtained for Au_7Ti (n = 8) cluster implying that this is the stable structure of the Ti-doped Au clusters. The absence or the small visibility of the staggering pattern was also observed in the study of gold nanoclusters by [Jain 2005] and the results show the cluster with ten atoms to be the most stable with a high peak at ≈ 4 eV. $\Delta_2 E_B$ in the zinc-doped gold nanoclusters decreases in their values from 2 to 4 atoms but soon find the even-odd staggering pattern as in the Pt-doped clusters. The Au_4Zn (n = 5) cluster shows the highest peak at 0.07 eV/atom followed by the Au_6Zn (n = 7) cluster with a peak not as high as in Au_4Zn (0.3 eV/atom). In addition, as in the Pt-doped clusters, the cluster with lower stability is the Au_5Zn (n = 6) cluster. On the contrary, for the palladium (Pd)-doped Au clusters we find a decreasing $\Delta_2 E_B$ up to n = 5 while the highest peak occurs at Au_5Pd (n = 6). The Pt- and Zn-doped clusters show odd numbered clusters as stable structures and in the Ti- and Pd-doped clusters the even numbered clusters are the most stable. However, owing to good oscillations, we were able to get one or more stable structures for Pt and Zn-doped clusters.

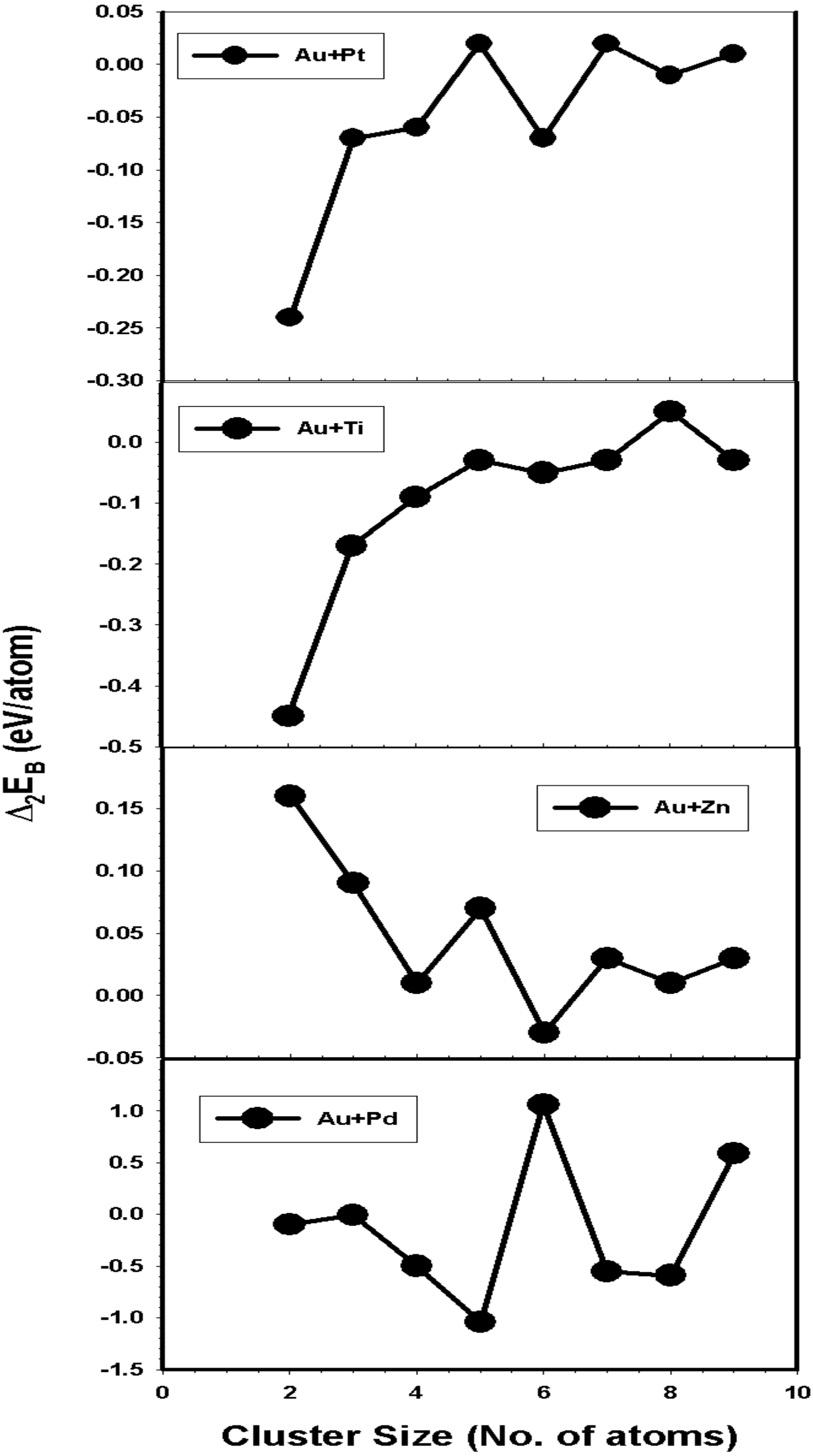

Figure 4.7 shows the second difference in the binding energy (Δ_2E_B) for various dopants in the gold clusters.

4.1.1.4. Magic Spherical Clusters

Gold nanoclusters that show some degree of stability are referred to as magic clusters. The known magic gold nanoclusters are the structures with 13, 19, 38, 55, 147 and 309 atoms [Cleveland *et al*. 1998; Fries *et al*. 2006]. There may be certain sizes of clusters that could fall in this category that we are not aware of. In view of computer power limitations we were only able to study up to the nanocluster with 55 atoms. We have studied the five different spherical nanoclusters, e.g. Au_{13}, Au_{19}, Au_{38}, Au_{43}, and Au_{55}. Structural changes of the clusters as the size is increased will be discussed, and the stability with respect to the binding energies for the pure and doped structures will be checked.

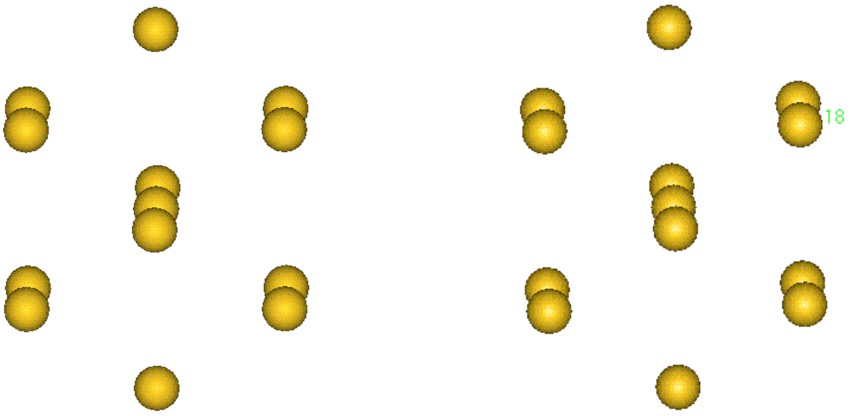

Au_{13} - Initial **Au_{13} - Optimized**

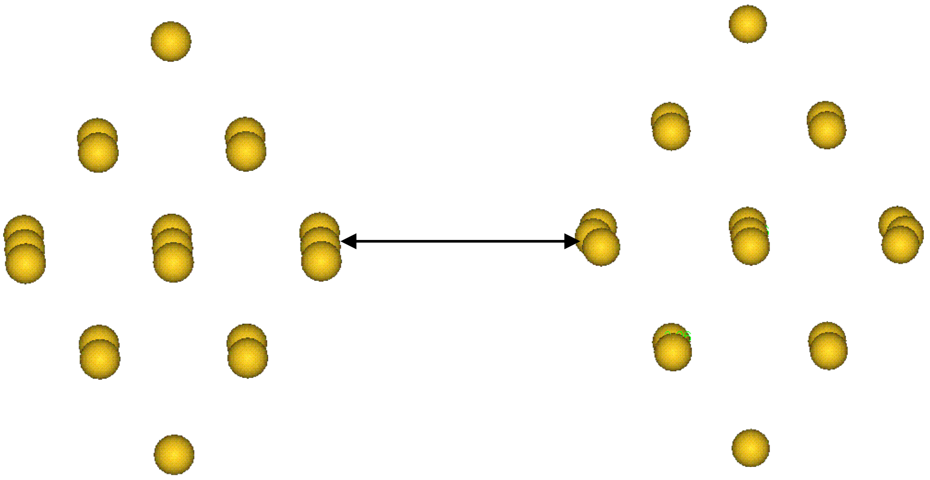

Au_{19} - Initial **Au_{19} - Optimized**

Figure 4.8. The Au_{13} and Au_{19} nanoclusters before and after optimization.

Figure 4.8 shows two nanoclusters of gold with less than 20 atoms. The Au_{13} structure is the smallest cluster studied in this type of nanoclusters and behaves differently to the other structures. The spherical nanoclusters fall under the same *Oh (m -3 m)* symmetry group and have the starting bond length as 2.88 Å. The Au_{13} nanocluster shows no change in the geometry after optimization. The difference is noted in bond lengths which attain a value of 3.18 Å on relaxation, an indication of the outer movement of the atoms. The three atoms in the centre maintain their straight line pattern achieving an angle of 180.0^0. However, the scenario changes when we look at the structure with 19 atoms in Figure 4.8. The initial configurations show a near spherical structure with four traceable corners. The optimized structure of the cluster depicts a change in the geometry with regard to the central atoms where three atoms are aligned on the left and right side of the cluster. The central pattern does not show any difference relative to the initial arrangement. The central atom in the outer atoms, bulge outwards, where three atoms form a line as illustrated by the two-way arrow. The angle changes from 180.0^0 to 175.3^0 making the bond lengths to increase from 2.88 Å to 3.13 Å. The change in the interatomic distances is not uniform. In the cases where there are two atoms in a line, the bond length change is from 2.88 Å to 3.26 Å.

The larger nanoclusters with 38, 43 and 55 atoms are shown Figure 4.9. There is generally more bulging in the movement of the atoms in all the structures. In the Au_{38} nanocluster, we observe four places (in top and bottom halves) where such change (bulging or slanting) in the atomic arrangement occurs. The Au-Au bond length changes to 3.20 Å in cases where bulging occurs and 3.21 Å where there is no bulging. The Au_{43} cluster reflects the same trend although the central atoms arranged in the quartet form show some outwards slanting. The angle changes from 180.0^0 to 174.3^0 with the changes in the Au-Au bond distance going from 2.88 Å to 3.16 Å and 3.31 Å. In the Au_{55} cluster, more bulging is noted owing to the increased number of atoms resulting in more triplets and quartets. We observe three lines with slanting of the middle atom and the bond length varies accordingly. The top and the bottom lines show a change in the bond length to 3.18 Å while the middle row slanting atom makes a distance of 3.23 Å. The bond distance changes to 3.22 Å and 3.25 Å at the quartets and 3.31 Å at the triples. The Au-Au-Au angle decreases to 176.1^0. The bulging of atoms eliminates corners, making the structures to be rounder.

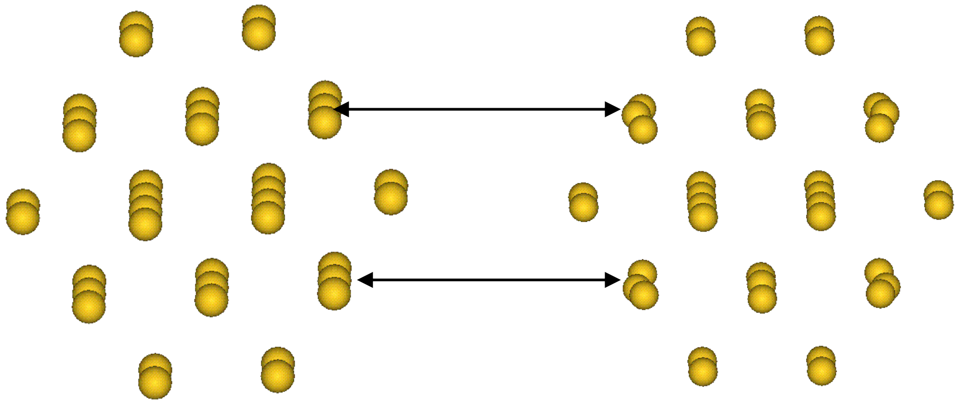

Au_{38} - Initial **Au_{38} - Optimized**

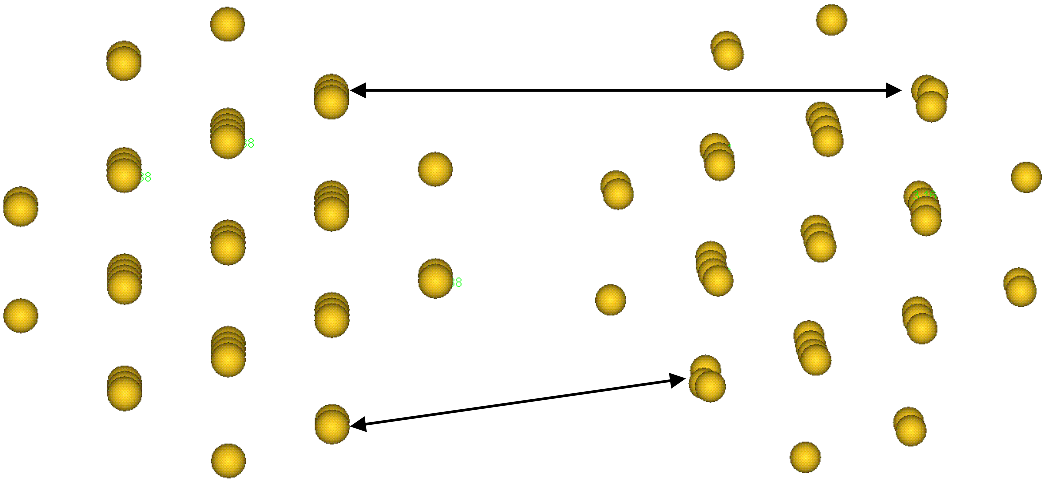

Au_{43} - Initial **Au_{43} - Optimized**

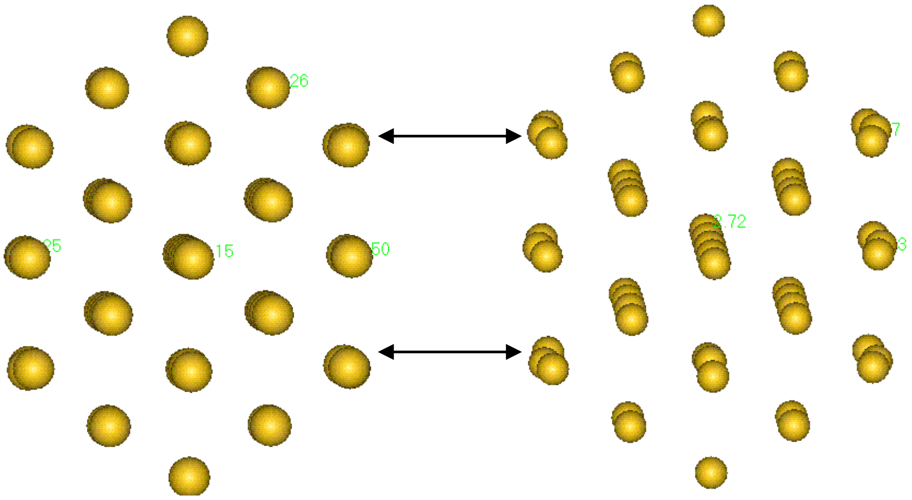

Au_{55} - Initial **Au_{55} - Optimized**

Figure 4.9. The initial and geometrically optimized structures of the Au_{38}, Au_{43} and Au_{55} clusters are shown.

4.1.1.4.1. The Binding Energy of the Spherical Clusters

The plot in Figure 4.10 shows the binding energy of the clusters becoming more negative with the increasing cluster size, although the Au_{43} cluster deviates slightly from the trend. The Au_{43} structure is perceived as less stable compared to the Au_{38} and Au_{55} clusters, a suggestion that it does may not belong to the magic clusters.

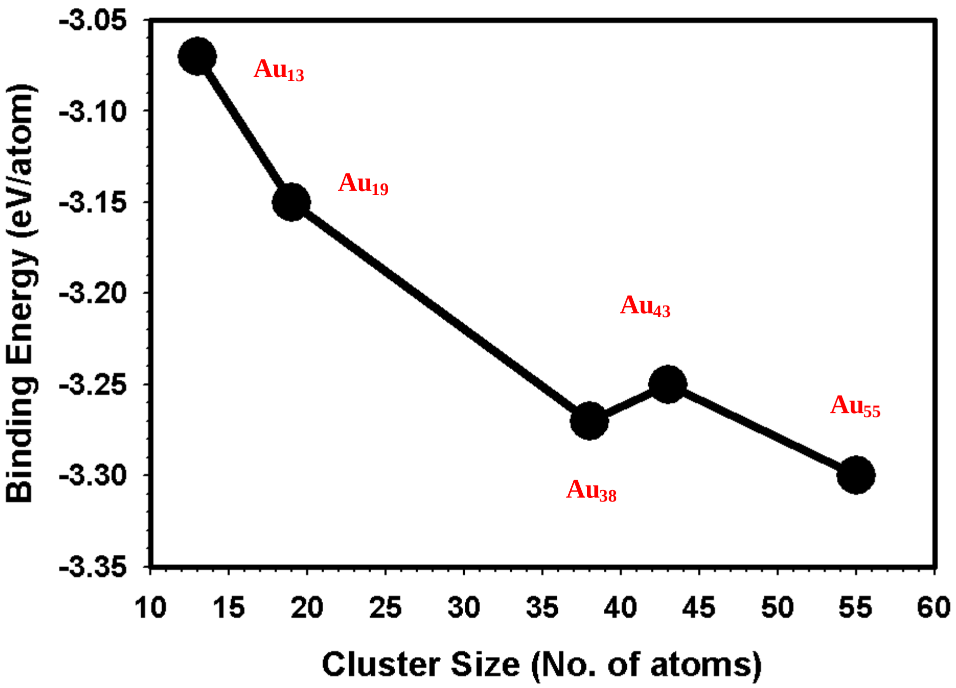

Figure 4.10. The binding energy is shown for the spherical clusters from 13 to 55 atoms.

4.1.2. The Interaction of a Gold Atom with the Graphite Surface

The conversion of a toxic carbon monoxide (CO) to the environmental friendly carbon dioxide (CO_2) is promoted by the inclusion of the gold catalyst, Au/TiO_2 [Goodman 2004, Haruta 2004]. The catalyst is functional even at temperatures lower than 100 K at the preferred size of 3.5 nm thereby defying the notion that gold is not a reacting metal [Valden *et al*. 1998, Boccuzzi *et al*. 2001]. Bulk gold is, of course, very noble and does not react with more reactive elements such as sulphur [Pudephatt 1978]. We investigate the reaction between carbon atoms in graphite surfaces with a gold atom as an adatom.

We have used DMOL^3 and QMERA codes for this type of calculation in order to compare emanating results. The DMOL^3 calculations were performed on the periodic systems and the QMERA simulations, as mentioned earlier, uses the non-periodic systems with DMOL^3 as the quantum mechanical server. Graphite surfaces were first built for the geometry optimization calculations in DMOL^3 in order to determine their surface and binding energies. The QMERA program caters for bigger systems because of its dual mode operation (QM/MM) and DMOL^3 is limited in that capacity but the calculations are fully electronic.

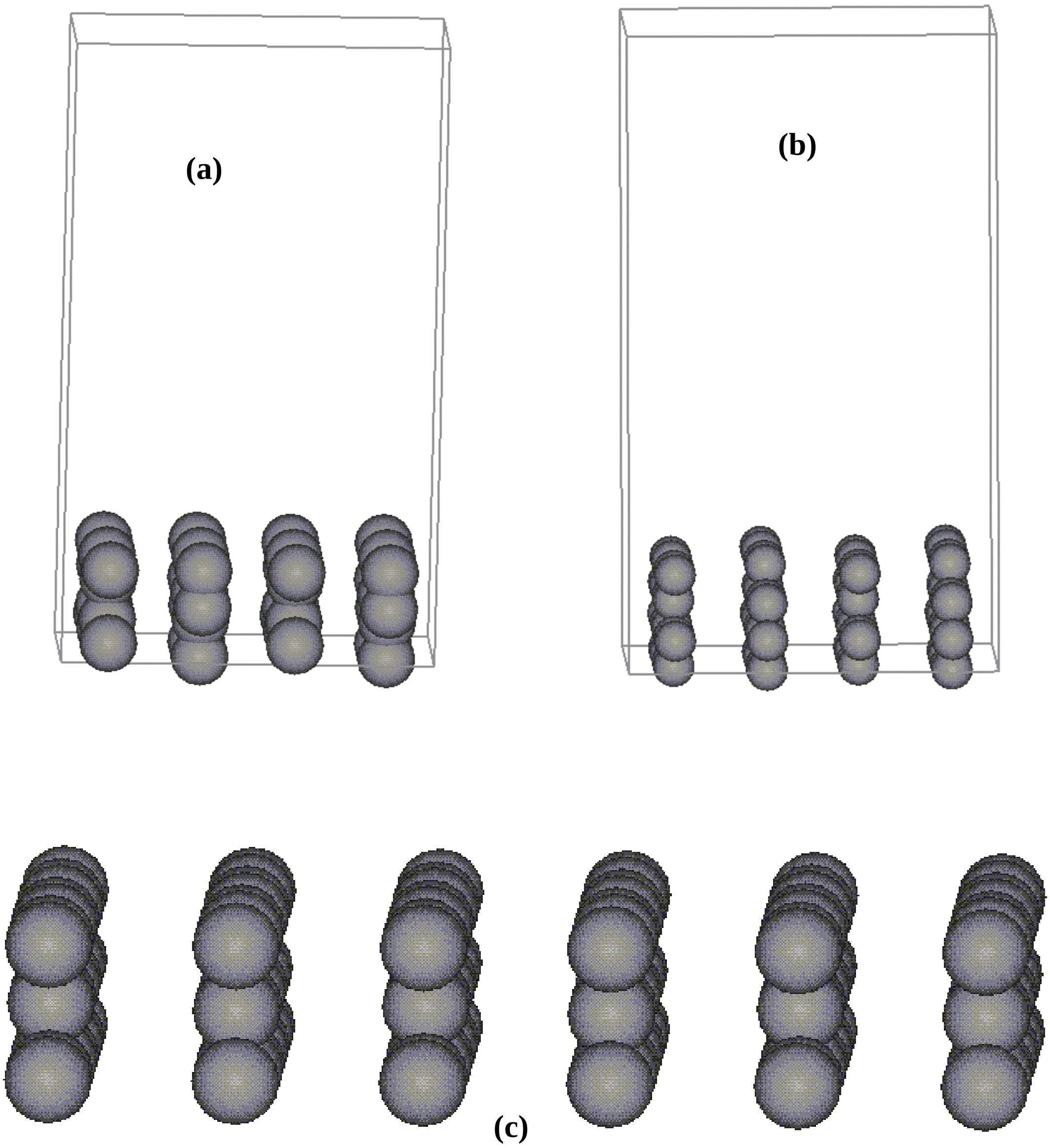

Figure 4.11 shows the graphite surfaces with different number of atoms and layers. The picture at the top left (a) shows a surface with 3 layers and 32 atoms and on the top right (b) we show the surface with 4 layers and 64 atoms. A non-periodic graphite surface with 120 atoms is shown below by (c).

The surface energies of the graphite surfaces are shown in Table 4.3. The surface energy for the surface with the same number of atoms as the bulk is calculated using equation 4.4. Equation 4.5 is used for cases where the surface has different number of atoms to the bulk. E_s is the total energy of the slab, E_b the total energy of the bulk, A the area in the x-y direction and n is the number of atoms.

$$\gamma = \frac{[E_s - E_b]}{2A} \tag{4.4}$$

Or

$$\gamma = \frac{[n_b E_s - n_s E_b]}{2A} \tag{4.5}$$

The surface energy is mainly used to determine the stability pattern of different surfaces of the same material. The surface with the highest surface energy is considered to be the least stable. The values for the surface energy shown in Table 4.3 indicate that the nonperiodic (110) surface with 120 atoms has the highest surface energy. The periodic (110) surface with 64 atoms produce the lowest value. Reactions occur easily on unstable surfaces as there is enough energy that can be used for that purpose. We aim to investigate the effect of the surface energy to the rate of the reaction process. The last row represents results from QMERA.

Table 4.3. The surface energies and the binding energies for the different graphite surfaces are shown. *indicates the QMERA results.

Type of Surface (No. of atoms)	Surface Energy ($J.m^{-2}$)	Binding Energy (eV/atom)
100 (32)	4.065	-7.21
110 (64)	3.158	-7.59
110 (120)	4.501	-7.09
110 (40)*	2.188	-6.45

The QMERA (110) graphite surface behaves differently from the DMOL^3 ones. The surface is illustrated in Figure 4.12 before and after optimization. The QM region is chosen as the two central lines of atoms leaving the outer rows to the molecular mechanics (MM) server. The calculations on the surface give a surface energy of 2.188 J.m^{-2} and the binding energy is -6.45 eV/atom. The value for the surface energy is smaller as compared to the DMOL^3 surfaces implying that the QMERA program provide a stable graphite surface. The binding energy is less negative with respect to the other surfaces in Table 4.3. This is assumed to be the effect of the less number of atoms in the QM region. The binding energy is given by the QM server (DMOL^3) suggesting that only the red atoms in Figure 4.12 are considered. However, the structure of the surface is of particular interest if we look at the configurations before and after optimization in Figure 4.12. The initial configurations show a well ordered pattern of atoms arranged in six rows. The surface has three layers. The MM atoms bend outwards in the middle resulting in the tip atoms going inwards. The QM atoms form a circle or a ring in the centre of the surface resulting in a totally different structure.

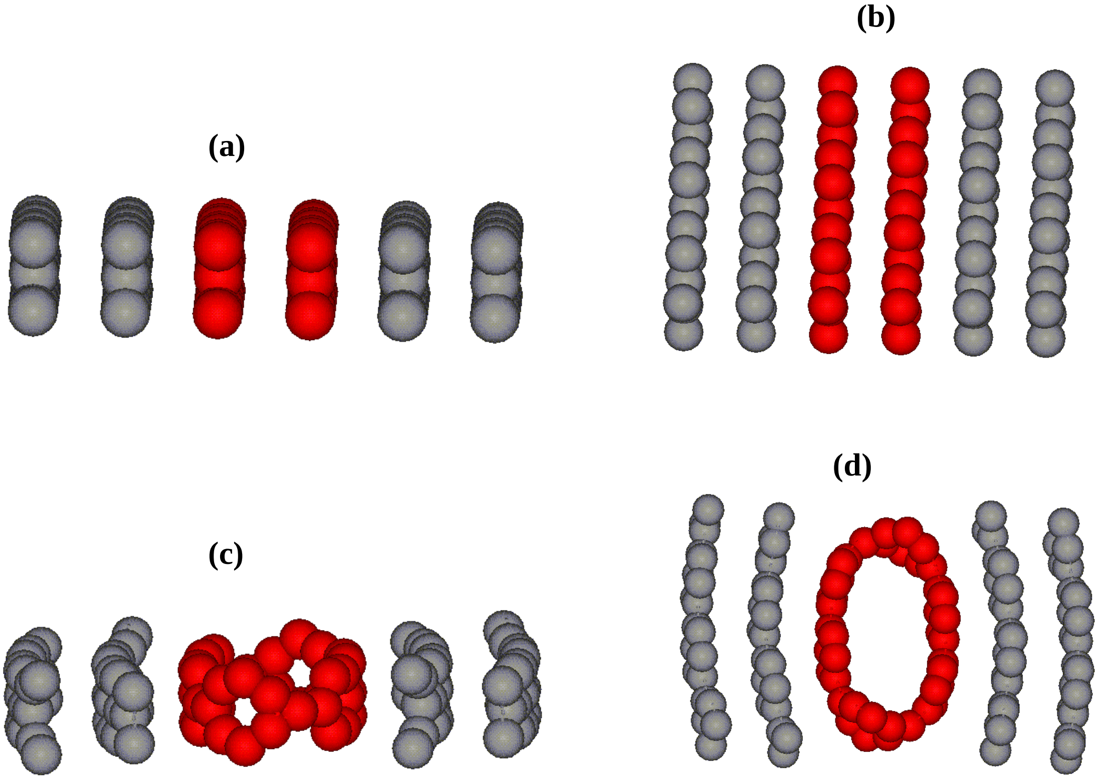

Figure 4.12. The (110) graphite surface is viewed from different angles before (a and b) and after optimization (c and d). The red colour denoted the quantum mechanical (QM) region of chosen atoms.

The interaction of the gold atom with the graphite surface using the QMERA program is shown in Figure 4.13. It has been mentioned that gold catalysts speed up the formation of carbon dioxide (CO_2) from carbon monoxide (CO). This happens when fuel cells generate energy from hydrogen. Hydrogen produced by the usual process contains large amounts of CO which, if not removed from the hydrogen, it impairs the function of a fuel cell. Therefore gold nanoparticles on a support (TiO_2) with a high surface area are good catalysts (like Au/TiO_2) for the room temperature oxidation of CO to CO_2. The balanced chemical reaction is then written as:

$$2CO + O_2 \rightarrow 2CO_2 \tag{4.6}$$

Gold in this case displays hidden value or extra power and is used as a catalyst to clean CO from hydrogen fuel.

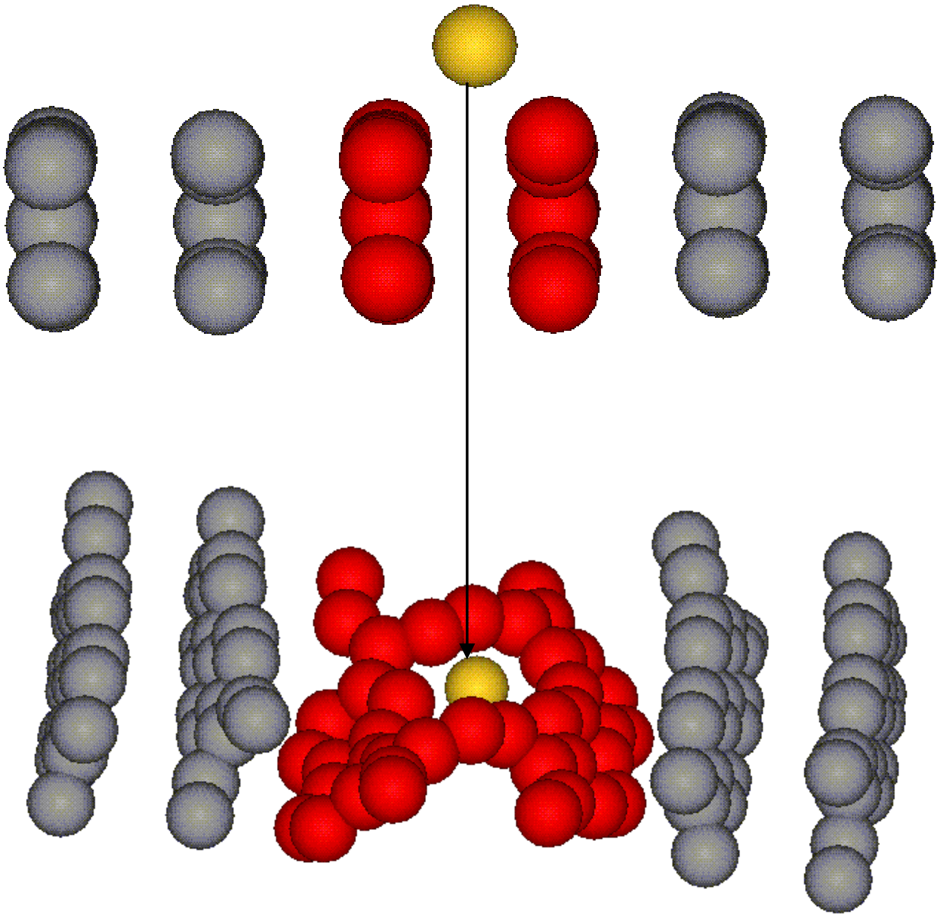

Figure 4.13. The results from QMERA are shown with a gold represented by the yellow colour. The arrow indicates the position and movement made by the Au atom.

In Figure 4.13 the gold atom and the carbon atoms coloured red belong to the quantum mechanical region. The gold adatom was strategically positioned on top between the two central rows of graphite atoms. Some separation of more than 2.5 Å was carefully adjusted so that the adatom is not forced into the surface. The carbon and gold quantum atoms cluster at the centre of the surface forming a near round shape. The gold atom is inserted inside the graphite atoms which form a disordered steep or hill centred between the left and right rows. The outer MM atoms on the right-hand and left-hand side of the slab bend inwards towards the middle atoms at the top meaning that the bottom atoms move away from the central atoms. The degree of curvature differs between the rows, i.e. the atoms closer to the central atoms show more inward bending than the atoms at the extreme outer rows. The implication of this calculations is that there is some attraction by the middle quantum mechanical (QM) atoms towards the outer molecular mechanics (MM) atoms but happens stronger for the top atoms because of the orientation of those middle atoms. Or possibly the graphite outer molecular mechanics atoms interact with each other through the help of hydrogen atoms that are included in the output of the QMERA program. The addition of the gold atom makes the binding energy less negative with a change from -6.45 eV/atom to -5.17 eV/atom.

The behaviour of the QM atoms in the graphite surface with a gold atom is similar to the QM atoms in the surface without a gold atom. They all form curves at the exterior and have an opening at the centre. The difference lies in the fact the clean surface QM atoms form a nice spherical circle while the atoms in the surface with a gold impurity form a steep or hill which is caused by the presence of a gold atom as an impurity.

We would like to compare results from the QMERA program to the fully electronic DMOL^3 code where periodic surfaces are considered. The structure of the periodic surface in Figure 4.14 undergoes the slanting deformation with the gold atom remaining at the centre of the two central layers. The results for the periodic surface concur well with those of the nonperiodic surface.

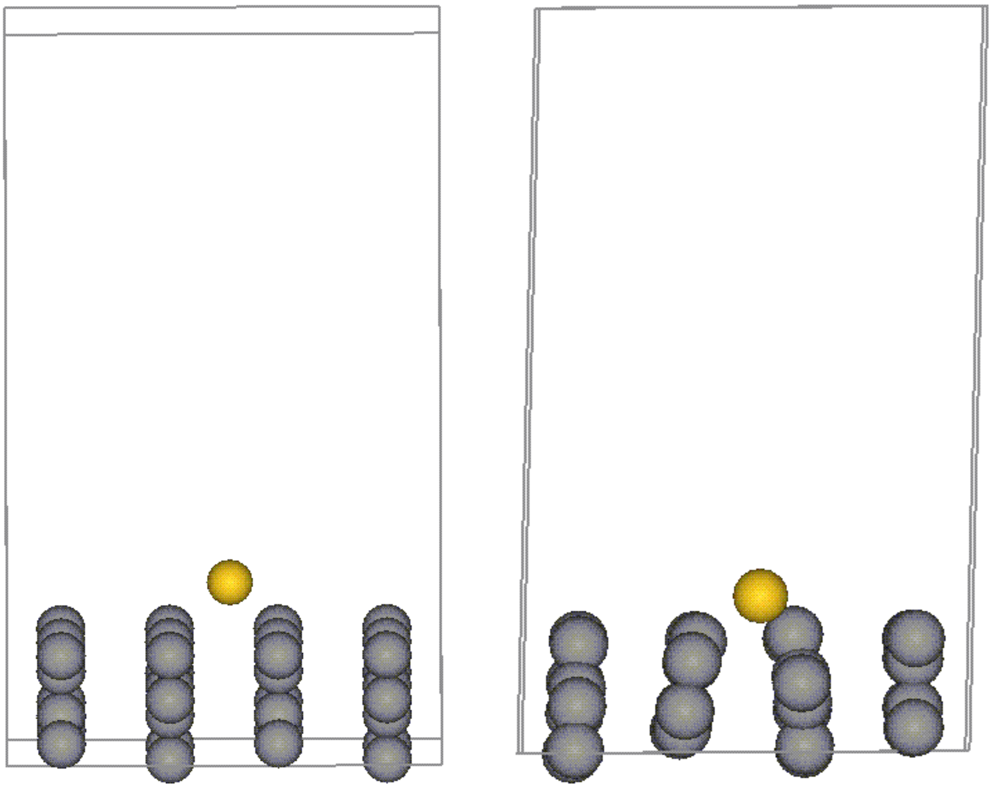

Figure 4.14. The periodic graphite surface simulated with DMOL^3 code. A gold atom remains between the central layers even at slanting.

CHAPTER 5: Conclusion and Recommendation

5.1. Conclusion

The atomistic molecular dynamics was fully implemented to simulate different gold nanomaterials in order to determine their properties under certain thermodynamic conditions using the many-body Sutton-Chen (SC) potential in the DLPOLY code. Of specific interest were gold nanoclusters and nanotubes where calculations were carried out at various temperatures and, melting temperatures, structure, density, etc. were determined. Our calculations showed that size does have an effect on melting of the studied structures although the rule is not universal. Gold nanoclusters melted well below the bulk melting temperature except for the cluster with 55 atoms. The Au_{55} cluster melted above the bulk melting temperature and such observation is attributed to the cluster having undergone reconstruction in order to reduce the tensile stress. A similar observation was made for tin nanoclusters with respect to their bulk material. However, above the Au_{55} cluster, the melting temperature increased almost linearly with cluster size. All the nanoclusters were able to show a sudden jump in the plot of the total energy as a function of temperature and, this was instrumental in the determination of melting temperatures. The temperature was increased by small amounts to achieve the sudden increase in the energy as the temperature was raised. The structure of clusters transforms from a spherical shape to the tetragonal or face-centred cubic (fcc) structures at higher temperatures.

Gold nanotubes show different structural behaviour at higher temperatures compared to the bulk and nanoclusters. Single wall nanotubes (SWNTs) form single spherical clusters under the NVT conditions while patches of clusters are formed under the NPT conditions. Multi-wall gold nanotubes (MWNTs) form spherical shapes in the NVT Berendsen ensemble compared to the fcc structures in the NPT ensemble. The small clusters formed in small single-wall nanotubes are placed at different positions in the unit cell due to the different mobilities at different temperatures. The NPT ensemble gives more atom mobility. Exact melting temperatures were not determined for these structures; however we were able to establish that all the nanotubes melt below the bulk and the nanoclusters. Melting in the multi-wall nanotubes commences from the outside and the nanotube with three separate walls show the three walls even at melting suggesting simultaneous melting. Diffusion coefficients in the nanotubes are generally higher than in the nanoclusters and the bulk.

The annealing process was carried out in the small steps of decreasing temperatures with the final structure in the previous temperature serving as the starting configurations. The lowest temperature achieved was 50 K and this was lower enough to give satisfying results in terms of the energy and the structure. The annealing of the gold nanocluster and nanotube showed that the initial configurations cannot be restored although the final annealed structure is more stable. The annealed structures give more negative energies and are very compact. The three nanoclusters in the nanotube coalesce to form one big spherical nanocluster.

A stepped nanowire was simulated in the NVT ensemble and the steps or kinks on the nanowire were found to disappear as the temperature was raised. This is because the atoms become mobile at higher temperatures and as such the steps are destroyed and the nanowire becomes a continuous line distribution of atoms.

The ab initio calculations carried out in the DMOL^3 code on gold nanoclusters show that the stability of the nanoclusters increases with the increasing cluster size. The nanoclusters with three and eight atoms are the most stable while the Au_9 cluster depicts lowest stability. The Au-Au bond length in a dimer was determined as 2.42 Å and is in reasonable agreement with the experimental value of 2.49 Å. Titanium (Ti) forms the strongest bond with Au while palladium forms the longest bond with gold at 2.97 Å. The weakest bond is obtained for a zinc (Zn) dopant. The dopants enhance the stability of the gold clusters with platinum and titanium giving more negative values at smaller sizes. For bigger gold clusters zinc is more effective in improving the stability. The bigger clusters assume more spherical shapes on optimization through bulging. The central atom moves outwards in cases where trimers are formed. The binding energy becomes more negative with size.

The morphology of the surface changes for the quantum atoms in the QMERA calculations where transformation is made to form a spherical configuration. The outer rows of atoms curve outwards at the centre while the tip atoms move inwards. The inclusion of the gold atom makes the quantum atoms to form a steep with the outer rows atoms curving inwards at the top and outwards at the bottom. The gold atom is inserted in the steep of carbon atoms although they do not form any bonds with the gold atom. The binding energy of the surfaces decreases with the addition of the gold impurity. The surface energy of the pure surface shows the QMERA surface is stable compared to the DMOL^3 ones. The DMOL^3 results with periodic systems confirm results from QMERA.

5.2. Recommendation

Since gold has found great applications in catalysis through the support of metal oxides like TiO_2, it is of fundamental importance to explore the structure of such catalysts as computational methods are well behind in that regard. The chemical reaction where carbon monoxide (CO) is converted to carbon dioxide (CO_2) can be studied in detail and could lead to insights into the reactive capabilities of gold in such cases (Equation 4.6 refers). Both the atomistic and ab inito methods can be used to study the structure and participation of a gold catalyst during the conversion of CO to CO_2. Structural properties of bigger systems can be explored using the atomistic methods while structures with fewer atoms can be studied using ab inito methods for more precise results. The importance of gold nanotubes as transport materials is subject to investigations where the strength of the materials will be tested. This can be achieved by putting different nanofluids to flow through the tubular structure, varying the size of the fluids. The atomistic methods will be preferred because bigger systems will have to be taken into consideration. The electronic structure of the nanoclusters and nanotubes can be studied further with the inclusion of the charge differences and density of states. The interaction between gold atoms and graphite surfaces can always be taken to larger sizes in order to study the mobility of such atoms as the size is increased and different adatoms can be tested against those of gold.

6. REFERENCES

Allen M. P. and Tildesley D. J., Computer Simulation of Liquids (Oxford University Press, Oxford), 1987.

Artacho E., Sanchez-Portal D. and Soler J. M., Phys. Rev. Lett., **81** (1998), 1600.

Atkins P. W., Physical Chemistry, 6th Edition, Oxford University Press, 1998.

Berendsen H. J., Postma J. P. M., van Gunsteren W. F., DiNola A. and Haak J. R., Jnl. Chem. Phys., **81** (1984), 3694.

Bilalbegović G., J. Phys.: Condens. Matter., **13** (2001), 11531.

Bilalbegović G., Phys. Rev. B., **58** (1998), 15412.

Bilalbegović G., Solid State Comm., **115** (2000), 73.

Bilalbegović G., Vacuum, **71** (2003), 165.

Blair A., Plating and Surface Finishing, August 2002.

Boccuzzi F., Chiorino A. and Manzoli M., Mater. Sci. and Engineering C, **15** (2001), 215.

Buffat Ph. and Borel J.-P., Phys. Rev. A, **13** (1976), 2287.

Chen M-X. and Yan X-H, Density functional calculations for stability of Titanium-doped Gold, http://cdsweb.cern.ch/record/1015071 (external link: http://arxiv.org/ftp/physics/papers/0702/0702026.pdf).

Chin K. C., Gohel A., Chen W. Z., Elim H. I., Ji W., Chong G. L., and Wee A. T. S., Chem. Phys. Lett., **409** (2005), 85.

Cleveland C. L., Luedtke W. D. and Landman U., Phys. Rev. Lett., **81** (1998), 2036.

Cleveland C. L., Luedtke W. D. and Landman U., Phys. Rev. B, **60** (1999), 5065.

Collins P. G. and Avouris P., Scientific American, **283** (2000), 62 (www.sci.com).

Cortie M. B. and van der Lingen E., Mater. Forum, **26** (2002), 1.

da Silva E. Z., da Silva A. J. R., and Fazzio A., Phys. Rev. Lett., **87** (2001), 256102-1.

Daw M. and Baskes M. I., Phys. Rev. B, **29** (1984), 6443.

Delley B., J. Chem. Phys., **113** (2000), 7756.

Delley B., J. Chem. Phys., **92** (1990), 508.

Delogu F., Nanotechnology, **18** (2007), 325706.

Doye J. P. K. and Wales D. J., New Jnl. Chem., **22** (2001), 733.

Dreizler R. M. and Gross E. K., Density Functional Theory (Springer Verlag, Berlin), (1990).

Ercolessi F., Andreoni W., and Tosatti E., Phys. Rev. Lett., **66** (1991), 911.

Ercolessi F., Parinello M. and Tosatti E., Philos. Mag. A, **58** (1988), 213.

Evans D. J., J. Chem. Phys., **78** (1983), 3293.

Evans D. J., J. Chem. Phys., **78** (1983), 3297.

Fermi E., Z. Phys., **48** (1928), 73.

Finnis M. W. and Sinclair J. E., Philos. Mag. A, **50** (1984), 45.

Fock V., Z. Phys., **61** (1930), 126 and 62, 795.

Freeman A. J., Wimmer E., Ann. Rev. Matter. Sci., **25** (1995), 7.

Fries Th, Becker C., Wandelt K., Schmid G. and Fauth K., Physica Status Solidi (a), **131** (2006), 29.

Gôspôr R., Acta Phys. Acad. Sci., **3** (1954), 263.

Garzón I. L., Michaelin K., Beltran M. R., Posada-Amarillas A., Ordejon P.,

Goodman D. W., Dekker Encyclopedia of Nanoscience and Nanotechnology (2004), 611.

Goring P., Pippel E., Hofmeister H., Wehrspohn R. B., Steinhart M. and Gosele U., Nano Letters, **4** (2004), 1121.

Grant G. H. and Richards W. G., Computational Chemistry (Oxford University Press), 1995.

Gülseren O., Ercolessi F. and Tosatti E., Phys. Rev. Lett., **80** (1998), 3775.

Gülseren O., Ercolessi F., and Tosatti E., Phys. Rev. B., **51** (1995), 7377.

Hakkinen H., Merikoski J. and Mannien M., J. Phys.: Condens. Matter, **3** (1991), 2755.

Hartree D. R., Proc. Cambridge Philos. Soc., **24** (1928), 89.

Haruta M. and Date M., Appli. Cat. A: General, **222** (2000), 427.

Haruta M., Jnl. New Mater. Electrochemical Systems, **7** (2004), 163.

Heidin L. and Lundvist S. J., J. Phys. C, **33** (1972), 3.

Hohenberg P. and Kohn W., Phys. Rev. B, **136** (1964), 864.

Holender J. M., Phys. Rev. B, **41** (1990), 8054.

http://contrystudies.us/south-africa/66.html.

http://www.engr.wisc.edu/news/headlines/2004/Mar01.htm.

http://www.mbendi.com/indy/ming/gold/af/sa/p0005.htm.

http://www.personal.reading.ac.uk/~scsharip/tubes.htm.

http://nevada-outback-gems.com/prospect/gold_specimen/Natural_gold.htm.

http://www.efunda.com/processes/heat_treat/softening/annealing.cfm.

http://www.chemicalelements.com/elements/au.html.

Iijima S., Nature, **354** (1991), 56.

Iijima S., Nature, **363** (1993), 603.

Jain P. K., Structural Chemistry, **16** (2005), 421.

Joshi A. M., Delgass W. N. and Thomson K. T., J. Phys. Chem., **110** (2006), 23373.

Kang J. W., Seo J. J. and Hwang H. J., J. Phys.: Condens. Matter, **14** (2002), 8997.

Kohn W. and Sham L. L., Phys. Rev. A, **140** (1965), 1133.

Kusche R., Hippler Th., Schmidt M., von Isserndorff B. and Haberland H., Eur. Phys. J. D, **9** (1999), 1.

Leach A. R., Molecular Modelling: Principles and Applications (Glaxo Wellcome Research and Development and the University of Southampton), 1996. L. Verlet, Phys. Rev., **159** (1967), 98. R.W. Hockney, Methods in Computational Physics, **9** (1970), 136. W.C. Swope, H.C. Anderson, P.H. Berens and K.R. Wilson, Jnl. Chem. Phys., **76** (1982), 637.

Luedtke W. D. and Landman U., The Jnl. Phys. Chem., **100** (1996), 13323.

Mahladisa M. A., Computer simulation studies of bulk and surface properties of gold, M.Sc Thesis (University of Limpopo), 2004.

MedeA User's Guide, Computational of Materials Properties, Theoretical Background: Density Functional Theory.

Michaelin K., Rendon N. and Garzon I. L., Phys. Rev. B, **60 (**1999**)**, 2000.

Mizoguti E., Nihey F., Yudasaka M., Iijima S., Ichihashi T. and Nakamura K., Chem. Phys. Lett., **321** (2000), 297.

Nakamura J., Kobayashi N. and Aono M., Rirken Rev., **No.37** (2001), 17.

Nakamura J., Kobayashi N., Watanabe S. and Aono M., Surf. Sci., **482** (2001), 1266.

Novaes F. D., da Silva E. Z., da Silva A. J. R. and Fazzio A., Surf. Sci., **566** (2001), 367.

Oshima Y., Koizumi H., Mouri K., Hirayama H., Takayanagi K. and Kondo Y., Phys. Rev. B, **65** (2002), 121401-1.

Parr R. G., Ann. Rev. Phys. Chem., **34** (1983), 631.

Perdew J. P. and Wang Y., Phys. Rev. B, **45** (1992), 13244.

Perdew J. P., in Electronic Structure of Solids, **91**, Ed. P. Ziesche and H. Eschrig (Akademie Verlay, Berlin, 1991).

Potential applications of nanotubes, http://www.ncnr.nist.gov/staff/taner/nanotube/-potapplications.html.

Puddephatt R. J., The Chemistry of gold, (Armsterdam-Oxford-New York) 1978.

Rafii-Tabar H. and Sutton A. P., Philos. Mag. Lett., **63** (1991), 217.

Ravelo R. and El-Batanouny M., Phys. Rev. B, **40** (1989), 9574.

Ravelo R. and El-Batanouny M., Phys. Rev. B, **47** (1993), 12771.

Rodriguez-Lopez J. L., Montejano-Carrizales J. M. and Jose-Yacaman M., Appl. Surf. Sci., **219** (2003), 56.

Rogan J., Ramirez R., Romero A. H. and Kiwi M., Eur. Phys. J. D. **24** (2003), 2301.

Roth R., Burghard M., Krstic V., Liu K., Muster J., Philipp G., Kim G. T., Park J. G. and Park Y. W., Current Appl. Phys., **1** (2001), 56.

Rubio-Bollinger G., Bahn S. R., Agrait N., Jacobsen K. W. and Vieira S., Phys. Rev. Lett., **87** (2001), 026101-1.

Schmidbaur H. H. and Chichester W., J. Mater. Proc. Tech., **110** (2001), 249.

Schmidt M., Kusche R., von Issendorf B. and Haberland H., Nature, **393** (1998), 238.

Senger R. T., Dag S. and Ciraci S., Phys. Rev. Lett., **93** (2004), 196807-1.

Sherwood P. and de Vries A. H., ChemShell User Manual, 1997-2000, available online at http://www.cse.clrc.ac.uk/qcg/chemshell.

Sherwood P., de Vries A. H., Guest M. F., Schrekenbach G., Catlow C. R. A., French S. A., Jnl. Mol. Structure (Theochem), **632** (2003), 1.

Simard B. and Hackett P. A., J. Mol. Spectros., **142** (1990), 310.

Singh A. and Tsai A. P., Sādhanā, **28** (2003), 63.

Slater J. C., Phys. Rev., **81** (1951), 385.

Smith W., Forester T. R., Todorov I. T. and Leslie M., THE DL_POLY_2 USER MANUAL (CCLRC Daresbury Laboratory), Vesion 2.16, March 2006.

Soler J. M., Garzon I. L. and Joannopoulos J. D., Sol. State Comm., **117** (2001), 621.

Sumithra S., Tyagi A. K., and Umari A. M., Mater. Sci. and Eng. B, **116** (2005), 14.

Sutton A. P. and Chen J., Philos. Mag. Lett., **61** (1990), 139.

Tans S. J., Devoret M. H., Dai H., Thess A., Smalley R. E., Geerlings L. J. and Dekker C., Nature, **386** (1997), 474.

The Star, 22 August 2006.

Thelander C., Magnusson M., Deppert K. and Samuelson L., Appl. Phys. Lett., **79** (2001), 2106.

Thomas L. H., Proc. Cambridge, Philos. Soc., **23** (1926), 542.

Tian W. Q., Ge M., Gu F. and Aoki Y., J. Phys. Chem. A, **109** (2005), 9860.

Tian W. Q., Ge M., Sahu B. R., Wang D. X., Yamada T. and Mashiko S., J. Phys. Chem. A, **108** (2004), 3806.

Todd B. D. and Lyndell-Bell R. M., Surf. Sci., **281** (1993), 191.

Valden M., Lai X. and Goodman D. W., Science, **281** (1998), 1647.

Vlachos D. G., Schmidt L. D. and Aris R., Suppl. to Z. Phys. D, **26** (1993), 156.

Wang B., Yin S., Wang G., Buldum A. and Zhao J., Phys. Rev. Lett., **86** (2001), 2046.

Wang J., Chen X., Wang G., Wang B., Lu W., Zhao J., Phys. Rev. Lett., **66** (2002), 085408.

Wang Y., Teitel S., and Dellago C., Chem. Phys. Lett., **394** (2004), 257.

Wimmer E., Density Functional Methods in Chemistry, (1991), 7.

Wimmer E., Electronic Structure Methods, Appl. Sci., **198** (1991), 171.

Wimmer E., Molecular Simulation Inc. documentation, (1998).

Xiang J., Wei S. H., Yan X. H., You J. Q. and Mao Y. L., Jnl. Chem. Phys., **120** (2004), 4251.

Xiang J., Yan S. H., You J. Q. and Mao Y. L., J. Chem. Phys., **120** (2004), 4251.

Yang Y., Perdew J. P., Cevary J. A., MacDonald L. D. and Vosko S. H., Phys. Rev. A, **41** (1990), 78.

Yuan D. W., Wang Y. and Zeng Z., J. Chem. Phys., **122** (2005), 114310.

Zhao J., Yang J. and Hou J. G., Phys. Rev. B, **67** (2003), 085404-1.

7. APPENDIX

7.1. Papers Presented at Conferences

MA Mahladisa, Determination of the stability of different clusters with size and temperature. Presented at the 2nd International Conference of the African Materials Research Society, Held at the University of the Witwatersrand, December 2003.

MA Mahladisa, The study of the stability of gold nanoclusters. Presented at the 49th South African Institute of Physics (SAIP) Conference, Held at the University of Free State, July 2004.

MA Mahladisa, The study of gold nanoclusters and nanotubes at different temperatures. Presented at the 50th South African Institute of Physics (SAIP) Conference, Held at the University of Pretoria, July 2005.

MA Mahladisa, Electronic and Atomistic Study of Gold Nanoclusters and Nanotubes. Presented at the 52nd South African Institute of Physics (SAIP) Conference, Held at the University of the Witwatersrand, July 2007.

7.2. Published Papers

MA Mahladisa *et al.*, Determination of the stability of different clusters with size and temperature, proceedings of the African Materials Research (MRS-Africa) held at the University of Witwatersrand, December 2003.

MA Mahladisa *et al.*, South African Journal of Science, **101** (2005), 1.